National Library of Canada
Bibliothèque nationale du Canada

Canadian Theses Service
Service des thèses canadiennes

Ottawa, Canada
K1A 0N4

NOTICE

The quality of this microform is heavily dependent upon the quality of the original thesis submitted for microfilming. Every effort has been made to ensure the highest quality of reproduction possible.

If pages are missing, contact the university which granted the degree.

Some pages may have indistinct print especially if the original pages were typed with a poor typewriter ribbon or if the university sent us an inferior photocopy.

Previously copyrighted materials (journal articles, published tests, etc.) are not filmed.

Reproduction in full or in part of this microform is governed by the Canadian Copyright Act, R.S.C. 1970, c. C-30.

AVIS

La qualité de cette microforme dépend grandement de la qualité de la thèse soumise au microfilmage. Nous avons tout fait pour assurer une qualité supérieure de reproduction.

S'il manque des pages, veuillez communiquer avec l'université qui a conféré le grade.

La qualité d'impression de certaines pages peut laisser à désirer, surtout si les pages originales ont été dactylographiées à l'aide d'un ruban usé ou si l'université nous a fait parvenir une photocopie de qualité inférieure.

Les documents qui font déjà l'objet d'un droit d'auteur (articles de revue, tests publiés, etc.) ne sont pas microfilmés.

La reproduction, même partielle, de cette microforme est soumise à la Loi canadienne sur le droit d'auteur, SRC 1970, c. C-30.

NL-339 (r. 88/04)

Canada

THE UNIVERSITY OF ALBERTA

COMPOSITE ICE-RESISTING WALLS

by

© BRENDAN O'FLYNN

A THESIS

SUBMITTED TO THE FACULTY OF GRADUATE STUDIES AND RESEARCH

IN PARTIAL FULFILMENT OF THE REQUIREMENTS FOR THE DEGREE

OF DOCTOR OF PHILOSOPHY

DEPARTMENT OF CIVIL ENGINEERING

EDMONTON, ALBERTA

FALL 1987

Permission has been granted to the National Library of Canada to microfilm this thesis and to lend or sell copies of the film.

The author (copyright owner) has reserved other publication rights, and neither the thesis nor extensive extracts from it may be printed or otherwise reproduced without his/her written permission.

L'autorisation a été accordée à la Bibliothèque nationale du Canada de microfilmer cette thèse et de prêter ou de vendre des exemplaires du film.

L'auteur (titulaire du droit d'auteur) se réserve les autres droits de publication; ni la thèse ni de longs extraits de celle-ci ne doivent être imprimés ou autrement reproduits sans son autorisation écrite.

ISBN 0-315-41066-3

THE UNIVERSITY OF ALBERTA

RELEASE FORM

NAME OF AUTHOR BRENDAN O'FLYNN

TITLE OF THESIS COMPOSITE ICE-RESISTING WALLS

DEGREE FOR WHICH THESIS WAS PRESENTED DOCTOR OF PHILOSOPHY

YEAR THIS DEGREE GRANTED FALL 1987

Permission is hereby granted to THE UNIVERSITY OF ALBERTA LIBRARY to reproduce single copies of this thesis and to lend or sell such copies for private, scholarly or scientific research purposes only.

The author reserves other publication rights, and neither the thesis nor extensive extracts from it may be printed or otherwise reproduced without the author's written permission.

(SIGNED) B.O'Flynn

PERMANENT ADDRESS:

c/o 10715 157 St.,
Edmonton,
Alberta

DATED July 31 1987

THE UNIVERSITY OF ALBERTA

FACULTY OF GRADUATE STUDIES AND RESEARCH

The undersigned certify that they have read, and recommend to the Faculty of Graduate Studies and Research, for acceptance, a thesis entitled COMPOSITE ICE-RESISTING WALLS submitted by BRENDAN O'FLYNN in partial fulfilment of the requirements for the degree of DOCTOR OF PHILOSOPHY.

.....

Supervisor

.....

.....

.....

External Examiner

Date...July 31/87.....

TO MY FATHER

TO MINA-ANN AND AISLINN

AND

TO GORDON AND LYNDA

ABSTRACT

Composite steel-concrete-steel sandwich walls have been proposed as an economical and structurally efficient system for resisting local ice pressures on Arctic offshore structures. It is envisioned that a typical composite ice-resisting wall in a prototype structure would have a span-to-depth ratio of about five, with the two steel skins separated a distance of about one meter. The wall would then act as a deep concrete member in which "shear" behaviour dominates.

A research program was carried out to develop a rational procedure for the analysis of the strength of composite ice-resisting walls, to calibrate the procedure by means of a series of laboratory tests, to investigate the effects of various design details on the wall behaviour, and to propose suitable details for composite ice-resisting wall construction.

The proposed analytical method utilises the lower bound theorem of plasticity. Graphical techniques are developed for the construction of statically admissible stress fields under general loading. Since the predicted failure load is highly dependent on the effective concrete strength when failure occurs in the concrete core, a rational expression for the concrete effectiveness factor is proposed.

Seventeen beam-type steel-concrete-steel sandwich specimens were tested in the laboratory in order to calibrate the expression for the effectiveness factor and to

examine the effects of various design details. It was found that short stud-type shear connectors could provide the necessary shear transfer capabilities to ensure composite action between the steel and the concrete. Both plain concrete and steel-fiber-reinforced concrete are seen as potentially attractive infill materials. Early distress may be encountered in the concrete if stiffened plate bulkheads with excessively large stiffener spacings are used. Finally, heat-affected zones due to welding near the supports may significantly reduce the post-crushing-ductility of the wall.

A composite ice-resisting wall configuration which incorporates the preferred details is proposed, and areas for further research are suggested.

ACKNOWLEDGEMENTS

I sincerely thank Dr. J.G. MacGregor for his encouragement and guidance through all aspects of this work. The research was jointly funded by Grant A1673 from the Natural Science and Engineering Research Council of Canada and by C-FER (Centre for Frontier Engineering Research). I am grateful to Mr. Tom Zimmerman from C-FER for his interest and input in ensuring that the research program was compatible with the needs of industry.

The testing program could not have been completed without the invaluable expertise of Larry Burden, Richard Helfrich and Vijay Parmar at the Morrison Structural Laboratory. The steel fibres for the test specimens were supplied by Dome Crete Canada Inc. at no cost.

I am endebted to Dr. J.N. Sheahan, Department of Statistics and Applied Probability, University of Alberta for his advice on the choice of appropriate mathematical models and for his assistance in the interpretation of the statistical analyses.

Finally, I am deeply grateful to my wife, Mina-Ann, for her patience and support during the ungodly working hours which were often required over the past four years.

Table of Contents

Chapter — Page

1. INTRODUCTION 1

1.1 Motivation 1

1.2 Object and Scope 4

2. LITERATURE REVIEW 6

2.1 Ice Loading on Offshore Structures. 6

2.2 Externally-reinforced Concrete Construction. 12

2.2.1 Non-offshore Applications. 12

2.2.2 Steel/concrete/steel Sandwich Cylinders for Offshore Construction. 14

2.2.3 Steel/concrete/steel Sandwich Walls for Offshore Construction. 15

2.2.3.1 Discussion. 19

2.3 Concrete Plasticity. 20

3. EXPERIMENTAL PROGRAM 21

3.1 Introduction 21

3.2 Test Specimens 23

3.2.1 B4 Test Series (l/d = 4) 23

3.2.2 B6 Test Series (l/d = 6) 32

3.2.3 B5 Test Series (l/d = 5) 39

3.3 Material Properties 42

3.3.1 Concrete 42

3.3.2 Steel 46

3.4 Instrumentation of Composite Specimens 48

3.4.1 Displacement Measurement 48

3.4.2 Concrete Strains 51

3.4.3 Steel Strains 55

3.5 Test Setup 59

3.5.1 General 59

3.5.2 Load Application and Load Measurement 62

3.5.3 Load/Reaction Devices 64

4. TEST RESULTS 70

4.1 Introduction 70

4.2 General Test Observations 70

4.2.1 Failure Loads and Modes of Failure. 70

4.2.2 Load-deflection Response, Ductility and Load Cycling. 72

4.3 Effects of Details Investigated in the B4 Series. 80

4.3.1 Concrete Confinement Near the Supports. ...80

4.3.2 Type of Shear Connector. 80

4.3.3 Type of Support. 81

4.3.4 A Note on the Effect of Roller Assemblies vs. Teflon-based Slip Surfaces at the Load and Reaction Points. 81

4.4 Effects of Details Investigated in the B6 Series. 82

4.4.1 Concrete Strength. 82

4.4.2 Type of Concrete (Plain or Steel-fibre-reinforced) in an Over-reinforced Specimen. 84

4.4.3 Type of Concrete (Plain or Steel-fibre-reinforced) in an Under-reinforced Specimen. 84

4.4.4 Shear Studs on the Span of the Support Plate of an Over-reinforced Specimen. 85

4.4.5 Loading Arrangement. 86

4.5 Effects of Details Investigated in the B5 Series. 86

4.5.1 Diaphragm Plates at the Supports. 87

4.5.2 Shear Studs on the Span of an Under-reinforced Specimen. 87

4.5.3 Rotational Restraint at the Supports. 87

4.6 Strain and Curvature in the Steel Plates. 88

4.6.1 Longitudinal Strain and Curvature Profiles 88

4.6.1.1 Loaded Plate. 88

4.6.1.2 Support Plate. 93

4.6.2 Orthogonal Strain Ratios 96

4.6.3 Variation of Longitudinal Strain across the Width of the Plate. 100

4.6.4 Lateral Curvature Profiles Between Stiffened Plate Supports 105

4.7 Concrete Strains 108

4.7.1 General Remarks 108

4.7.2 Principal Strains 109

5. ANALYTICAL MODEL 123

5.1 Introduction 123

5.2 Fan-Type Stress Fields 125

5.3 Simply Supported Composite Ice-Resisting Wall: Fan Stress Field 130

5.4 Stress Field for a Continuous Composite Ice-Resisting Wall 136

5.4.1 Introduction 136

5.4.2 Zone 1 138

5.4.3 Zone 2 138

5.4.4 Zone 3 142

5.4.5 Numerical or Graphical Techniques? 147

5.5 Eccentric Patch Loading. 148

5.6 Interfacial Shear Transfer 151

5.7 Mechanism for Shear Transfer 155

5.8 Principal Stresses at an Internal Point 157

6. ANALYSIS OF TEST RESULTS 159

6.1 Introduction 159

6.2 Analysis Procedure 160

6.2.1 Basic Stress Field 160

6.2.2 Critical Stress Location and Failure Mode 161

6.3 Failure Stress in Tested Beams 166

6.4 Failure Criterion: Effective Concrete Strength .166

6.5 Summary of Analytical Procedure 184

6.6 Comparisons of observed failure loads with those predicted by other theories 185

6.6.1 CAN3 A23.3 - M84, General Method 185

6.6.2 CAN3 A23.3 - M84 Simplified Method 189

6.6.3 Niwa's Equation 193

6.7 Comparison of Measured and Predicted Steel Strains 194

6.7.1 Loaded Plate 194

6.7.2 Support Plate 206

7. CONCLUSIONS AND RECOMMENDATIONS 208

7.1 Introduction 208

7.2 Conclusions 209

7.2.1 General 209

7.2.2 Construction Details. 210

7.2.3 Fan-type Stress Fields. 211

7.2.4 Failure criterion. 212

7.3 Recommendations. 213

7.3.1 An Appropriate Composite Ice-Resisting Wall Configuration. 213

7.3.2 Future Work. 215

7.4 Closure. 217

REFERENCES 219

APPENDIX A: CONCRETE TEST RESULTS. 225

APPENDIX B: CALCULATIONS FOR THE BASIC STRESS FIELDS. ...237

B.1 Uniform Loading: Basic Stress Field for l/d = 5. 237

B.2 Eccentric Patch Load: Basic Stress Field for Specimen B6/7. 242

APPENDIX C: REGRESSION ANALYSIS TO DETERMINE AN EXPRESSION FOR THE EFFECIVENESS FACTOR υ. 250

List of Tables

Table		Page
3.1	Parameters associated with each test specimen.	24
3.2	Dimensions of test specimens.	25
3.3	Concrete mix proportions.	43
3.4	Compressive cylinder strengths of concrete in specimens	45
3.5	Mechanical properties of steel.	49
4.1	Failure loads and descriptions of failure.	71
4.2	Ductility ratios.	77
6.1	Summary of calculations to determine σ_{1K} and σ^{*}_{1K} for the test specimens.	167
6.2	Calculation of input data for regression analysis of v.	176
A.1	Mix designations and age at testing for each specimen.	227
A.2	Concrete test results for Mix H4.	228
A.3	Concrete test results for Mix H6.	229
A.4	Concrete test results for Mix H5.	230
A.5	Concrete test results for Mix L6.	231
A.6	Concrete test results for Mix H6/1.5 (1.5% fibres/vol.).	231
A.7	Concrete test results for Mix H6/1.0 (1.0% fibres/vol.).	232

List of Figures

Figure		Page
1.1	Components of an offshore structure	2
2.1	Some possible mechanisms for global ice loading.	7
2.2	Parameters which influence local ice pressures.	10
2.3	Suggested ice pressure/loaded area curve.	11
3.1	Beam specimen from a composite ice-resisting wall	22
3.2	B4 series: Loading system.	26
3.3	Idealised shear stress distribution at the steel/concrete interface of the loaded plate.	28
3.4	B4 series; shear connector layouts.	29
3.5	Lateral confinement system	31
3.6	Stiffened plate support.	33
3.7	B6 series: Loading system.	34
3.8	B6 series: Shear connector layouts.	36
3.9	Contribution of friction at the steel/concrete interface.	37
3.10	B5 series: Loading system.	40
3.11	B5 series: Shear connector layouts.	41
3.12	Tension coupons: Dimensions and gauge locations.	47
3.13	Displacement transducer layout.	50
3.14	B4 series: Rosette layout.	52
3.15	B6 series: Rosette layout.	53
3.16	B5 series: Rosette layout.	54
3.17	B4 series: Strain gauge layout.	56
3.18	B6 series: Strain gauge layout.	57
3.19	B5 series: Strain gauge layout.	58

Figure Page

3.20 Internal gauge protection system. 60

3.21 Loading frame. 61

3.22 Hydraulic circuit diagram. 63

3.23 Loading devices and braces. 65

3.24 Load application at large deformations. 66

3.25 Reaction devices. 68

4.1 B4 series: Load - midspan deflection plots. 73

4.2 B6 series: Load - midspan deflection plots. 74

4.3 B5 series: Load - midspan deflection plots. 75

4.4 Enlarged load-deflection plot for specimen B5/5, showing the areas used in the definition of the ductility ratios PYD and PCD. 78

4.5 Comparison of load-relative support displacement plots for Teflon pads and roller assemblies. 83

4.6 B4/1: Longitudinal strain and curvature profiles in the loaded and support plates. 89

4.7 B6/1: Longitudinal strain and curvature profiles in the loaded and support plates. 90

4.8 B6/7: Longitudinal strain and curvature profiles in the loaded and support plates. 91

4.9 B5/1: Longitudinal strain and curvature profiles in the loaded and support plates. 92

4.10 Curvature formation in the support plate. 94

4.11 Effect of a biaxial stress state on the assumption of uniaxial stress conditions. 98

4.12 Calculated values of $F_x/F_{x(u)}$ 99

Figure Page

4.13 Use of the three-point Gauss rule for the numerical evaluation of ϵ_{av}. 101

4.14 B4/4 B6/1 and B5/1: Best-fit longitudinal strain distributions across the loaded plate. 103

4.15 Calculated values of ϵ_{av}/ϵ_x. 104

4.16 Local failure at a stiffened plate support. 106

4.17 B4/4: Lateral curvature in the support plate between the stiffeners of the stiffened plate supports. 107

4.18 Assessment of the reliability of multiple Mohr circles of strain (tension positive). 110

4.19 B6/1 and B6/7: Principal strain profiles in the concrete core. 112

5.1 Strut-and-tie model for a normalised corbel with discrete concentrated loads. 126

5.2 Definition of a fan-strut. 129

5.3 Fan stress field for a normalised corbel under uniform load. 131

5.4 Fan stress field for a simply supported reinforced concrete beam with top reinforcement and under uniform load. 132

5.5 Fan stress field for a simply supported composite beam under a uniform load. 134

5.6 Fan stress field for a continuous composite beam under a uniform load. 137

5.7 Zone 1. 139

5.8 Zone 2. 140

5.9 Zone 3. 143

5.10 Flowchart to calculate the applied load p. 145

5.11 Free body diagram of half-beam. 146

Figure		Page
5.12	Fan stress field for a continuous composite beam under an eccentric patch load.	149
5.13	Geometry for interfacial shear transfer.	152
5.14	Theoretical interfacial shear stress distribution at the loaded surface of a corbel.	154
5.15	Mechanical shear connector evaluation.	156
5.16	Evaluation of internal stress at an arbitrary point within the concrete core.	158
6.1	Failure location "K".	162
6.2	Secondary load path after concrete has crushed at K.	164
6.3	Crack width w at K.	171
6.4	Interaction between f'_c and G_K at K.	174
6.5	Scatter plot for the measured effectiveness factor υ_t against the confinement characteristic G_K.	177
6.6	Relationships between measured and predicted (a) effectiveness factors, and (b) loads, using equation [6.12].	179
6.7	Relationship between υ and f'_c using equation [6.12].	181
6.8	Details of beams B1/1.0, B1/1.5 and B1/2.0 as tested by Rogowsky and MacGregor (1983).	183
6.9	Measured principal strain in the concrete near K .vs. the applied load p (MPa) for the B6 and B5 series.	187
6.10	Test-to-predicted ratios for failure load using the CAN3 A23.3 M-84 General Method.	188
6.11	Stress field for a uniformly loaded simply supported reinforced concrete deep beam according to the CAN3 A23.3 M-84 General Method.	190

Figure Page

6.12 Test-to-predicted failure load ratios using the CAN3 A23.3 M-84 Simplified Method. 192

6.13 Test-to-predicted failure load ratios using Niwa's equation. 195

6.14 Theoretical shear stress distribution at the loaded plate/concrete core interface of a continuous composite beam. 197

6.15 Calculation of $\epsilon_{1p}(x)$. 198

6.16 Predicted and measured strain distributions at failure in the loaded plates of the uniformly loaded specimens B4/1, B6/1 and B5/1. 199

6.17 Explanation for the peak strains which were observed in the loaded plate of specimen B5/1. 200

6.18 Predicted and measured strain distributions in the loaded plate of the patch-loaded specimen B6/7 at failure. 202

6.19 Measured strain distributions in the loaded plate of specimen B6/7 at various load levels. 204

6.20 Compatibility shear stresses in specimen B6/7. 205

6.21 Predicted and measured strain distributions in the support plates of specimens B4/1, B6/1, B6/7 and B5/1. 207

7.1 Recommended configuration for a composite ice-resisting wall. 214

A.1 Mix H4: Least squares estimate of cylinder strength/time curve. 233

A.2 Mix H6: Least squares estimate of cylinder strength/time curve. 234

A.3 Mix H5: Least squares estimate of cylinder strength/time curve. 235

A.4 Mix H6/1.0: Load/midspan deflection plots for modulus of rupture beams. 236

Figure Page

B.1 Basic stress field for the B5 series with uniform loading. 238

B.2 Basic stress field for the B4 series with uniform loading. 243

B.3 Basic stress field for the B6 series with uniform loading. 244

B.4 Basic stress field for for specimen B6/7 with a patch load. 245

B.5 Details of the construction of the imaginary hydrostatic nodes near the supports of specimen B6/7. 247

List of Plates

Plate		Page
4.1	B4/2: Failure mode.	113
4.2	B4/3: Failure mode.	114
4.3	B6/1: Failure mode.	115
4.4	B6/3: Failure mode.	116
4.5	B6/4: Final deformed shape.	117
4.6	B6/4: Stud failure in cantilever.	117
4.7	B6/6: Horizontal crack over the support.	118
4.8	B6/7: Failure mode.	119
4.9	B5/1: Failure mode.	120
4.10	B5/3: Failure mode and plate fracture.	121
4.11	B5/4: Failure mode.	122
6.1	Secondary load path in specimen B6/1.	165

LIST OF SYMBOLS.

a	horizontal projection of the length of a crack in the concrete.
b	width of specimen.
d	depth of concrete core.
E_c	modulus of elasticity of concrete.
E_{lp}	modulus of elasticity of the steel in the loaded plate.
E_{sp}	modulus of elasticity of the steel in the support plate.
f	shear friction coefficient between steel and concrete.
f_r	modulus of rupture.
f_t	splitting cylinder strength.
f'_c	concrete cylinder strength.
f^*_c	effective concrete strength.
F_y	yield stress of steel.
F_u	ultimate stress of steel.
g	support width.
g'	effective support width.
G_K	confinement characteristic.

l	centre-to-centre distance between supports.
L	length of cantilever.
M	multiplier to convert from the basic stress field to the stress field at failure.
p	applied load, expressed in MPa, corresponding to the hydrostatic stress u_c, and calculated from the basic stress field.
p_p	predicted applied load at failure, expressed in MPa.
p_t	applied load at failure as observed from the test, expressed in MPa.
P	load applied by a hydraulic ram, expressed in MPa.
q	average ice-crushing pressure.
r	a distance measured along a fan line, as defined in Fig. 5.2.
R	radius of curvature of a fan line at its intersection with a hydrostatic node, as defined in Fig. 5.2.
t_{lp}	thickness of the loaded plate.
t_{sp}	thickness of the support plate.
T_{sp}	tension force in the support plate.
u_c	hydrostatic stress in the concrete nodal zone in the basic stress field.
V	shear force at a section.

w	crack width.
ϵ_{lp}	longitudinal strain in the loaded plate.
ϵ_{sp}	longitudinal strain in the support plate.
ϵ_y	yield strain of steel.
ϵ_u	ultimate strain of steel.
ϵ_2	strain in concrete transverse to a fan line.
Θ	angle between a fan line and the vertical axis.
μ	Poisson's ratio.
ρ	a distance along a fan line, as defined in Fig. 5.2.
σ_1	stress in concrete along a fan line.
σ_2	stress in concrete transverse to a fan line, taken equal to zero.
τ	shear stress.
v	concrete effectiveness factor.

1. INTRODUCTION

1.1 Motivation

The discovery of significant oil deposits beneath the Canadian Beaufort Sea and off the east coast of Canada has created a need for offshore structures capable of withstanding the rigors of these harsh environments. In particular, the walls of these structures must resist pressures of the order of 10 MPa which result from ice impact.

Existing exploration structures for the Arctic have been constructed using either structural steel or reinforced concrete walls. Composite ice-resisting walls have been proposed as an alternative to these systems (Matsuishi et al., 1977). A composite ice-resisting wall consists of two continuous steel plates separated by a plain concrete core and supported by internal bulkheads, as shown in Fig. 1.1. Composite action between the steel and concrete layers is provided by a combination of interfacial friction and mechanical shear connectors.

Composite ice-resisting walls offer several advantages over wall systems using either structural steel or reinforced concrete alone. The advantages over steel walls are:

1. The possibility of hard ice features punching through the wall is reduced.
2. Concentrated loads are distributed over a larger

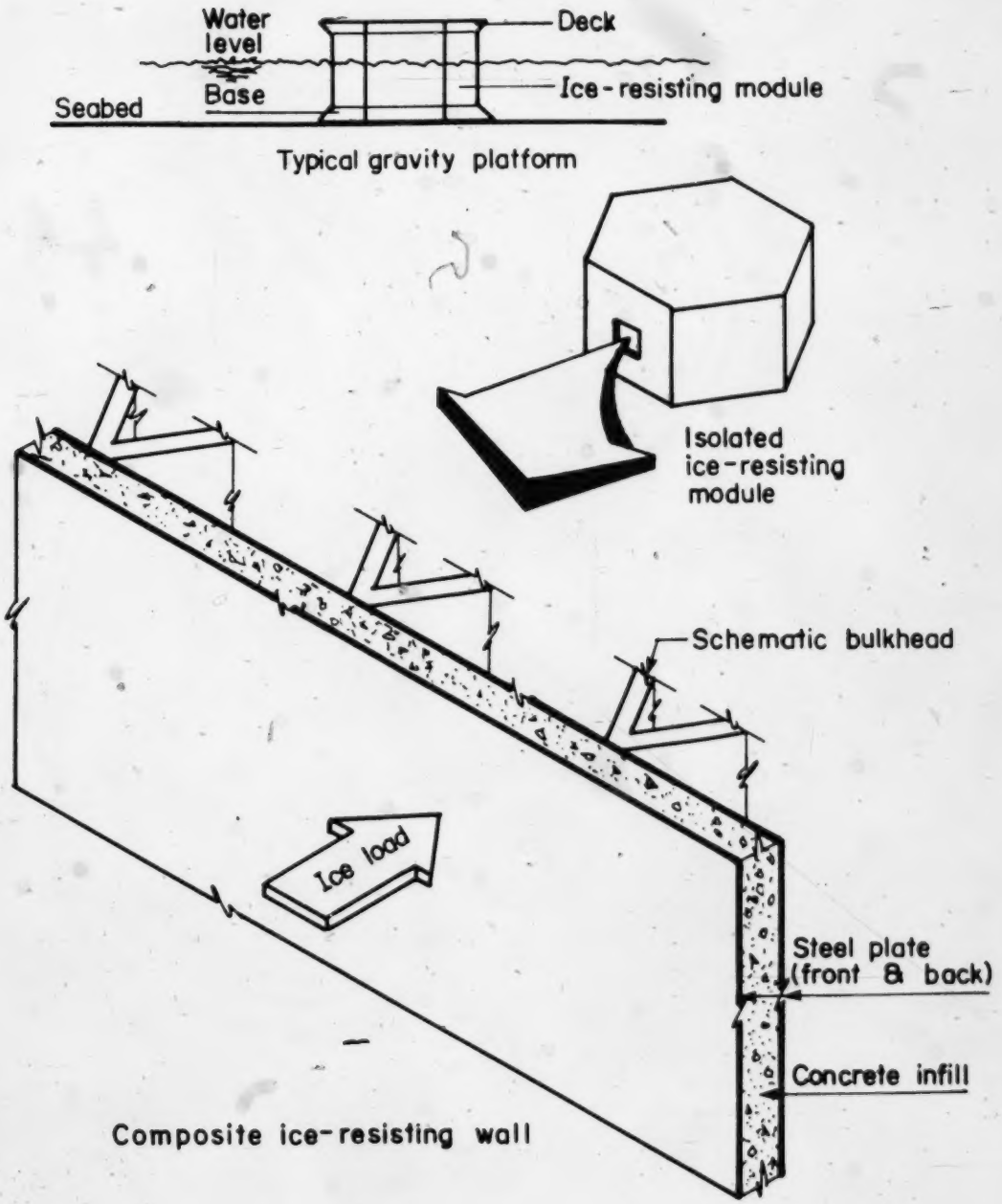

Figure 1.1 Components of an offshore structure

bulkhead area, thereby permitting more efficient bulkhead design.

A composite ice-resisting wall also offers the following advantages over a reinforced concrete wall:

1. Durability is enhanced, since no concrete is exposed.
2. Falsework is not required during concrete pouring, because the two plates act as forms.
3. No reinforcement is needed, since the external plates serve as reinforcement.

A possible configuration for an offshore structure utilising composite ice-resisting walls is shown in Fig. 1.1. This three-component system is based on the Concrete Island Drilling System (Yee et al., 1984). The mudbase acts as a pedestal for the structure, and is located below the zone of ice-contact. The ice-resisting module is approximately centered about the water line, and is also used for oil storage. The production deck is located above this module.

The bulkhead spacing within the ice-resisting module is a function of the ice-loading, the external wall and bulkhead thickness, and the global requirements of the module. Preliminary design considerations and industrial concensus indicate a reasonable bulkhead spacing to be approximately five meters. The minimum thickness of a composite ice-resisting wall is dictated by the accessability of the interstitial space to welders, concrete placers and inspectors during construction. One meter is

adequate. The foregoing considerations indicate, then, that a span-to-depth ratio approximately equal to five is practical for a composite ice-resisting wall, provided that strength and stiffness requirements are satisfied using these proportions.

1.2 Object and Scope

The objectives of this research program are;

1. To develop a rational procedure for the analysis of the strength of composite ice-resisting walls. Such a procedure should be simple and versatile.
2. To calibrate the analytical procedure by means of a series of tests.
3. To investigate the effects of various design details on the behaviour of composite ice-resisting walls.
4. To propose suitable details for composite ice-resisting wall construction.

The effects of the following parameters on the behaviour of composite ice-resisting walls with span-to-depth ratios from four to six, inclusive, are investigated:

1. Concrete strength.
2. Concrete type (plain or steel-fiber-reinforced).
3. Type and layout of mechanical shear connectors.
4. Type of bulkhead (solid or stiffened plate).
5. Lateral concrete confinement.
6. Type of loading (uniform or patch).

7. Extent of rotational restraint at supports.
8. Load cycling.

Chapter 2 of this thesis presents a review of the literature on ice pressures on offshore structures and tests on sandwich sections. The test specimens and the test program are described in Chapter 3, and the main test results are discussed in Chapter 4. Statically admissible stress fields which are suitable for the analysis of composite ice-resisting walls are developed in Chapter 5. The analytical model is applied to the test results in Chapter 6, and a failure criterion for composite ice-resisting walls is proposed. The conclusions and recommendations are presented in Chapter 7, and areas for future work are suggested.

2. LITERATURE REVIEW

2.1 Ice Loading on Offshore Structures.

The economical and efficient design of offshore structures for the Beaufort Sea demands that the origins and subsequent behaviour of the ice loading events be understood. Several ongoing independent research efforts have been undertaken within the last decade, with a view to developing a better understanding of the ice/structure interaction. A summary of these efforts is provided by Allyn (1986). Despite these ongoing investigations, design ice loads are not yet available due to the sensitivity of the loading conditions to the drilling location, the difficulty in estimating 100-year design loads from 10-year samples, and also the proprietary nature of much of the data. In lieu of this information, it is important that at least the general characteristics of ice loading be understood.

Croasdale (1984) provides a review of the origins and effects of global ice loads on offshore structures. Three possible scenarios for global ice loads are proposed, as shown in Fig. 2.1.

1. Limit stress load (F_{LS}): A very large ice feature is in continuous contact with the structure (Fig. 2.1(a)). The maximum load to the structure is controlled by the "average crushing pressure" (q) of the ice, i.e.

$$F_{LS} = q \times t \times D$$

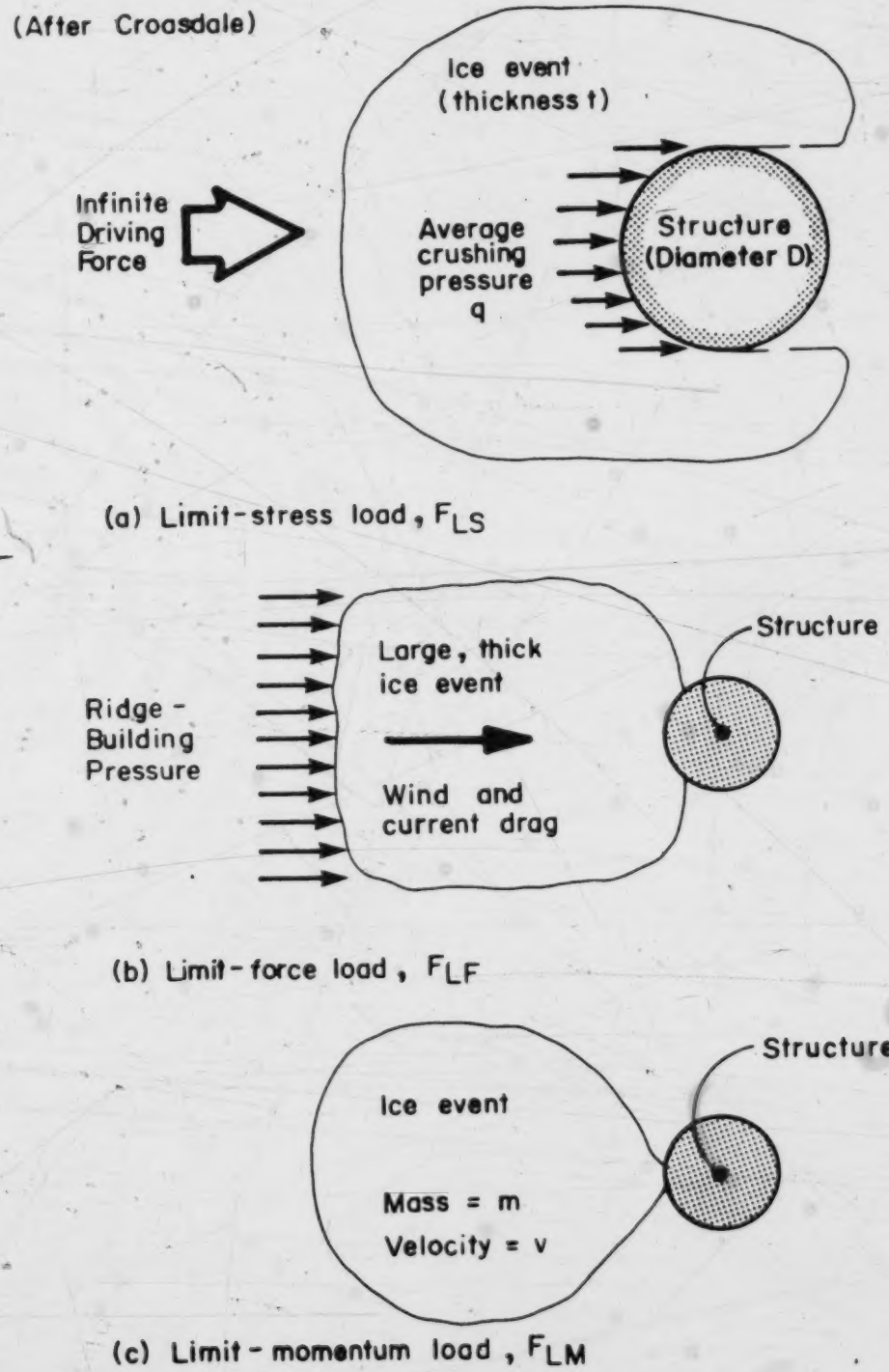

Figure 2.1 Some possible mechanisms for global ice loading.

where t is the thickness of the ice sheet and D is the diameter of the structure. In this case, the force which is driving the ice sheet can be considered to be infinite.

2. Limit force load (F_{LF}): The ice sheet is in continuous contact with the structure, but ice-crushing does not occur at the ice/structure interface. The global load on the structure is that which equilibrates the external forces acting on the floe (Fig. 2.1(b)), i.e. the combination of the ridge-building force behind the sheet and the wind and current drags on the sheet.
3. limit momentum load (F_{LM}): An ice feature of mass m and velocity v impacts against the structure (Fig. 2.1(c)), thereby imparting a force F_{LM} which is consistent with the conservation of total energy within the ice/structure system.

The critical global load to the structure is then defined as

$$F = \max\left[F_{LM},\ \min(F_{LS},\ F_{LF})\right],$$

as stated by Allyn(1986), and is of particular importance when the global stability of the structure is being examined.

It is also necessary to estimate the local ice pressures associated with the global load in order that the individual elements of the structure (and in particular the ice-resisting wall) can be designed. Bercha et al. (1985) have examined the local pressures associated with ice/structure interaction, and state that:

> "the explicit dependence of localised contact pressure on ice and structural stiffness and mechanical properties for given interaction conditions has been known to significantly affect the local pressure magnitude and distribution..... Pressures generated can range from 7000 psi (48 MPa) for the high speed impact associated with ice-contact zone rheology, to barely significant 50 psi (0.34 MPa) pressures for slow interactions in which even quasi-static crushing is not developed."

The parameters of the ice and the structure which affect local ice pressure have been listed by Bercha, and are reproduced in Fig. 2.2. Determination of the ice pressure distribution is a complex procedure, and is certainly not accurately modelled using an "average crushing strength" approach. A finite element analysis (also by Bercha), during which an energy inventory was kept at intervals of time, yielded the conclusion that the local ice pressure decreases as the thickness of the ice-resisting wall increases. This is not surprising since, for a given total strain energy, the required stress regime within the wall will be lower as the volume of the wall material increases.

In view of the complexities of the ice/structure interaction as shown in Fig. 2.2, the formulation of ice pressure/loaded area curves is a difficult task. Nevertheless, the curves shown in Fig. 2.3 were suggested by Watt (1984). Although by no means final, these curves at least provide the designer with an estimate of the local loads for which the structure should be proportioned.

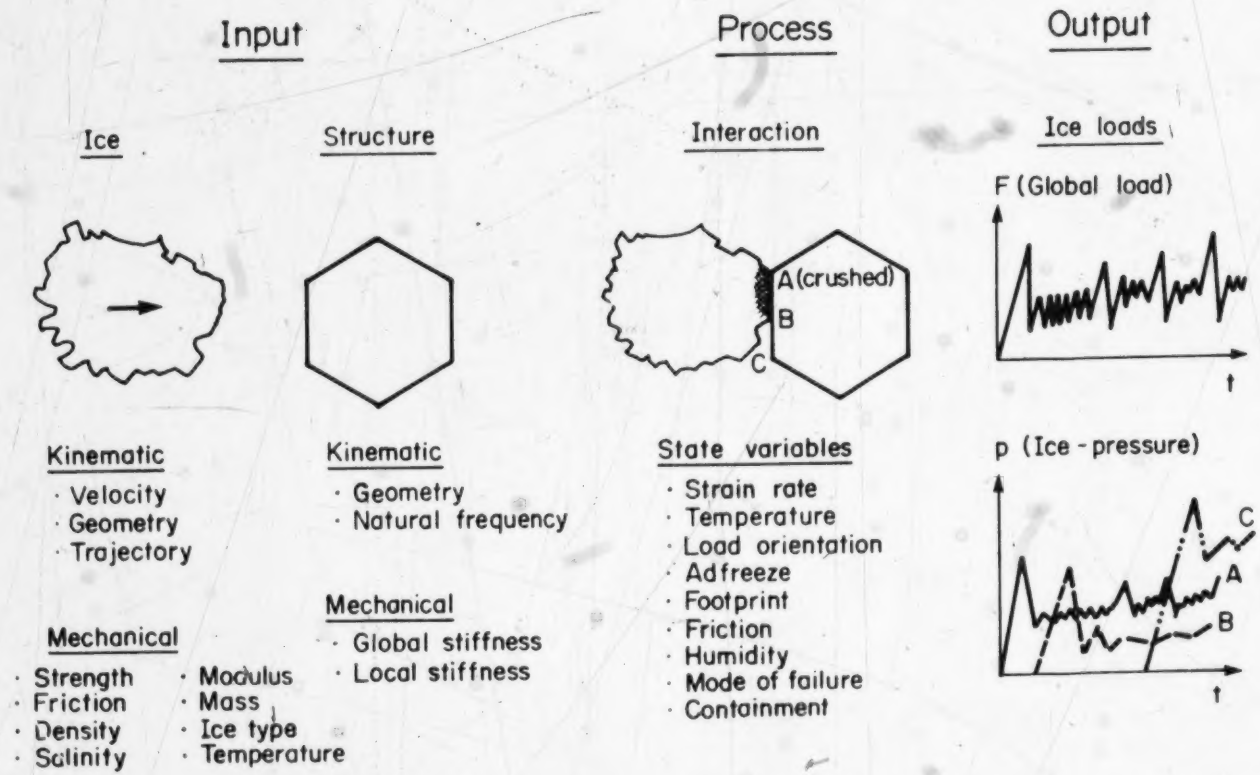

Figure 2.2 Parameters which influence local ice pressures.

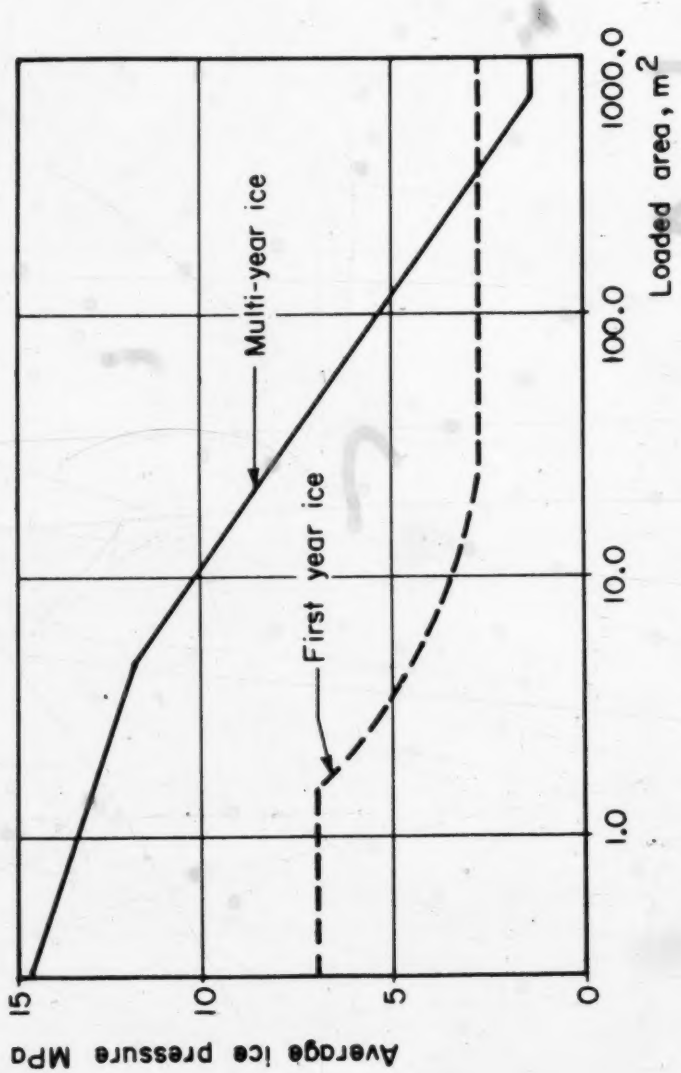

Figure 2.3 Suggested ice pressure/loaded area curve.

2.2 Externally-reinforced Concrete Construction.

2.2.1 Non-offshore Applications.

Considerable attention is being paid to the use of steel-concrete-steel sandwich members for offshore structures. However, the advantages of externally-reinforced concrete for non-offshore structural engineering applications have been recognised for several years.

1. Concrete slabs supported on and interconnected with structural steel members were proposed for floor systems as early as 1929 (Knowles, 1973). Systems in which concrete slabs are connected to steel beams or welded steel trusses by means of welded stud shear connectors are now widely used. An history of the evolution of this system is given by Brattland and Kennedy (1986).
2. Taylor et al. (1976, 1978) proposed the use of steel channels with welded stud shear connectors as the soffits for cast-in-place concrete beams, as part of a complete composite building system. These channels would act as both reinforcement and formwork. Tests showed that the behaviour of such beams was essentially the same as that for the reinforced concrete equivalents.
3. L'Hermite and Bresson (1967) carried out tests on plain concrete beams which had steel plates glued to the soffit only, and also on beams which had steel plates glued to both the soffit and the vertical sides. These tests led to the construction of a frame in which the

concrete for the beams was poured into U-shaped steel forms which were coated with glue, and the performance of the frame was monitored over time. Bresson (1971) investigated the shear distribution along such glued joints, and the mechanical properties of the adhesives which were used.

4. Lerchenthal (1967) carried out tests on simply supported two-way slabs reinforced with a steel plate glued to the soffit. The bond between the concrete and the sheet reinforcement was achieved using a "grip layer" i.e. a matrix of stone grit and adhesive which was pre-applied to the metal surface. This eliminated the time constraints associated with pouring the concrete immediately after the application of the adhesive.
5. A program to invesigate the use of external sheet reinforcement for one-way bridge decks was initiated at The University of Dundee in Scotland in th early 1970's. Solomon et al. (1976) carried out tests on steel/concrete/steel sandwich beams and slabs, in which the plates were again glued to the concrete. It was found that the top plate carried very little load because of the difficulty in post-bonding the plate to the troweled and hardened concrete. A series of tests on open sandwich slabs (i.e. with the top plate omitted) was then carried out, and the results were published by Ong et al (1982). A variation of the open sandwich concept was investigated by Solomon and Gopalani (1979)

and Mays and Smith (1980), in which the soffit steel plate was curved to form arch-type "inverted catenary" slabs.

6. Ozawa et al. (1986) and Akiyama et al. (1986) carried out tests on both "open" and "closed" steel/concrete/steel sandwich sections in which the steel plates were bonded to the concrete using T-shaped shear connectors. The specimens were, in general, detailed to model components of structures subjected to loads which are significantly lower that those anticipated in the Arctic offshore.
7. Tests to investigate the strengthening effect of bonding steel plates to existing reinforced concrete beams have been reported by Macdonald (1978, 1982).
8. Nuclear containment structures have used interior steel liner plates (Halligan, 1976). The liner plate provides

> ".... an extremely low leak rate during maximum pressure and temperature associated with a postulated loss of coolant incident. Because the elongation of the containment cylindrical wall due to internal pressure is less than the unconfined thermal growth, the liner plate had to be designed to preclude buckling. Therefore, stiffeners were used which would serve as anchors as well as make the liner structurally adequate as the interior form for the concrete."

2.2.2 Steel/concrete/steel Sandwich Cylinders for Offshore Construction.

Over 100 tests were performed on steel/concrete/steel sandwich cylinders at The University of Manchester in England between 1976 and 1985 (Goode and Fatheldin, 1980;

Montague et al., 1985, 1986). The 1/40 scale specimens had a diameter/wall thickness ratio generally between 10 and 25, and were tested to model the behaviour of prototype 12 m diameter tubular members. A particularly interesting result of these tests was that the addition of shear connectors along the steel/concrete interfaces had no apparent effect on the behaviour of the cylinders. It is also interesting to note that, as part of this program, a parallel test series was also carried out to investigate the multiaxial stress behaviour of plain concrete by subjecting plain concrete cylindrical shells to external pressure (Quazzaz, 1984).

2.2.3 Steel/concrete/steel Sandwich Walls for Offshore Construction.

Several research programs have been carried out over the past decade to investigate experimentally the use of steel/concrete/steel sandwich members for offshore applications, and to develop design methods for these members. Some of these programs are ongoing but proprietary: those results which have been published are summarised hereunder.

1. Matsuishi et al. (1977) initiated the current interest in sandwich construction. The program was described in more detail in three subsequent reports (Nishimaki et al., 1977; Matsuishi et al., 1979, 1980). Static tests to failure were were carried out on eighteen beam-type specimens (Nishimaki et al., 1977). The specimens were

proportioned to investigate bending, shear, and combined bending and shear. They were simply supported and point-loaded with very small bearing areas, and a variety of shear connector and diaphragm arrangements was examined. In general, the specimens failed by crushing of the concrete at midspan after the tension plate had yielded. It was reported that, in some of these tests, the compression plate buckled prior to crushing of the concrete.

Two methods were proposed to predict the ultimate strength of these members. Firstly, equations based on the equilibrium and material capacities of the beam cross section at midspan were proposed, without explicit consideration of the concrete in the remainder of the beam. Secondly, the beams were modelled as simple trusses, where the diaphragm plates acted as the posts and lines of diagonal compression were assumed to act within the concrete. Subsequently, the behaviour of these beams was modelled using the finite element method, and the results were described by Matsuishi et al. (1978).

The effect of repeated loading on similar specimens was reported by Matsuishi et al. (1980). In general, it was concluded that capacity was not affected unless the tension plate yielded or a fatigue failure occurred.

2. Hattori and Matsuishi (1985) reported a continuation of Matsuishi's previous work. Four two-span specimens were

point loaded at the centre of each span. Short T-section shear connectors were welded across both the top and bottom plates. Three of the specimens had longitudinal plate stiffeners welded to the outside of the bottom plate to increase the shear rigidity of the beams. The fourth specimen did not have such stiffeners, but the bottom plate had an equivalent area of steel. Two of the three specimens with longitudinal stiffeners were subjected to 20 and 40 freeze-thaw cycles respectively, prior to loading to failure. The bottom plate had yielded in all of these tests when the maximum load was reached, and the concrete did not fail. It was found that the longitudinal stiffeners increased the capacity of the specimens (presumably because of the increased effective depth). There was no apparent decrease in the strength of the members due to the freeze-thaw cycling.

In addition to a finite element analysis, a truss model which explicitly recognised the finite widths of the concrete struts was also proposed. However, the specimen strengths were governed by the capacities of the steel plates rather than the concrete struts.

3. Nojiri and Koseki (1986) carried out tests on 24 sandwich sections. Of these, 14 were single span beams: the remainder were continuous over two spans. All spans were loaded with a central point load. The emphasis in this program was to investigate the effect of shear reinforcement on ductility, and so only one specimen

failed by crushing of the concrete prior to yielding of the steel.

A design method was proposed to include members both with and without shear reinforcement. The method suggests that the capacity of the section be limited to the lesser of its flexural capacity as governed by the steel plates and its shear capacity as governed by Niwa's equation (1984) for members without web reinforcement or by the ACI (1983) shear equations for members with web reinforcement.

4. Shioya et al. (1986) conducted 12 flexural tests and 5 shear tests on sandwich beams. The beams were single span, and were loaded by two point loads located at the 1/3 points for the flexural tests and at the 1/4 points for the shear tests. In general, the specimens were without web reinforcement, and plate type shear connectors were used. The flexural tests were carried out primarily to to investigate the buckling behaviour of the compression plate. In the shear tests, failure occurred by shear compression before the bottom plate yielded. It was found that the shear capacity was accurately predicted using Niwa's equation (1984). It was also noted that the shear capacity was reduced when slip occurred at the steel/concrete interfaces. Shioya's paper also addressed the constructability requirements for sandwich walls, and the results for some concrete injection tests were reported.

2.2.3.1 Discussion.

Two common threads seem to link most of the tests which were described above. Firstly, the emphasis seems to have been on producing flexural failures. Increased member capacity can be obtained by increasing the thicknesses of the plates, but when this is done the member tends to fail in a shear mode. The shear capacity of sandwich sections therefore needs to be further investigated.

Secondly, all of the specimens were loaded using either single or two-point loading. The shear span is readily defined in such cases, and conventional shear equations (ACI, 1983: Niwa, 1984) can be applied. However, as indicated in Chapter 1 and in Section 2.1, it is more realistic to model the ice loads as uniform or patch loads rather than as point loads. In these cases, the shear span is not readily defined, and the conventional shear equations cannot be used. (This will be illustrated later, in Section 6.6.3). A method for predicting the capacity of the concrete core in a sandwich section under general loading needs to be developed. Chapters 5 and 6 of this thesis are primarily devoted to this task.

2.3 Concrete Plasticity.

The analytical method which is developed in Chapters 5 and 6 utilises the methods of plasticity as applied to deep concrete sections, and the literature necessary for the development is cited as required throughout those chapters. Several other plastic solutions for deep sections, although not directly relevant to this thesis, are given by Nielsen (1984). Two additional references on concrete plasticity which may be of interest in other areas of steel/concrete/steel sandwich analysis are given here for completeness.

1. A solution for the moment capacity of a one-way sandwich slab was developed by Nelson et al. (1985).
2. Brandli (1985) proposed a statically admissible stress field for a two-way reinforced concrete slab in which the concrete in compression is idealised as a concrete plate, the reinforcement is smeared to form a biaxially stressed steel plate, and the remainder of the concrete acts as a shear core. If the compressive plate is assumed to be constructed from steel instead of concrete, it may be possible to adapt the stress field for shallow two-way sandwich systems.

3. EXPERIMENTAL PROGRAM

3.1 Introduction

To model the behaviour of a composite ice-resisting wall in the laboratory, the wall was initially idealised as a series of continuous horizontal strips. (Fig. 3.1). The width of the strip was chosen as 1.5 times the wall thickness. A continuous strip was further idealised as a simply supported beam with cantilevers. These alterations to the kinematic boundary equations are permissible, since a lower bound to the wall capacity was sought.

Within the context of these beam-type specimens, two modes of failure were possible: yielding and strain hardening of the steel plates (ductile behaviour), or failure of the concrete core (brittle behavour). Most of the test specimens in the experimental program were overreinforced in order to investigate the effect of various parameters on the beam strength when this is governed by the concrete capacity. However, some underreinforced specimens were also included to observe some general characteristics of ductile behaviour.

Seventeen 1/4 - scale beam-type specimens were constructed and tested in this program. Five specimens with span-to-depth ratio (l/d) = 4 were tested first, followed by seven specimens with l/d = 6. The results of these two series were used to optimise details for five further specimens with l/d = 5. Accordingly, the experimental

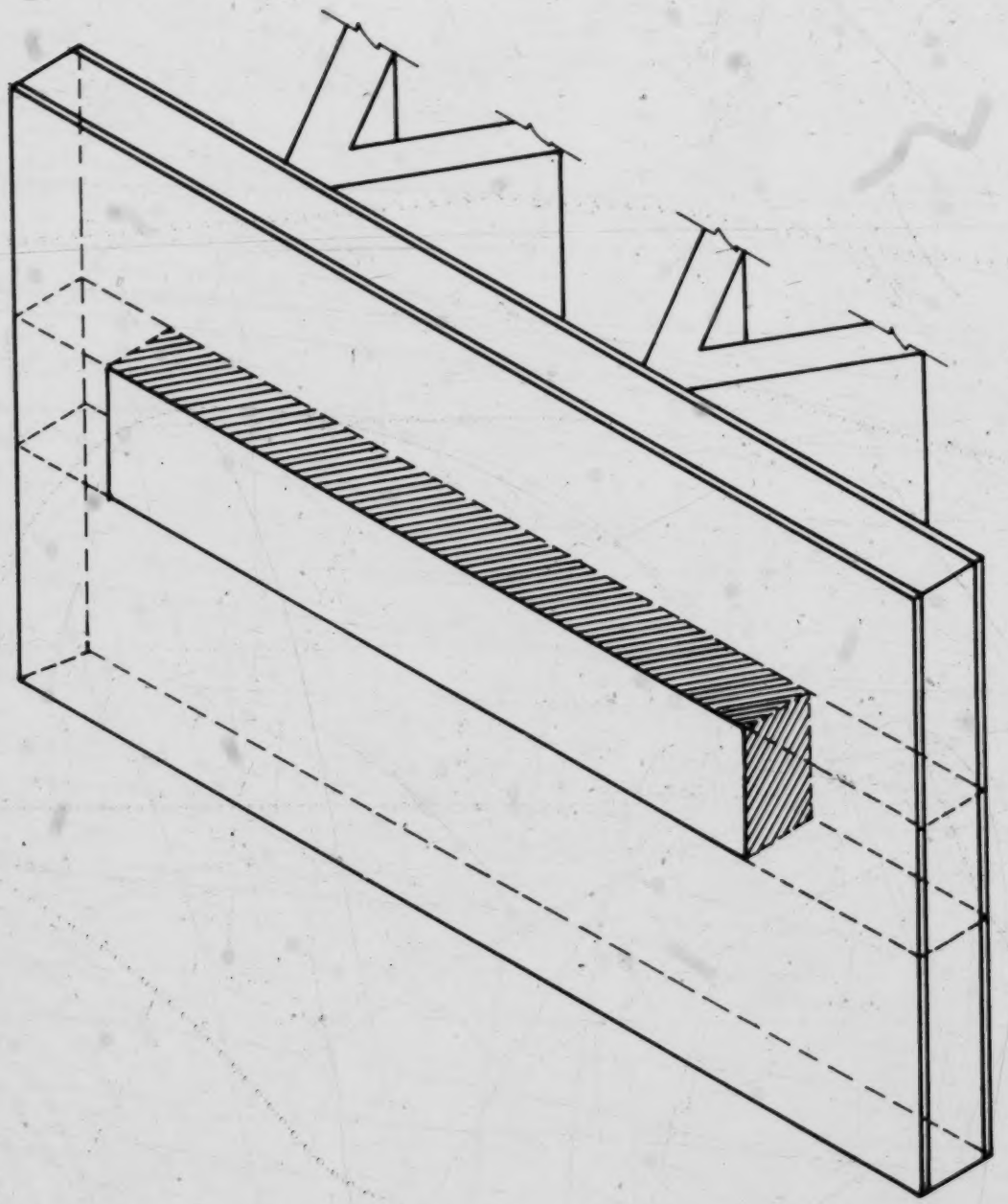

Figure 3.1 Beam specimen from a composite ice-resisting wall

program will be reported in the sequence l/d = 4, 6, 5. This is done to maintain the logic of the program development.

3.2 Test Specimens

Table 3.1 summarises the parameters associated with each test specimen. It also outlines the purpose of each specimen, and gives the companion specimens with which results should be compared. The dimensions of the specimens are given in Table 3.2.

3.2.1 B4 Test Series (l/d = 4)

The B4 series consisted of five overreinforced specimens. The objective of the series was to examine the effect of the following parameters on the beam strength governed by failure of the concrete;

- Type of shear connector (stud or plate)
- Concrete confinement near the support
- Solid support or stiffened plate support (representing a stiffened plate bulkhead)

The specific parameters associated with B4/1 through B4/5 are given in Table 3.1.

The loading system for the B4 series is shown in Fig. 3.2. The load was applied through sixteen 450 kN hydraulic rams. Since the load in every ram was equal, this loading arrangement simulated the distributed load system shown in Fig. 3.2(b). The test rig actually applied the loads P on the bottom of the specimen and reacted these loads on the

Table 3.1 Parameters associated with each test specimen.

Span / Depth	Specimen N°.	High strength concrete	Low strength concrete	Plain concrete	Steel-fibre-reinforced concrete	Over-reinforced	Under-reinforced	Concrete confinement	Stiffened plate support	Solid support	Support rotation	Uniform load	Patch load	Diaphragm at support	Studs on support plate	Stud shear connectors	Plate shear connectors	Parameter investigated:	Compare with:
4	B4/1	•		•		•		•		•	•	•				•		Control specimen	—
	B4/2	•		•		•		•		•	•	•					•	Connector type	B4/1
	B4/3	•		•		•		•	•		•	•					•	Support type	B4/2
	B4/4	•		•		•		•	•		•	•				•		Support type	B4/1
	B4/5	•		•		•			•		•	•				•		Confined concrete	B4/1
6	B6/1	•		•		•				•	•	•				•		Control specimen	—
	B6/2	•		•			•			•	•	•				•		Under-reinforcement	B6/1
	B6/3	•			•	•				•	•	•				•		Fibre-reinforcement	B6/1
	B6/4	•			•		•			•	•	•				•		Under-reinforcement	B6/3
	B6/5	•		•		•				•	•	•			•	•		Support plate studs	B6/1
	B6/6		•	•		•				•	•	•				•		Concrete strength	B6/1
	B6/7	•		•		•				•	•		•			•		Load type	B6/1
5	B5/1	•		•		•				•	•	•				•		Control specimen	—
	B5/2	•		•		•				•	•	•		•		•		Diaphragms at supports	B5/1
	B5/3	•		•			•			•	•	•				•		Under-reinforcement	B5/1
	B5/4	•		•			•			•		•			•	•		Support rotation	B5/5
	B5/5	•		•			•			•	•	•			•	•		Support plate studs	B5/3

Table 3.2 Dimensions of test specimens.

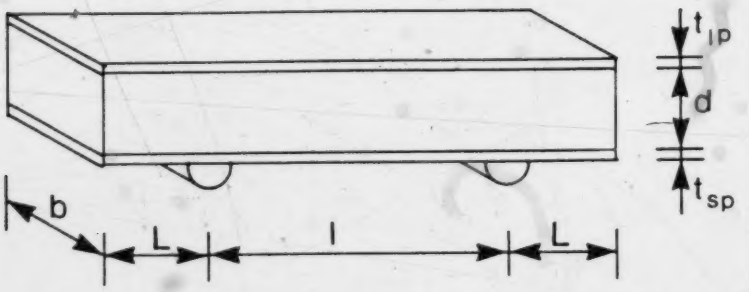

Specimen #	b (mm)	L (mm)	l (mm)	t_{lp} (mm)	t_{sp} (mm)	d (mm)
B4/1	375	400	1000	10.28	10.20	250
B4/2	375	400	1000	10.14	9.45	250
B4/3	375	400	1000	9.35	9.42	250
B4/4	375	400	1000	10.09	10.25	250
B4/5	375	400	1000	10.18	10.22	250
B6/1	375	500	1500	13.30	13.17	250
B6/2	375	500	1500	6.43	6.31	250
B6/3	375	500	1500	13.17	13.26	250
B6/4	375	500	1500	6.32	6.34	250
B6/5	375	500	1500	13.35	13.26	250
B6/6	375	500	1500	13.37	13.30	250
B6/7	375	500	1500	13.31	13.26	250
B5/1	375	500	1250	16.22	16.18	250
B5/2	375	500	1250	16.26	16.21	250
B5/3	375	500	1250	6.97	6.70	250
B5/4	375	500	1250	6.98	6.68	250
B5/5	375	500	1250	6.96	6.70	250

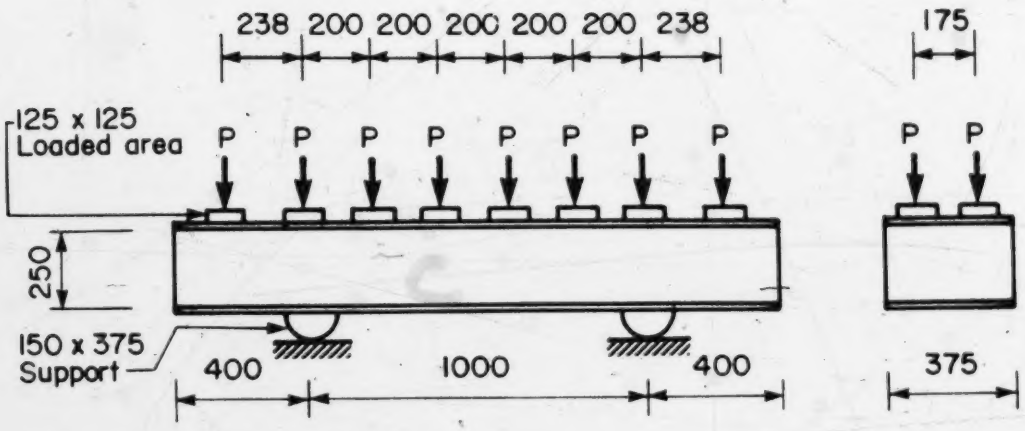

(a) Point loads

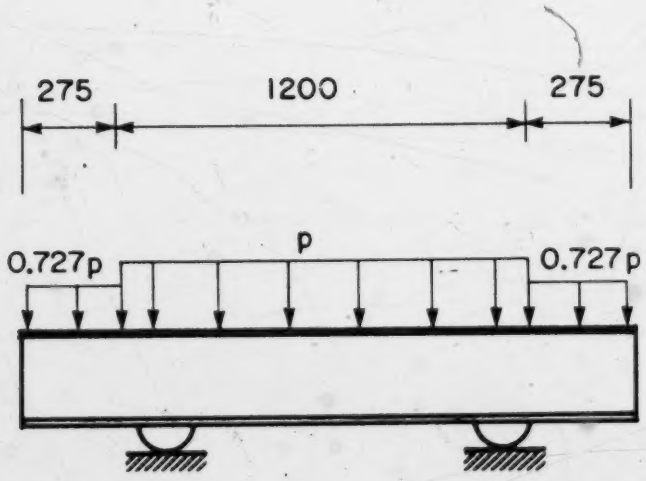

(b) Equivalent distributed load

Figure 3.2 B4 series: Loading system.

top of the specimen as shown in Fig. 3.21, discussed later. However, to prevent confusion, the orientation of Fig. 3.2 will be used throughout.

A graphical method for predicting the strength of these composite sections was developed. The method is discussed in Chapter 5. The technique indicates that the capacity of the beam is largely insensitive to the magnitude of the cantilever load. (This is indirectly verified in the B5 series). The load intensity on the cantilevers (0.727p) was therefore arbitrarily chosen to model some degree of statical continuity with the adjacent spans, but was not expected to have a strong effect on the load capacity of the beam.

Once inclined cracking has occurred and loads are transferred by arch action, the graphical method of analysis indicates that the distribution of shear stress at the steel/concrete interface of the loaded plate for full composite action can be represented as in Fig. 3.3. When choosing the shear connector layouts for the B4 series, it was assumed that the shear transfer due to interfacial friction was zero. This assumption is very conservative, but it was implemented to ensure that failure would occur by exceeding the concrete capacity, rather than by loss of composite action. The shear connector layouts for the loaded plates used in the B4 series are given in Fig. 3.4 (a) and (c). The shear connectors are more closely spaced near the centres of the loaded plates so as to correlate with the

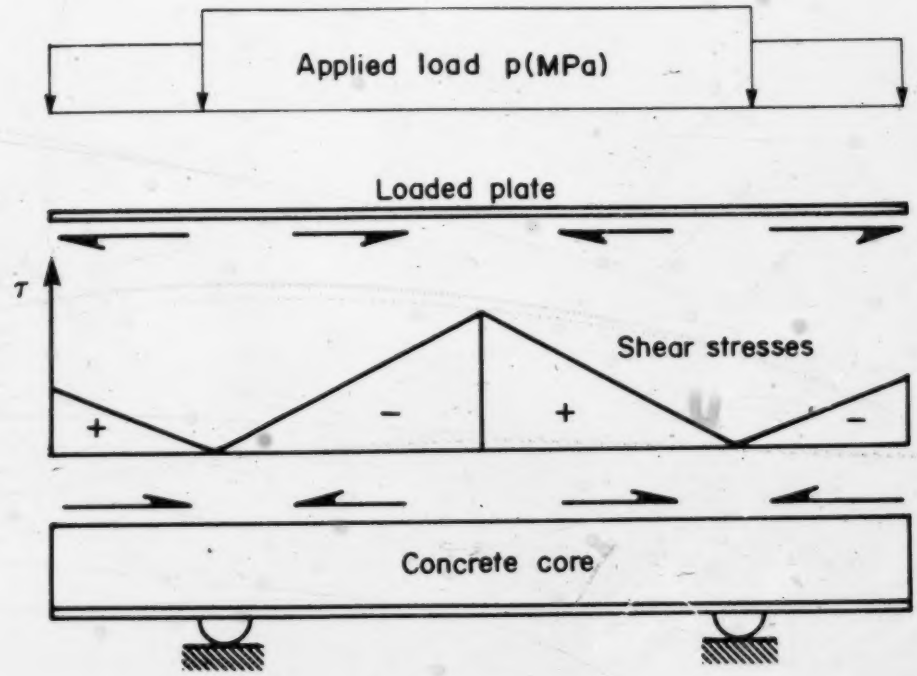

Figure 3.3 Idealised shear stress distribution at the steel/concrete interface of the loaded plate.

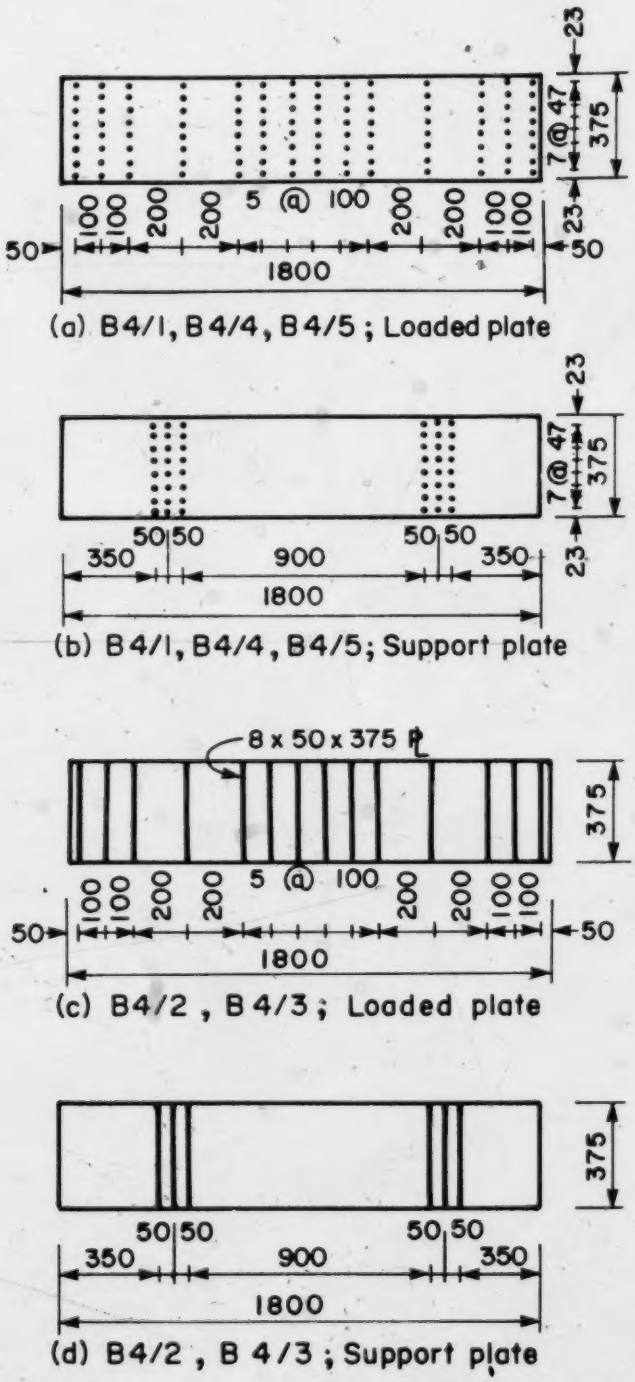

Figure 3.4 B4 series; shear connector layouts.

larger shear requirements in these areas as shown in Fig. 3.3. The total shear capacity of the shear connectors was equal to the total horizontal shear force which can be calculated from the shear stress distribution as typically shown in this figure.

The shear connector layouts for the support plates are shown in Fig 3.4 (b) and (d). These connectors were concentrated near the supports because it was expected that arching action would dominate in these tests, and that the horizontal components of the arch reactions would be transferred to the support plate by mechanical shear transfer at the supports. The shear force to be transferred at the support is equal to the tensile force in the span of the support plate, and is calculated using equation [5.15], developed later.

The system used for lateral confinement of the concrete in the support regions of specimens B4/1 through B4/4 is shown in Fig. 3.5. The inside surfaces of the triangular plates were polished. The plates were pressed against Lubrite-coated square steel pads which were glued to the sides of the specimen. These pads confined the concrete, but were able to slide relative to the confining plates. The lateral confinement system models the influence of the concrete in the adjacent strips at the support regions when the wall is subjected to ice loading. The tie rods were preloaded to simulate the weight of 10 meters of concrete above the strip in the prototype. The axial stiffnesses of

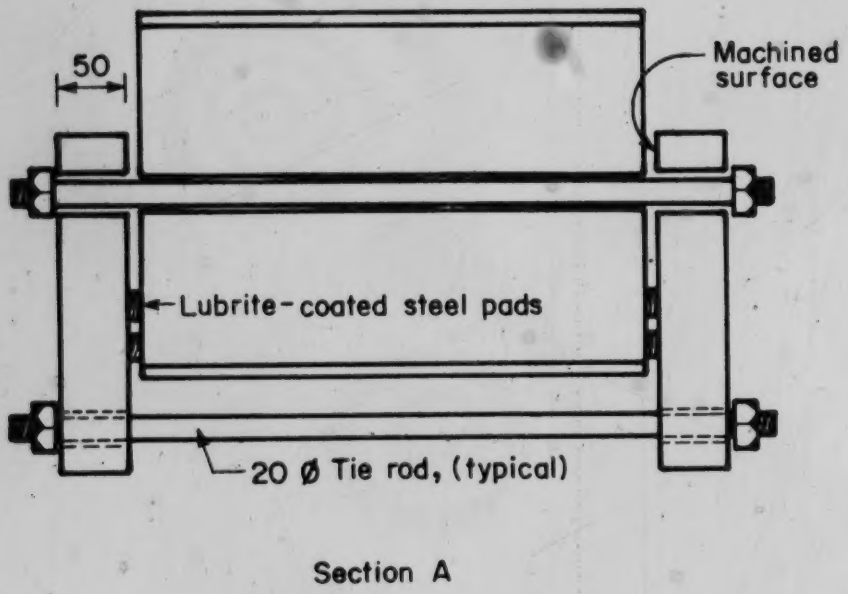

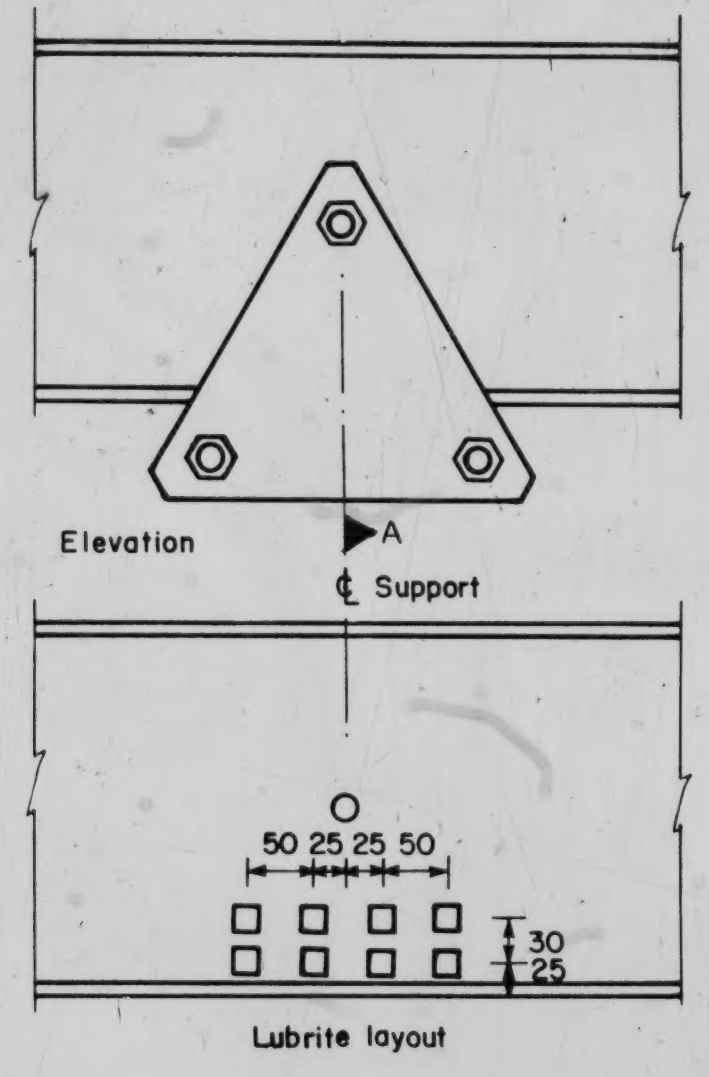

Figure 3.5 Lateral confinement system

the tie rods were designed such that the lateral stress in the concrete over the supports would be approximately 50% of that which is associated with plane strain conditions, assuming the concrete to be both linear and elastic. Specimen B4/5 did not have confinement at the supports.

Three of the five specimens (B4/3, B4/4 and B4/5) reacted against support devices representing the stiffened plate bulkheads which might be encountered in a prototype structure. B4/1 and B4/2 reacted against solid supports. The dimensions of the stiffened plate supports are given in Fig. 3.6. These were used to investigate the mechanism of load transfer from the concrete to this support type to see if this affected the load carrying capacity of the beam.

3.2.2 B6 Test Series (l/d = 6)

Seven specimens were tested in the B6 series. The series was designed to investigate the effects of:

- Concrete strength (high or low)
- Concrete type (plain or steel-fiber-reinforced (SFRC))
- Presence of studs on the support plate between supports
- Type of loading (uniform or eccentric patch loading).

The ram spacings and equivalent uniform loads for both loading types are shown in Fig. 3.7. The lateral confinement system was not used in the B6 series. Shear studs were used as mechanical connectors throughout, and all supports simulated solid bulkheads.

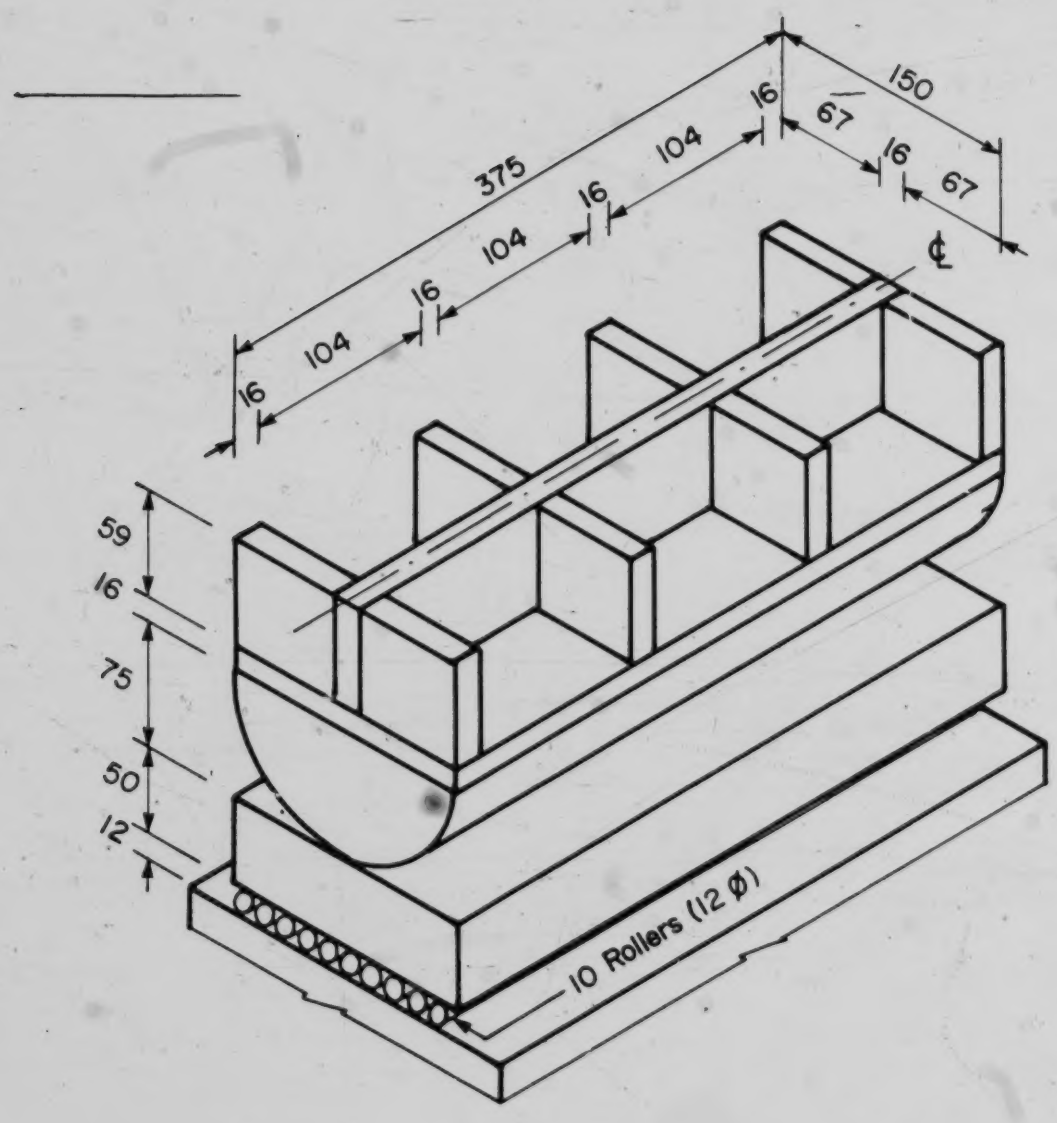

Figure 3.6 Stiffened plate support.

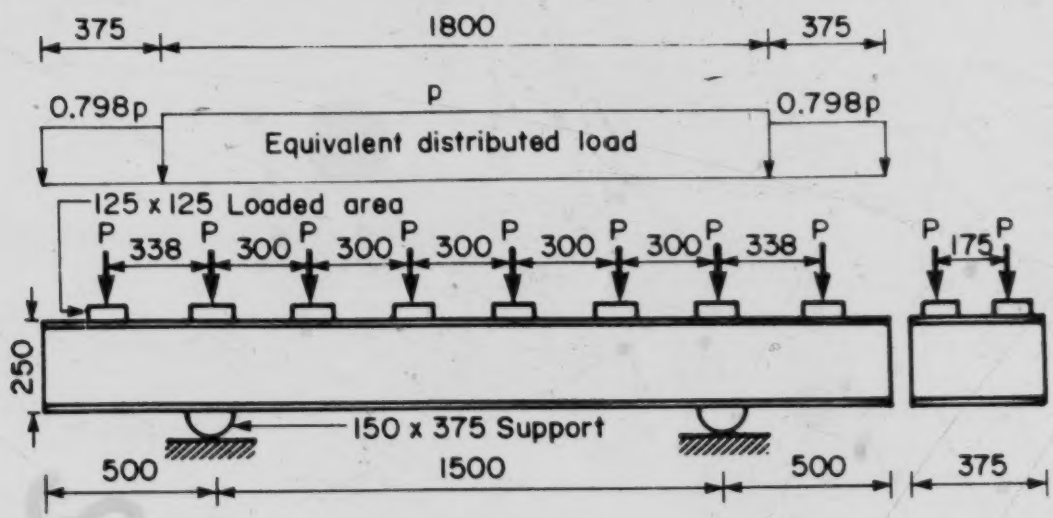

All B6 series except B6/7

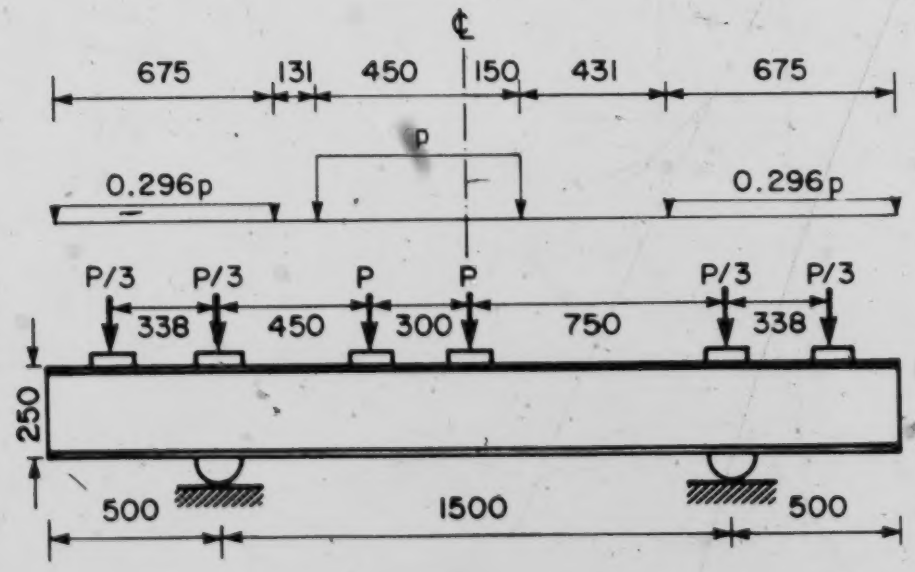

B 6/7

Figure 3.7 B6 series: Loading system.

The layout of the studs for the B6 series is shown in Fig. 3.8. The contribution of interfacial friction was recognised in choosing the layout of the studs on the loaded plate, as shown in Fig. 3.9. At any point, the frictional transfer was assumed equal to f × p, where the coefficient of friction, f, was taken as 0.6 as suggested by Clause 11.7.4.3(d) of CAN3-A23.3-M84. All shear in excess of this was assumed to be transferred by stud shear connectors. The total number of studs thus required for the span between supports was evenly spaced along the span, resulting in a more practical stud layout than that used in the B4 series. The contribution of friction was similarly recognised in the design of the studs for the support plates. Additional studs were attached to the cantilever portions of the loaded plates so as to reduce the possibility of failure of the test specimens by failure of the cantilevers.

A composite ice-resisting wall on a prototype structure may require shear connectors between the supports on the support plates as well as on the loaded plates. These would be necessary to accomodate pattern loads, and to prevent a gap from opening between the tension plate and the concrete core. The effect of such additional studs was investigated in specimen B6/5, as shown in Fig. 3.8(c). These additional studs were not expected to contribute significantly to the transfer of the horizontal components of the arch reactions to the support plate, and so the number of studs directly over the support was not reduced from that which was used

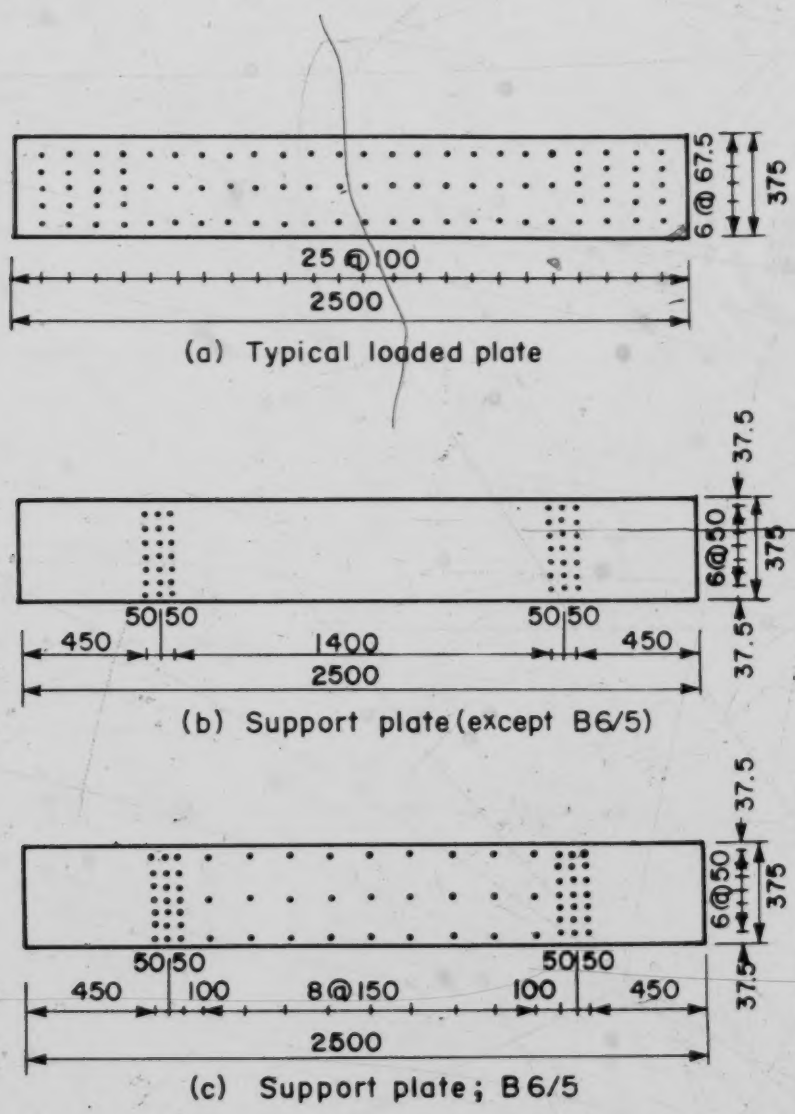

Figure 3.8 B6 series: Shear connector layouts.

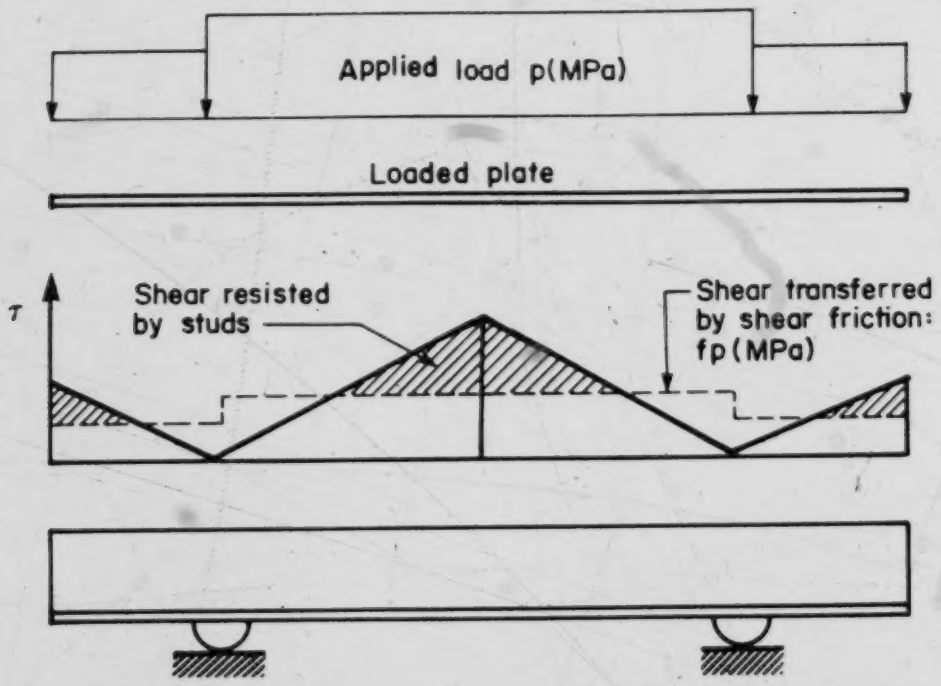

- f = Shear friction coefficient = 0.6
- Shaded area represents shear force to be resisted by studs.

Figure 3.9 Contribution of friction at the steel/concrete interface.

for the other B6 series specimens.

The addition of steel fibres to a concrete mix can significantly increase the apparent tensile strength of the concrete. The compressive strength remains largely unaffected (ACI 544.1R, 1982). Specimen B6/3 was included to determine whether the load-carrying capacity of the beam was more strongly affected by the tensile or compressive strength of the concrete.

Specimen behaviour under a patch load was investigated in B6/7. The cantilevers were loaded to model beam continuity. The patch was eccentrically located to force an unfavourable load path to the most remote support.

A specimen with a low-strength concrete core (B6/6) was included to investigate the effect of f'_c on specimen behaviour.

Each of the aforementioned specimens was overreinforced in order to investigate the effects of the various parameters on the specimen capacity when this was controlled by failure of the concrete. It is also of interest, however, to observe the ductile behaviour of underreinforced composite ice-resisting walls, since prototype walls would probably be so reinforced. Two underreinforced specimens were also tested (B6/2 and B6/4). B6/2 had a plain concrete core; B6/4 had a steel fibre reinforced concrete (SFRC) core.

3.2.3 B5 Test Series (1/d = 5)

The results of the B4 series and the B6 series were used to optimise the parameters for the B5 series. A prototype wall was envisioned as having the following characteristics:

- Underreinforced
- Studs on both plates
- A diaphragm plate at each support
- High-strength concrete.

The B5 series consisted of five specimens, and investigated the following parameters:

- Effect of a diaphragm plate at each support
- Effect of studs on the support plate of an underreinforced specimen
- Effect of rotational end restraint on the behaviour of an underreinforced specimen.

The ram spacing and equivalent uniform loads for the B5 series are shown in Fig. 3.10. The shear connector layouts are given in Fig. 3.11. The studs were also uniformly spaced in these tests.

A diaphragm plate may be necessary in the prototype both to separate the plates during construction and to provide a tensile link to the bulkhead in case of pattern loadings. B5/2 investigated the effect (if any) of such a diaphragm on the strength of the concrete.

Specimens B5/3, B5/4 and B5/5 were underreinforced. B5/5 examined the effect of a uniform distribution of studs

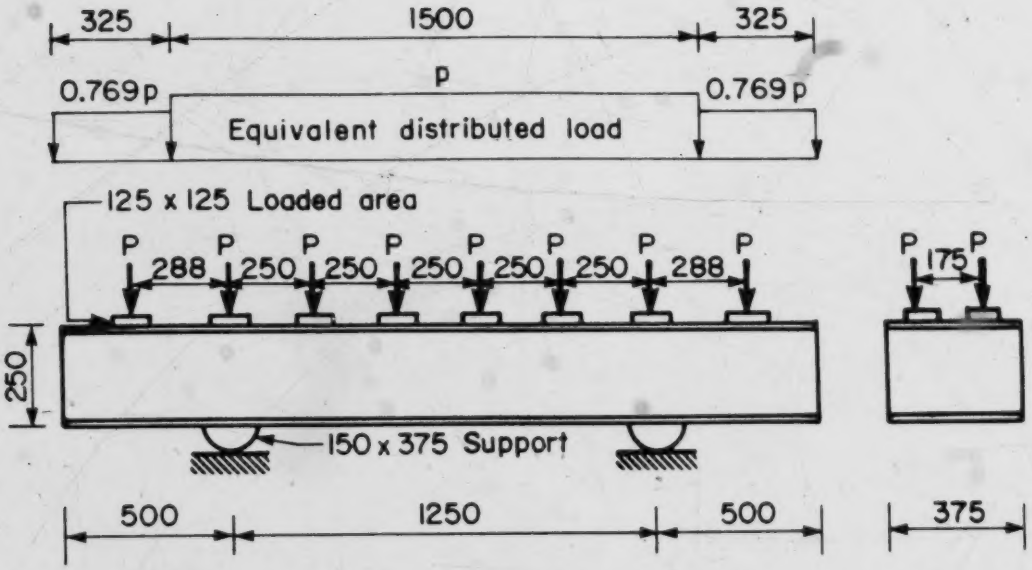

All B5 series except for B5/4

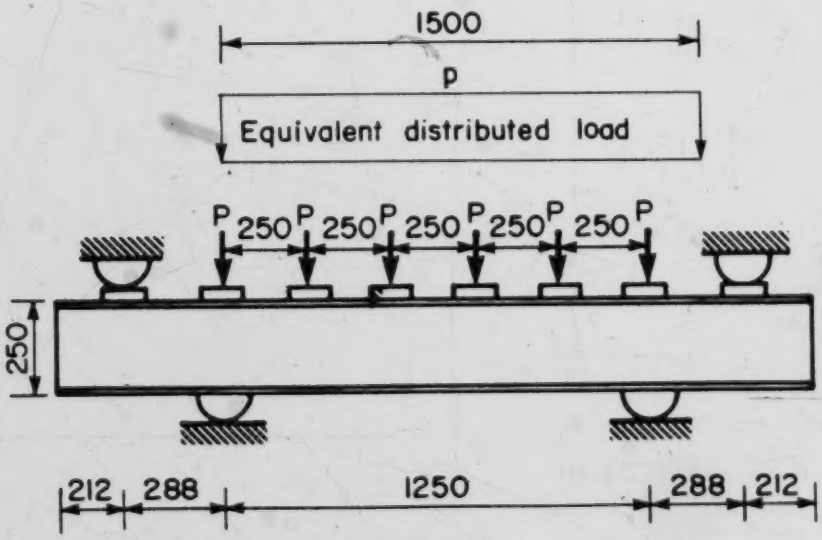

B5/4

Figure 3.10 B5 series: Loading system.

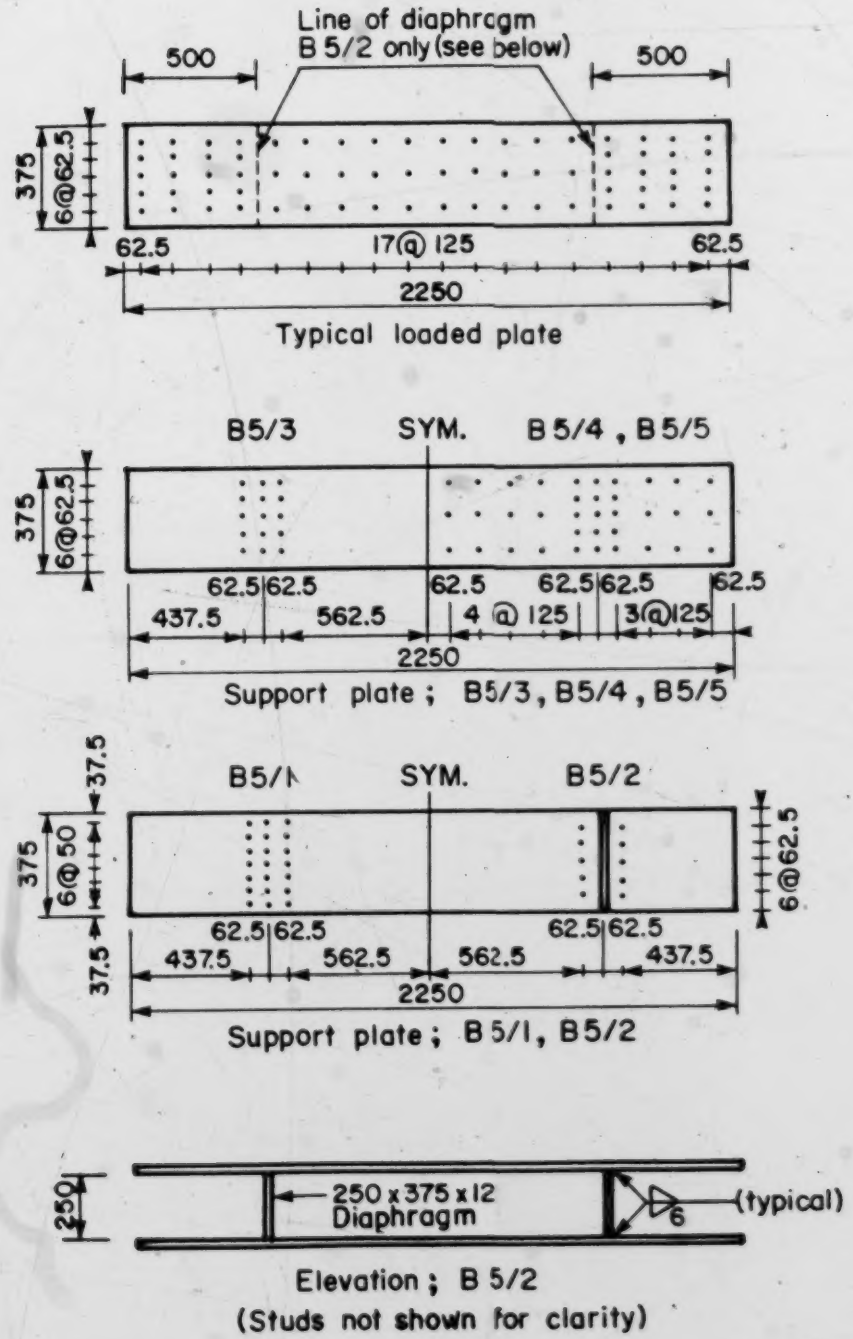

Figure 3.11 B5 series: Shear connector layouts.

on the support plate. End rotations were prevented in B5/4, mainly to examine the effect of such a kinematic restraint on ductility. The restraint was provided by preventing the flow of hydraulic fluid from the rams acting on the cantilevers.

3.3 Material Properties

3.3.1 Concrete

High strength concrete (f'_c from 45 MPa to 64 MPa)was used in all specimens except B6/3 and B6/4, which were made of high strength steel-fibre-reinforced concrete, and B6/6, which was cast using a lower strength mix (f'_c = 39.5 MPa). The high strength concrete was purchased from a local ready-mix supplier. Mix proportions are given in Table 3.3. This low-water, superplasticized mix had been used extensively in a major local construction project, and had 28-day strengths of about 50 MPa. The concrete for specimen B6/6 (low strength) was mixed in the laboratory. The mix proportions for B6/6 are also given in Table 3.3.

The B4, B5, and B6 series were cast on separate dates. All of the concrete for a given series came from the same ready-mix truckload (except for B6/6, in which case the concrete was mixed in the laboratory). The compressive cylinder strength, static modulus of elasticity, splitting tensile strength and modulus of rupture were measured at intervals during the testing of a given series. The results

Table 3.3 Concrete mix proportions.

	High strength	Low strength (B6/6 only)
Item	Quantity/m^3	Quantity/m^3
Cement	465 kg	404 kg
Sand	752 kg	653 kg
Aggregate (15 mm max)	1100 kg	974 kg
Water	160 kg	195 kg
Conchem-SPN retarding-type superplasticizer	3.49 litres	-

are given in Appendix A. The data were fitted with regression curves of the form $f'_c(t)=a+b\times\ln(t)$ by the least squares method. The resulting best-fit equations for each concrete mix are also shown in Appendix A. The estimated compressive cylinder strength on the day of testing for each specimen is given in Table 3.4. With the exceptions of B6/3 and B6/4 (steel-fibre-reinforced), and B6/6 (low strength), these values were obtained from the regression equations. The compressive cylinder strengths for specimens B6/3, B6/4, and B6/6 were estimated using

$$f'_c(t_1) = f'_c(t_0)\left[\frac{0.75 + (7/t_0)}{0.75 + (7/t_1)}\right] \qquad [3.1]$$

where

t_1= age at which composite specimen was tested

t_0= age at which cylinders were tested

and $f'_c(t_0)$, t_0 and t_1 are from Appendix A.

For B6/3 and B6/4, "Xorex" steel fibres were added to the ready-mix concrete using the concrete mixer in the laboratory. The fibres were 50 mm long and crimped at intervals of approximately 8 mm to a minimum specified height of 1.02 mm. The crescent-shaped cross-section of a fibre had a minimum specified width of 2.3 mm and a minimum specified height of 0.3 mm. The minimum specified yield for the fibres was 970 MPa. B6/3 was reinforced with 1.5% fibres/volume: B6/4 had 1.0% fibres/volume. The addition of this large proportion of fibres significantly reduced the workability of the mix, but proper compaction was

- Table 3.4 Compressive cylinder strengths of concrete in specimens

Specimen #	f'_c (MPa)
B4/1	62.9
B4/2	62.4
B4/3	61.3
B4/4	63.3
B4/5	56.6
B6/1	54.5
B6/2	57.8
B6/3	57.0
B6/4	59.6
B6/5	60.2
B6/6	39.5
B6/7	61.3
B5/1	44.6
B5/2	46.3
B5/3	48.7
B5/4	50.8
B5/5	51.7

nevertheless obtained.

Cylinders and modulus of rupture beams were made from the steel fibre reinforced concrete. In compliance with the recommended practice (ACI 544.2R, 1978), the load-deflection curve was recorded for each steel-fibre-reinforced beam. The plots, and all steel-fibre-reinforced cylinder test results, are given in Appendix A. The cylinders and modulus of rupture beams were rodded during casting. This action affected the random orientation of the fibres, and so the (low) tensile strength values must be treated with suspicion.

3.3.2 Steel

Two coupons were manufactured from each source plate used in the testing program. All source plates were specified as CAN3 - G40.21 - M81, Grade 300W. The longitudinal axes of the coupons coincided with the longitudinal axes of the composite specimens. The coupons were manufactured and tested in accordance with ASTM A370 (1977). Every coupon exhibited a well-defined yield plateau. Two longitudinal and two transverse strain gauges were mounted on each coupon, and the average reading of each pair was used, thereby eliminating any bending effects. The dimensions of a typical coupon as well as the locations of the strain gauges are shown in Fig. 3.12.

The coupons were tested in a 1000 kN capacity MTS testing machine. Load and strains were recorded using a Data

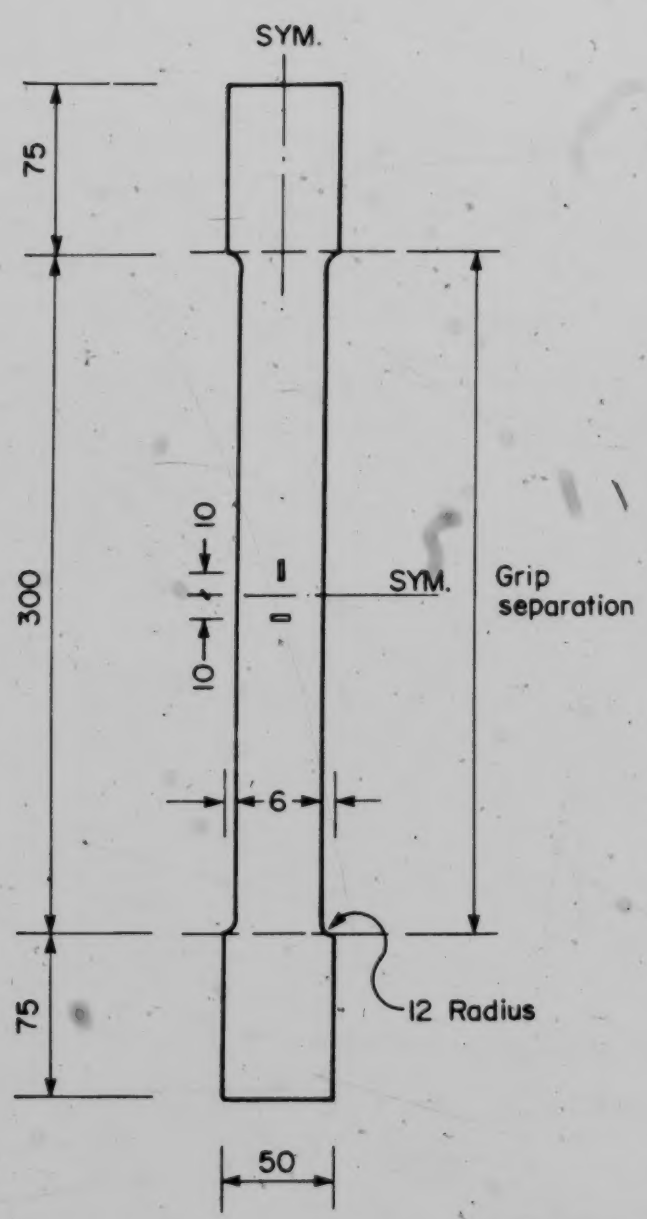

Figure 3.12 Tension coupons: Dimensions and gauge locations.

General data aquisition system. In this way, the elastic modulus (E), static yield strength (F_y), ultimate strength (F_u), yield strain (ϵ_y) and Poisson's Ratio (μ) were recorded for each coupon. Estimates for the strain-hardening strain (ϵ_{st}) and elongation at break were made by recording the crosshead movement of the testing frame.

Table 3.5 gives the mechanical properties for the plates in each composite specimen. The values reported are the averages for the two coupons. For each source plate, the values for E, F_y and μ from the two coupons agreed within 5%. The strain-hardening strain was not always well-defined on the stress-strain curves, and so the best estimates for the two coupons varied by up to 100%. Nevertheless, the average is also reported in Table 3.5. In all cases, the elongations at break for pairs of coupons agree within 20%.

3.4 Instrumentation of Composite Specimens

3.4.1 Displacement Measurement

The displacements were recorded electronically using linear variable displacement transducers (LVDTs). The location and the total range of each LVDT is shown in Fig. 3.13. Measurements were considered reliable within the middle 80% of this range. All measured displacements were those from the support plate. The following displacements were recorded:

- Midspan deflection (two readings)

Table 3.5 Mechanical properties of steel.

	LOADED PLATE						
Beam #	E (MPa)	F_y (MPa)	F_u (MPa)	ϵ_y ($\mu\epsilon$)	ϵ_{st} ($\mu\epsilon$)	ϵ_u ($\mu\epsilon$)	μ
B4/1	218 000	325	497	1491	14 000	211 000	0.292
B4/2	218 000	325	497	1491	14 000	211 000	0.292
B4/3	202 000	362	491	1795	13 000	218 000	0.290
B4/4	218 000	325	497	1491	14 000	218 000	0.292
B4/5	218 000	325	497	1491	14 000	218 000	0.292
B6/1	211 000	363	516	1720	20 000	212 000	0.271
B6/2	208 000	279	412	1379	11 000	236 000	0.280
B6/3	211 000	363	516	1720	20 000	212 000	0.271
B6/4	208 000	279	412	1379	11 000	236 000	0.280
B6/5	211 000	363	516	1720	20 000	212 000	0.271
B6/6	211 000	363	516	1720	20 000	212 000	0.271
B6/7	211 000	363	516	1720	20 000	212 000	0.271
B5/1	211 000	319	476	1512	18 000	278 000	0.270
B5/2	211 000	319	476	1512	18 000	278 000	0.270
B5/3	216 000	334	489	1550	19 000	228 000	0.285
B5/4	216 000	334	489	1550	19 000	228 000	0.285
B5/5	216 000	334	489	1550	19 000	228 000	0.285

	SUPPORT PLATE						
Beam #	E (MPa)	F_y (MPa)	F_u (MPa)	ϵ_y ($\mu\epsilon$)	ϵ_{st} ($\mu\epsilon$)	ϵ_u ($\mu\epsilon$)	μ
B4/1	218 000	325	497	1491	14 000	211 000	0.292
B4/2	202 000	362	491	1795	13 000	218 000	0.290
B4/3	202 000	362	491	1795	13 000	218 000	0.290
B4/4	218 000	325	497	1491	14 000	218 000	0.292
B4/5	218 000	325	497	1491	14 000	218 000	0.292
B6/1	211 000	363	516	1720	20 000	212 000	0.271
B6/2	208 000	279	412	1379	11 000	236 000	0.280
B6/3	211 000	363	516	1720	20 000	212 000	0.271
B6/4	208 000	279	412	1379	11 000	236 000	0.280
B6/5	211 000	363	516	1720	20 000	212 000	0.271
B6/6	211 000	363	516	1720	20 000	212 000	0.271
B6/7	211 000	363	516	1720	20 000	212 000	0.271
B5/1	211 000	319	476	1512	18 000	278 000	0.270
B5/2	211 000	319	476	1512	18 000	278 000	0.270
B5/3	219 000	331	445	1516	34 000	254 000	0.265
B5/4	219 000	331	445	1516	34 000	254 000	0.265
B5/5	219 000	331	445	1516	34 000	254 000	0.265

LVDT	Range (mm)
① ② ⑦ ⑧	50
③ ④ ⑤ ⑥	150

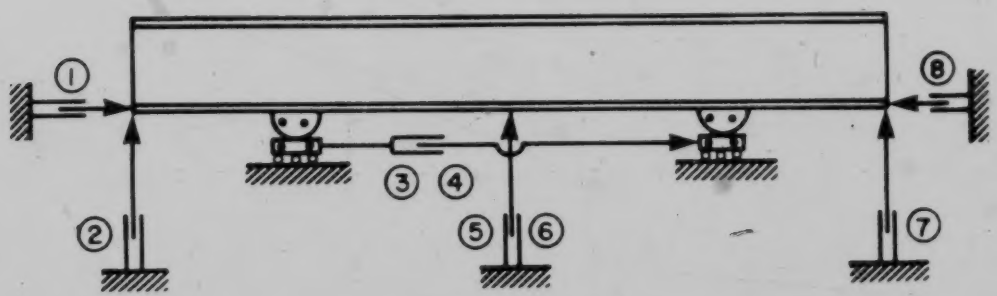

Elevation

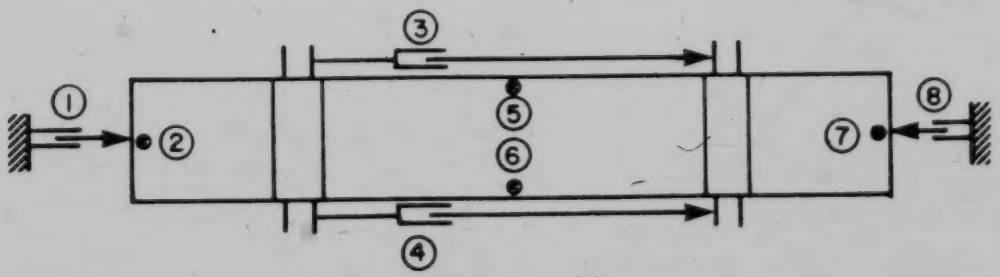

View from underside

Figure 3.13 Displacement transducer layout.

- Relative horizontal movement at the supports (two readings)
- Horizontal and vertical movements at the cantilever tips.

In specimens where the midspan deflection exceeded the range of the LVDT, additional displacements were recorded manually.

3.4.2 Concrete Strains

Concrete strains were recorded manually using 50.8 mm gauge length Demec rosettes. Each rosette consisted of four gauge lengths; horizontal, vertical and 45° each way from vertical. The redundancy within this rosette allows four Mohr circles of strain to be plotted for each point. Approximately six sets of Demec readings were taken at intervals during each test. The smallest division of the gauge corresponded to 25 microstrain ($\mu\epsilon$). Concrete strains were measured on one face only.

The rosette layout for each test specimen is given in Figs. 3.14 - 3.16. The following points are noted:

- Concrete strains could not be measured at the supports for B4/1, B4/2, B4/3 and B4/4, due to the presence of the triangular confining plates. An attempt was made to use concrete-compatible electrical resistance strain gauges (25 mm gauge length) at the support areas in B4/3. However, local undulations on the concrete surface, combined with early cracking through the

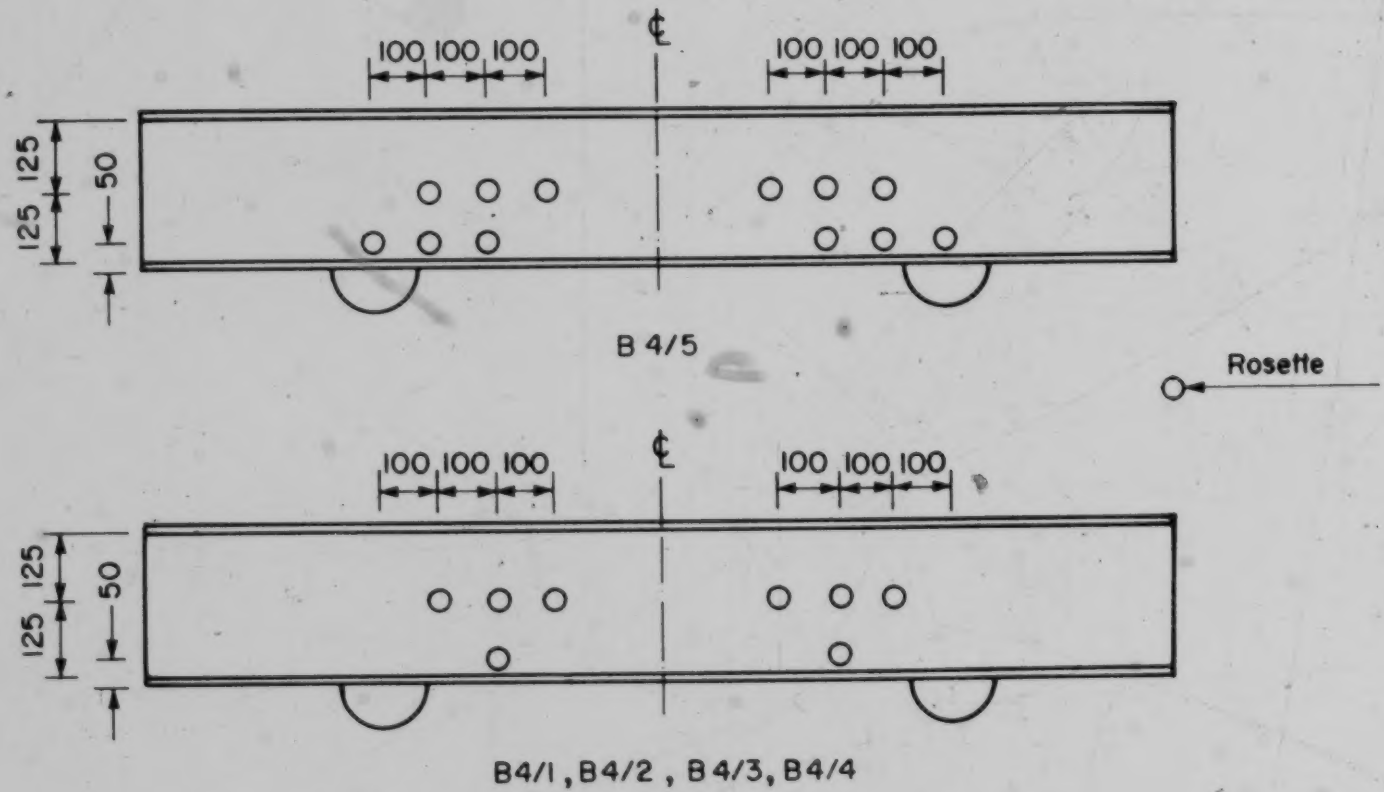

Figure 3.14 B4 series: Rosette layout.

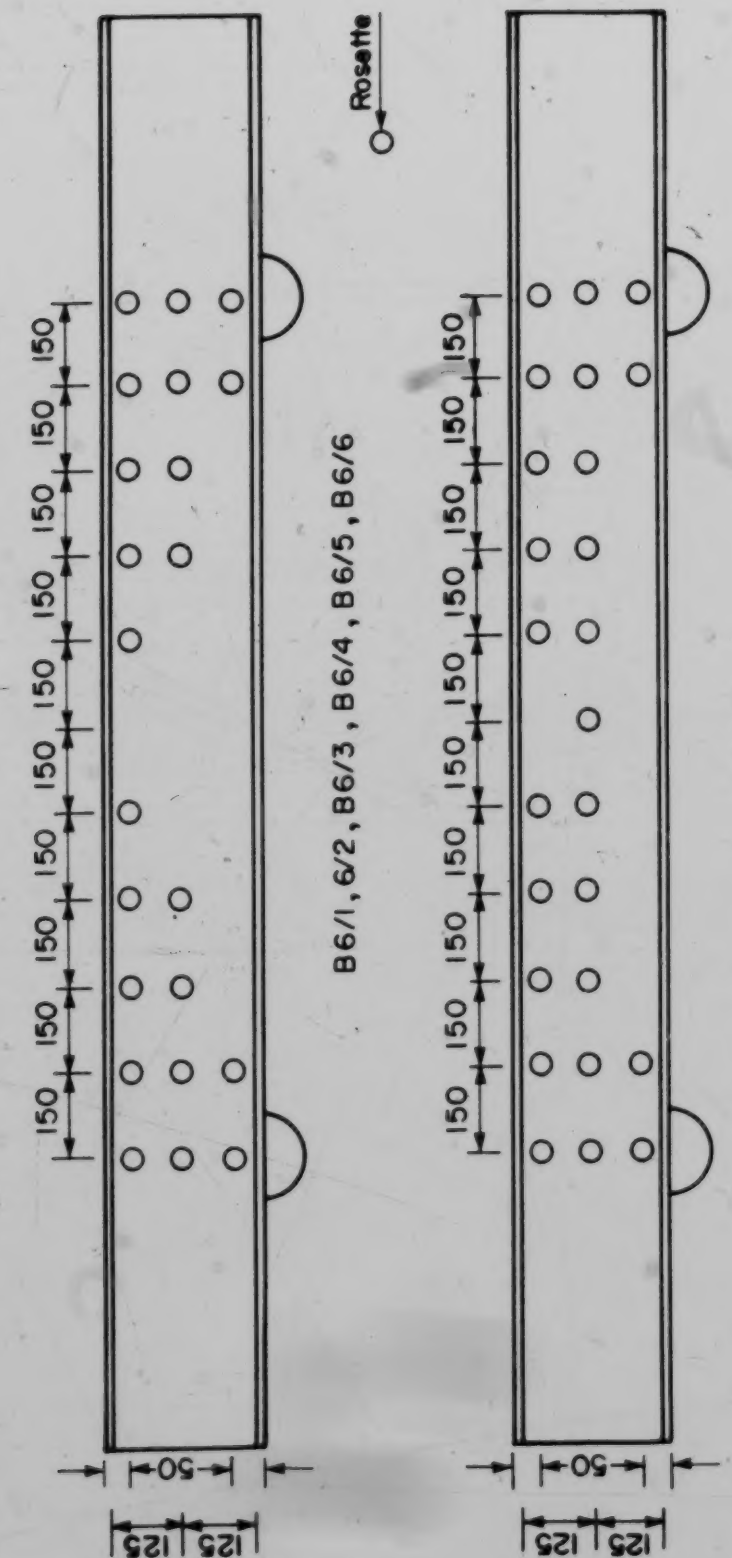

Figure 3.15 B6 series: Rosette layout.

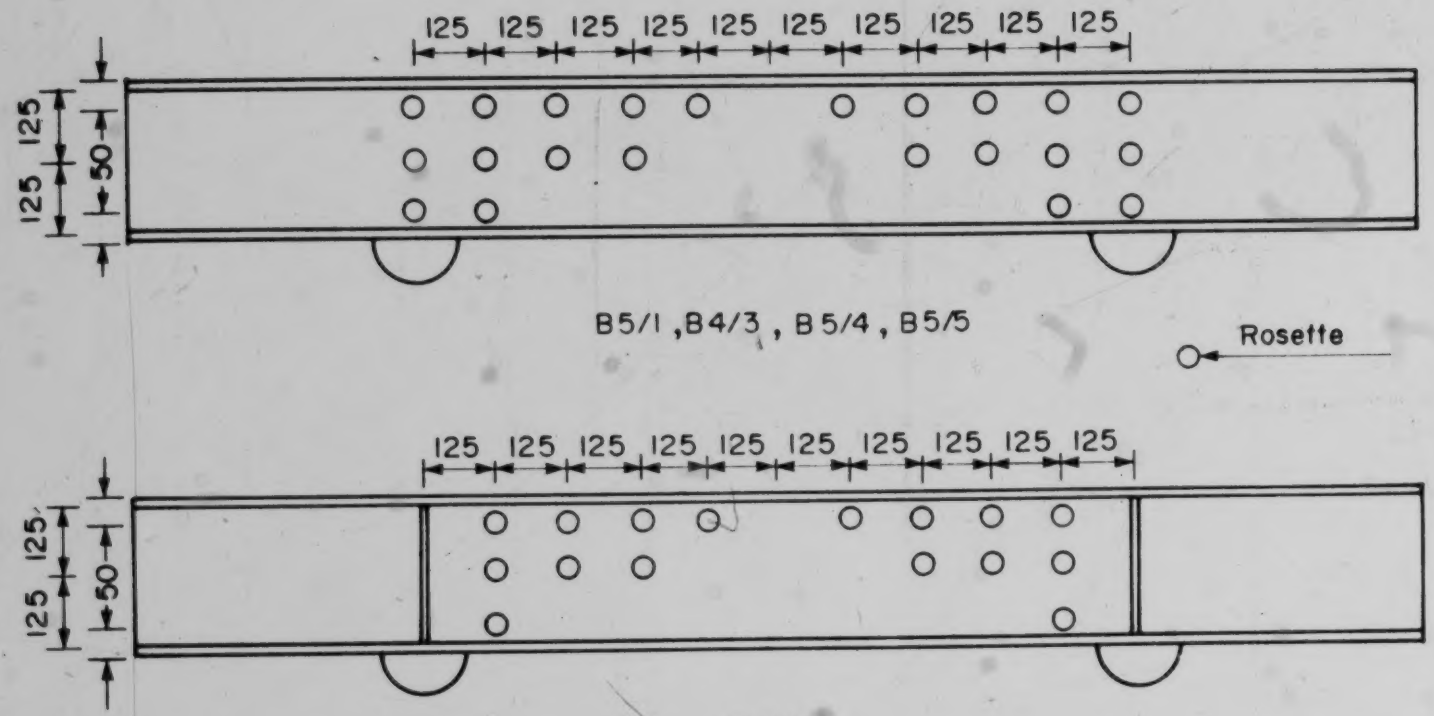

Figure 3.16 B5 series: Rosette layout.

gauges, rendered this method ineffective.

- Additional rosettes were included near the midspan of B6/7, since this specimen was loaded by an eccentric patch load.
- Rosettes were not attached over the supports in B5/2, because these would have been bisected by the diaphragm plates.

3.4.3 Steel Strains

All steel strains were measured using electrical resistance strain gauges. The gauges employed were Showa foil strain gauges, type N11-FA-5-120-11, with the following characteristics:

- Gauge length: 5 mm.
- Nominal resistance: 120 Ohms
- Gauge factor: 2.11 $\pm$ 1%
- Temperature compensation for steel.

These gauges give meaningful results up to 1.5% strain. All gauges were installed using the three-wire system to minimize the effect of lead wire resistance.

The strain gauge layout for each beam is given in Figs. 3.17 - 3.19. Longitudinal gauges on the loaded plates were located midway between the shear connector lines. Lateral gauges were located close to selected longitudunal gauges. Both internal and external gauges were used at locations where it was anticipated that plate bending may be significant. These layouts were chosen to allow

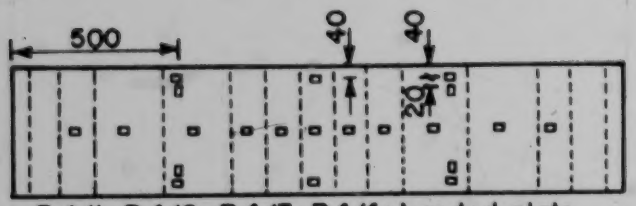

B4/1, B4/2, B4/3, B4/4; Loaded plate

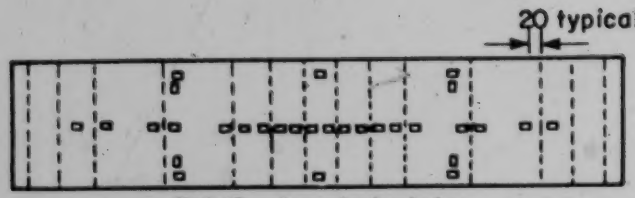

B4/5, Loaded plate

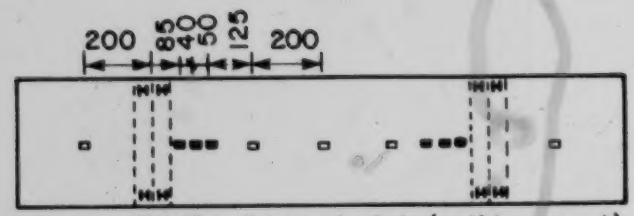

B4/2 ; Support plate (solid support)

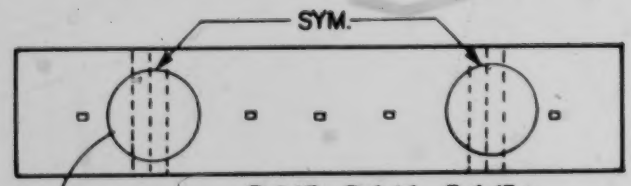

B4/3, B4/4, B4/5;
Support plate (stiffened plate support)

Legend

- External gauge
- Internal gauge
- External & internal gauge
- ------- Line of shear connectors

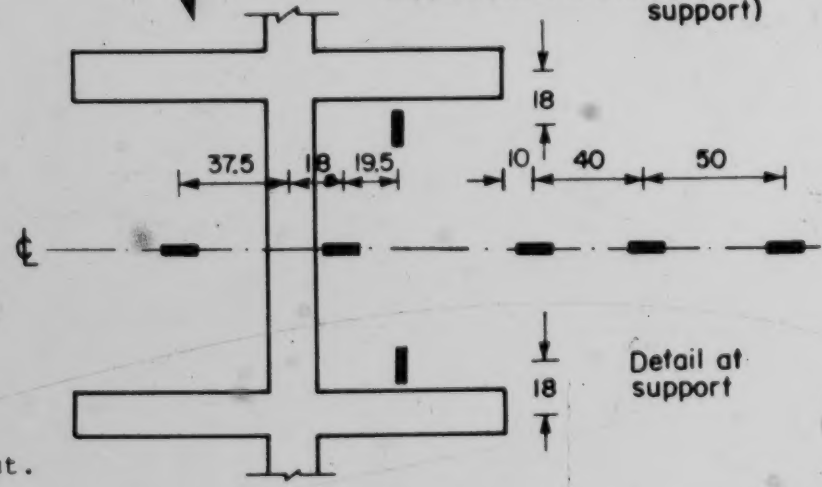

Figure 3.17 B4 series: Strain gauge layout.

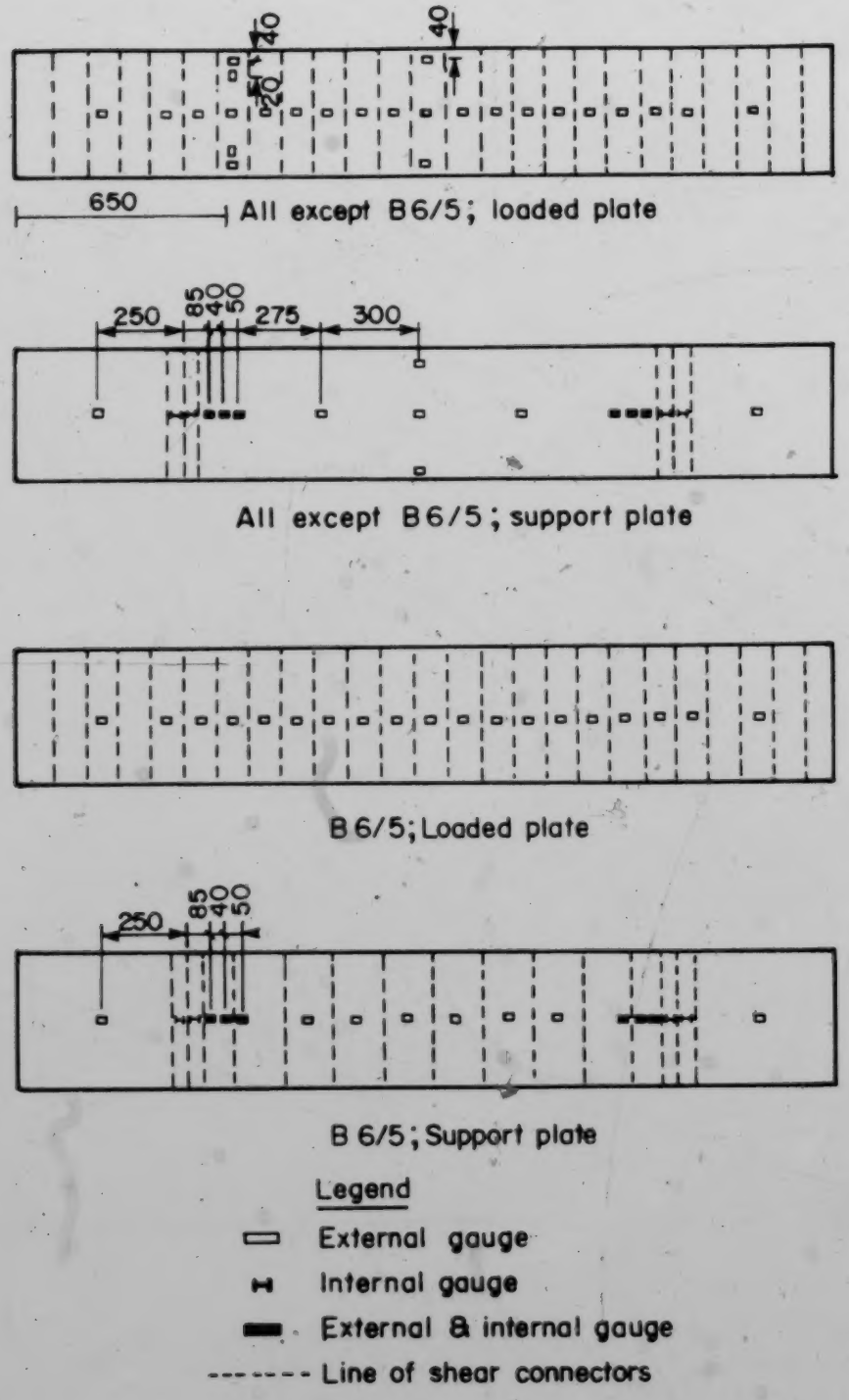

Figure 3.18 B6 series: Strain gauge layout.

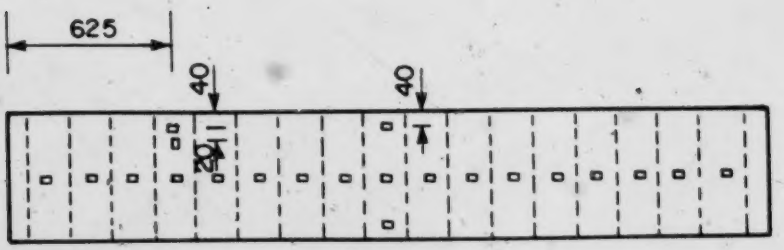

Loaded plate

Support plate

(Note: Additional stud lines on B5/4 and B5/5 not shown for clarity)

Legend

- External gauge
- Internal gauge
- External & internal gauge
- ------- Line of shear connectors

Figure 3.19 B5 series: Strain gauge layout.

determination of longitudinal and lateral strain and curvature profiles, and to measure orthogonal strain ratios at selected points.

The internal gauges were protected by steel caps, as shown in Fig.3.20. Several small caps were used at each internal gauge location so as to minimize the reinforcing effect. The gauges were sealed from the wet concrete by means of a 3 mm thick epoxy coating, and the caps were embedded 1 mm into this coating before it had set. The lead wires from the internal gauges passed through 4.0 mm holes located 20 mm from the centres of the gauges. According to the Kirsch solution for a circular hole in an infinite plate (Timoshenko and Goodier, 1970), the consequence of such a hole is to reduce the longitudinal stress at the gauge location by 1.4%. This is considered to be negligible. In no case did a plate fracture near such a hole.

3.5 Test Setup

3.5.1 General

A schematic layout for the frame used to load the specimens is given in Fig. 3.21. The tension-leg/crosshead assemblies were moveable, allowing beams to be tested with varying spans.

The specimens were inverted and loaded by hydraulic rams. Interaction between the test specimens and the loading frame was minimised by means of rocker and roller

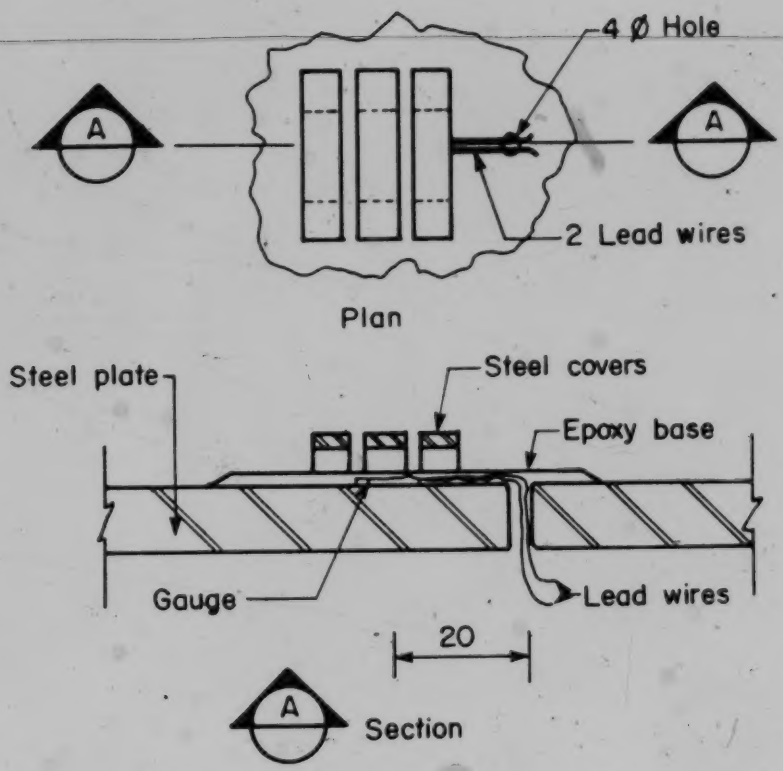

Figure 3.20 Internal gauge protection system.

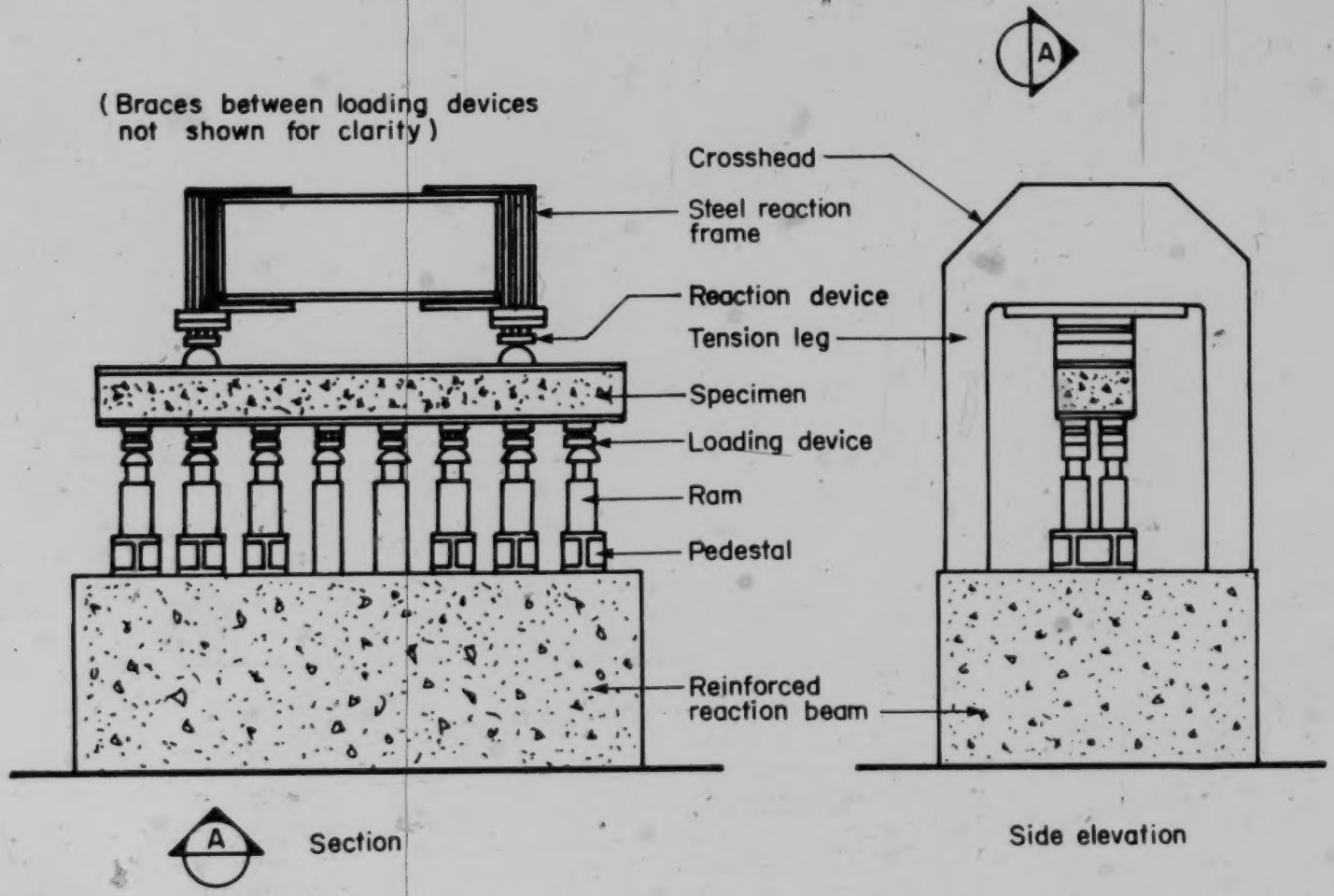

Figure 3.21 Loading frame.

assemblies. These load/reaction devices are discussed in Section 3.5.3. To further reduce the influence of the test frame on the load/deflection response of a test specimen, it was desirable to make the frame as stiff as possible. The frame stiffness, governed mainly by the axial stiffness of the tension legs, is estimated as 3400 kN/mm. Since the maximum reaction is approximately 3600 kN, the maximum anticipated elongation of the tension legs was approximately 1 mm.

3.5.2 Load Application and Load Measurement

Load was applied to the specimens by sixteen single-acting hydraulic rams, each of 450 kN capacity. The four rams used at midspan had 325 mm stroke so as to accomodate large deflections. The remaining 12 rams had 150 mm stroke. All pistons were extended 35 mm before each test in order to allow for piston retraction at the cantilevers during loading.

Fig. 3.22 shows the hydraulic circuit used. With the exception of B6/7 (patch load) and B5/4 (no cantilever rotation), all valves were open for all tests. In B6/7, rams 5,6,11 and 12 were disconnected, and rams 7,8,9 and 10 were repositioned. For B5/4, the in-line valves for rams 1,2,15 and 16 were closed, thereby preventing outflow of hydraulic fluid from these branches.

Load was measured at the pressure gauge near the pump, and at the load cell as shown in Fig. 3.22. Ram No. 17 was

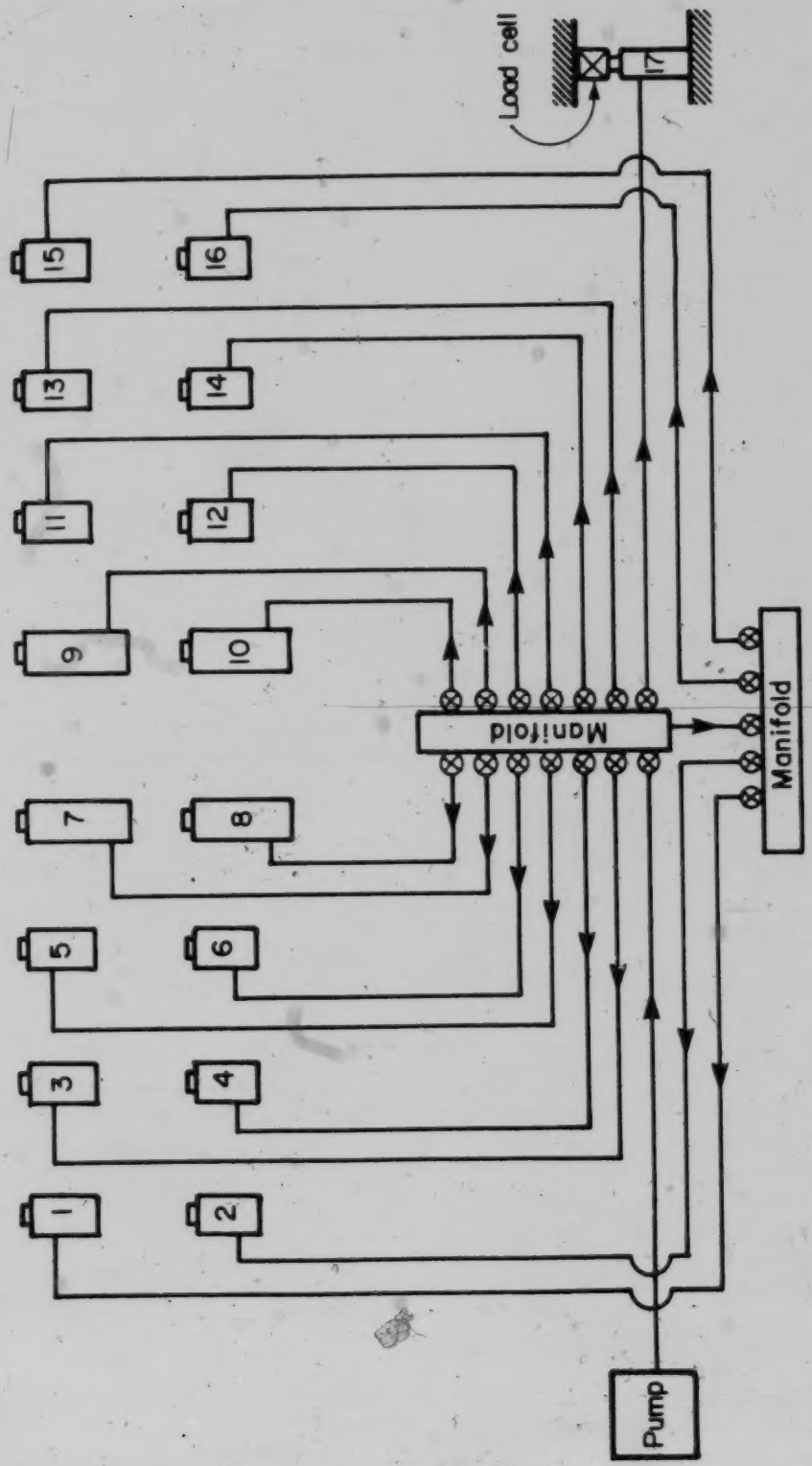

Figure 3.22 Hydraulic circuit diagram.

similar to rams 1 to 6 and 11 to 16. All rams had the same nominal piston diameter. The tension legs in the reaction frame were also instrumented to measure the reactions. These three independent load measurements were checked intermittently throughout each test. In all cases, agreement between the checks was highly satisfactory.

3.5.3 Load/Reaction Devices

Load and reaction devices allow rotational and translational freedom at the external boundary of the test specimen. Rotational freedom is provided by rockers at the load and reaction locations: rollers allow translational movement.

The loading devices and their interconnecting braces are shown schematically in Fig. 3.23. The pistons from the rams fit into recesses which are machined into the undersides of the rockers. Corresponding sets of rams (about the centreline) are braced against each other. The braces are bolted to the undersides of the rockers, and move vertically as rigid bodies when the pistons are extended. The rollers are mounted above the rockers.

The rocker/roller/brace assembly was designed to simulate the continued application of ice-loading as the specimen underwent large deformations (Fig.3.24). The following features are apparent:

- The applied load is always perpendicular to the loaded surface of the specimen. This simulates the situation

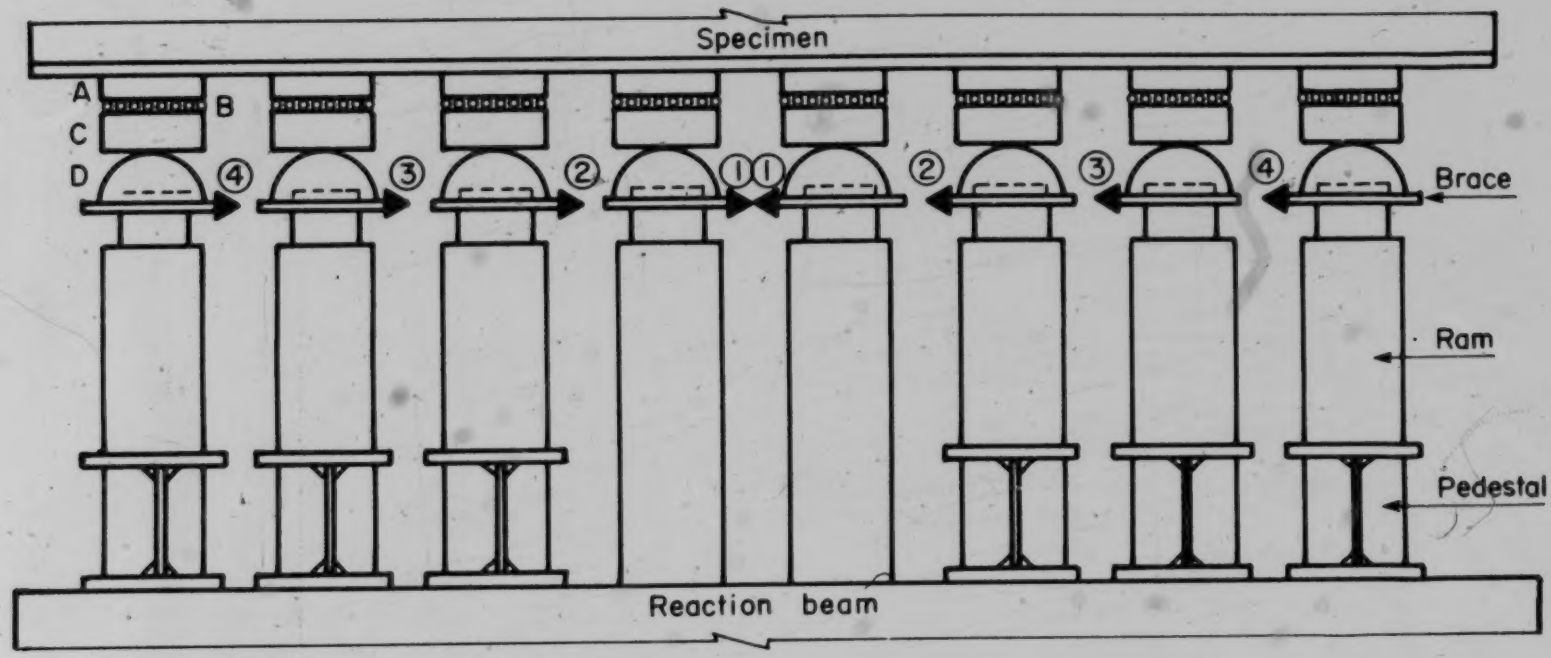

Specifications

A Roller plate - 125 x 125 x 40 ℄ - 700 Q
B Rollers (8) - 12 Ø x 125 stressproof
C Rocker Plate - 125 x 125 x 50 ℄ - AISI 4140
H.T. 35 Rc.
D Rocker - 125 Ø x 125 - AISI 4140
H.T. 35 Rc.

All plates ground smooth both sides

Figure 3.23 Loading devices and braces.

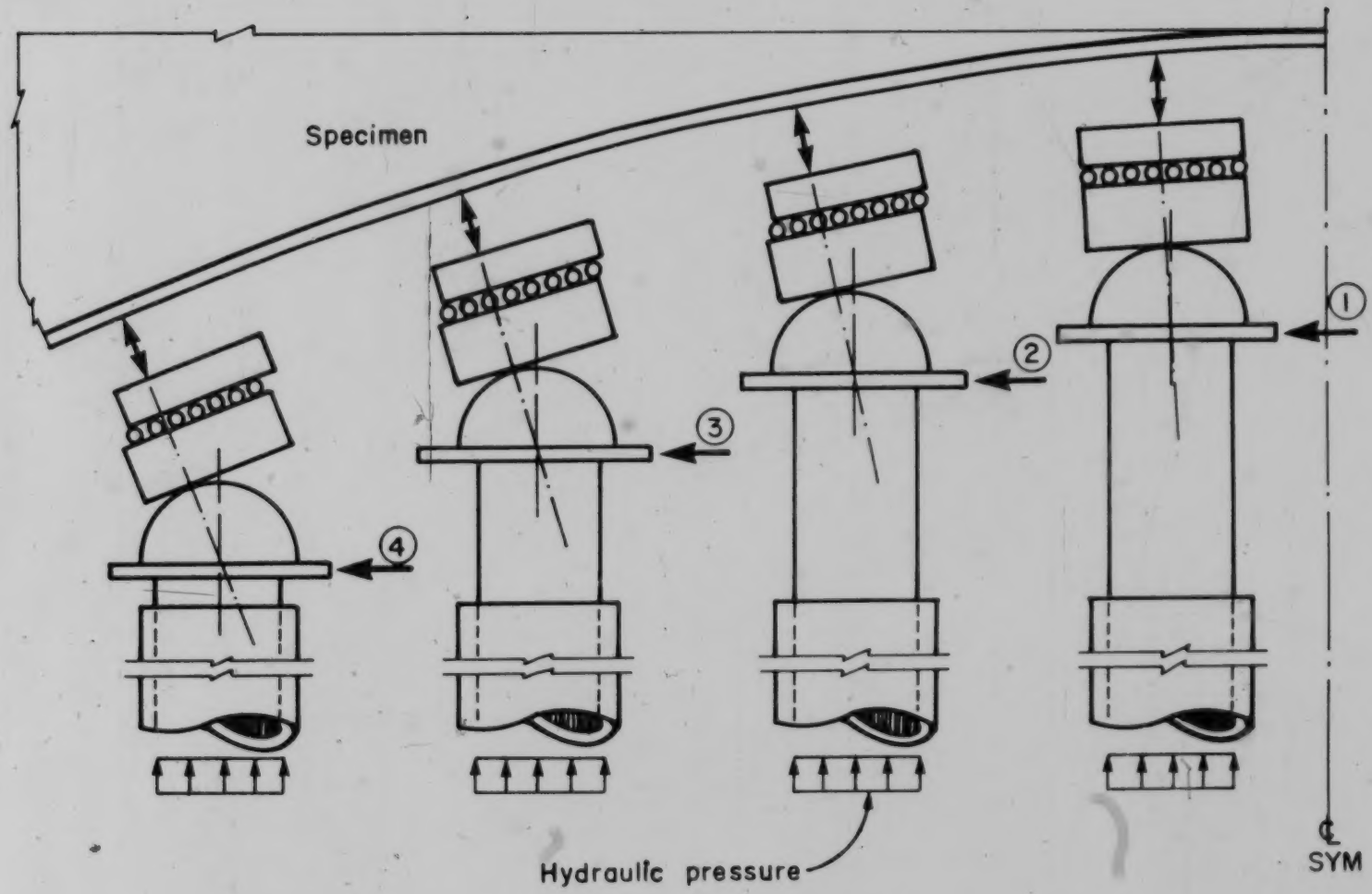

Figure 3.24 Load application at large deformations.

where frictional interaction is small between the ice-resisting wall and the crushed ice.

- The horizontal components of the forces on the semi-cylindrical rockers are reacted by forces in the braces between pairs of rams so that the lines of action of the force in the rams remains essentially vertical through large specimen deformations, provided the deformations of the specimen are essentially symmetrical.

The rocker/roller system utilised at the supports is shown in Fig. 3.25(a). This assembly is shown in its disturbed state in Fig. 3.25(b). The reaction always remains vertical, and its line of action always passes through the same point on the support plate of the specimen.

Because of the magnitude of the applied loads, special consideration was given to the contact stresses in the rockers, and to the contact stresses and coefficient of static rolling friction in the rollers. Contact stresses in the rockers and rollers (calculated from Hertzian theory) were allowed to reach 3000 MPa (F_y = 700 MPa). Orlov (1976) indicated that this level of stress could be used without permanent flattening occurring along the line of contact due to the triaxial stress state at the interface.

The use of several small diameter rollers (as opposed to a few of larger diameter) gave an economical and efficient solution to the problem of limiting rolling friction effects. It is noted here that estimating the

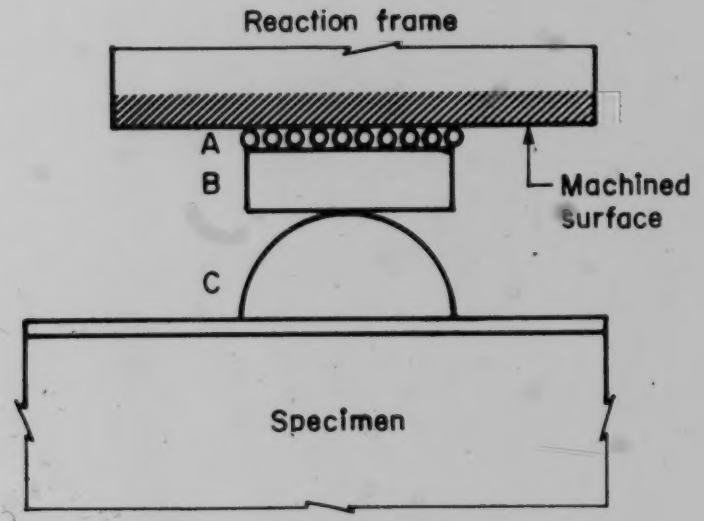

(a)

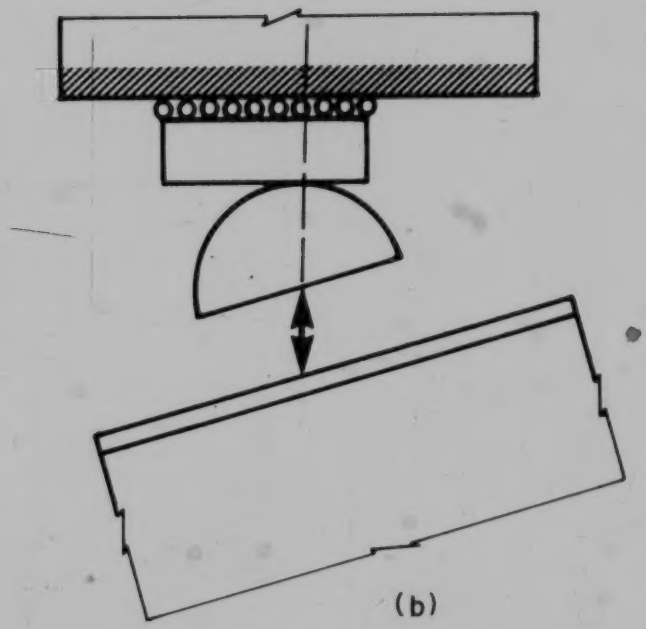

(b)

Specifications

A Rollers (10) - 12 Ø x 375 stressproof bar.

B Rocker plate - 150 x 50 x 375 ℓ
AISI 4140
H.T. 35 Rc.

C Rocker - 150 Ø x 375, AISI 4140, H.T. 35 Rc.

Figure 3.25 Reaction devices.

static coefficient of rolling friction from simple rolling theory, i.e.

$$s = \frac{e}{D}$$

where

s= coefficient of static rolling friction

e= width of contact strip (from Hertzian theory)

D= diameter of roller

appears to be grossly inaccurate. The static coefficient of rolling friction for a typical load-point eight-roller assembly was measured, and was found to vary essentially linearly between 0.65% for an applied load of 150 kN and 0.90% for an applied load of 400 kN. (Simple rolling theory predicts a value of 1.7% under an applied load of 400 kN). The maximum ram loads for the B4, B6, and B5 series were 415 kN, 339 kN and 384 kN, respectively.

4. TEST RESULTS

4.1 Introduction

The following quantities were recorded at regular intervals for each test.

1. Applied loads
2. Steel strains
3. Concrete strains
4. Concrete crack patterns
5. Relative horizontal movement of the supports
6. Vertical deflection of the support plate at midspan
7. Vertical deflection of the ends of the cantilevers
8. Horizontal movement of the ends of the cantilevers.

Items (1) to (5) are necessary for comparisons with the analytical model developed in Chapter 5. These comparisons are performed in Chapter 6. Item (6) is used to observe the post-failure ductility of the system. Items (7) and (8) are not used in this report. They were recorded for future correlation with finite element analysis, and will be reported in that publication.

4.2 General Test Observations

4.2.1 Failure Loads and Modes of Failure.

Table 4.1 lists the failure loads and describes the type of failure for each test specimen. The failure loads are given in terms of the average pressure p on the loaded

Table 4.1 Failure loads and descriptions of failure.

Specimen #	Failure Load (MPa)	Description of Failure
B4/1	10.00	Fan-type cracking pattern. Closely spaced tensile cracks followed by crushing near the support.
B4/2	11.03	Fan-type cracking pattern. Closely spaced tensile cracks followed by crushing near the support. (Plates 4.1(a) and 4.1(b)).
B4/3	10.02	Fan-type cracking pattern. Concrete crushed at mid-depth of beam (Plate 4.2).
B4/4	11.06	Fan-type cracking pattern. Crushing near support.
B4/5	10.70	Fan-type cracking pattern. Crushing near support.
B6/1	4.74	Fan-type cracking pattern. Crushing near support. (Plates 4.3(a) and 4.3(b)).
B6/2	3.52	Extensive strain hardening of the support plate, followed by diagonal cracking and crushing near support.
B6/3	6.02	Steel-fibre-reinforced beam. Crushed near support without fan formation. (Plate 4.4).
B6/4	4.70	Steel-fibre reinforced beam. Did not fail on span. Very large deflection at midspan at end of test. (Plate 4.5). Cantilever failed early (Plate 4.6).
B6/5	5.09	Fan-type cracking pattern. Crushing near support.
B6/6	3.90	Horizontal crack along top of studs at support (Plate 4.7). Closely spaced tensile cracks, followed by crushing near support.
B6/7	5.42	Eccentric patch load. Failed on long shear span. Closely spaced tensile cracks followed by crushing near support (Plate 4.8).
B5/1	8.15	Fan-type cracking pattern. Overall crushing of concrete in fan (Plate 4.9).
B5/2	8.20	Fan-type cracking pattern. Overall crushing of concrete in fan.
B5/3	5.15	Fan-type cracking pattern. Crushing near support followed by fracture of the support plate (Plates 4.10(a) and 4.10(b)).
B5/4	5.10	Support rotation prevented. Fan-type cracking pattern. Crushing near both supports followed by very large midspan deflection (Plates 4.11(a) and 4.11(b)).
B5/5	5.01	Fan-type cracking pattern. Crushing near support.

plate, expressed in MPa. The loads P applied by each pair of rams can be determined by multiplying p by the tributary area for a pair of rams. For the B4 series this was 75000 mm^2, for the B6 series it was 112500 mm^2, and for the B5 series 93750 mm^2 (see Figs. 3.2, 3.7 and 3.10). Correlation with Plates 4.1 to 4.11 is also indicated in Table 4.1. The plates are grouped at the end of this chapter. In these plates, the supports are at the top of the test specimen and are hidden behind the vertical steel members. Loads were applied through eight pairs of plate and roller assemblies bearing on the bottom plate.

4.2.2 Load-deflection Response, Ductility and Load Cycling.

The load vs. midspan deflection plots for the B4, B6, and B5 series are given in Fig. 4.1, Fig. 4.2 and Fig. 4.3, respectively. In order that a full series could be included in one plot, it was necessary to compress the scale on the abscissa. The inclined cracking load is designated by "IC" in these plots, and major crushing of the concrete is shown as "MC". This crushing occurred in the region of the inclined cracks as shown typically in Plates 4.1(b) and 4.2. Generally, the crushing was limited to one end of the span between supports. Most of the tests were terminated due to asymmetry in the loading system after crushing had occurred at one support, and not because of any inability of the specimens to undergo further deformation. It can be seen that most of the specimens continued to carry a decreasing

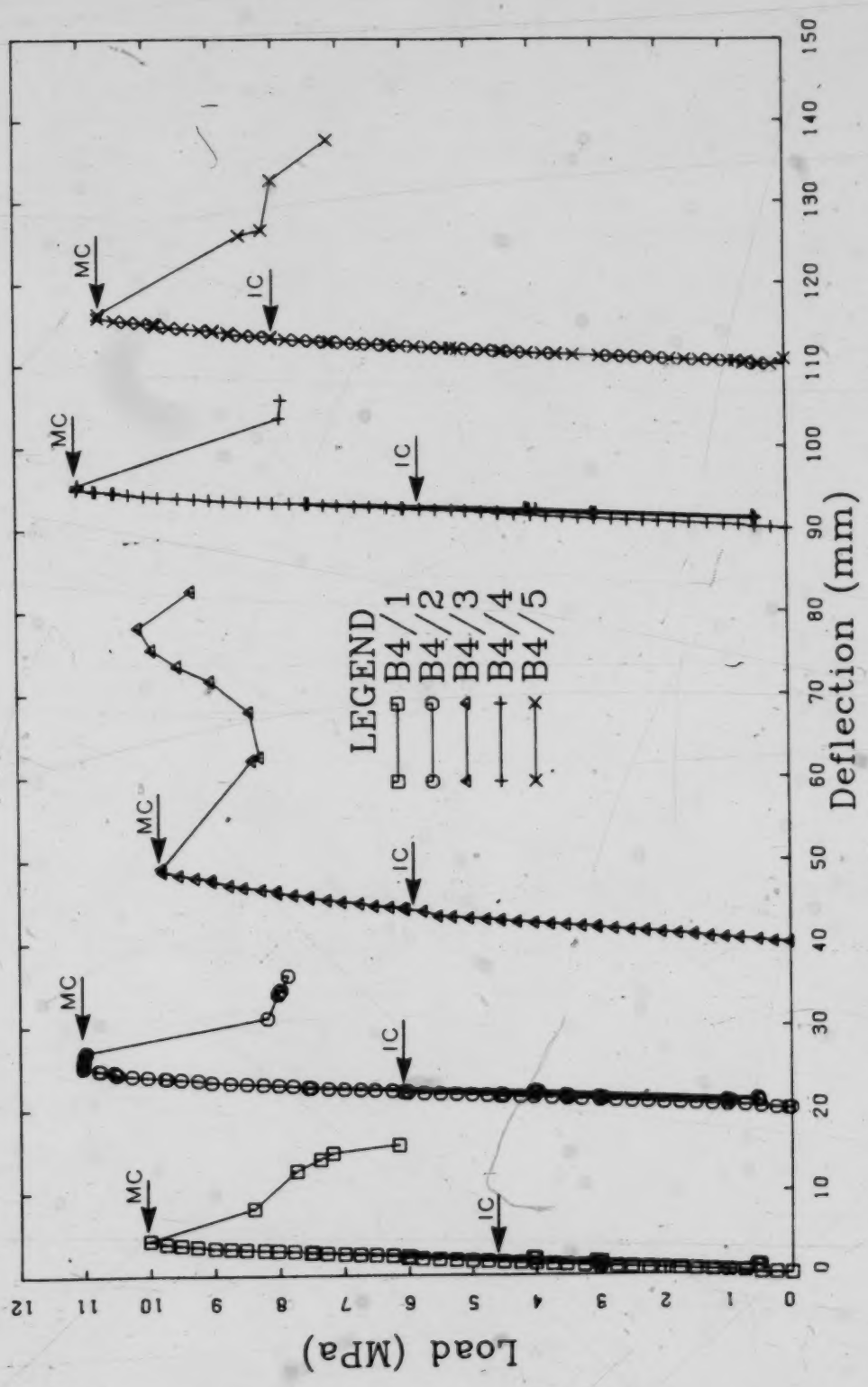

Figure 4.1 B4 series: Load - midspan deflection plots.

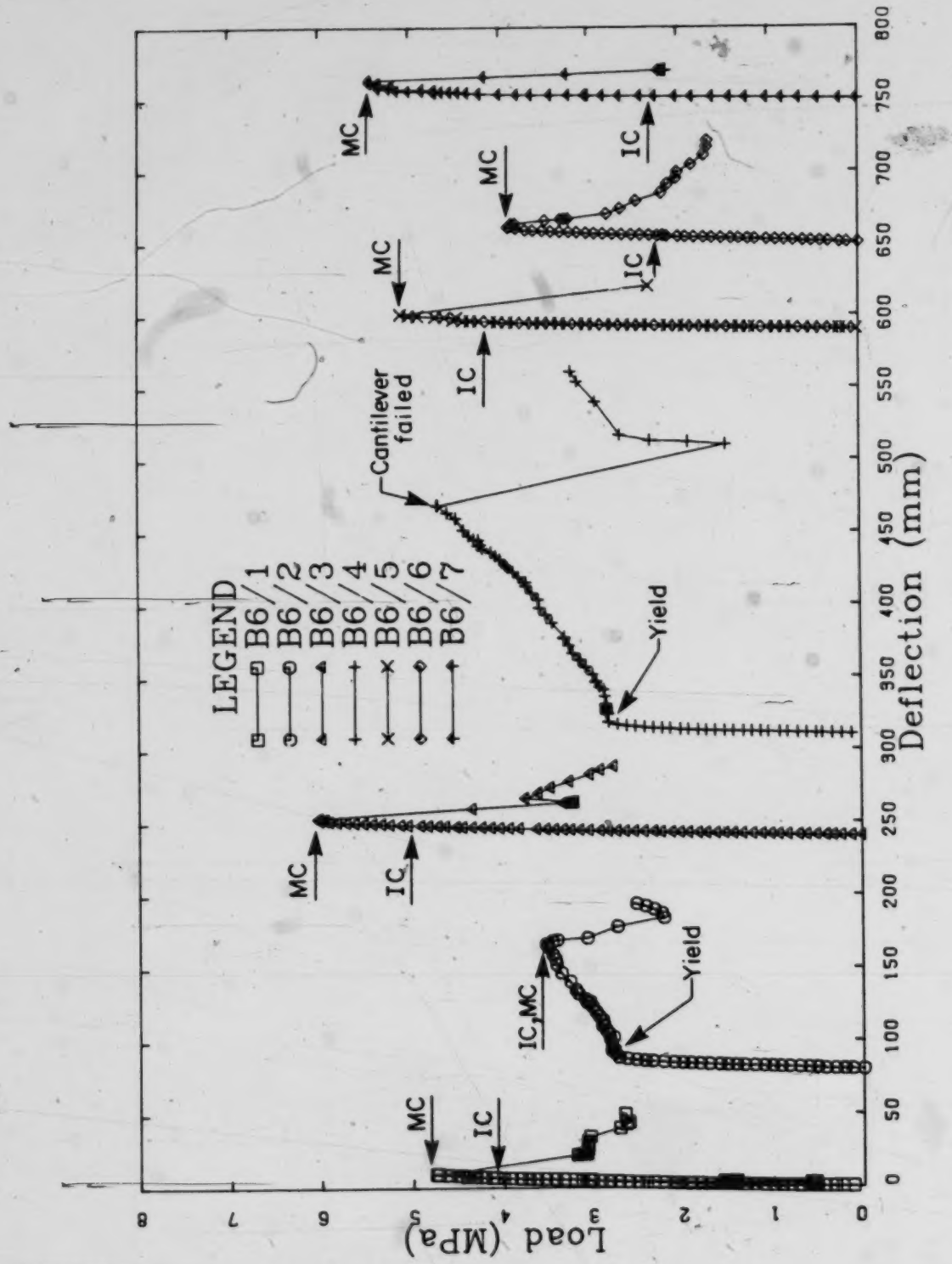

Figure 4.2 B6 series: Load - midspan deflection plots.

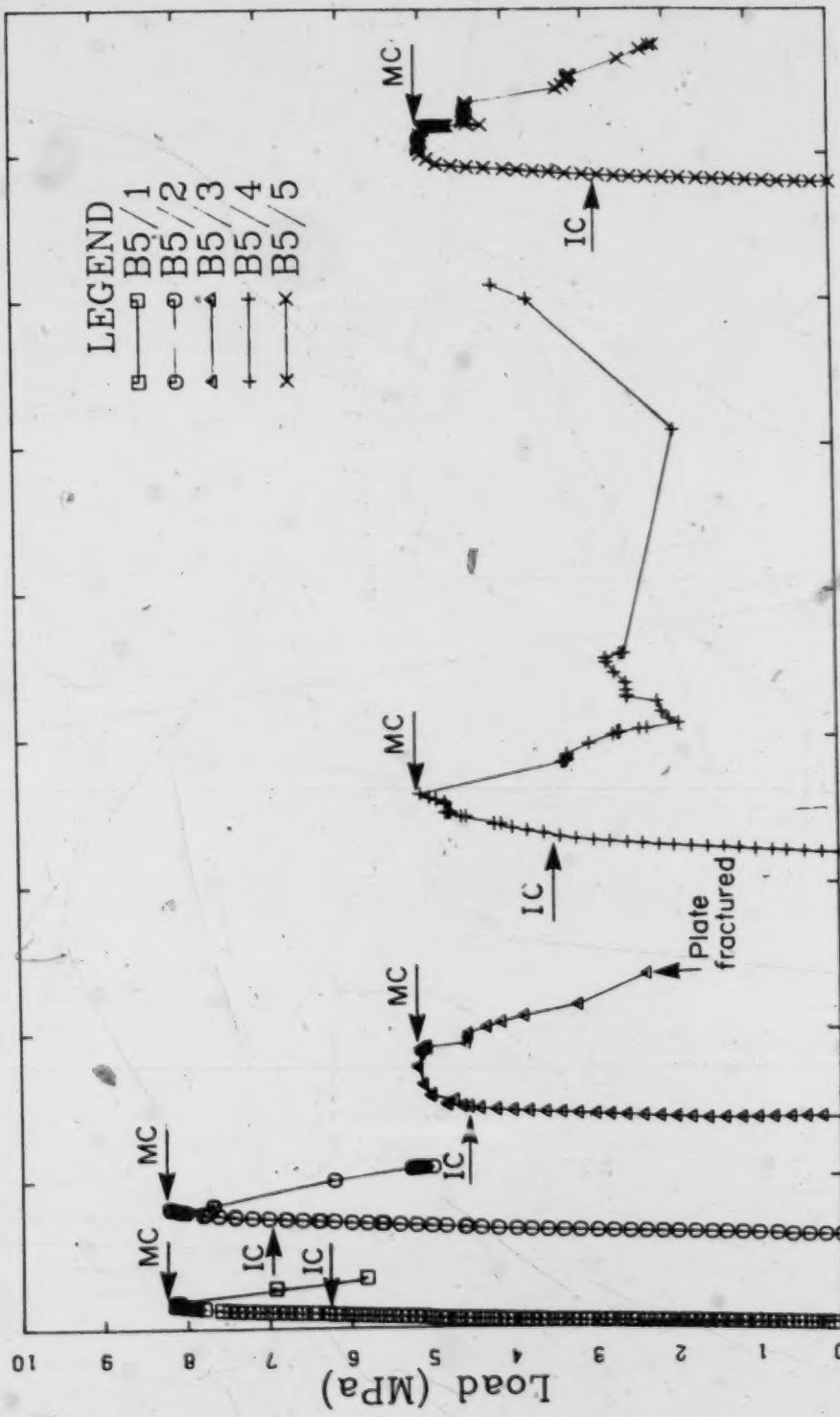

Figure 4.3 B5 series: Load - midspan deflection plots.

load after the maximum load had been reached.

The area under a load-deflection curve is important, because it is representative of the energy absorbed by the specimen. In a prototype structure, this absorbed energy would result from the change in kinetic energy of the ice event. The load-deflection response for specimen B5/5 is repeated in Fig 4.4, where the scale on the abscissa has been enlarged in comparison with Fig. 4.3. With reference to this figure, the energy absorption capability of a typical test specimen is defined in terms of the post-yield ductility ratio (PYD) and the post-crushing ductility ratio (PCD). The post-yield ductility ratio (PYD) is defined as

$$PYD = \frac{\text{Energy absorbed at maximum load } (B_1+B_2)}{\text{Energy absorbed when steel plate yielded } (B_1)},$$

and the post-crushing ductility ratio (PCD) is defined as

$$PCD = \frac{\text{Total energy absorbed } (A_1+A_2)}{\text{Energy absorbed at concrete failure } (A_1)}$$

where the areas B_1, B_2, A_1 and A_2 are defined in Fig. 4.4, and it can be seen that $A_1 = B_1+B_2$. It is noted that $A_1 = B_1+B_2$ only in those cases when the plate yielded. If the plates did not yield, B_1 is undefined. The values of PYD and PCD for all of the tests are given in Table 4.2. The post-yield ductility ratio (PYD) could only be calculated for the specimens in which the support plate yielded (i.e. the specimens B6/2, B6/4, B5/3, B5/4 and B5/5).

Specimen B5/3 failed by tearing of the support plate at the inside face of the support, shortly after the concrete crushed (Plate 4.10(b)), thereby preventing any further

Table 4.2 Ductility ratios.

Specimen #	PCD $\frac{A_1 + A_2}{A_1}$	PYD $\frac{B_1 + B_2}{B_1}$
B4/1	4.1	-
B4/2	3.8	-
B4/3	6.1	-
B4/4	4.7	-
B4/5	5.4	-
B6/1	6.2	-
B6/2	1.3	22.0
B6/3	4.7	-
B6/4	-	45.0
B6/5	2.5	-
B6/6	7.7	-
B6/7	1.6	-
B5/1	1.9	-
B5/2	3.6	-
B5/3	2.3	2.3
B5/4	4.1	1.4
B5/5	3.8	4.2

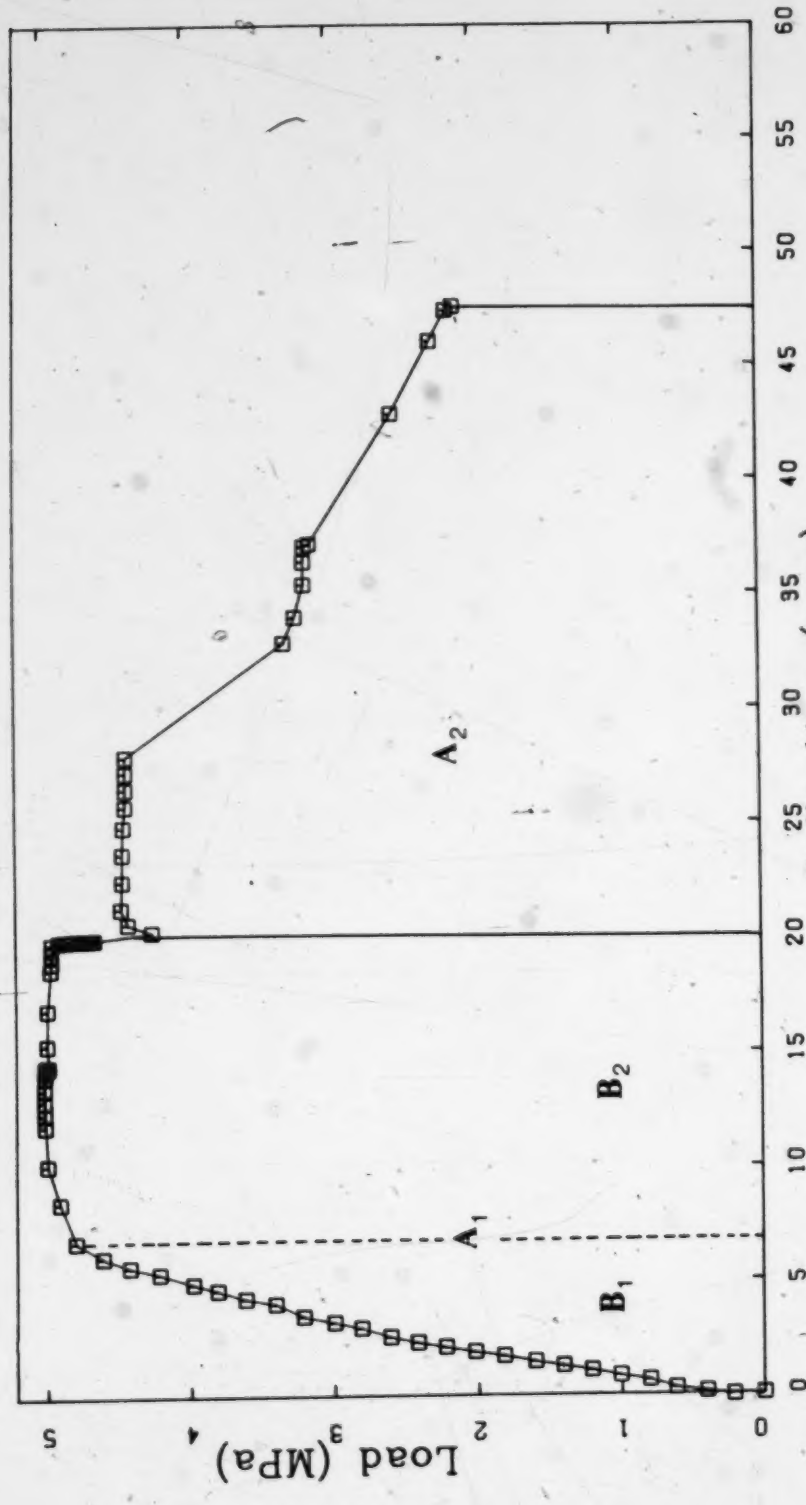

Figure 4.4 Enlarged load-deflection plot for specimen B5/5, showing the areas used in the definition of the ductility ratios PYD and PCD.

post-crushing ductility. This occurred because the studs at the support in the B5 series were placed in rows centered at 62.5mm about the centreline, whereas in the B4 and B6 series, the row spacing was 50 mm. As a result, the heat-affected zones due to the welding of the studs extended beyond the face of the support and into the span. These zones appear to have reduced the ductility of the plate and initiated the early rupture. The indentations on the failure surface due to the heat-affected zones can be seen in Plate 4.10(b), where the white dots indicate the locations of the studs at the support. The consequences of this result are serious; post-crushing ductility may be curtailed due to rupture of the support plate at the heat-affected zones near the support regions.

The load was cycled five times between 0.5 MPa and 6.0 MPa and five times between 0.5 MPa and 7.5 MPa in specimens B4/1, B4/2 and B4/4. The first inclined cracks appeared in these specimens during the monotonic loading phase at loads of 4.5 MPa, 5.9 MPa and 5.9 MPa, respectively. In B4/1, two new diagonal cracks appeared during cycling to 7.5 MPa. In specimen B4/2, some cracks elongated during cycling to 7.5 MPa. In B4/4, however, crack elongation was noticed during cycling at the lower load level (6.0 MPa), and cycling at 7.5 MPa caused existing independent cracks to propagate and join. Noise from the concrete was also detected during the unloading phases in B4/4. It was concluded that B4/4 exhibited significantly

more distress than either B4/1 or B4/2 during cycling. Specimens B4/1 and B4/2 were supported on solid bulkhead supports, whereas B4/3 utilised a stiffened plate bulkhead support. The significance of this is discussed in more detail in Section 4.6.4. Load was also cycled in B6/1, but with no visible effect.

4.3 Effects of Details Investigated in the B4 Series.

4.3.1 Concrete Confinement Near the Supports.

The test series was designed such that the effect of concrete confinement could be assessed by comparing the results of B4/5 (unconfined) with B4/4, which had the confinement devices of Fig. 3.5 at the supports. However, it was found that the confinement devices attracted very little load, possibly because the lateral bending stiffness of the studs at the support provided internal confinement to the concrete. There was no apparent difference in load capacity due to the addition of the confining plates. Accordingly, no conclusion as to the effect of concrete confinement could be drawn.

4.3.2 Type of Shear Connector.

An indication of the effect of the type of shear connector on the behaviour can be seen by comparing tests B4/1 (stud connectors) and B4/2 (plate connectors). Both of these specimens had solid supports. Flexural cracking in the

negative moment region started earlier when plate connectors were used, and the cracks initiated at the plate connector locations. The type of connector did not appear to have a strong influence on the failure load or the load-deflection response. Since stud connectors were deemed to be easier to use in practice, they were used exclusively for the rest of the program.

4.3.3 Type of Support.

The effect of support type was investigated by comparing the results of specimens B4/4,which had stiffened plate supports as shown in Fig. 3.6, and B4/1, which had solid supports. Both of these specimens had stud shear connectors. For beams with plate shear connectors, the effect of support type was assessed by comparing specimens B4/3 (stiffened plate support) and B4/2 (solid support). The average capacity of beams B4/3 and B4/4 was 10.59 MPa, compared to 10.52 MPa for beams B4/1 and B4/2. Although the support type had no appreciable effect on the load capacity of the beams, local behaviour at the support was greatly affected. This effect is discussed in Section 4.6.4.

4.3.4 A Note on the Effect of Roller Assemblies vs. Teflon-based Slip Surfaces at the Load and Reaction Points.

Specimen B4/5 had Teflon-based slip pads at the load and reaction locations, whereas all other tests used roller

assemblies. The high coefficient of friction (approximately 4%) associated with these pads prevented monotonic slip from occurring at the supports. This is shown in Fig. 4.5, where the load vs. relative support displacement curves for Teflon pads and roller assemblies are compared. Large frictional restraint was built up at the supports, with only very slight release occurring at discrete load levels. The effect of this restraint is difficult to quantify accurately. Accordingly the results for specimen B4/5 will not be used for the development of a failure criterion in Chapter 6.

4.4 Effects of Details Investigated in the B6 Series.

The B6 series was designed to investigate the effects of concrete strength, concrete type, degree of reinforcement (over-reinforced or under-reinforced), presence of studs on the span of the support plate, and load arrangement on member behaviour. All specimens in this series used stud connectors and solid supports.

4.4.1 Concrete Strength.

The effect of concrete strength was observed by comparing B6/1 (f'_c = 54.5 MPa) and B6/6 (f'_c = 39.5 MPa). The failure modes for the two specimens were essentially identical, but the ratio of the failure loads was 1.22 while the ratio of the cylinder strengths was 1.38, suggesting that the member capacity increases at a slower rate than cylinder strength. This concept is treated in more depth in

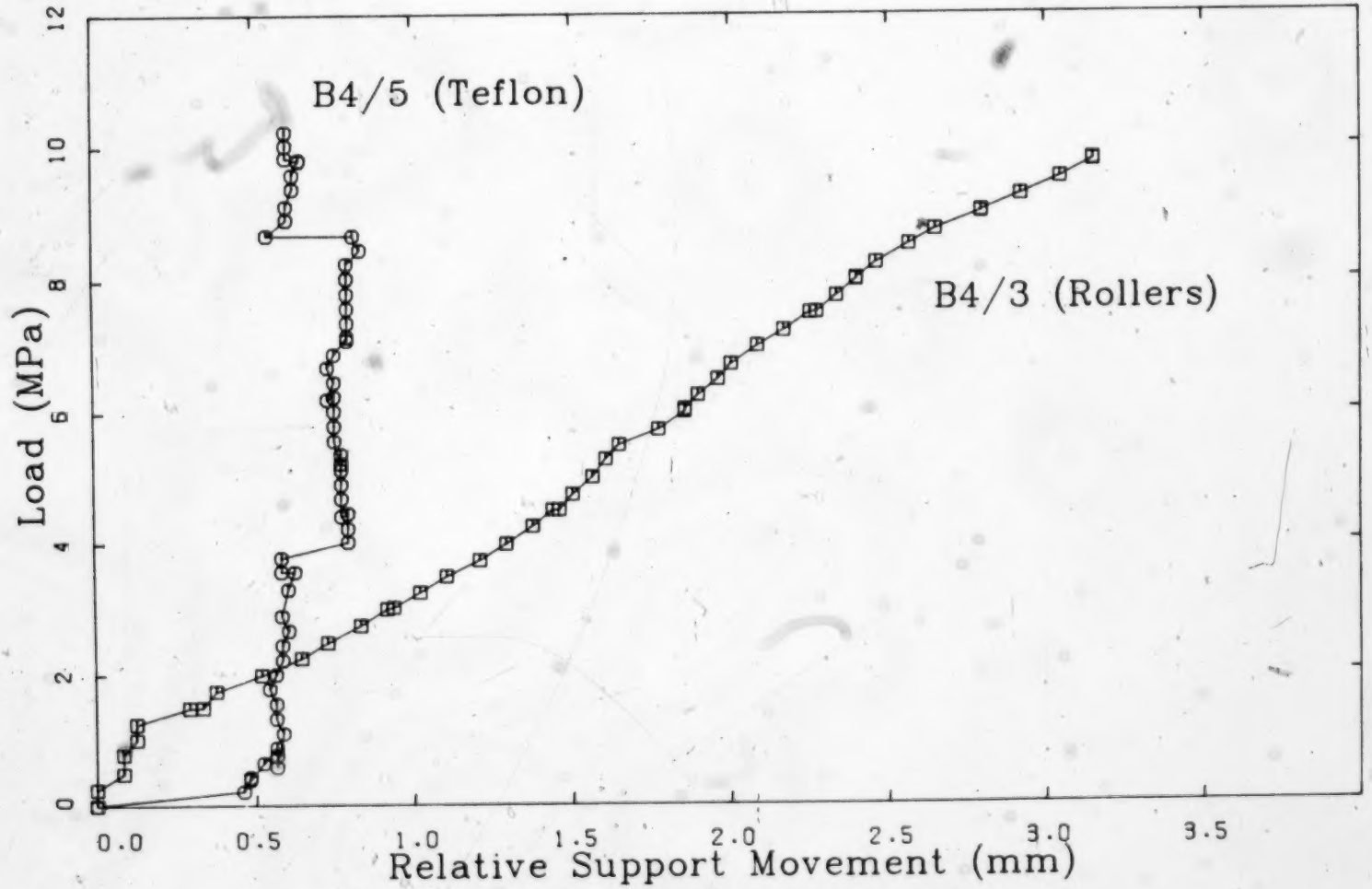

Figure 4.5 Comparison of load-relative support displacement plots for Teflon pads and roller assemblies.

Chapter 6.

4.4.2 Type of Concrete (Plain or Steel-fibre-reinforced) in an Over-reinforced Specimen.

Steel-fibre-reinforced concrete (SFRC) was used in specimens B6/3 and B6/4. The effect of SFRC in an over-reinforced specimen was observed by comparing B6/3 with B6/1. The ratio of failure loads was 1.22 compared to a ratio of cylinder strengths of 1.05. This increase in member capacity for similar cylinder strengths is not surprising since SFRC is a material very different from unreinforced concrete. The addition of a reasonable amount of steel fibres (say, 1.0%/vol) doubles the tensile strength of the "concrete" and also increases its toughness by a factor of at least 10 (ACI 544.1R, 1982). The presence of steel fibres across tension cracks tends to reduce the rate of crack width opening, and it will be demonstrated in Chapter 6 that the effect of this restraint is to increase the apparent compressive strength of the "concrete".

4.4.3 Type of Concrete (Plain or Steel-fibre-reinforced) in an Under-reinforced Specimen.

The effect of SFRC in an under-reinforced specimen is seen by comparing specimens B6/4, which had a SFRC core, and B6/2, which had a plain concrete core. Because of the increased tensile strength of SFRC, very large deformations were obtained in B6/4 without any diagonal tensile cracking

(Plate 4.5). In contrast, B6/2 ultimately failed through the formation of a shallow diagonal tension crack and subsequent crushing of the concrete, even though the support plate had reached the strain hardening range at this stage. It is noted that one cantilever in B6/4 failed prematurely due to "unzipping" caused by the inadequate fusion of one stud (Plate 4.6). Because of this failure, the beam was loaded on the span only for the latter portion of the test. However, this different loading pattern contributed only slightly to the large deformations obtained (Fig. 4.2).

4.4.4 Shear Studs on the Span of the Support Plate of an Over-reinforced Specimen.

In many of the test specimens, the shear connector studs on the tension plate were concentrated near the supports, while those on the compression plate were distributed more uniformly. In a prototype structure, it is anticipated that studs would be fastened more or less uniformly in the spans of both plates. The effect of such studs in over-reinforced specimens was observed by comparing B6/5 with B6/1. Specimen B6/5 had stud shear connectors on the span of both plates, but B6/1 had studs on the span of the loaded plate only. When studs were included in the span of the support plate, the initial flexural cracks were distributed along the span, and started at the stud locations. However, the extra studs did not appear to influence either the load at which diagonal cracks appeared

or the failure load of the specimen.

4.4.5 Loading Arrangement.

The effect of non-uniform load was investigated in B6/7, which was loaded by an eccentric patch load as shown in Fig. 3.7 and Plate 4.8. The most interesting facet of this test was that failure occurred in the long shear span. The load carrying mechanism for B6/7 is discussed in detail in Chapters 5 and 6.

4.5 Effects of Details Investigated in the B5 Series.

The details for the B5 series were chosen on the basis of the results of the B4 and B6 series. In addition, the effects of support diaphragms and rotational restraint at the support were investigated. It was intended that B5/1 and B5/2 would be over-reinforced, and that B5/3, B5/4 and B5/5 would fail in a ductile manner. However, it was found that specimens B5/3, B5/4 and B5/5 failed by crushing of the concrete shortly after yielding of the support plate. It should not be deduced from these three tests that, as a general rule, the concrete will crush immediately after yielding of the support plate since, as mentioned in Section 4.4.3, specimen B6/2 failed by crushing of the concrete only after significant strain hardening had occurred in the support plate. Nevertheless, these tests gave valuable insight into the effect of the thickness of the support plate on the load-carrying capacities of the specimens. This

information is used in Chapter 6.

4.5.1 Diaphragm Plates at the Supports.

In order to hold the plates apart at a fixed distance, it is expected that a prototype structure would incorporate diaphragm plates at the bulkhead lines. B5/2, which had diaphragm plates, was compared with B5/1, which did not have such plates. It was found that B5/1 and B5/2 yielded essentially identical results, and so no apparent effect of diaphragm plates was observed.

4.5.2 Shear Studs on the Span of an Under-reinforced Specimen.

Specimens B5/3 and B5/5 differed only in the fact that B5/5 had studs fixed along the span of the support plate. These were found to have no influence on the member behaviour.

4.5.3 Rotational Restraint at the Supports.

B5/4 was fixed against rotation at the supports. This kinematic restraint had no appreciable effect on the failure load. However, it allowed both ends of the specimen to fail simultaneously (Plate 4.11(a)), and post-failure ductility was immediately and graphically obtained (Plate 4.11(b)). From this plate, it can be seen that the load-carrying capacity after failure was obtained from a combination of the shallow concrete arch and the hanging action of both

steel plates.

4.6 Strain and Curvature in the Steel Plates.

4.6.1 Longitudinal Strain and Curvature Profiles

The longitudinal steel strain profiles for the loaded and support plates are required in order that the composite nature of the specimens may be examined. Since several of the specimens were tested to investigate the effect of details on strength, only specimens B4/1, B6/1, B6/7 and B5/1 are shown here. These specimens had evenly spaced studs on the loaded plate and studs over the support on the support plate. These results may be considered as representative of the other over-reinforced specimens. The strain profile plots for B4/1, B6/1, B6/7 and B5/1 at maximum load are presented in Figs. 4.6 to 4.9 respectively. These plots also show the yield strain of the material in each plate.

4.6.1.1 Loaded Plate.

The strain gradients in the loaded plate indicate that composite interaction (shear transfer) is taking place between the loaded plate and the concrete. The profiles for B4/1, B6/1 and B5/1 are essentially symmetric while the distribution for B6/7 is skewed, since this specimen was loaded with an eccentric patch load. Comparison between the measured strain distributions and those given by an analytical model is

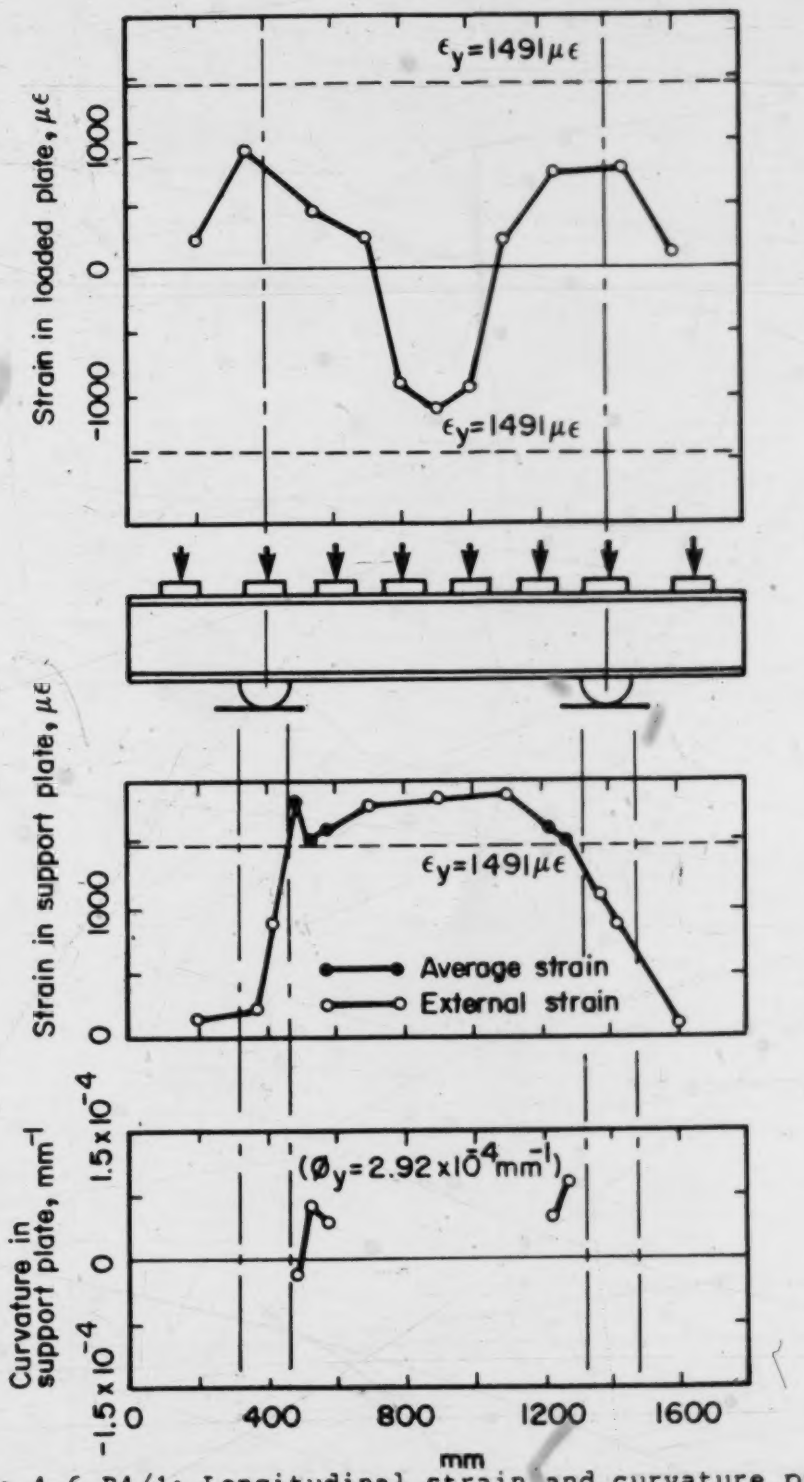

Figure 4.6 B4/1: Longitudinal strain and curvature profiles in the loaded and support plates.

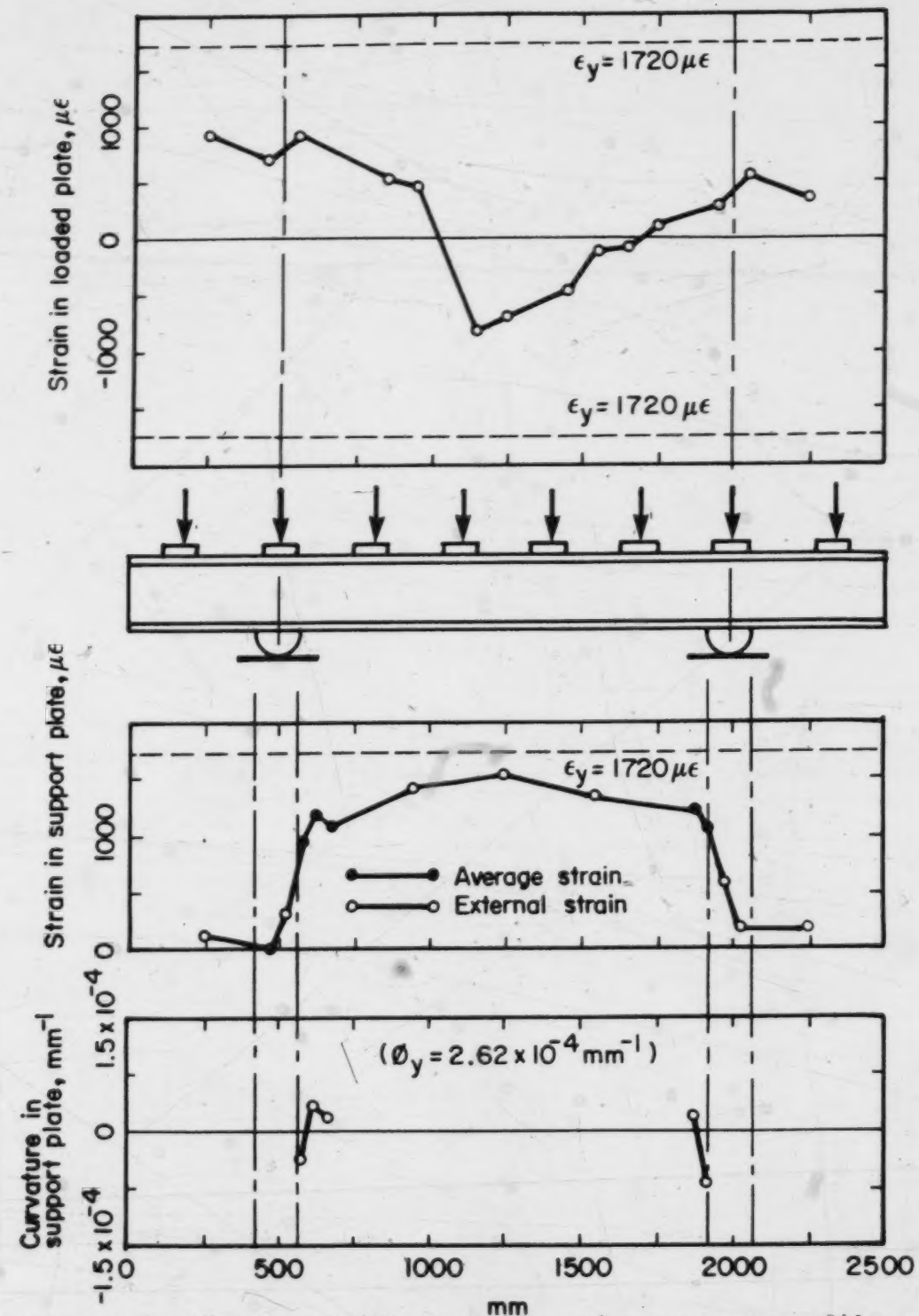

Figure 4.7 B6/1: Longitudinal strain and curvature profiles in the loaded and support plates.

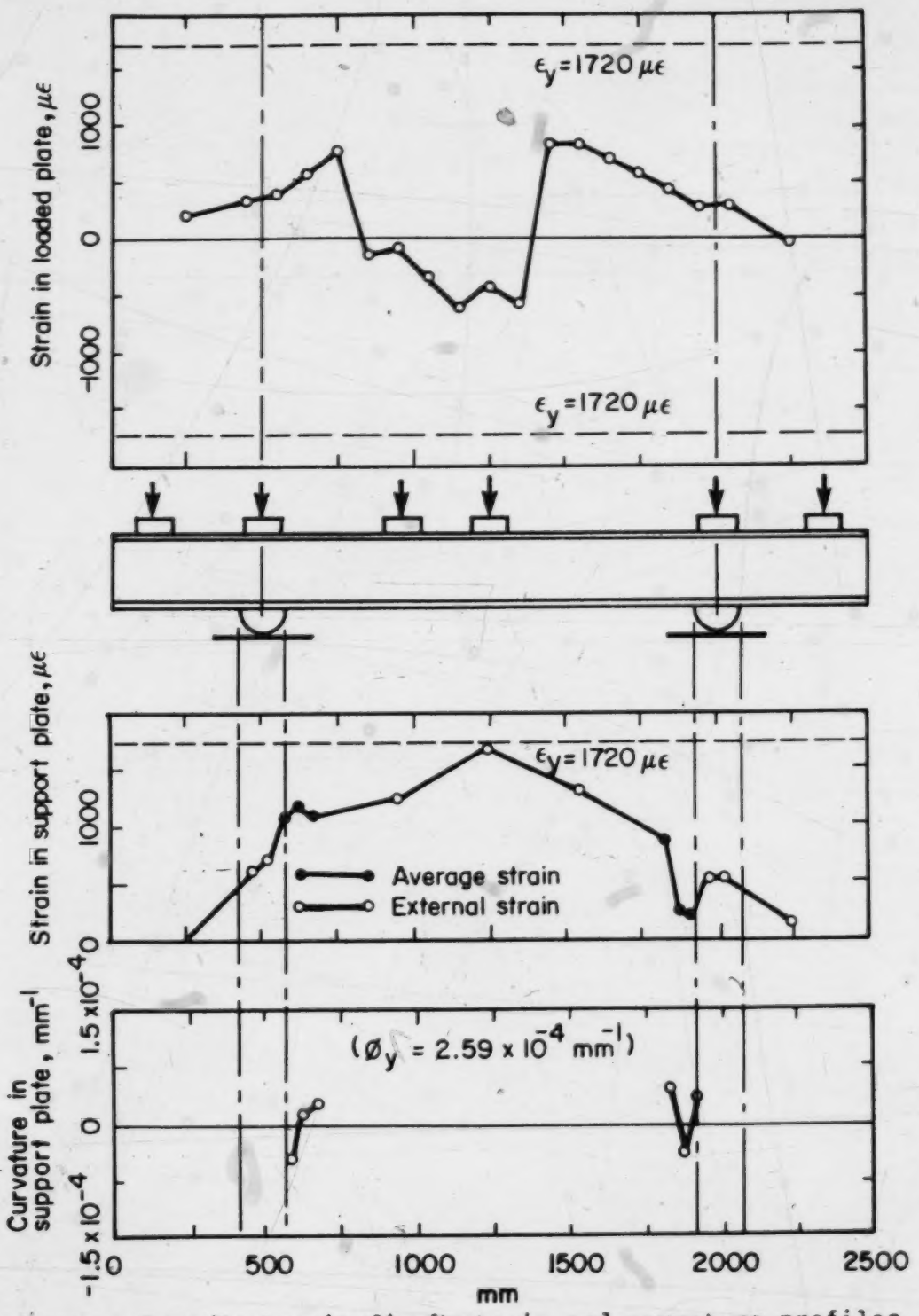

Figure 4.8 B6/7: Longitudinal strain and curvature profiles in the loaded and support plates.

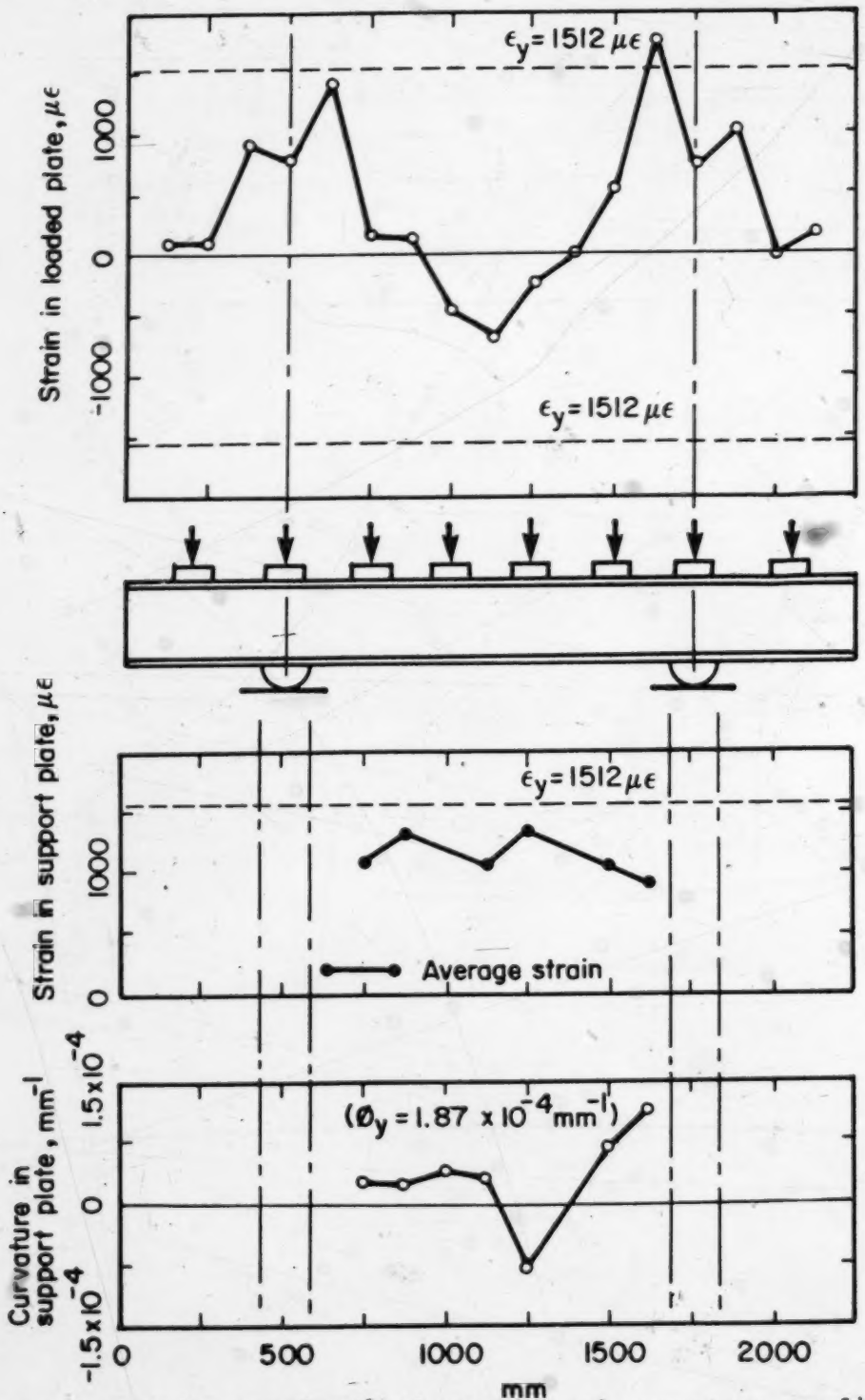

Figure 4.9 B5/1: Longitudinal strain and curvature profiles in the loaded and support plates.

given in Chapter 6.

4.6.1.2 Support Plate.

In tests in which the support plate was not mechanically bonded to the concrete in the span (i.e. all tests except for B6/5, B5/4 and B5/5), it was observed that the support plate separated from the concrete over the entire clear span at very early loading stages. The gap between the plate and the concrete remained open throughout the tests. It was therefore anticipated that the strain in the support plate should be constant along the clear span .

This "tied arch" behaviour is confirmed by the strain profiles in the support plates. However, the plots are complicated by the fact that bending coexisted with axial tension in the support plate (Fig. 4.10). The bending was induced by the vertical component (q) of the arch reaction near the supports, the deflection (Δ) at midspan and the "T-Δ" effect due to axial tension (T) acting on the deflected shape . Fig 4.10(a) shows the form of the observed equilibrium shape of the support plate when a typical specimen was loaded. (This figure is not drawn to scale; the observed deformations are exaggerated for the purpose of the following development). Using symmetry, a free body diagram of one half of the support plate is shown in Fig. 4.10(b). The horizontal component of the inclined arch reaction is omitted from this figure for clarity, since it does not

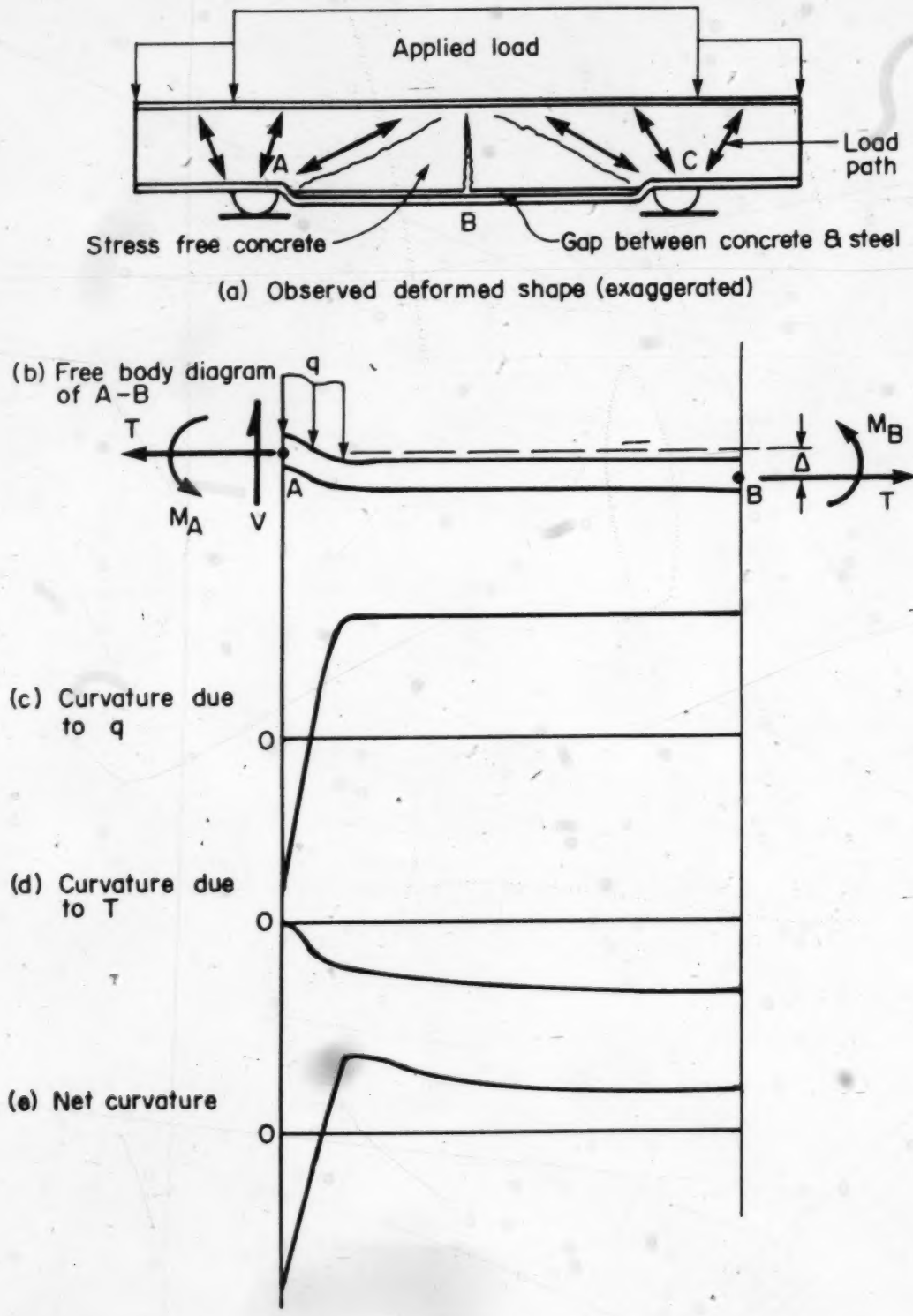

Figure 4.10 Curvature formation in the support plate.

significantly influence bending in the plate. The flexural stiffness of the support plate is small, and large curvatures can be induced along the length of the plate from the local transverse loading q which is applied near the supports. The magnitude of the curvature at A is sensitive to the amount of rotation at the support, and is shown qualitatively in Fig. 4.10(c). The curvature due to the restoring moment field which is caused by the tension T acting on the deformed equilibrium shape is shown qualitatively in Fig. 4.10(d), and the net curvature field is shown in Fig 4.10(e).

Since several of the gauge locations had strain gauges mounted only on the external face of the plate, these measurements include a bending effect and are not considered to be reliable indicators of the average axial strain. These strain readings are indicated by open circular symbols on the plots. However, gauges were fixed to both the internal and external surfaces of the support plate near the supports in the B4 and B6 series and throughout the span in the B5 series (see Chapter 3). The average of these two readings gives the average tensile strain in the plate. These locations are designated by solid circular symbols. The curvature (Φ) in the support plate at locations where both internal and external gauges are present is calculated using

$$\Phi = \frac{\epsilon_{out} - \epsilon_{in}}{t_{sp}} \qquad [4.1]>$$

where t_{sp} = thickness of the support plate (mm). These plots are also shown in Figs. 4.6 -4.9. For comparison, the curvature associated with the yield moment (with no axial tension present) is calculated using

$$\Phi_y = \frac{2F_y}{t_{sp}E} \qquad [4.2]$$

and is also indicated on the plots. It is seen that the shape of Fig. 4.10(e) is in reasonable agreement with the measured curvature fields of Fig. 4.6 and Fig. 4.7, and with the left hand sides of Fig. 4.8 and Fig. 4.9. Bending was generally less significant in the loaded plates because of the clamping action of the loading devices, and so the external gauge readings are taken to represent axial strain only.

4.6.2 Orthogonal Strain Ratios

In Chapter 6, it is assumed that both the loaded and support plates are uniaxially stressed. In this case, the constitutive relationship is simply

$$F_{x(u)} = E\epsilon_x \qquad [4.3]$$

where the x-direction is the longitudinal axis of the plate. For [4.3] to be valid, the orthogonal strain ratio (ϵ_y/ϵ_x) must equal $-\mu$, where μ is Poisson's Ratio. Otherwise, the plate is biaxially stressed , and the appropriate constitutive relationship is

$$F_x = \frac{E}{(1-\mu^2)}\left[\epsilon_x + \mu\epsilon_y\right] \qquad [4.4]$$

If $\epsilon_y/\epsilon_x = \lambda$, then [4.4] and [4.3] can be combined to give

$$\frac{F_x}{F_{x(u)}} = \frac{1+\mu\lambda}{1-\mu^2}. \qquad [4.5]$$

The values for Poisson's Ratio which were obtained from the uniaxial tension coupon tests (Table 3.5) confirm that μ=0.3 is a reasonable number. Using μ=0.3, [4.5] can be written as

$$\frac{F_x}{F_{x(u)}} = 1.099 + 0.330\lambda. \qquad [4.6]$$

Equation [4.6] is plotted in Fig. 4.11. It can be seen that, for λ=0, (i.e. ϵ_y=0) the longitudinal stress in the plate (F_x) is 9.9% higher than that which would be calculated from the strain gauge readings assuming a uniaxial stress state ($F_{x(u)}$).

Since Poisson's Ratio for concrete is less than that for steel, it can be expected that the lateral restraint offered to the loaded plate by the concrete through the mechanical action of the studs will induce a biaxial stress state into the plate. Furthermore, it can be anticipated that $-\mu < \lambda < 0$. Orthogonal pairs of gauges were located on all loaded plates, as shown in Figs. 3.17 to 3.19. The gauges were located midway between the lateral stud lines, to obtain the minimum biaxial effect. Plots of λ vs. applied load for these gauge pairs indicated that λ converged to an essentially constant value for each gauge pair after the applied load had exceeded approximately 60% of the maximum applied load. Most of these values for λ were in the range $-0.3<\lambda<-0.2$, but a few were inexplicably less than -0.3. These values for λ were used to compute $F_x/F_{x(u)}$ from [4.6] and the results are shown in Fig. 4.12. When λ is less than -0.3, $F_x/F_{x(u)}$ is less than 1.0. The mean value for $F_x/F_{x(u)}$ is

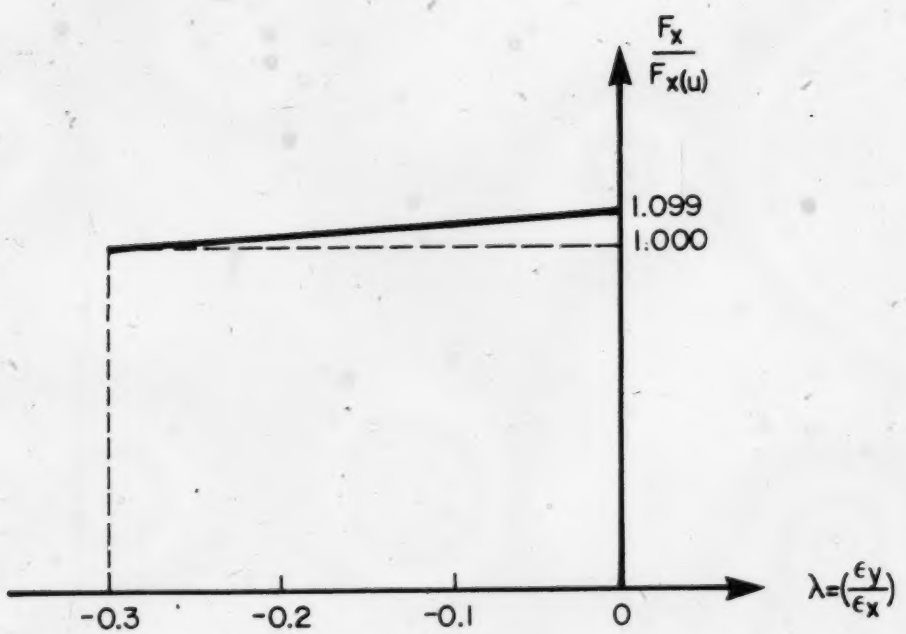

Figure 4.11 Effect of a biaxial stress state on the assumption of uniaxial stress conditions.

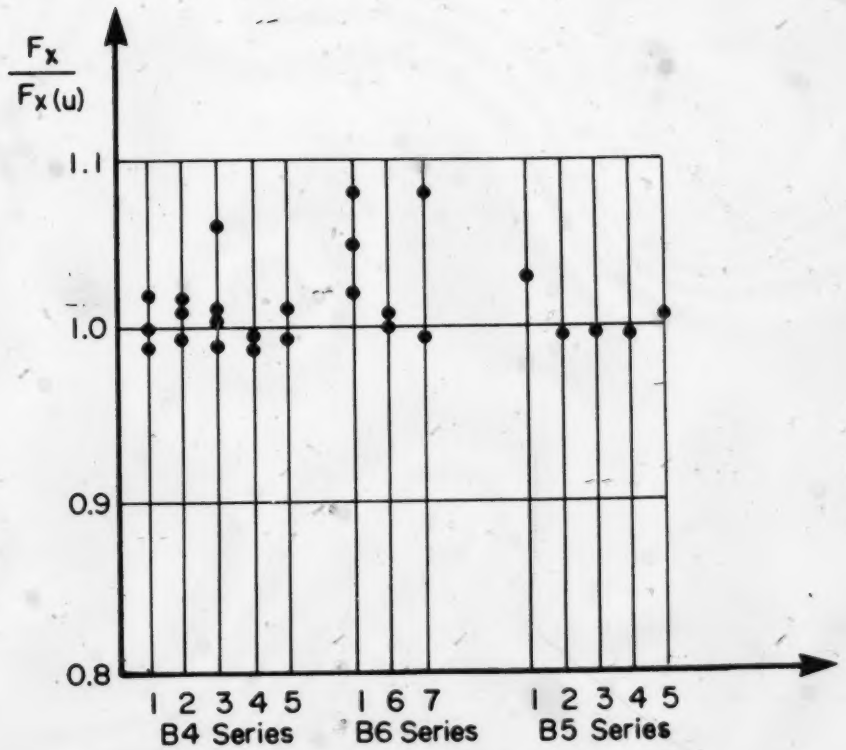

Figure 4.12 Calculated values of $F_x/F_{x(u)}$

1.010, and the standard deviation is 0.0245. It is therefore concluded that the assumption of uniaxial stress in the plates is reasonable.

4.6.3 Variation of Longitudinal Strain across the Width of the Plate.

It was shown in Section 4.6.2 that it is reasonable to assume that both the loaded and supported plates are uniaxially stressed. If the total force in either plate is to be calculated from

$$T = EA\epsilon_x$$

where ϵ_x is the strain at the mid-width of the plate, then it must be verified either that ϵ_x is uniform across the plate or that the average strain ϵ_{av} is close to ϵ_x.

To check this assumption, additional longitudinal gauges were located 40 mm from the edges of both the loaded and supported plates at midspan, as indicated in Chapter 3. For three sample points, the best estimate for the average strain is obtained using the three-point Gauss rule for numerical integration (Zienkiewicz, 1977). The values for the weights (W_i) and the positions (ξ_i) of the sampling points for the generalised normalised case are given in Fig. 4.13(a). The application of the three-point Gauss rule to a 375 mm wide plate is shown in Fig. 4.13(b). It is noted that

$$(1.0 - 0.77459)\frac{375.0}{2} = 42.0 \text{ mm},$$

and so it is reasonable to use the gauges which were located 40 mm from the plate edges for the three-point Gauss rule.

i	W_i	ξ_i
1	5/9	0.77459
2	8/9	0
3	5/9	-0.77459

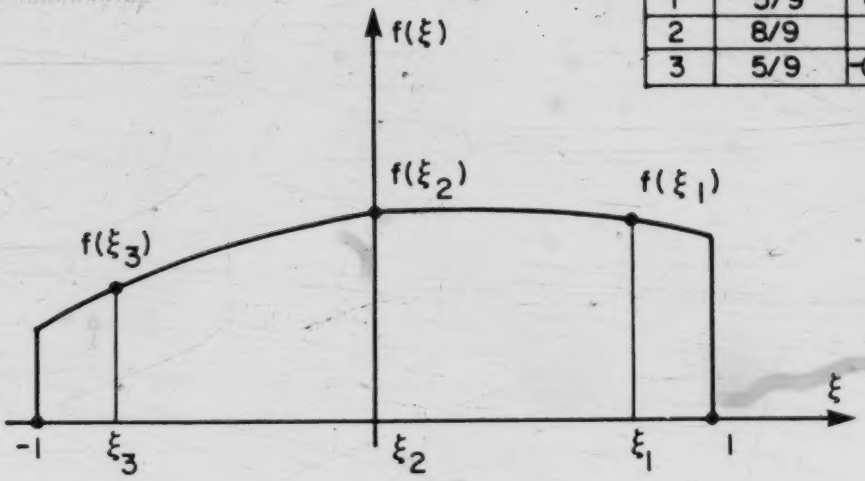

$$\int_{-1}^{1} f(\xi)\,d\xi = \sum_{i=1}^{3} W_i\, f(\xi_i)$$

(a) 3 – Point Gauss rule for integration

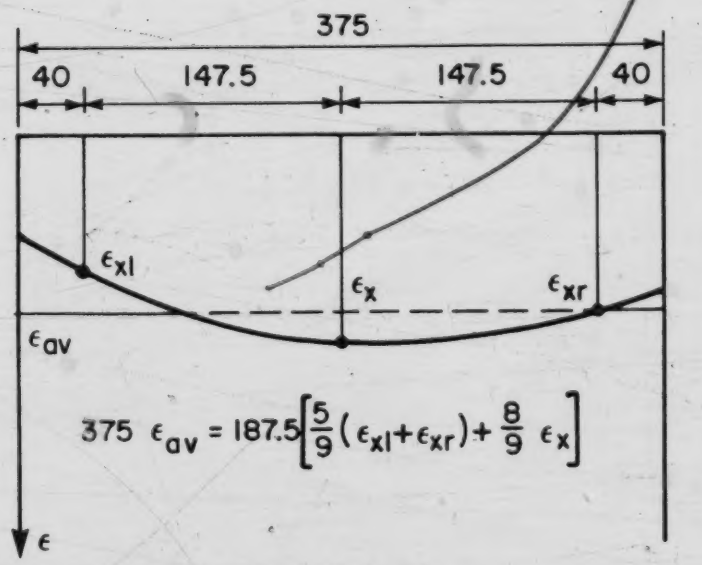

$$375\ \epsilon_{av} = 187.5\left[\frac{5}{9}(\epsilon_{xl}+\epsilon_{xr}) + \frac{8}{9}\,\epsilon_x\right]$$

(b) Average strain ϵ_{av}

Figure 4.13 Use of the three-point Gauss rule for the numerical evaluation of ϵ_{av}.

From Fig. 4.13 it is seen that

$$\epsilon_{av} = \frac{187.5}{375.0}\left[\frac{5}{9}(\epsilon_{x1}+\epsilon_{xr}) + \frac{8}{9}\epsilon_x\right]$$

$$= \frac{1}{18}\left[5(\epsilon_{x1}+\epsilon_{xr}) + 8\epsilon_x\right]$$

and

$$\frac{\epsilon_{av}}{\epsilon_x} = \frac{1}{18}\left[5\left(\frac{\epsilon_{x1}+\epsilon_{xr}}{\epsilon_x}\right) + 8\right] \qquad [4.7]$$

The best-fit longitudinal strain distributions across the loaded plates of specimens B4/4, B6/1 and B5/1 at failure are shown in Fig. 4.14. These are typical of the results obtained for the other specimens, and show that the longitudinal strain varies across the width of the loaded plate.

To determine $\frac{\epsilon_{av}}{\epsilon_x}$, Equation [4.8] was applied to all loaded plates for which three strain gauges were available at midspan. The results are given in Fig. 4.15. The mean value of the ratio is 0.892, and the standard deviation is 0.063. These statistics are used in Chapter 6, where comparisons are made between the measured and predicted strains in the loaded plates; the measured strains are found to be consistently larger than those predicted.

In conclusion, it is noted that it is meaningless to apply [4.8] to the support plate, since, as mentioned in Section 4.6.1., the external gauges on the spans of the support plates include bending effects.

4.6.4 Lateral Curvature Profiles Between Stiffened Plate Supports

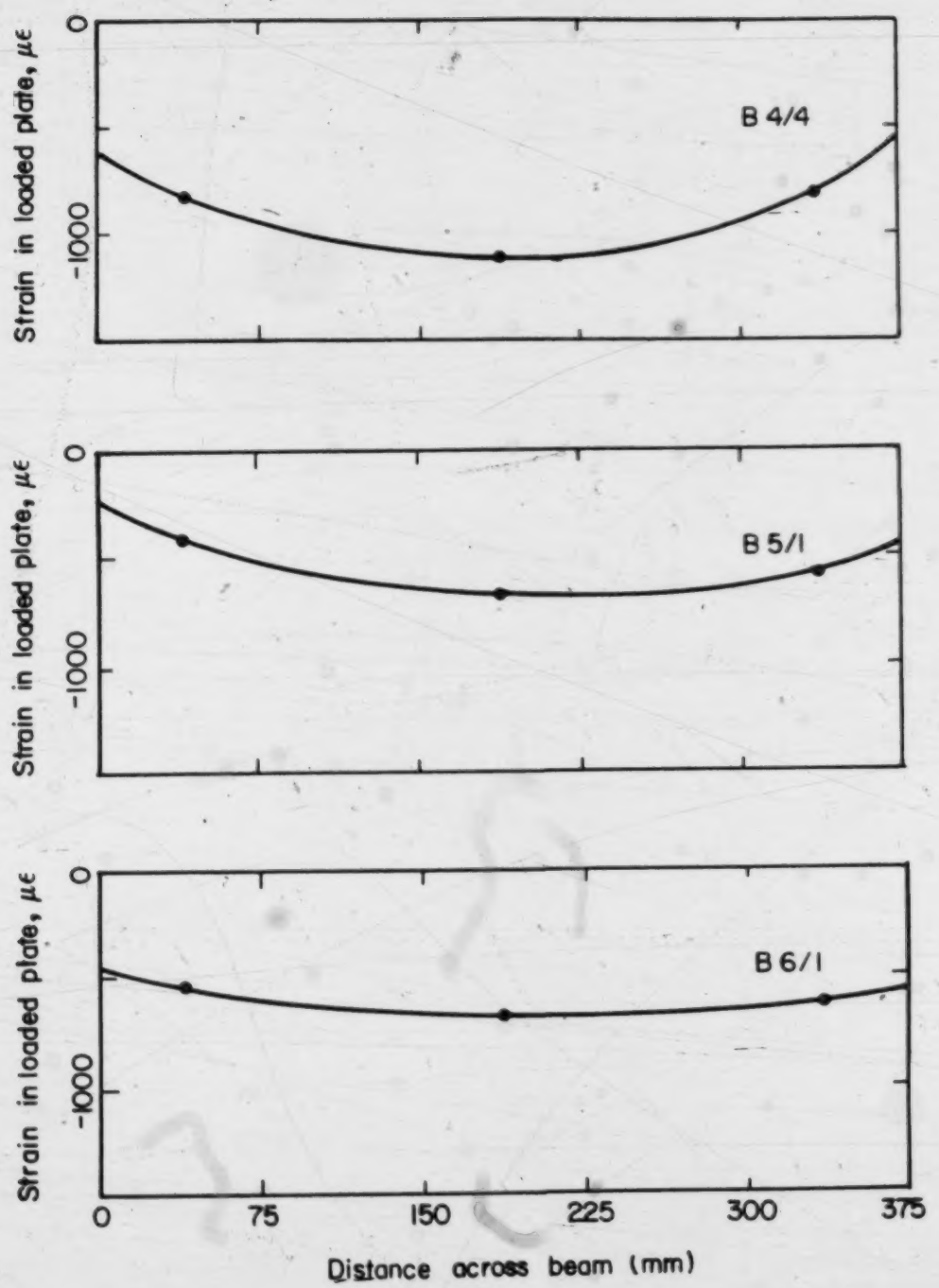

Figure 4.14 B4/4 B6/1 and B5/1: Best-fit longitudinal strain distributions across the loaded plate.

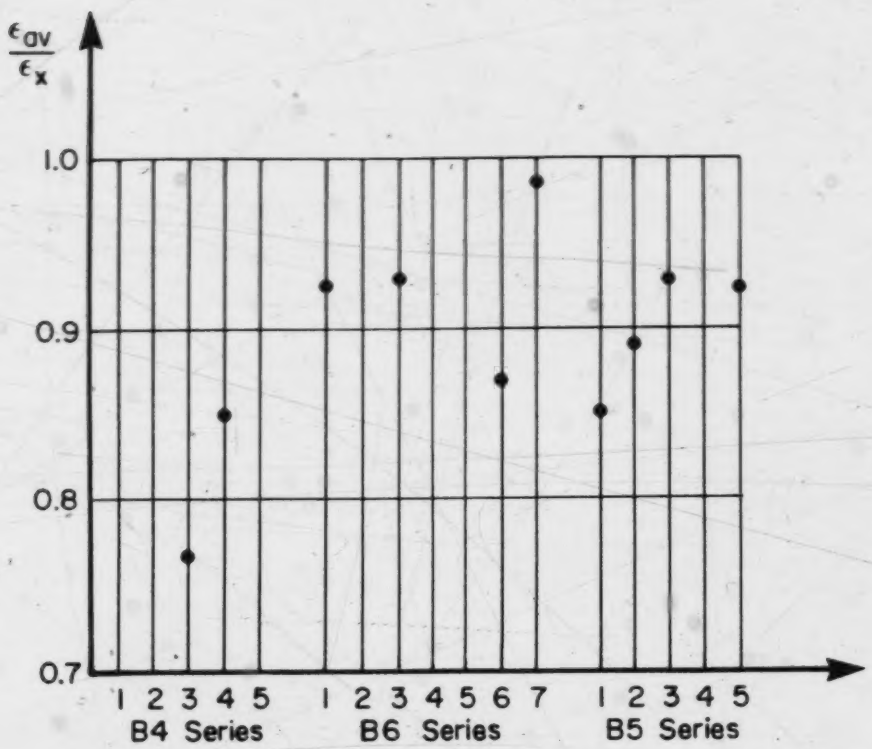

Figure 4.15 Calculated values of ϵ_{av}/ϵ_x.

Two types of bulkhead were considered in the testing program; solid supports and stiffened plate bulkheads. The dimensions of a stiffened plate bulkhead are given in Fig. 3.6. A cross-section through the beam and bulkhead is given in Fig. 4.16 which shows the locations of internal and external strain gauges.

In order that the applied load can be reacted at the discrete stiffener locations, lateral arches must form locally between the stiffeners, as shown in Fig. 4.16(a). Very high contact stresses will occur at the bases of the arches, and local deterioration of the arches is possible (Fig. 4.16(b)) before the maximum capacity of the beam is attained. Such a local failure can be detected by sudden increase in curvature in the support plate in the lateral direction between stiffeners. This curvature is measured using Equation [4.1], i.e.

$$\Phi = \frac{\epsilon_{out} - \epsilon_{in}}{t_{sp}}$$

Stiffened plate supports were used in B4/3, B4/4, and B4/5. Plots of lateral curvature vs. applied load for specimen B4/4 are shown in Figs. 4.17. The results are alarming. It can be seen that sudden degeneration of the arches occurred at approximately 60% of the maximum load. The effect of this degeneration was particularly observed in B4/4, where significant crack propagation was observed during five cycles of loading from 0.5 MPa to 6.0 MPa, along with audible evidence of internal distress. It is possible that further cycling could cause appreciable damage within

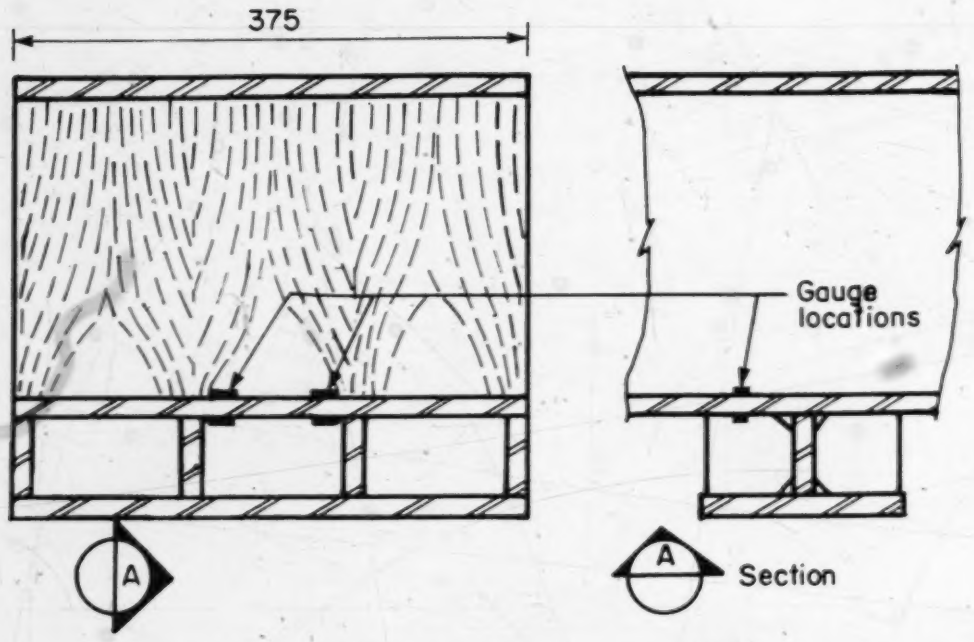

(a) Local arching and incipient crushing

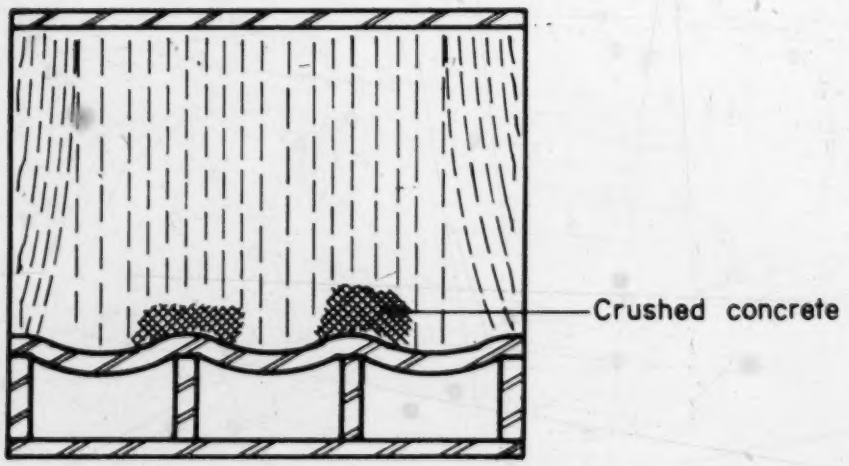

(b) Plate bending after local concrete crushing

Figure 4.16 Local failure at a stiffened plate support.

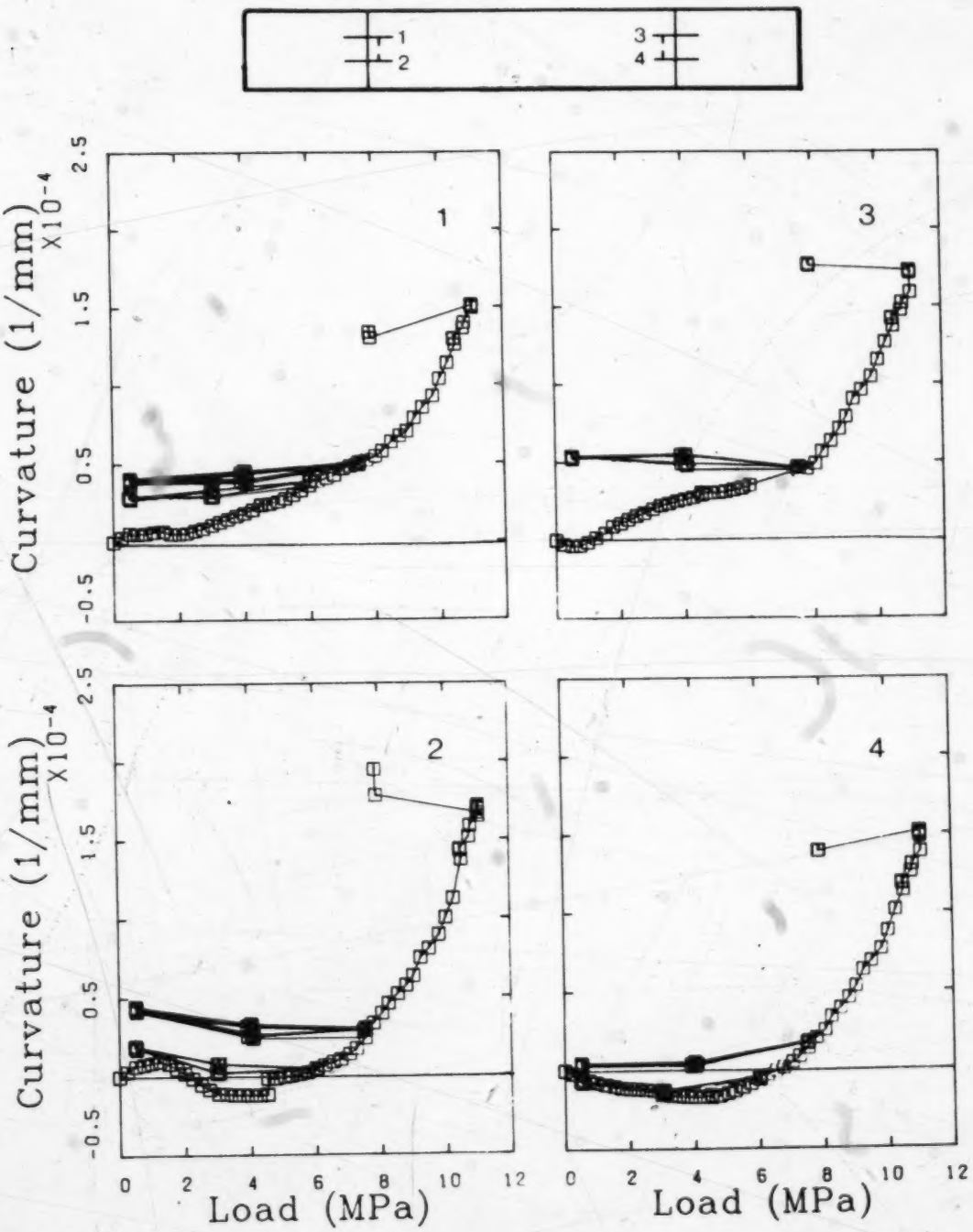

Figure 4.17 B4/4: Lateral curvature in the support plate between the stiffeners of the stiffened plate supports.

the concrete core, and lead to a reduction in load-carrying capacity. These concerns should be taken into account during the design of stiffened plate bulkheads.

4.7 Concrete Strains

4.7.1 General Remarks

Concrete strains were measured using four-arm Demec rosettes, as indicated in Section 3.4.2. The gauge length for each arm was 50.8 mm. Since a Mohr strain circle can be drawn when the strains in three different directions are known, the presence of the fourth arm introduces a redundant measurement. Accordingly, four Mohr strain circles can be constructed for each point at each load step.

Strain calculations were performed using DEMSTR, a program for converting DEmec readings to STRain readings. (Sundararaj, 1986). In accordance with the preceeding discussion, four values for the maximum and minimum principal strains and four angles to define the orientaton of the maximum principal strain (counterclockwise relative to the horizontal axis) could be calculated. In a homogeneous strain field, the four circles thus defined should theoretically coincide. However, strain gradients across a rosette will cause the circles to differ from each other. Also, any cracking larger than "hairline" cracking through a rosette will cause further differences between the circles.

To estimate the reliability of the four sets of readings, the means and standard deviations were calculated for principal strains and angles for each rosette. If the standard deviations were consistently less than 10% of the means, the rosette was considered reliable. Using this criterion, 54% of all rosettes used in the testing program gave meaningful results at loads near failure . Fig. 4.18 shows plots of Mohr strain circles at an applied load of 6.0 MPa for two rosettes which were symmetrically located about the centreline of specimen B4/2. In these plots, tensile strain is positive. The mean values for Fig. 4.18(a) are reliable, but they are unacceptable for Fig. 4.18(b).

Concrete strains were recorded for two purposes. Firstly, an indication of stress paths and magnitudes can be obtained by plotting the mean principal strain magnitudes and directions on the beam elevations. This is discussed in Section 4.7.2. Also, the principal tensile strains at the location of failure are required in the discussion of failure criteria in Chapter 6.

4.7.2 Principal Strains

Plots showing the magnitudes and directions of the principal strains at each rosette location on the beam elevation for each load step were produced using the computer program DEMSTR. Fig 4.19 shows plots for B6/1 and B6/7 at 3.00 MPa. These plots show only results from reliable rosettes. Lines with arrowheads indicate tensile

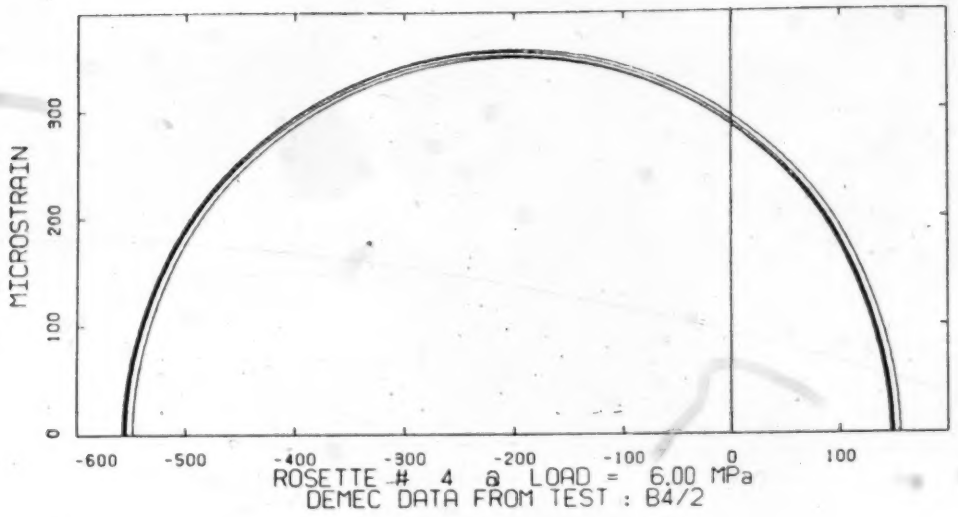

(a)

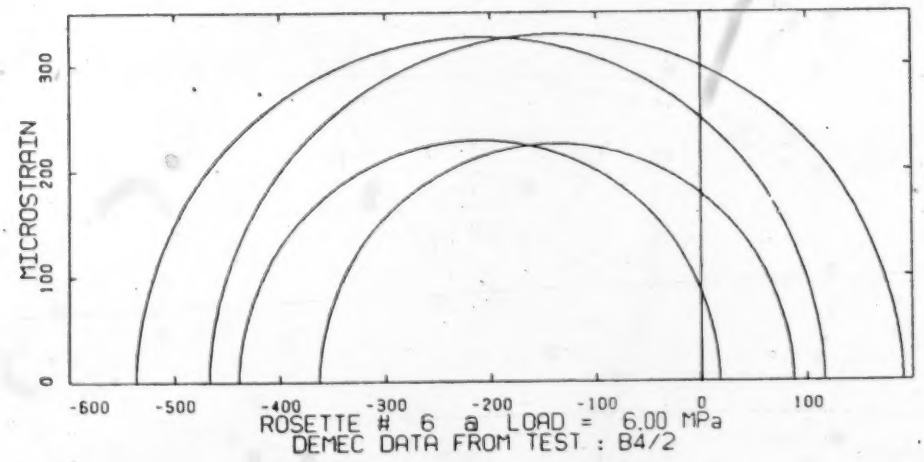

(b)

Figure 4.18 Assessment of the reliability of multiple Mohr circles of strain (tension positive).

strains.

Fig 4.19(a) is typical also of the the results obtained in the B4 and B5 series. It is seen that arching action dominates. Arching also occurs in the eccentrically patch-loaded specimen (B6/7) in Fig.4.19(b). The principal strains in the long shear span of specimen B6/7 at location "K_1" are almost as large as those in the short shear span at location "K_2", even though the shear force being carried in the short shear span is 50% higher than that in the long shear span. It will be shown in Chapter 6 that these locations "K" are critical for failure definition, and it is therefore not surprising that specimen B6/7 failed on the long shear span.

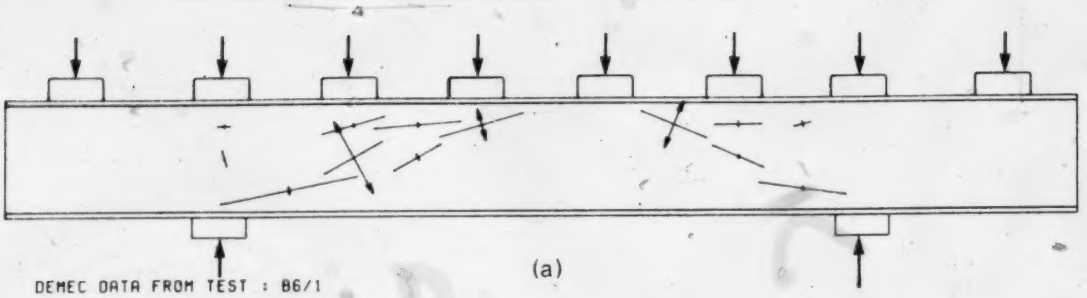

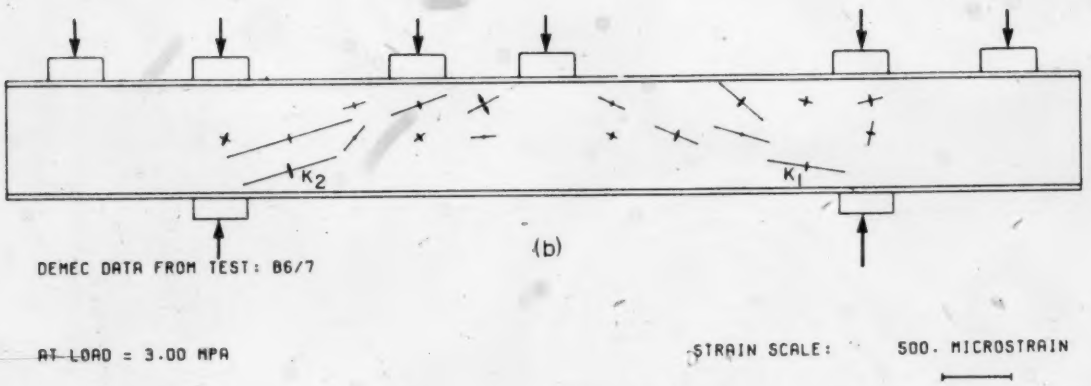

Figure 4.19 B6/1 and B6/7: Principal strain profiles in the concrete core.

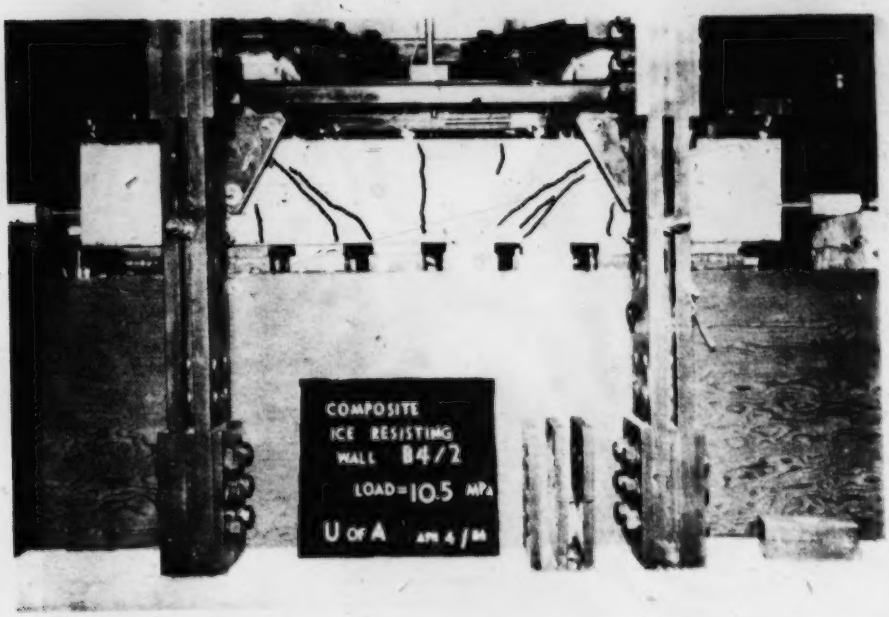

(a)

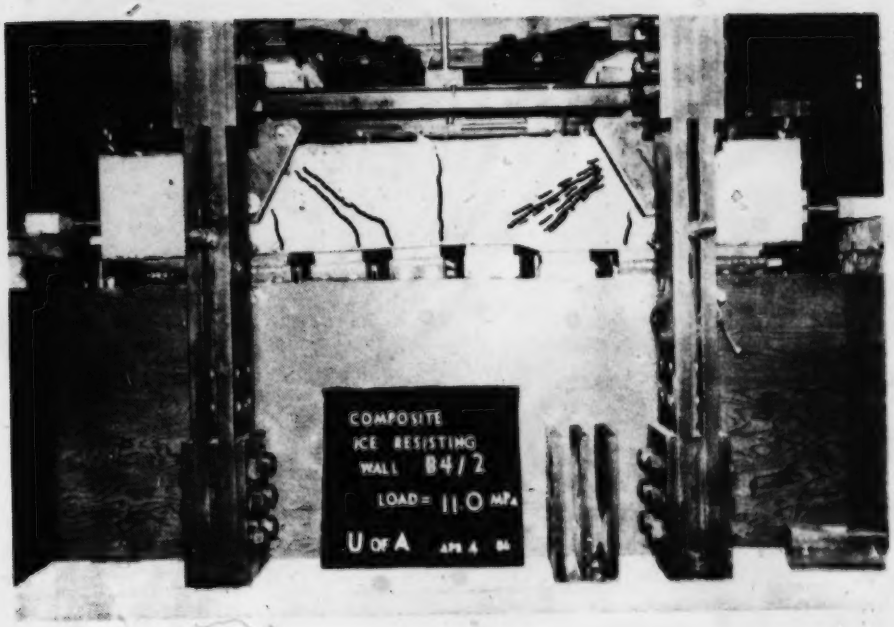

(b)

Plate 4.1 B4/2: Failure mode.

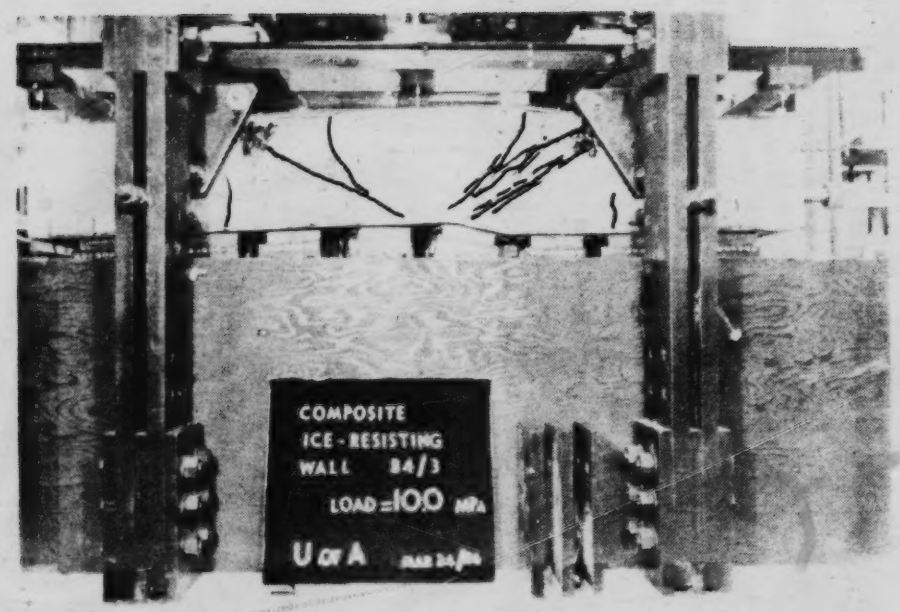

Plate 4.2 B4/3: Failure mode.

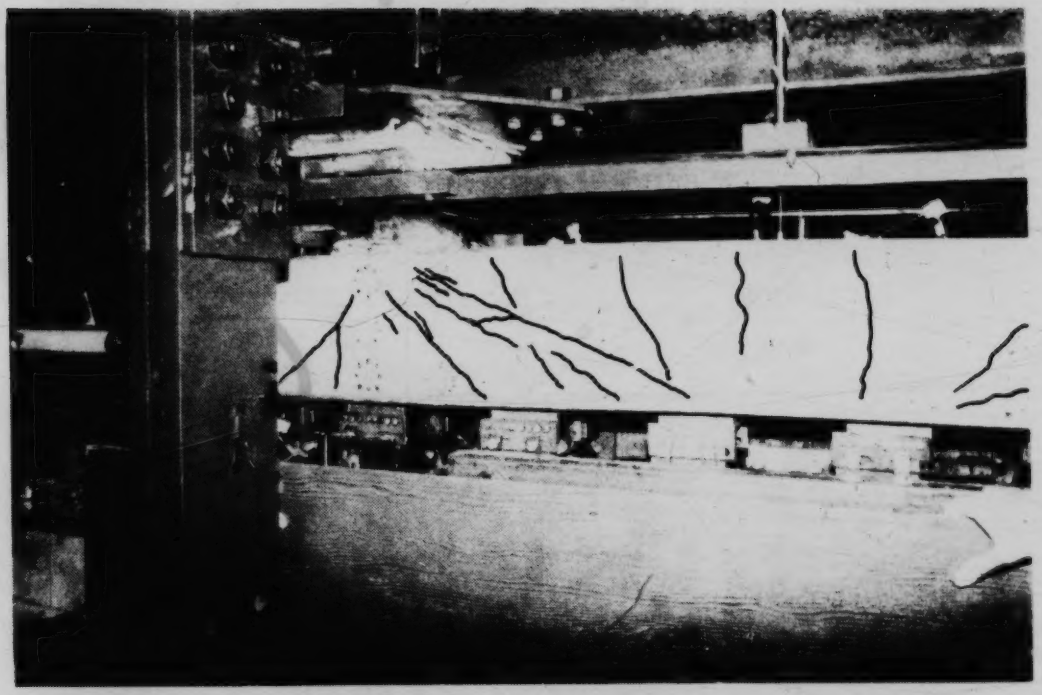

(a)

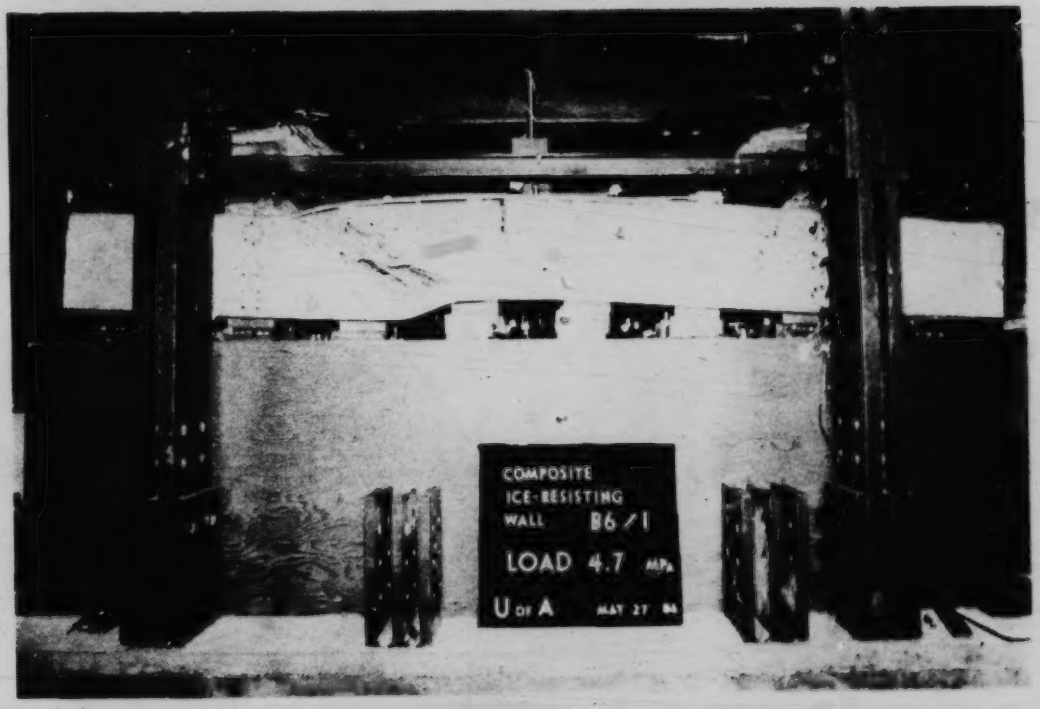

(b)

Plate 4.3 B6/1: Failure mode.

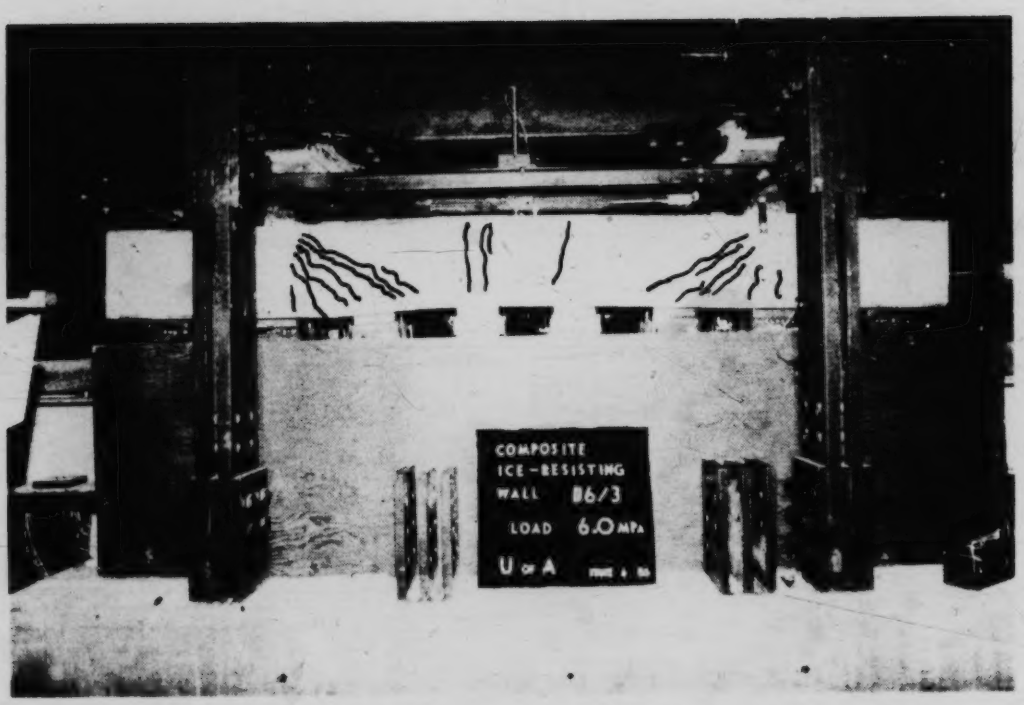

Plate 4.4 B6/3: Failure mode.

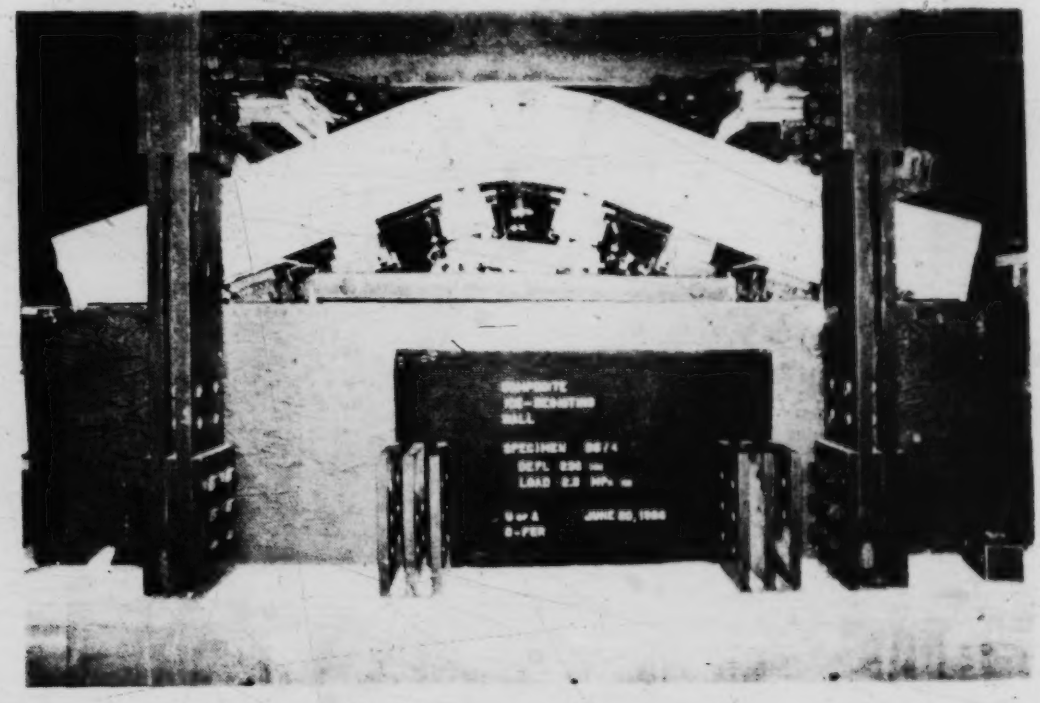

Plate 4.5 B6/4: Final deformed shape.

Plate 4.6 B6/4: Stud failure in cantilever.

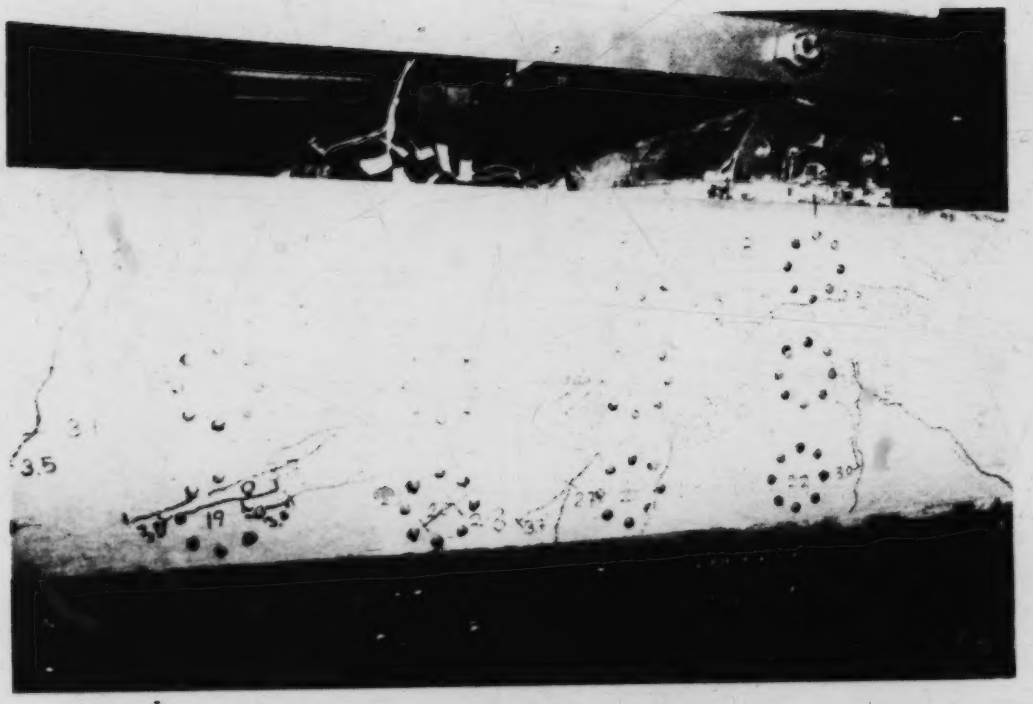

Plate 4.7 B6/6: Horizontal crack over the support.

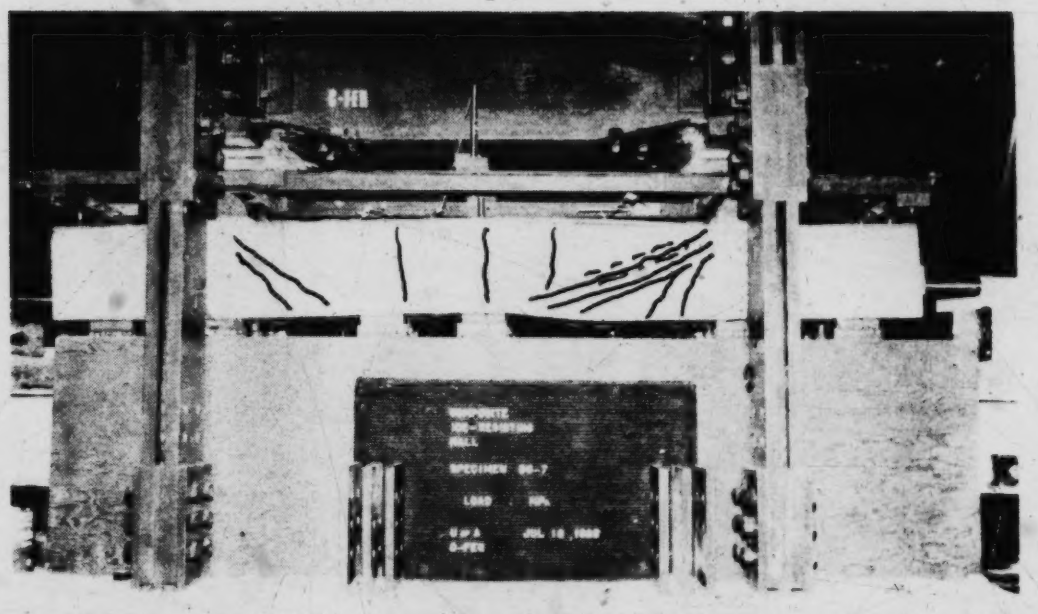

Plate 4.8 B6/7: Failure mode.

Plate 4.9 B5/1: Failure mode.

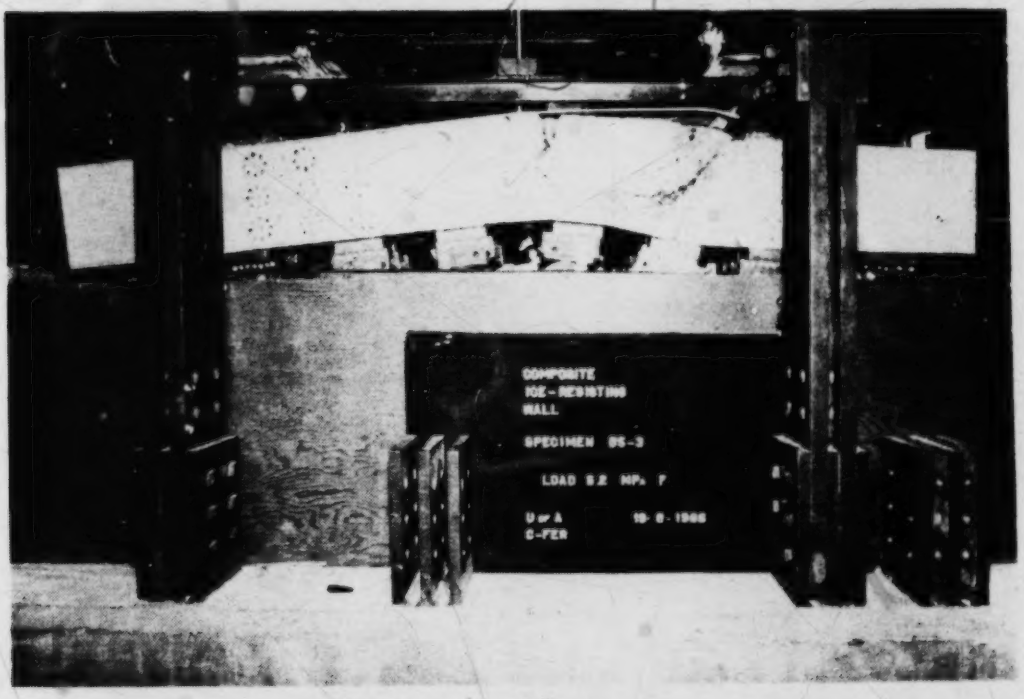

(a)

(b)

Plate 4.10 B5/3: Failure mode and plate fracture.

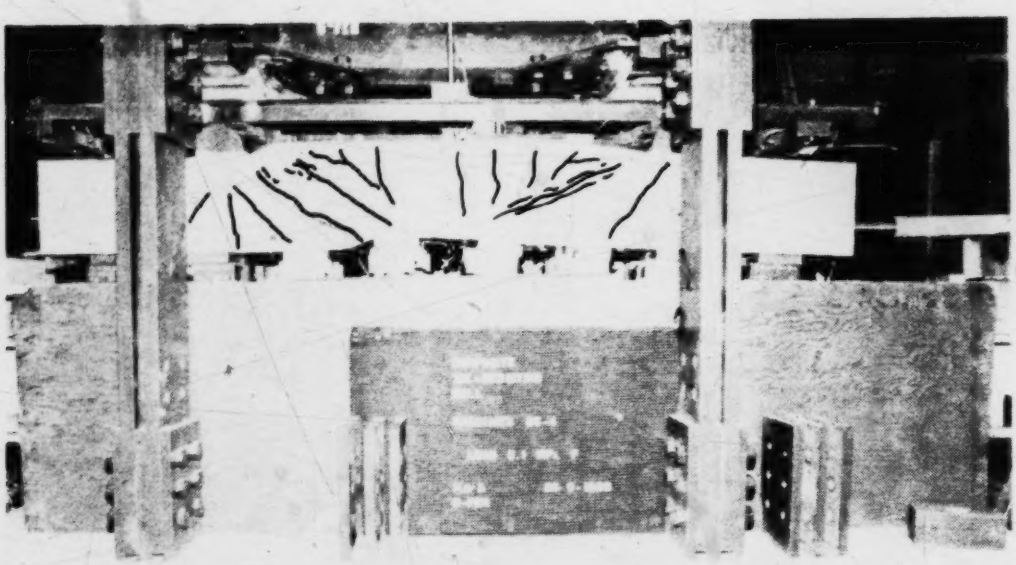

(a)

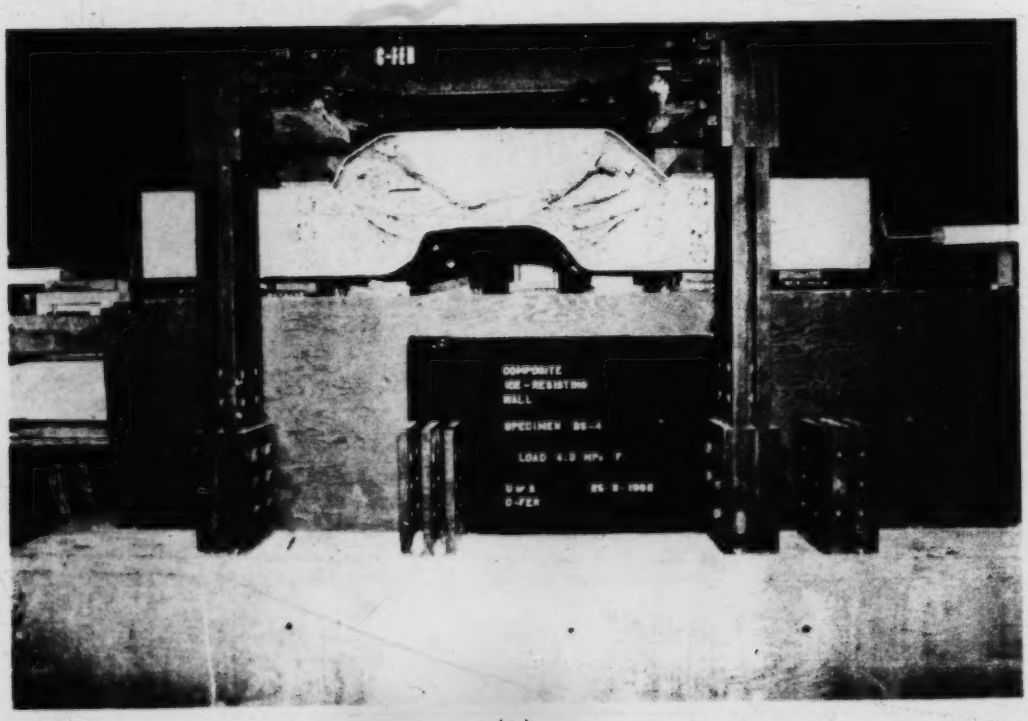

(b)

Plate 4.11 B5/4: Failure mode.

5. ANALYTICAL MODEL

5.1 Introduction

The requirements for an appropriate analytical model for composite ice-resisting walls are as follows:

- The strength of the wall must be accurately and easily obtained
- The shear distributions at the steel/concrete interfaces must be quantifiable
- The model must be sufficiently versatile to accomodate any arrangement of load.

Since the sections considered are "deep", prediction of the load vs. deflection response is not critical.

The analytical model detailed in this chapter is based on the lower bound theorem of plasticity. This theorem may be stated as follows (Lay 1982)

> "An estimate of the load capacity of a structure, based on some assumed distribution of internal forces and external reactions, will be a lower bound estimate, provided:
>
> (a) all the internal and external forces are in equilibrium;
>
> (b) the internal forces assumed nowhere exceed the relevant force capacity; and
>
> (c) behaviour is ductile, i.e. any section at any point, when loaded to its force capacity, can maintain that force during any subsequent

deformation."

The lower bound theorem, then, requires that static boundary conditions must be satisfied. However, the kinematic boundary restraints need not be observed. It is therefore permissible to accept the capacity of a cut-out strip (Fig. 3.1) as an estimate of the capacity of the overall wall.

The lower bound theorem must be applied with caution to concrete structures, since the ductility of concrete is limited. Schlaich et al. (1987) suggests that the assumed load path should be closely allied to the principal stress trajectories obtained from an elastic analysis. This limits the reorientation of the compressive load paths which is required after tensile cracking has occurred.

This chapter deals only with the development of statically admissible stress fields for composite ice-resisting walls (i.e. requirement (a) of the lower bound theorem). Material capacity is discussed in Chapter 6. Four quantities (p, u_c, σ_1, σ_2) which are used in the development all have units which are expressed in MPa. These quantities are distinguished from each other as follows:

- "p" is the load which is externally applied to the loaded plate, expressed as a pressure.
- "u_c" is the hydrostatic stress in the nodal area near the support. A nodal zone is defined in Section 5.2.
- "σ_1" and "σ_2" are the principal stresses in the concrete at any point within the concrete core.

It is assumed that the concrete is in a state of plane

stress ($\sigma_3 = 0$). Furthermore, it will be shown in Section 5.2 that σ_1 is compressive, and that $\sigma_2 = 0$ at all points in the concrete core unless such a point is within a hydrostatic node.

5.2 Fan-Type Stress Fields

Lower bound stress fields for deep sections (beams and corbels) subjected to point loads have been developed using strut-and-tie models, and are well documented (see, for example, Nielsen 1984, Marti 1985). The strut-and-tie model for a normalised corbel (i.e. unit depth) with four equal point loads (n=4) is shown in Fig. 5.1. Each point load is applied through a pad of length "a", and this dimension "a" is different for each point load. In this, and all ensuing figures, a member of unit width is used.

The area DEF is traditionally called a hydrostatic node, since the proposed state of stress in this region has equal in-plane stresses on the sides of the element. It is noted that the state of stress is not truly hydrostatic since the out-of-plane stress is zero. The node is bounded along DE by four concrete struts, and along DF and FE by hypothetical steel plates. The plates have the hydrostatic stress u_c acting on one face, and are equilibrated by the externally applied reactions of magnitudes C and 4P respectively, acting on the opposite faces.

Each strut has a constant cross section along its length, and is perpendicular to the nodal zone. The

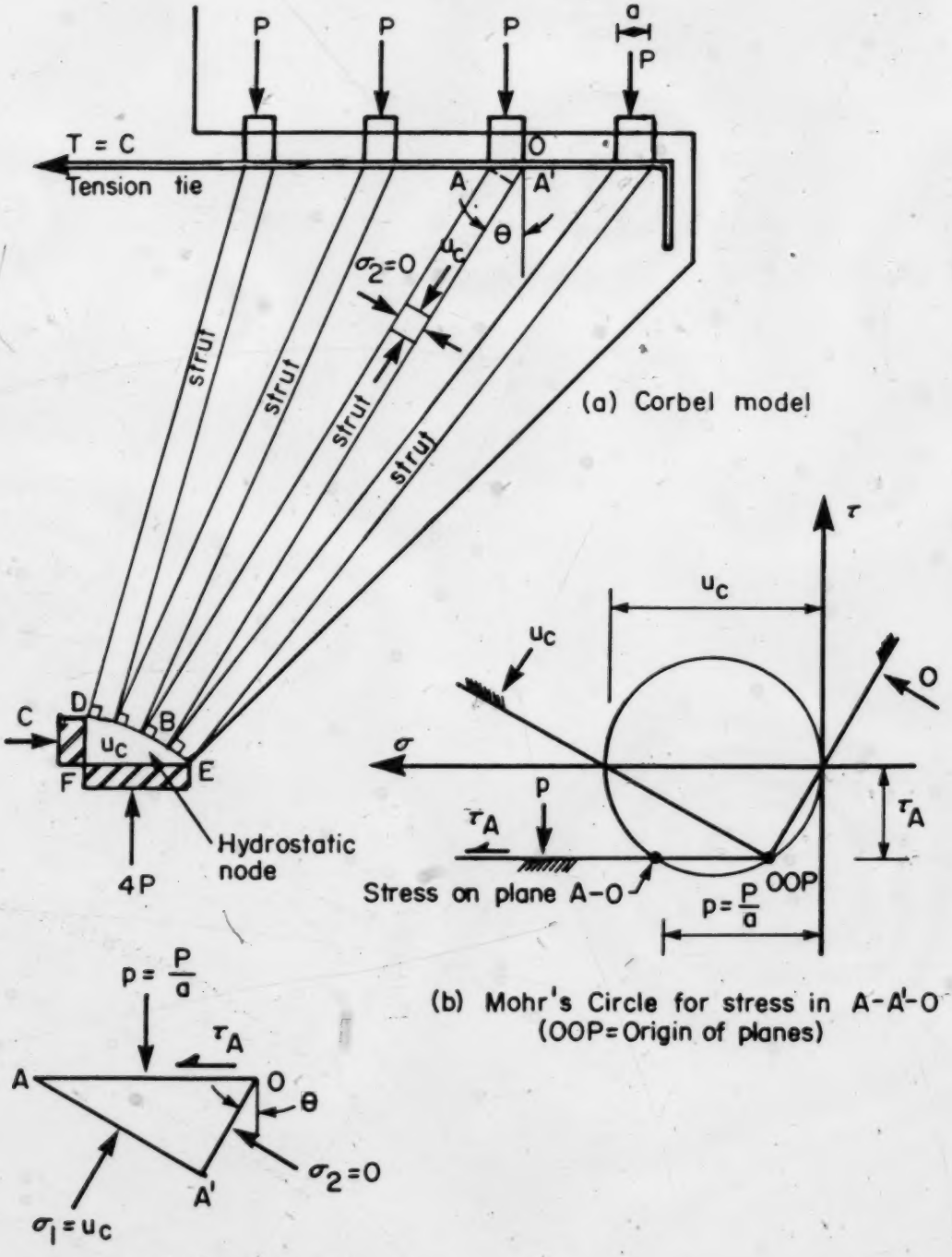

Figure 5.1 Strut-and-tie model for a normalised corbel with discrete concentrated loads.

equilibrium of the strut/node boundary therefore dictates that the principal stress σ_1 in the strut is equal to the hydrostatic stress u_c. The other principal stress (σ_2) in the strut is set equal to zero as, shown in Fig. 5.1(a). (The surface upon which σ_2 acts can be visualised as modelling a crack in the concrete). The Mohr circle of stress for any point in the typical strut along AB can be drawn as in Fig. 5.1(b) since the state of stress is homogeneous throughout the strut. In particular, the state of stress in the element A-A'-O at the interface of the strut and tension tie, shown in Fig. 5.1(c), is of interest and the Mohr circle in Fig. 5.2(b) can then be considered as representative of the state of stress in the element A-A'-O. The sign convention for stress used in this thesis specifies that tensile stress is positive and that positive shear stress causes clockwise rotation of the element on which it acts. Under these conditions, the origin of planes (OOP) for the Mohr circle of stress can be constructed as follows. A line which is parallel to the plane A-A' of Fig 5.1(c) is drawn through the point ($-u_c$, 0) in Fig. 5.1(b), since this point represents the state of stress on the plane A-A'. The point at which the line intersects the circumference of the circle is a unique point on the circle, and is called the origin of planes for the circle. The point of intersection of any line through the OOP with the circle represents the state of stress on the plane which is parallel to that line. Thus it can be seen from Fig. 5.1(b) that the coordinates

(p, τ_A) represent the state of stress on the horizontal plane A-O, and τ_A is the bond stress which must be developed between the tension-tie and the concrete.

In Fig. 5.1(a), the struts are seen to diverge as the loaded surface is approached. Even if the number of loads is increased from four to a very large number ($n \rightarrow \infty$) and a uniform load is more closely approximated, wedge-shaped gaps will still exist between the struts. To fill these gaps, the parallel faces of the struts in Fig 5.1(a) are fanned out to form fan-struts (Thürlimann et al., 1983), as shown in Fig. 5.2(a). A fan-strut may be considered as a small sector of a thick cylinder, with pressures applied to the inside and outside faces such that the circumferential stresses are equal to zero (Fig. 5.2(b)). The interface between the fan-strut and the hydrostatic zone is a circular arc of radius R. The state of stress in the fan-strut varies with the distance ρ, since equilibrium in the radial direction demands that

$$\sigma_{1N}(R+\rho)d\theta = u_c R d\theta$$

or

$$\sigma_{1N} = \left(\frac{R}{R+\rho}\right)u_c \qquad [5.1]$$

Equation [5.1] is plotted in Fig. 5.2(c). If σ_{1A} is the radial stress at point A, then equation [5.1] gives

$$\sigma_{1A} = \left(\frac{R}{R+r}\right)u_c$$

which can be re-arranged to give

$$R = \left(\frac{\sigma_{1A}}{u_c - \sigma_{1A}}\right)r \qquad [5.2]$$

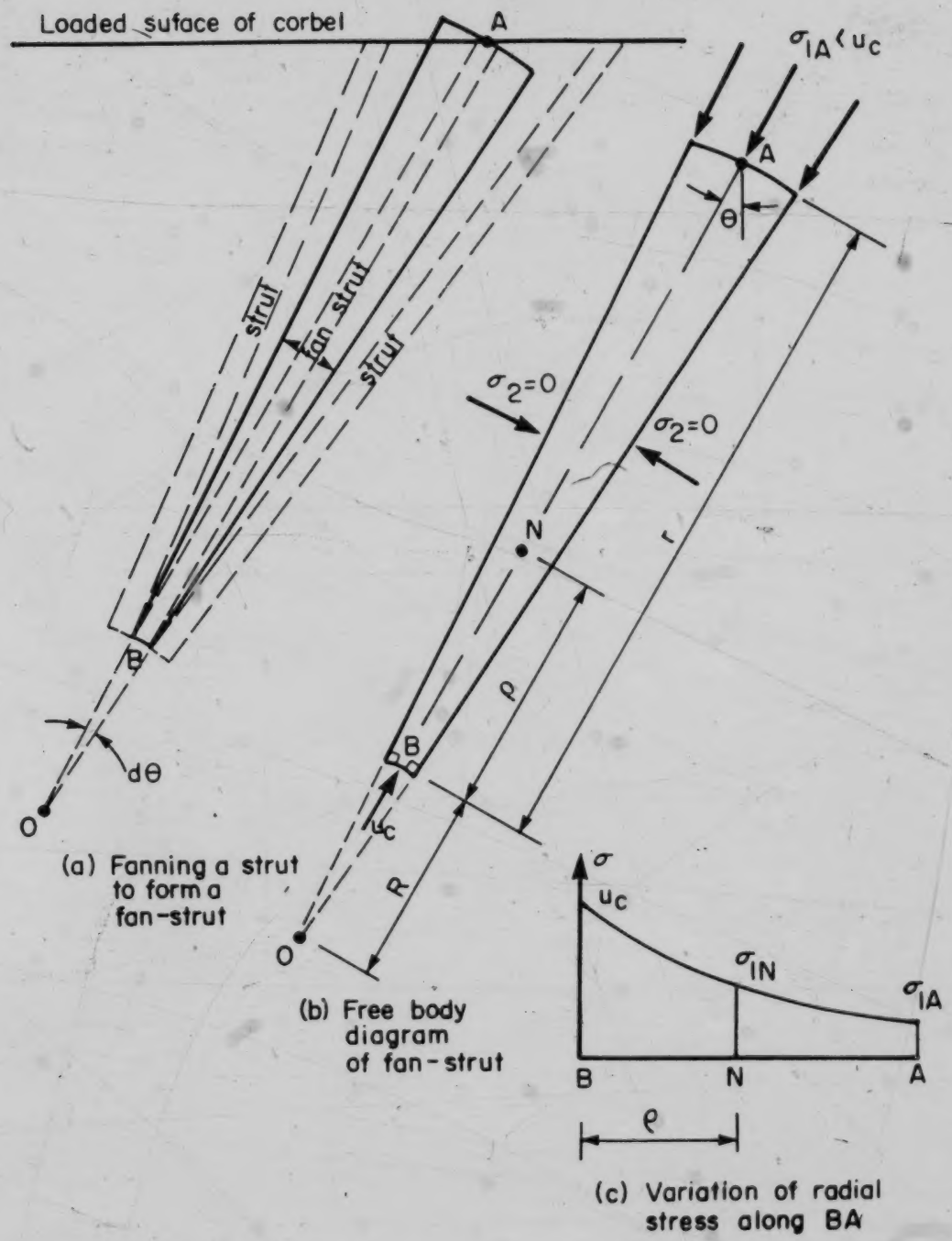

Figure 5.2 Definition of a fan-strut.

As $n \to \infty$, $d\theta \to 0$, and the fan-struts may be classified as fan-lines which radiate orthogonally from the hydrostatic node DEF, as shown in Fig. 5.3(a). The stress σ_{1A} is then dictated by the applied load p and the angle θ, as shown in Fig. 5.3(b), and so the radius R from equation [5.2] varies for each fan line. Accordingly, the surface DE becomes a smooth curve with varying radius of curvature. The solution for a corbel with uniform load (i.e. the equation for the curve DE) has been developed in normalised form ($d=1$) by Marti(1980) (Fig. 5.3(a)). The curve DE is the hyperbolic equation:

$$(\eta+1-\omega_0)^2 - \xi^2\left(\frac{u_c}{p}-1\right) = (1-\omega_0)^2 \qquad [5.3]$$

where the ξ and η axes and ω_0 are defined in Fig. 5.3.

5.3 Simply Supported Composite Ice-Resisting Wall: Fan Stress Field

A fan solution for a simply supported composite ice-resisting wall is developed as follows. First of all, the solution for a corbel is expanded to give a solution for a simply supported reinforced concrete beam with top reinforcement, as shown in Fig. 5.4. It can be seen from Fig 5.4(b) that the concrete cover over the top reinforcement has no effect on the stress field. Hence, the cover can be removed, and the top steel can be visualised as external plate reinforcement, provided that a satisfactory mechanism for shear transfer at the steel/concrete interface is provided. The bottom steel, however, must be located above

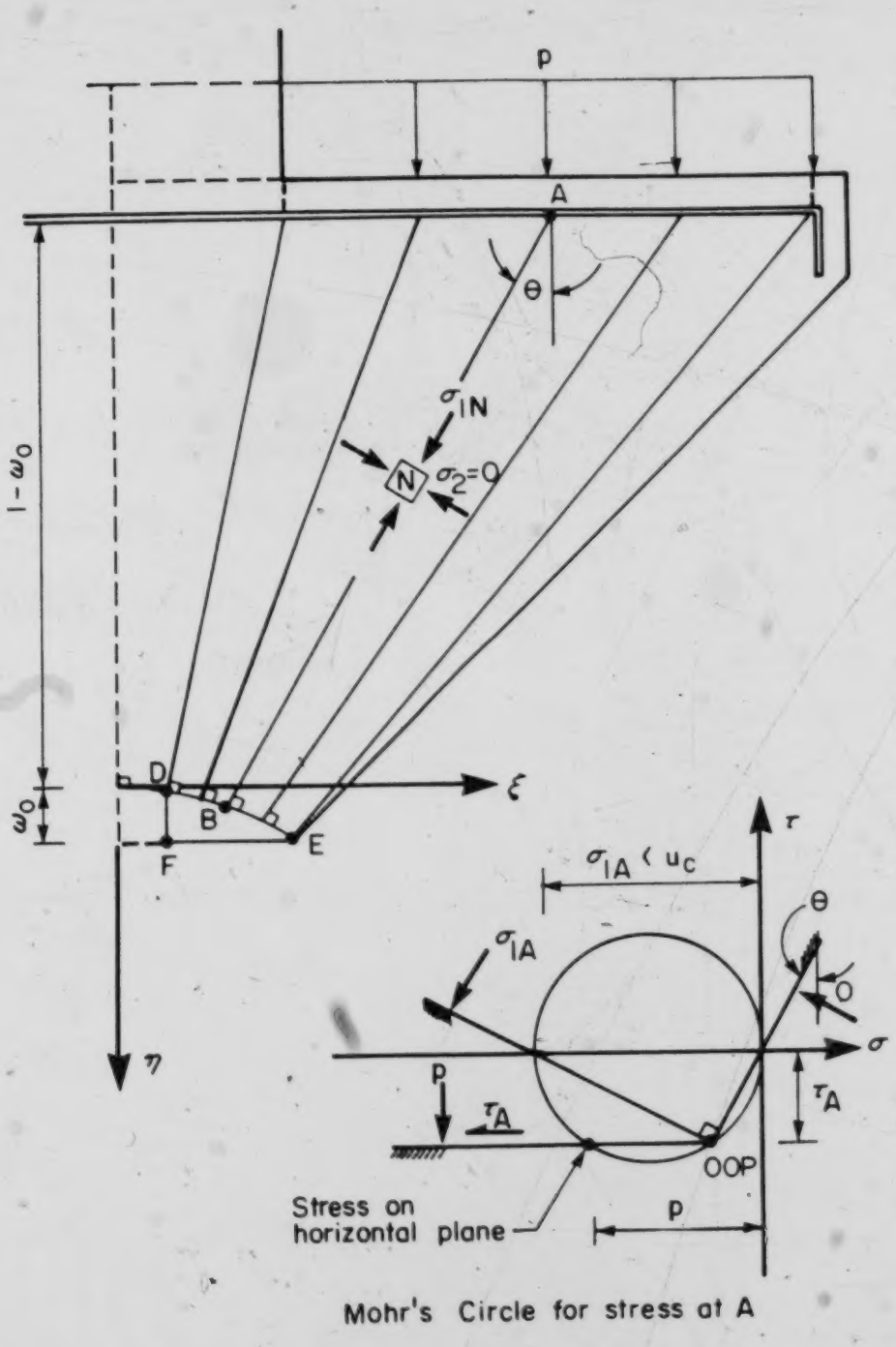

Figure 5.3 Fan stress field for a normalised corbel under uniform load.

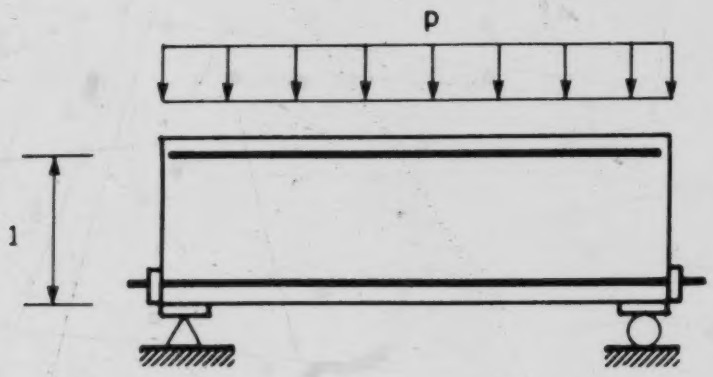

(a) Reinforced concrete beam with top steel

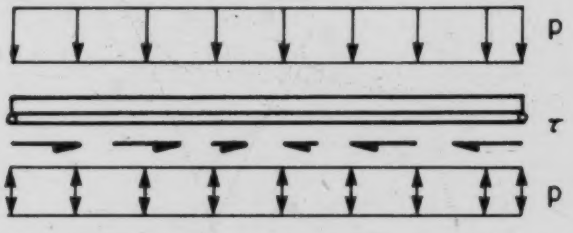

(b) Free-body diagram of top cover & steel

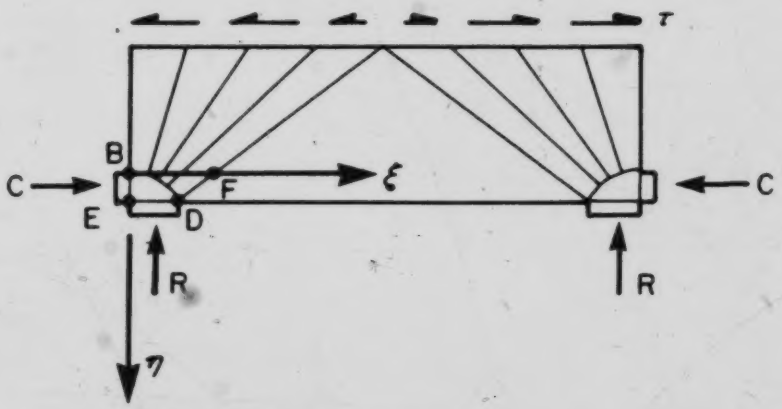

(c) Free body diagram of core

Figure 5.4 Fan stress field for a simply supported reinforced concrete beam with top reinforcement and under uniform load.

the soffit of the beam to equilibrate the stress u_c on the vertical face of the hydrostatic node (i.e. it must coincide with the force C in Fig. 5.4(c)).

In the case of a simply supported composite ice-resisting wall, both the top and bottom steel reinforcement is external. The solution for the simply supported reinforced concrete beam in Fig. 5.4. can be modified as shown in Fig 5.5 to allow for external bottom reinforcement, thereby giving the solution for a simply supported composite ice-resisting wall. Conceptually, a steel plate is embedded into the reinforced concrete beam along the ξ axis as shown in Fig. 5.5(a). If the support width is increased from ED to BF, the concrete and reinforcement below the ξ axis may be removed, and the normal and shear stress distributions necessary to equilibrate the fan along BF are supplied by the enlarged support and by shear transfer between the steel plate and the concrete (Fig. 5.5(b)). The normal and shear stress distributions vary along the length of the support because of the different radius $(R+\rho)$ and angle Θ for each fan-line which intersects the plate. The fan stress field for the simply supported composite ice-resisting wall, then, is shown in Fig. 5.5(c).

Conceptually, the steel plate is embedded just above the hydrostatic node because this is the optimum location for the plate. If the plate was embedded closer to the loaded surface, a wider support would be necessary to

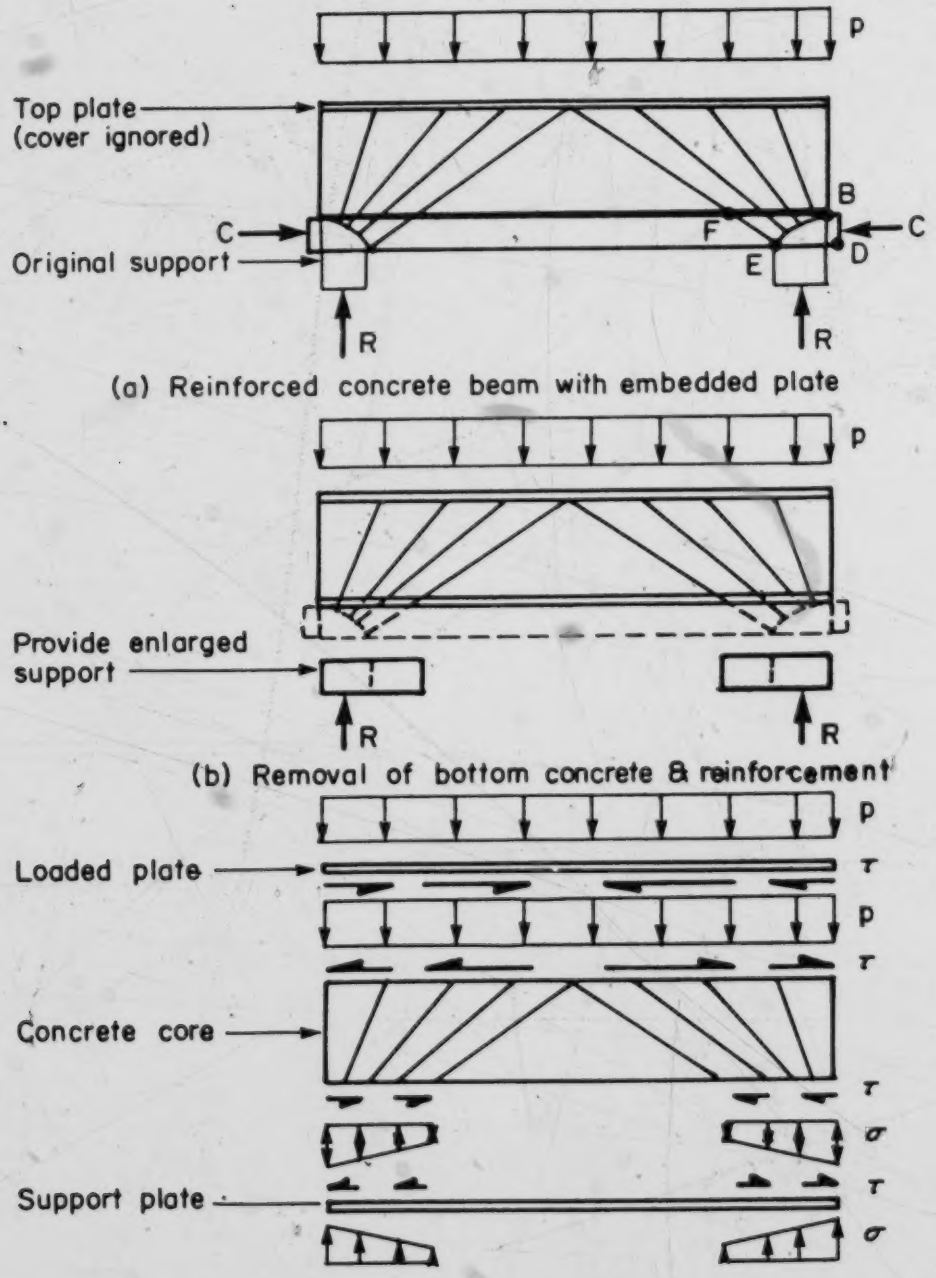

Figure 5.5 Fan stress field for a simply supported composite beam under a uniform load.

equilibrate the same applied load, since the point F (Fig. 5.5 (a)) would move closer to midspan. Alternatively, if the plate was embedded within the hydrostatic node, then the horizontal force which is necessary to equilibrate that portion of the hydrostatic node between the two plates could not be provided, and so equilibrium would not be satisfied.

Since the fan lines diverge through the thickness of the steel tension plate at the support, the effective support width which is available to the concrete core is slightly larger than that which is provided externally. Even though this increased support width is strictly a function of the beam geometry and loading pattern, it is simplified as

$$g' = g+2t_{sp}$$

where

g' = effective support width

g = actual width of the support

t_{sp} = thickness of the support plate,

and is shown in Fig. 5.6(a) discussed in Section 5.4.1.

It can be seen that there is no hydrostatic node in Fig. 5.5(c). However, it is useful to consider an imaginary hydrostatic node (Fig. 5.5(b)), since the tension in the support plate, T_{sp} can be found using

$$T_{sp} = \omega_0 u_c. \qquad [5.4]$$

The concept of an imaginary hydrostatic node is particularly useful in the analysis of continuous composite ice-resisting walls, as discussed in Section 5.4.

5.4 Stress Field for a Continuous Composite Ice-Resisting Wall

5.4.1 Introduction

If a single span of a continuous composite ice-resisting wall is isolated, it may be idealised as a simply supported beam with cantilevers. The length of the cantilever and its load intensity may be chosen to simulate the degree of continuity required. The general form of such a beam is shown in Fig. 5.6(a).

Since the stress field applies to the concrete core, and the steel plates are utilised only to provide the necessary static boundary conditions, the concrete core is isolated in Fig. 5.6(b). If both the beam and the loading are symmetric about the centreline, it is sufficient to consider one half of the beam. In the proposed stress field, load is transferred to the support through three distinct zones, as shown in Fig. 5.6(b). Each of these zones is a modification of a corbel stress field. The properties of these zones, including the locations of the hydrostatic nodes, are discussed in the ensuing sections. The upper case dimensions (X_1, X_2, X_3) of these zones refer to distances along the loaded plate, and the lower case dimensions (x_1, x_2, x_3) refer to distances along the support.

For a given value of u_c, only one value of the applied load p will allow the external equilibrium equations for all

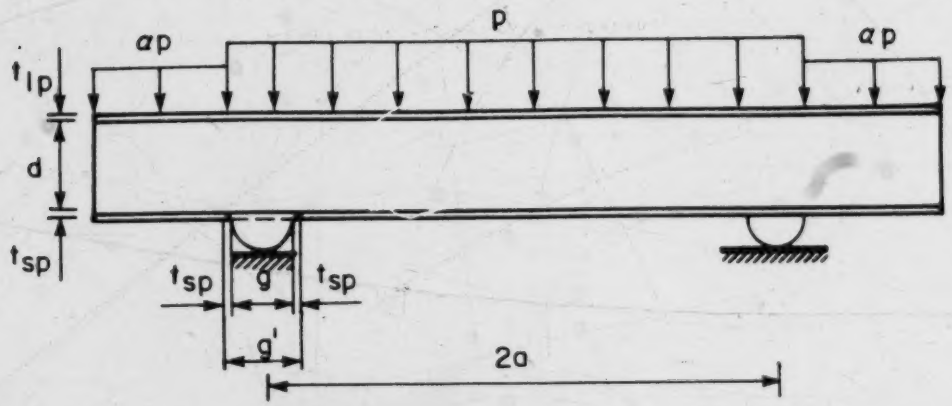

(a) Idealised single span of continuous composite beam

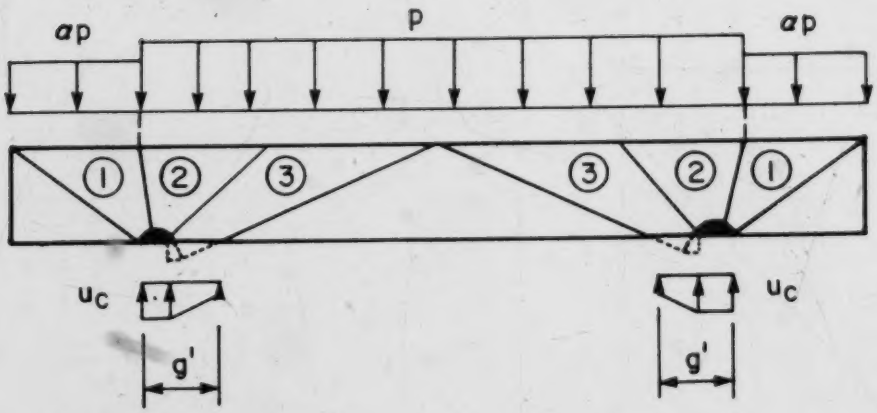

Legend

① - Zone 1
② - Zone 2
③ - Zone 3

Note ; Shear on boundary of core not shown

(b) Concrete core

Figure 5.6 Fan stress field for a continuous composite beam under a uniform load.

three zones to be satisfied simultaneously. Thus, the ratio p/u_c is constant for a given beam geometry. When constructing a stress field for a beam with cantilevers, the hydrostatic stress u_c is arbitrarily chosen and the procedure for choosing the correct value of p for an assumed value of u_c is iterative.

5.4.2 Zone 1

Zone 1 is used to provide a load path to the support for the cantilever load αp, and is shown in detail in Fig. 5.7. It can be seen from this figure that Zone 1 can be considered as a section cut from a corbel stress field (Fig. 5.3), where the cut lines are taken along the fan lines. Therefore, there are no normal or shear stresses along the boundaries defined by the fan lines. For a known (or assumed) value of u_c, the width x_1 of the real hydrostatic node can be calculated by summing forces in the vertical direction (since X_1 is known). The height, h_1, of the hydrostatic node is then found by summing moments about O.

5.4.3 Zone 2

The form of Zone 2 is shown in Fig. 5.8(a). The primary purpose of Zone 2 is to determine the amount (X_2) of the applied load p which is necessary to close the hydrostatic node so that the horizontal forces in Zones 1 and 2 are self-equilibrating, and the corresponding length (x_2) of the support width g' which is used by Zone 2. These two

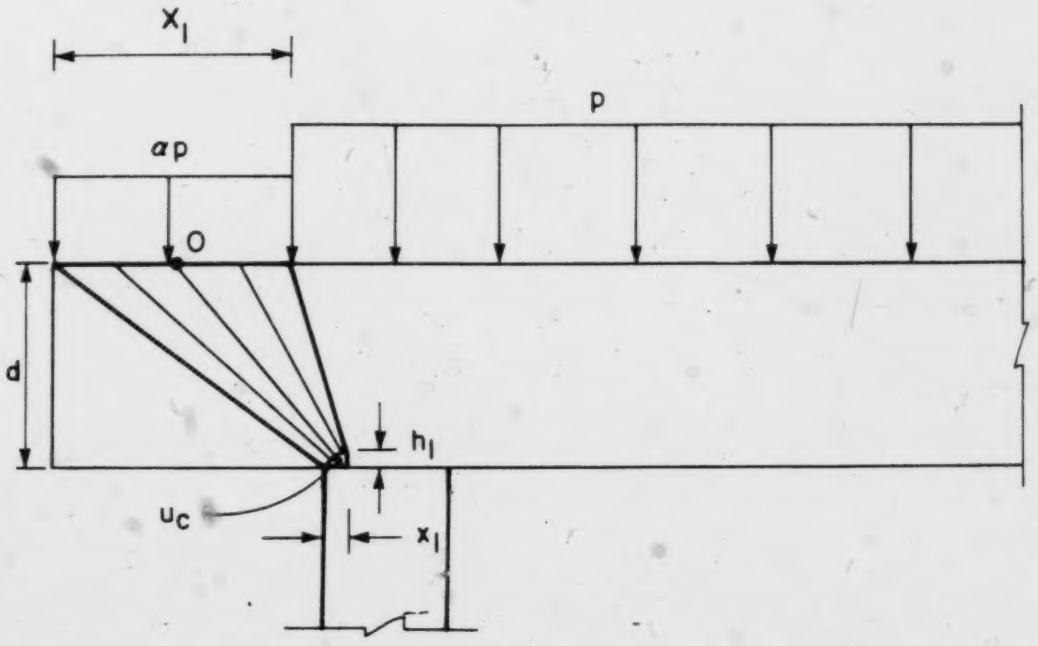

Figure 5.7 Zone 1.

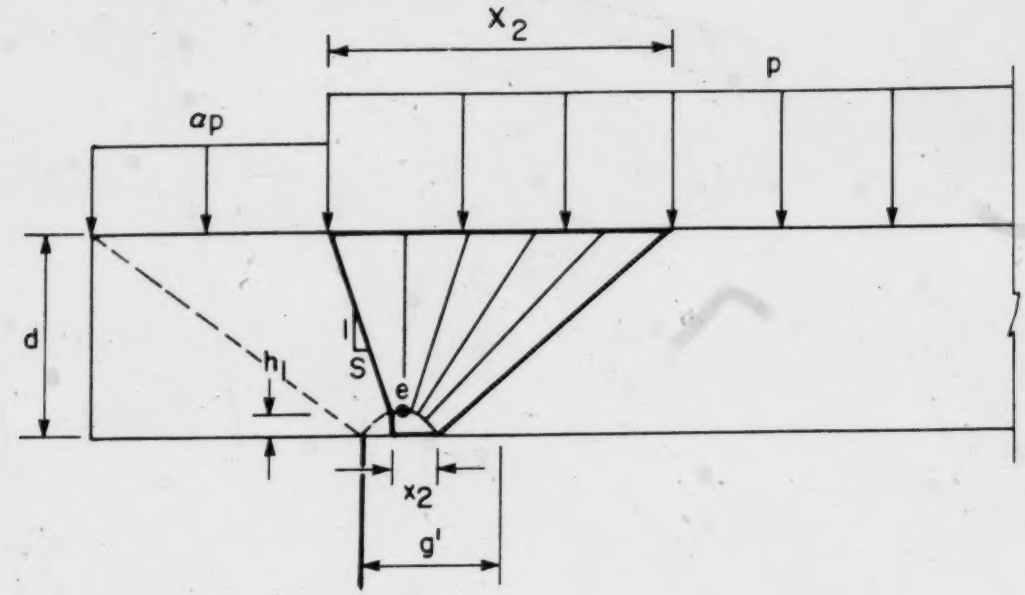

(a) Zone 2

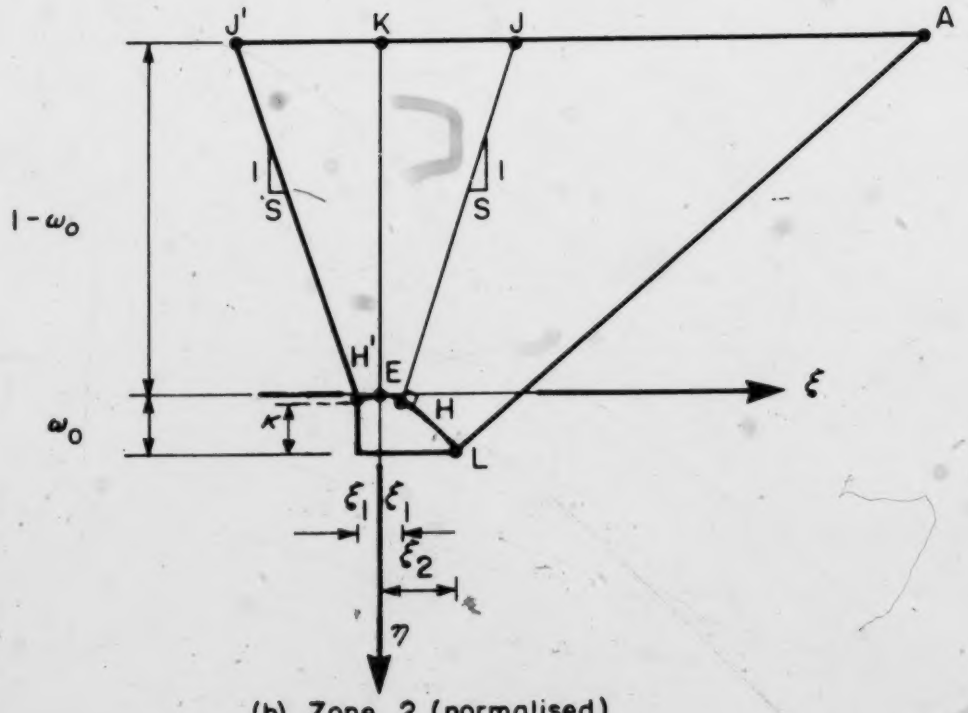

(b) Zone 2 (normalised)

Figure 5.8 Zone 2.

quantities could be directly evaluated by consideration of the vertical and rotational equilibrium of Zone 2. However, it is also advantageous to determine the location of the crest (e) of the hydrostatic node, since the point on the loaded surface which is vertically above point "e" is the point at which the interfacial shear stress is zero, as will be seen by consideration of equation [5.17].

In order to find X_2, x_2 and the location of the crest "e", it becomes mathematically more efficient to examine the normalised form of Zone 2, as shown in Fig. 5.8(b). The notation used in this figure is in accordance with Fig. 5.3. It can be seen that Zone 2 consists of a full corbel stress field (A-K-E-L) and a portion of its "mirror image". The slope s and the quantity κ (where $\kappa = h_1/d$) are known from the analysis of Zone 1. It is required to find ξ_1 and ξ_2, from which x_2 and X_2 can be found by proportion and equilibrium respectively, as shown later in equations [5.10] and [5.11].

ξ_1 and ξ_2 are found from the following development. Equation [5.3] describes the curve E-H-L:

$$(\eta+1-\omega_0)^2 - \xi^2\left(\frac{u_c}{p}-1\right) = (1-\omega_0)^2 \qquad [5.3]$$

This equation can be differentiated to give the slope of the tangent at H, which is equal to s. Therefore

$$s = \frac{\xi_1[(u_c/p)-1]}{(\eta_1+1-\omega_0)} \qquad [5.6]$$

where (ξ_1, η_1) are the coordinates of H.

Since $\eta_1=\omega_0-\kappa$, equation [5.6] can be rearranged to give

$$\xi_1 = \frac{s(1-\kappa)}{(u_c/p)-1} \qquad [5.7]$$

To find the expression for ξ_2, the coordinates of $L(\xi_2,\omega_0)$ are substituted into [5.3]. This gives

$$\xi_2 = \sqrt{\frac{\omega_0(2-\omega_0)}{(u_c/p)-1}} \qquad [5.8]$$

To evaluate ξ_2, it is necessary to know ω_0. This is achieved by combining [5.7] and [5.3] applied at H, and observing again that $\eta_1=\omega_0-\kappa$, to give

$$\omega_0 = 1-(1-\kappa)\sqrt{1-\frac{s^2}{(u_c/p)-1}} \qquad [5.9]$$

Once the dimensionless parameters ξ_1 and ξ_2 have been found, x_2 and X_2 are found using

$$x_2 = (\xi_1+\xi_2)d \qquad [5.10]$$

and

$$X_2 = \frac{u_c}{p}x_2 \qquad [5.11]$$

5.4.4 Zone 3

For the assumed values of p and u_c, Zones 1 and 2 have used a length x_1+x_2 of the support width g. The remainder is therefore available for use by Zone 3.

The geometry of Zone 3 is shown in Fig. 5.9. Zone 3 is a section of a corbel stress field, similar to Zone 1. For maximum utilization of concrete capacity, the imaginary hydrostatic node must be located just below the line LE (hereinafter referred to as the "optimum position" for the node). To construct this node, it must initially be assumed that the load p which has been used to construct Zones 1 and 2 is the correct applied load. (The validity of this

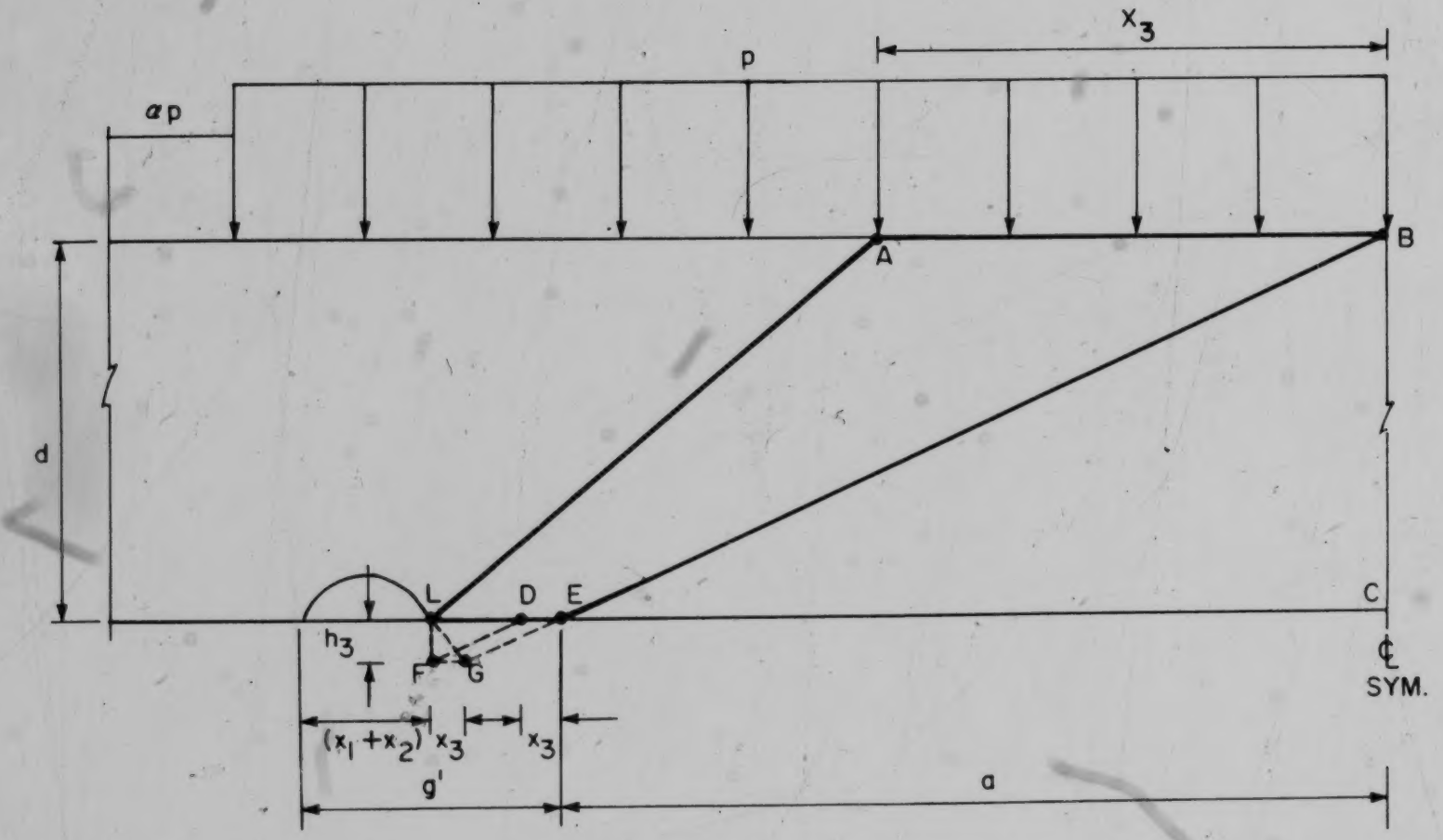

Figure 5.9 Zone 3.

assumption is checked later). The horizontal dimension of the imaginary node is then calculated using

$$x_3 = \frac{p}{u_c} X_3 \qquad [5.12]$$

since X_3 is known. If the line DF is constructed parallel to GE, as shown in Fig. 5.9, then, by consideration of the similar triangles LDF and EBC, the height of the node h_3 can be expressed as

$$h_3 = \frac{d}{a}\left[g' - (x_1 + x_2 + x_3)\right] \qquad [5.13]$$

The overturning moment, M_o, on Zone 3 is given by

$$M_o = pX_3\left[a + g' - x_1 - x_2 - \frac{(x_3 + X_3)}{2}\right] \qquad [5.14(a)]$$

and the restoring moment, M_r, is

$$M_r = u_c h_3 (d + \frac{h_3}{2}) \qquad [5.14(b)]$$

If $M_o = M_r$, Zone 3 is in equilibrium, and the correct value for p has been chosen. If $M_o < M_r$, then the assumed value of p is too small. If $M_o > M_r$, the converse is true. In either case, a new value of p must be chosen, and the process repeated until the correct value for p is found. The overall procedure is outlined in the flowchart of Fig. 5.10.

When the correct value for p has been obtained, the corresponding tension in the support plate, T_{sp}, is calculated using

$$T_{sp} = u_c h_3 \qquad [5.15]$$

since either the imaginary node or the support plate must supply the same horizontal force to equilibrate Zone 3. Finally, Fig. 5.11 shows that, for equilibrium,

$$C_{lp} = T_{sp} \qquad [5.16]$$

where C_{lp} is the compression in the loaded plate at midspan.

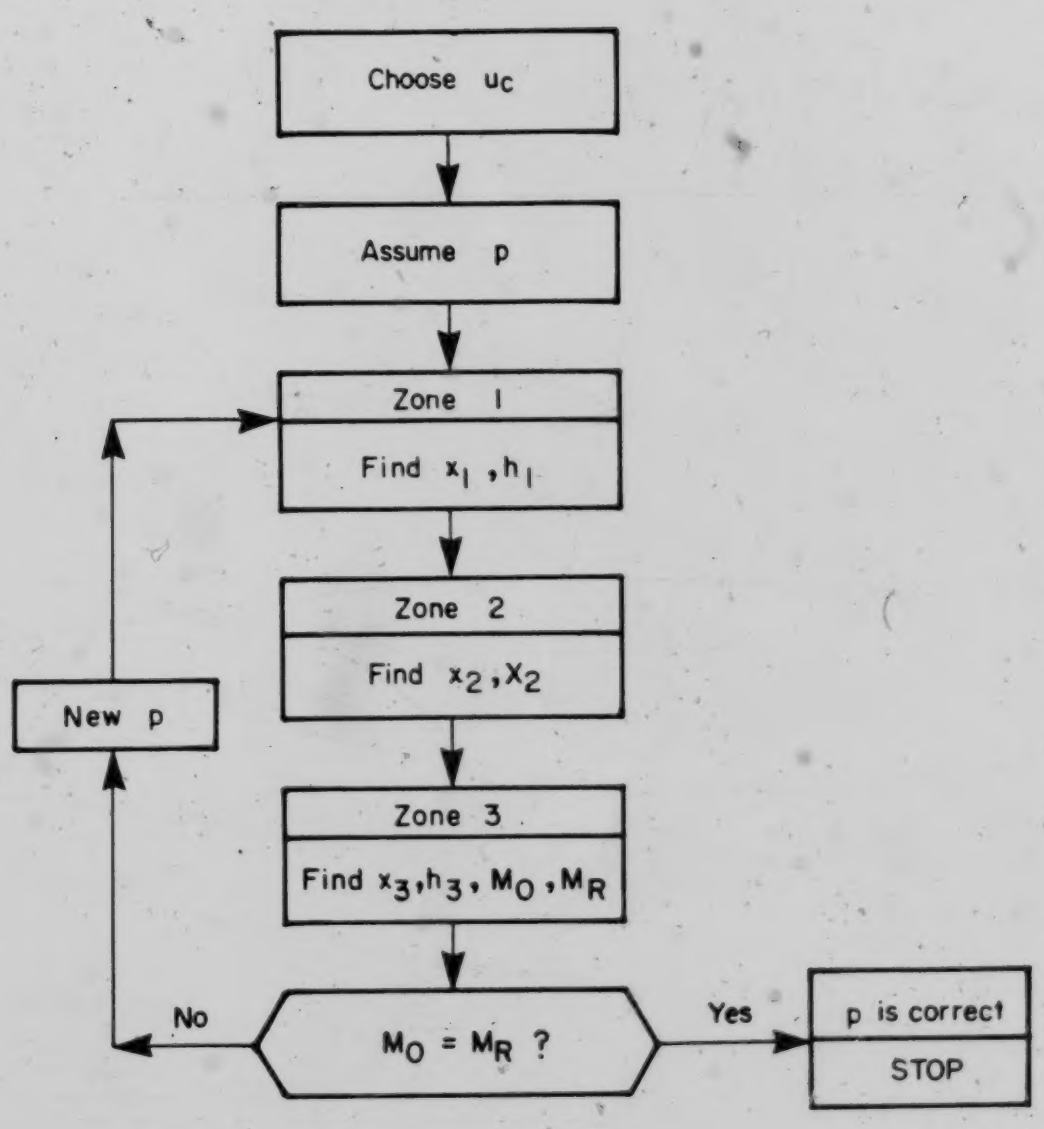

Figure 5.10 Flowchart to calculate the applied load p.

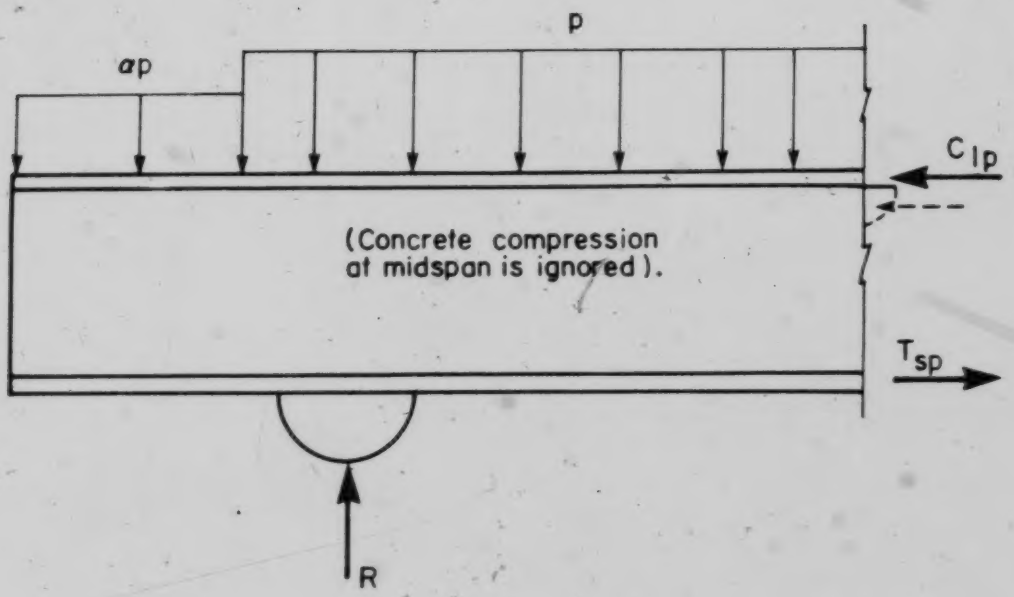

Figure 5.11 Free body diagram of half-beam.

Equation [5.16] assumes that the concrete does not carry compression at midspan. This assumption is made primarily for convenience, and it is recognised that the absence of such a compressive zone, coupled with the assumption of uniform longitudinal compressive stress through the thickness of the loaded plate, demands a strain discontinuity at the steel/concrete interface, which is not possible. A compressive zone does exist in the concrete at midspan, and the consequences of its neglect in the theory will be demonstrated in Chapter 6, where measured and predicted steel strains in the loaded plates are compared. However, the inclusion of the concrete compressive zone into the stress field formulation greatly complicates the mathematics and graphics involved. Since the regions within a prescribed stress field which are of greatest interest are those areas close to the supports where concrete failure initiates, the presence or absence of a compressive zone at midspan is deemed to be of little practical interest, and its neglect for convenience is thereby justified.

5.4.5 Numerical or Graphical Techniques?

The flowchart in Fig. 5.10 might indicate that the procedure for constructing a statically admissible stress field should be computerized, thereby removing the necessity for considering individual zones and manual iteration. However, the procedure developed in Section 5.4 applies only to a beam with symmetric loading. For the procedure to be

versatile, it must also be capable of providing a stress field for a beam loaded with an eccentric patch load. The algebra associated with deriving a solution for this general case becomes unreasonably complicated, and a graphical approach becomes more appealing.

The accuracy associated with the graphical approach is highly satisfactory if a suitably large scale is used. Furthermore, the determination of internal stresses (Section 5.8) demands the use of a graphical method.

5.5 Eccentric Patch Loading.

The properties of Zones 1 through 3 may be applied in constructing a stress field for a composite ice-resisting wall loaded with an eccentric patch load as shown in Fig. 5.12. This beam is also loaded on the cantilevers by a load of intensity αp. To start, a value of the hydrostatic nodal stress u_c is assumed, and the associated applied load p is estimated. Using the methods developed in Section 5.4, Zone 1 and Zone 3 stress fields are fitted to transfer the cantilever loads to the supports (Fig. 5.12). The remaining lengths of the supports which are available to resist the patch load are thus determined.

The patch load is to be transferred to the supports by means of two Zone 3 fields (Zone 3_L and Zone 3_R). The proportions of the patch load to be carried by each support are not immediately apparent. To find these proportions, it is assumed that the imaginary hydrostatic node is in the

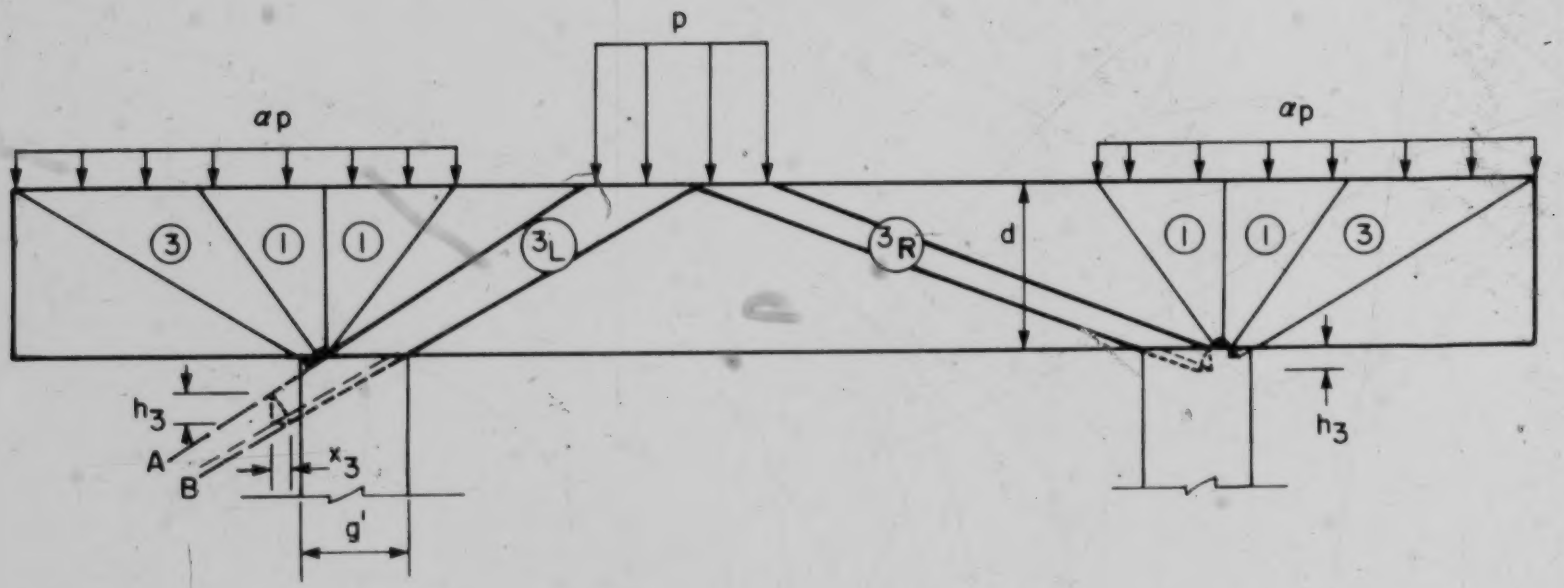

Figure 5.12 Fan stress field for a continuous composite beam under an eccentric patch load.

"optimum location" at one side (the right hand side in Fig. 5.12). The amount of the patch load which is necessary to provide both vertical and rotational equilibrium to Zone 3_R is then determined. (For simplicity, the dimension h_3 is scaled in this case.)

The remainder of the patch load is transferred to the left hand support through Zone 3_L. This Zone is simply a two-force member (as, indeed, are all other Zones), and the magnitude and direction of the resultant force in the member are determined by the vector addition of the resultant normal and shear forces at the loaded plate/Zone 3_L interface. In reality, this resultant force must be equilibrated by the resultant of the corresponding normal and shear forces at the support plate/Zone 3_L interface. However, for the purpose of constructing the stress field, it is convenient to consider the existence of an imaginary hydrostatic node with hydrostatic stress u_c at the left hand side also, and the resultant of the horizontal and vertical forces acting on this node is statically equivalent to that which is actually provided at the support. For the assumed value of applied load p, the horizontal dimension of this node, x_3, can be calculated using equation [5.12] from Section 5.4.4. The requirement that the tension in the support plate (T_{sp}) must be constant dictates that

$$h_3(\text{left hand side}) = h_3(\text{right hand side}).$$

Since x_3 and h_3 are both known, the imaginary node is fitted graphically into its unique location between the tapering

lines A and B using the technique developed in Section 5.4.4 and as shown in Fig. 5.12. If the assumption that the imaginary node in Zone 3_R is in the optimum location is correct, then the imaginary node in Zone 3_L will be below the soffit of the concrete core. Assuming that the assumption is correct, the rotational equilibrium of Zone 3_L is checked. For simplicity, the necessary dimensions are scaled from the drawing. If $M_o<M_r$, the load p must be increased, and the procedure repeated. The converse is true if $M_o>M_r$.

5.6 Interfacial Shear Transfer

In the preceeding sections it was recognised that unique shear stress distributions on the horizontal surfaces of the various zones were necessary for equilibrium to be satisfied. These stresses are supplied to the concrete core by the external steel plates. Since mechanical interaction between the plates and the concrete is required to provide this composite effect, it is necessary to accurately evaluate the interfacial shear distribution. The mechanical shear connector layout can then be safely and economically chosen.

The shear distribution along the loaded surface of a (normalised) corbel is evaluated as follows. The Mohr circle of stress in Fig. 5.13 shows that the surface shear/applied load relationship at the arbitrary point N is

$$\frac{\tau}{p} = \text{Tan}(\theta) \qquad [5.17]$$

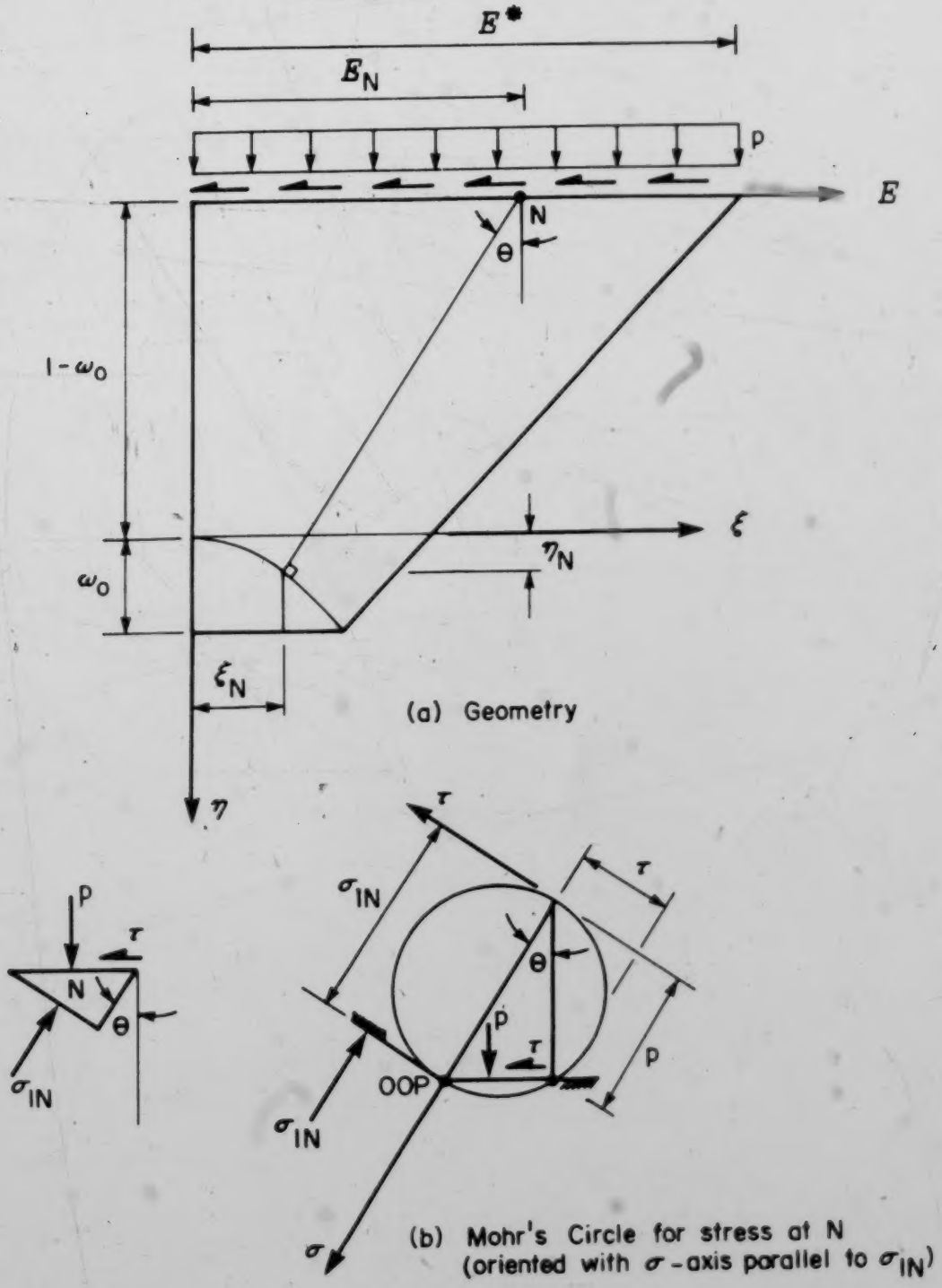

Figure 5.13 Geometry for interfacial shear transfer.

Referring to Fig. 5.13, Tan(θ) can be expressed as

$$\text{Tan}(\theta) = \frac{E_N - \xi_N}{1-\omega_0+\eta_N} \qquad [5.18]$$

From vertical equilibrium, the relationship between ξ_N and E_N is

$$\xi_N = \frac{p}{u_c} E_N \qquad [5.19]$$

Also, the governing equation for the nodal surface [5.3] can be rearranged as

$$(1-\omega_0+\eta_N) = \sqrt{\xi_N^2\left(\frac{u_c}{p}-1\right) + (1-\omega_0)^2} \qquad [5.20]$$

Equations [5.17] to [5.20] can then be combined to give the general equation

$$\frac{\tau}{p} = \left[\left(\frac{A}{E}\right)^2 + B\right]^{-0.5} \qquad [5.21]$$

where

$$A = \frac{1-\omega_0}{1-\beta} \qquad [5.22]$$

$$B = \frac{\beta}{1-\beta} \qquad [5.23]$$

$$\beta = p/u_c \qquad [5.24]$$

and E is the coordinate of any point along the E axis.

The τ - E relationship defined by [5.21] is plotted in Fig. 5.14(a). The curve is convex and is asymptotic to $1/\sqrt{B}$. If this curve is approximated by the dashed straight line in Fig. 5.14, then the theoretical shear stress will always be underestimated. It was shown in Sections 5.4 and 5.5 that a statically admissible stress field for a continuous composite member can be constructed using corbel-type stress fields. The shear stress distribution along the surface of the concrete core, then, will also be convex, and the linear approximation of Fig. 3.3 will always underestimate the theoretical shear requirements. However, the error is

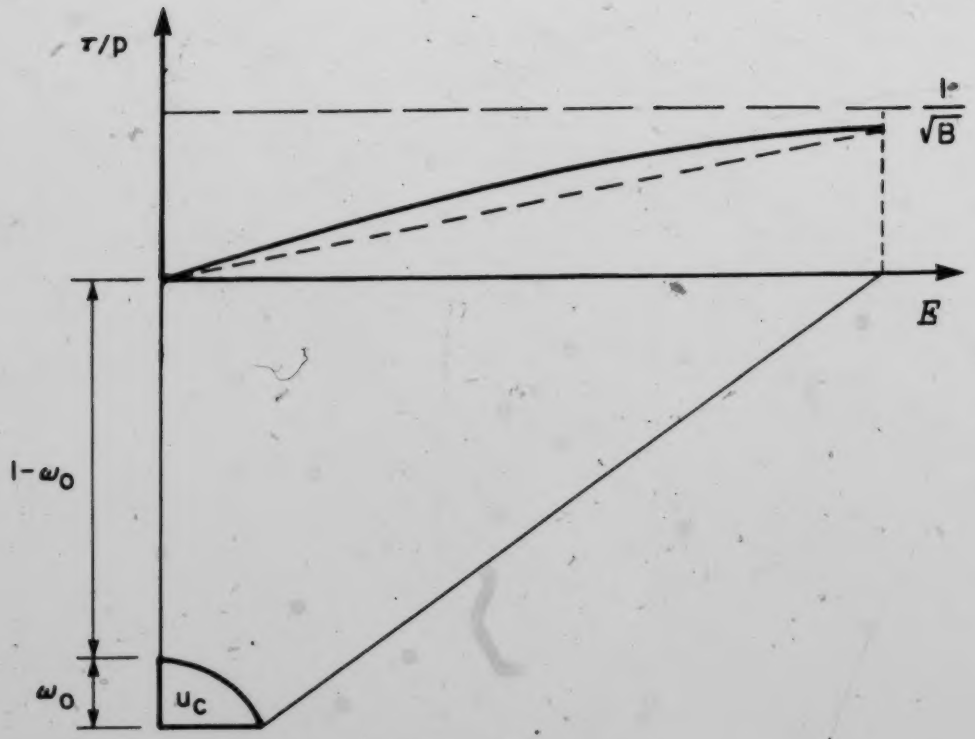

Plot of equation [5.21]

Figure 5.14 Theoretical interfacial shear stress distribution at the loaded surface of a corbel.

compensated by the neglect (in the model) of the concrete compression zone at midspan of the composite member, as discussed in Section 5.4.4, the presence of which tends to reduce the shear transfer requirements at midspan. The straight line approximation is therefore deemed appropriate, and this assumption greatly reduces the computational effort which is necessary to calculate the steel strains. (The computational method is outlined in Section 6.7).

5.7 Mechanism for Shear Transfer

The mechanism for shear transfer at the loaded steel/concrete interface of a simply supported composite beam was outlined in Chapter 3, but is repeated here for the case of a corbel for completeness. Shear transfer at the steel/concrete interface is provided by a combination of friction and mechanical shear connectors (Nelson studs). The shear friction coefficient between steel and concrete, f, is taken as 0.6, as recommended by CAN3 A23.3-M-84. Therefore, in regions where $v/p > f$, mechanical shear connectors must be added, as shown in Fig. 5.15. The shaded area represents the shear to be carried by the mechanical shear connectors.

The procedure outlined above can also be applied to Zones 1 to 3 , and to both loaded and supported surfaces. Test specimens with the required number of studs distributed uniformly over the entire area, rather than concentrated in the locations where they are theoretically required, behaved satisfactorily, suggesting that a uniform distribution would

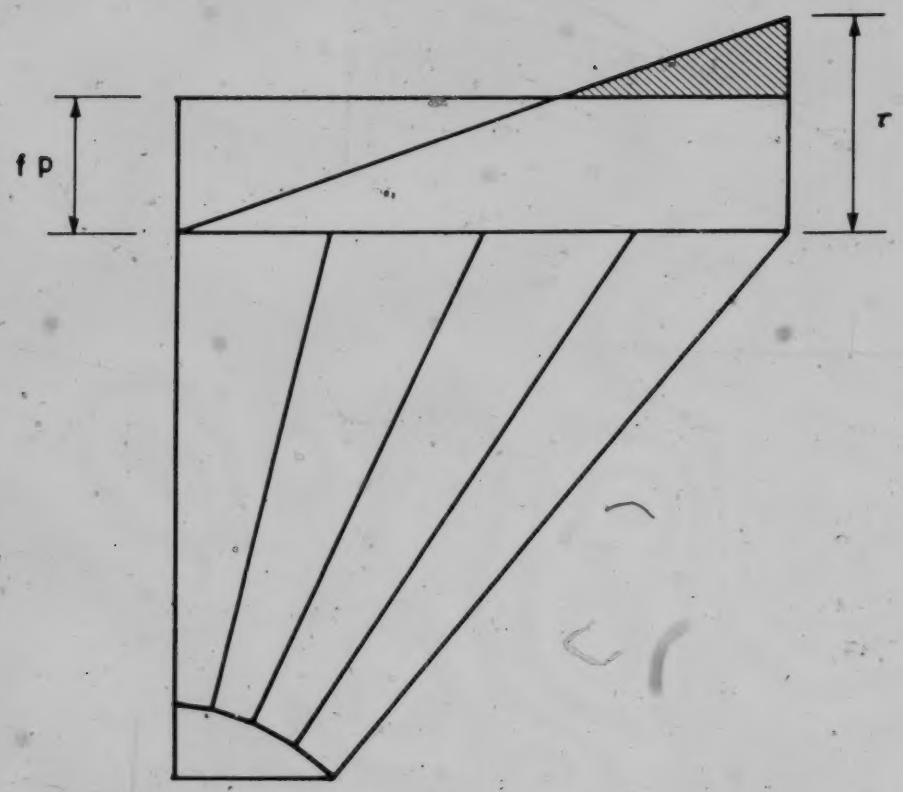

(Shaded area supplied by shear connectors)

Figure 5.15 Mechanical shear connector evaluation.

be acceptable. This is also a more practical approach.

5.8 Principal Stresses at an Internal Point

To find the principal stresses at any internal point, the correct fan line must be drawn through that point. This can be obtained graphically by trial and error by observing the fact that the regions of the zone bounded by the fan line must both be in vertical equilibrium (Fig. 5.16(a)). Once this line has been constructed, the principal stress at A (i.e. σ_{1A}) can be found using

$$\sigma_{1A} = \frac{2p}{1+\cos 2\theta} \qquad [5.25]$$

which is derived from the Mohr circle in Fig. 5.16(b). (It is reasonable to determine θ using scaled dimensions). The principal stress at B may then be calculated from [5.1] and [5.2], i.e.

$$R = \left(\frac{\sigma_{1A}}{u_c - \sigma_{1A}}\right) r \qquad [5.2]$$

and

$$\sigma_{1B} = \left(\frac{R}{R+\rho}\right) u_c \qquad [5.1]$$

where r and ρ can be scaled.

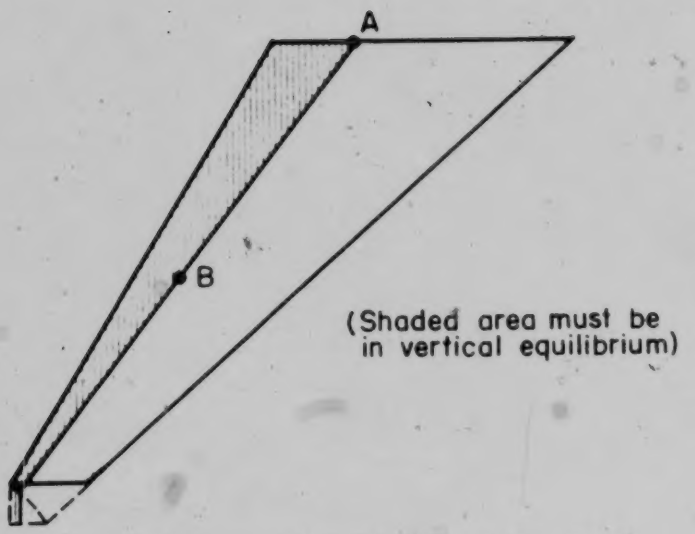

(a) Construction of internal fan line

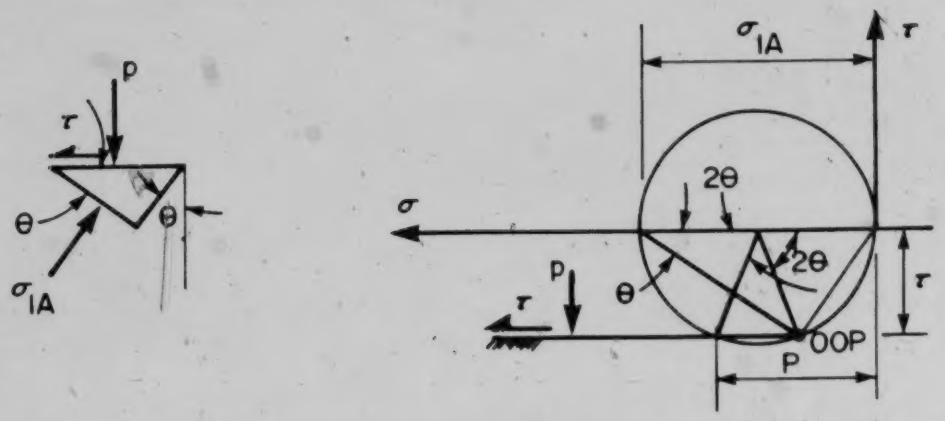

(b) Mohr Circle to define σ_{1A}

Figure 5.16 Evaluation of internal stress at an arbitrary point within the concrete core.

6. ANALYSIS OF TEST RESULTS

6.1 Introduction

The data reported in Table 4.1 give the measured failure loads for the test specimens. The purpose of this chapter is to determine why the beams failed at the reported loads. To this extent, it is necessary to develop a failure criterion to be used in conjunction with the load paths which were developed in Chapter 5. Seventeen beams were tested to failure in the series. However, the following four beams will be omitted during the development of the failure criterion.

Beam 4/5 was the first beam to be tested in the series. In this test, a high-load-capacity, teflon-based slip surface was used in place of rollers at the load and reaction points. Because of the external restraint introduced by the frictional interaction between the test specimen and the test frame, spurious moments were introduced, and the supports acted as buttresses for the concrete "arch". Accordingly, the beam is not simply supported, and the theory developed in Chapter 5 cannot be applied to this test.

B6/2 was underreinforced, and so failure of the concrete occurred only after the plates had strain hardened. Since the failure criterion to be developed assumes elastic behaviour in the plates at failure, this beam is also omitted during the calibration of the proposed failure

criterion.

Steel-fibre-reinforced concrete was used in B6/3 and B6/4. This exhibits properties which differ greatly from those shown by unreinforced concrete. Furthermore, B6/4 was also underreinforced. Since only one data point is therefore available, a failure criterion for steel-fibre-reinforced concrete cannot be proposed in this thesis.

6.2 Analysis Procedure

6.2.1 Basic Stress Field

In Chapter 5, it was shown that the ratio p/u_c could be determined for any span-to-depth ratio and loading arrangement. Such a stress field is hereinafter called a basic stress field for those conditions. The stress field in a test specimen at failure is obtained by scaling a basic stress field by the multiplier M:

$$M = \frac{p_t}{p} \qquad [6.1]$$

where p_t is the load (expressed as a pressure, MPa) which was applied to the test specimen at failure, and p is the applied load (MPa) from a basic stress field with an assumed value of hydrostatic stress u_c. Since the choice of u_c can be arbitrary, it was consistently chosen to be equal to 50 MPa in the forthcoming analysis.

6.2.2 Critical Stress Location and Failure Mode

The location within the concrete core at which failure is assumed to start is designated as K in Fig. 6.1. Crushing was first observed near this location in several of the tests, and its choice can also be rationalised for the following reasons:

- Even though the maximum stress at failure is the hydrostatic stress u_c^* (= Mu_c) in the nodal zone which falls within the region ABCD, this region is heavily reinforced with studs. Stiffness considerations indicate that load is shared by the concrete and the studs in this region according to the proportions $E_cA_c:E_sA_s$. The actual stress in the concrete in this region is therefore considerably less than u_c^*, and so failure does not occur here.
- BC is a potentially weak plane since the smooth heads of the studs all lie along this surface. The point K lies in an extension of this plane.
- High strain gradients exist across the line DL which separates the stressed and stress-free regions. These gradients can cause cracking along DL because of the inability of concrete to accomodate such a gradient. Failure can therefore be anticipated somewhere along CD.
- Concrete in the triangular region CDK is offered additional restraint by the region ABCD. Failure is therefore unlikely in this region.

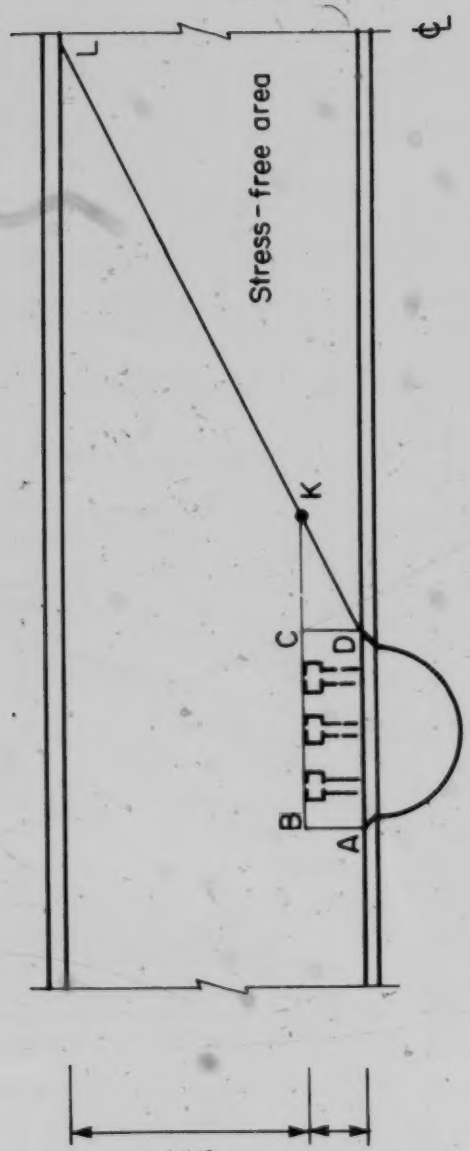

Figure 6.1 Failure location "K".

The principal compressive stress in the concrete at location K at failure can be expressed as σ^*_{1K}, where

$$\sigma^*_{1K} = M\sigma_{1K} \qquad [6.2]$$

Since the stress σ^*_{1K} equals the material capacity at K and crushing has started in this vicinity, the applied load which was formerly carried by strut action through this region must find an alternative load path. This secondary load path is shown schematically in Fig. 6.2, and was observed in the tests as typically shown for specimen B6/1 in Plate 6.1. The applied load which was previously carried through the crushed region K is now transferred through the concrete trapezoid (which includes the former "stress-free area), as shown in Fig. 6.2. This trapezoid reacts directly onto the support plate. A reaction point for the trapezoid can be observed in Plate 6.1(b) as that location where the gap closes between the support plate and the concrete core. The applied load near midspan is therefore transferred solely by the catenary action of the support plate. The capacity of this catenary is initially less than that of the original composite member, and so the applied load which can be tolerated becomes smaller. A secondary load path to allow additional applied load to be carried is therefore not available, and it is reasonable to say that failure of the concrete occurs by crushing at K. It may be noted in Plate 6.1 that crushing has not occurred in the triangle identified as CDK of Fig. 6.1.

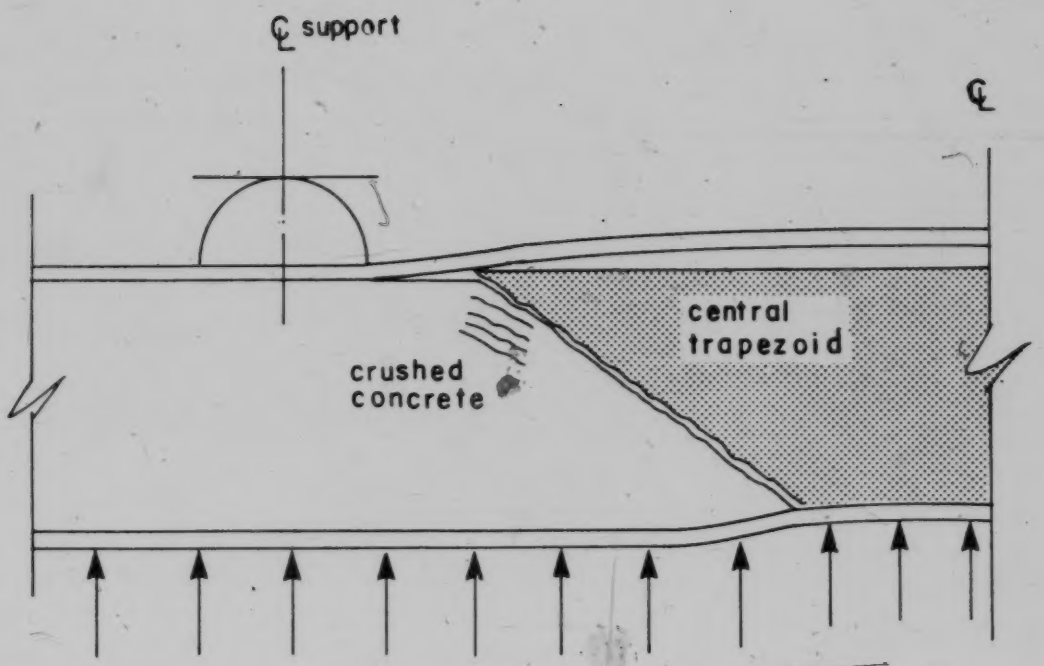

Figure 6.2 Secondary load path after concrete has crushed at K.

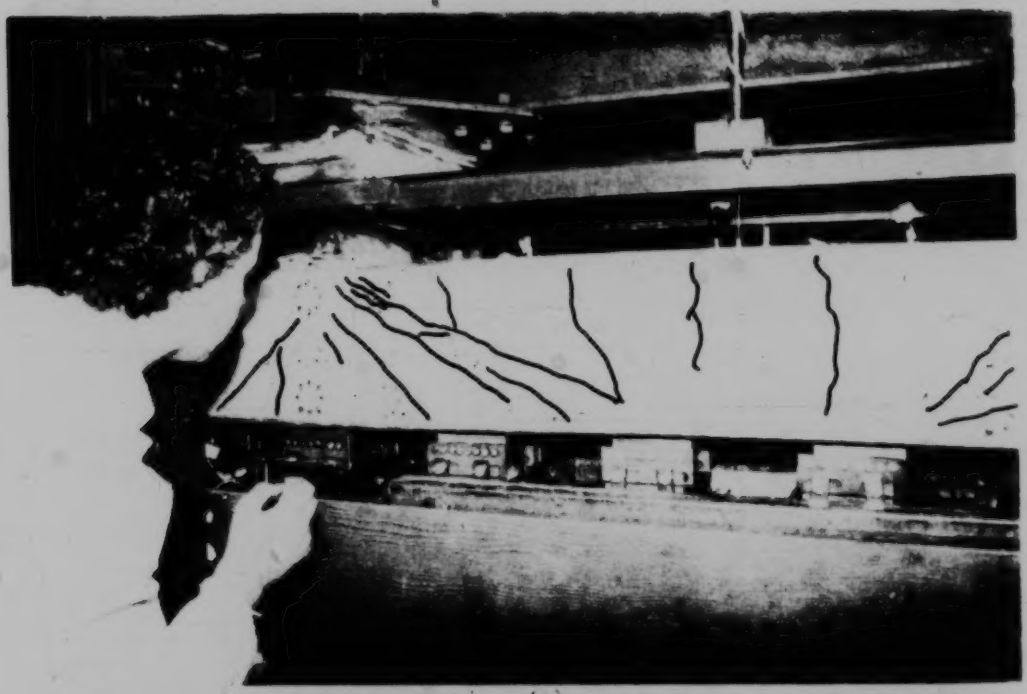

(a)

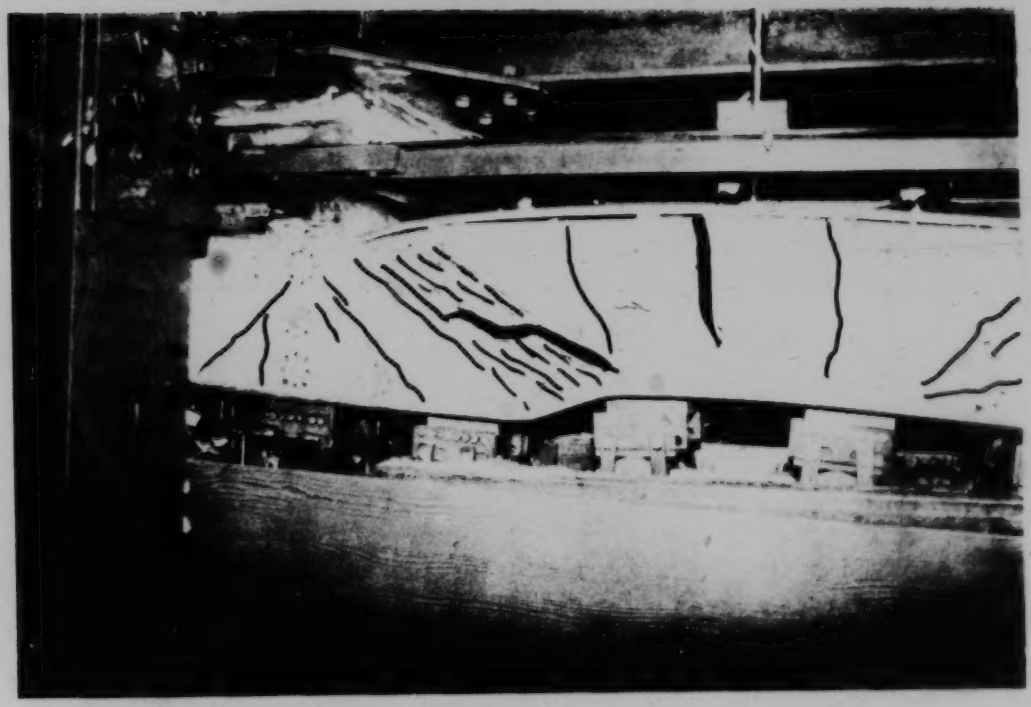

(b)

Plate 6.1 Secondary load path in specimen B6/1.

6.3 Failure Stress in Tested Beams

In order that the failure stress σ^*_{1K} can be found for the thirteen beams, it is necessary to construct only four basic stress fields. These are

1. Span-to-depth ratio = 4, symmetric loading,
2. Span-to-depth ratio = 6, symmetric loading,
3. Span-to-depth ratio = 6, patch loading,
4. Span-to-depth ratio = 5, symmetric loading.

The unknown cantilever loads induced into specimen B5/4 by rotational restraint at the supports were difficult to quantify accurately, but were estimated from the measured steel strains to be only 1.02 times the the controlled cantilever load for the remainder of the B5 series. Since Chapter 5 indicates that σ_{1K} is insensitive to small changes in cantilever load, the same basic stress field will be used for the entire B5 series.

The calculations to determine σ_{1K} from the basic stress fields are given in Appendix B. The results are summarised in Table 6.1. From these results, the failure stress σ^*_{1K} for each beam can be calculated using [6.1]. These results are also given in Table 6.1.

6.4 Failure Criterion: Effective Concrete Strength

The concrete in a composite beam reaches its load-carrying capacity when

$$\sigma^*_{1K} = f^*_c \qquad [6.3]$$

where f^*_c is the effective concrete strength at location K.

Table 6.1 Summary of calculations to determine σ_{1K} and σ^*_{1K} for the test specimens.

Specimen #	From Basic Stress Field p (MPa)	From Test p_f (MPa)	$M = p_f / p$	From Basic Stress Field σ_{1K}	$\sigma^*_{1K} = M\sigma_{1K}$
B4/1	6.0	10.00	1.667	35.78	59.64
B4/2	6.0	11.03	1.838	35.78	65.76
B4/3	6.0	10.12	1.687	35.78	60.36
B4/4	6.0	11.06	1.843	35.78	65.94
B6/1	2.4	4.74	1.975	32.97	65.12
B6/5	2.4	5.09	2.121	32.97	69.93
B6/6	2.4	3.90	1.625	32.97	53.58
B6/7	3.3	5.42	1.642	43.10	70.79
B5/1	4.0	8.15	2.038	35.60	72.55
B5/2	4.0	8.20	2.050	35.60	72.98
B5/3	4.0	5.15	1.288	35.60	45.85
B5/4	4.0	5.10	1.275	35.60	44.39
B5/5	4.0	5.01	1.253	35.60	44.60

The effective concrete strength is defined as

$$f_c^* = \upsilon f'_c \qquad [6.4]$$

where

υ= effectiveness factor,

f'_c= concrete cylinder strength.

The uniaxial stress field proposed in Chapter 5 is a simplification of the true state of stress in a composite section. In reality, the concrete will be biaxially stressed if plane stress conditions are assumed. The effectiveness factor υ is a measure of the amount by which the true state of stress at K differs from the state of stress in standard cylinder, and it can therefore be interpreted as a measure of the degree of confinement of the concrete at K. This can be seen by consideration of the behaviour of concrete cylinders under the following three different loading conditions. Firstly, a standard cylinder test with sulphur caps and steel loading platens is considered to be the datum, and gives an effectiveness factor υ equal to unity. The friction which is developed between the sulphur caps and the loading platens tends to confine the concrete in the cylinder, and so a standard cylinder test does not produce uniaxial stress conditions. If a companion cylinder is tested using steel brushes or a soft material between the platens and the cylinder, the failure load will be reduced due to the reduced confinement near the ends (Mindess and Young, 1981). In this case, the effective concrete strength f_c^* is less than the standard concrete cylinder strength, and

so the effectiveness factor υ is less than 1.0. Finally, it has been shown (Price, 1951) that the addition of a suitably large circumferential confining stress to an otherwise standard cylinder test can increase the axial load at failure by up to 14 times that which is obtained from a standard cylinder test, thereby giving an effectiveness factor equal to 14. Effectiveness factors can therefore be expected to vary from less than 1.0 (for uniaxially stressed concrete) up to as large as 14.0 (for concrete which is assumed to be uniaxially compressed but is actually triaxially confined). Effectiveness factors of the order of 14.0 are certainly not anticipated for biaxially stressed concrete (plane stress), a state of stress which more closely approximates the true state of stress in the composite specimens. However, effectiveness factors of approximately 1.0 can be interpreted from the classical biaxial tests of Kupfer et al. (1969). Also, Bach et al. (1980) have reported a value of υ equal to 1.22 when the reinforcement ratio of a reinforced concrete T-beam (overall depth 380 mm, flange width 800mm, flange thickness 90 mm, web width 200 mm) with stirrup reinforcement was made very large by bonding a 16 mm steel plate to the soffit of the beam by welding the stirrups to the plate before the concrete was poured. These conditions are similar to those which are obtained in a composite beam.

For design purposes, it is necessary that υ can be rationally evaluated. Several stress-based failure criteria

have been developed for multiaxially stressed concrete (Chen 1982). However, these all demand that the true multiaxial state of stress be known, and they cannot therefore be used in conjunction with lower bound fans which assume uniaxial stress conditions. Vecchio and Collins (1982) proposed a failure criterion which assumes that the effective concrete strength υ is inversely proportional to the transverse principal strain in the concrete at failure. The relationship is expressed as

$$\upsilon = \frac{1}{0.8 + 170\epsilon_2} \qquad [6.5]$$

where ϵ_2 is the transverse tensile strain at K at failure, and tensile strain is considered to be positive. However, it is not possible to evaluate the strain ϵ_2 at K at failure in the model used, again because of the artificial nature of the uniaxial stress field.

An alternative formulation for the effectiveness factor must therefore be developed. The formulation must recognise the contribution of the stress-free area (Fig. 6.1) in confining the concrete at K. For the purpose of this development, it is assumed that a crack exists along the critical fan line at all levels of loading, as shown in Fig. 6.3. It is also assumed that D moves horizontally to D', where

$$D\text{-}D' = \epsilon_{sp} a$$

and ϵ_{sp} is the strain in the support plate. By proportion, the crack width, w, at K may be expressed as

$$w = (1 - \frac{h_s}{d})\epsilon_{sp} a \cos\theta.$$

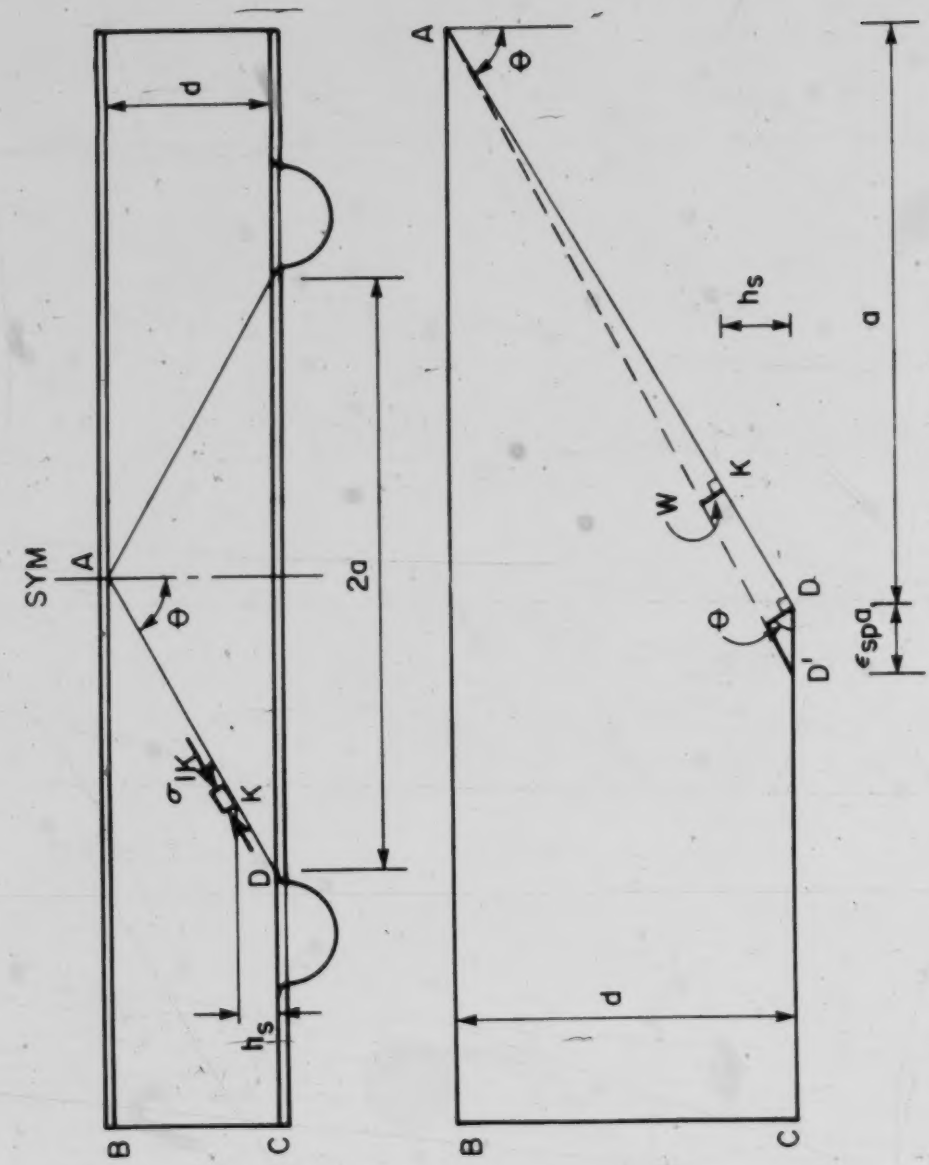

Figure 6.3 Crack width w at K.

But

$$\text{Cos}\theta = \frac{d}{\sqrt{a^2+d^2}}$$

$$= \frac{1}{\sqrt{1+(a/d)^2}}$$

and so

$$w = \frac{[1-(h_s/d)]a\epsilon_{sp}}{\sqrt{1+(a/d)^2}} \qquad [6.6]$$

For a given beam geometry, then, w is a function of ϵ_{sp} only.

In the development so far, it has been assumed that the concrete is a rigid material. In reality, the concrete along AD' will tend to expand into the crack. If is assumed that this expansion will cause contact between the stressed and stress-free areas at discrete locations, then it follows that, for a stressed area with a given f'_c, both the number of contact points and the intensity of the compressive stresses at these points of contact would increase for a smaller crack width w at a given applied load level p, i.e. at a lower value of w for a given value of σ_{1K}. The confinement characteristic at K, G_K, is therefore defined as

$$G_K = \frac{\sigma_{1K}}{w} \qquad [6.7]$$

and is interpreted as a measure of the lateral restraint offered to the concrete at K by the overall beam geometry and support plate. If the support plate remains elastic, G_K is independent of the load level.

The concrete in the beam has an associated generic transverse stiffness, which can be visualised with reference to consideration of a uniaxially stressed concrete cylinder of the same material as that used in the concrete core of

the composite beam. If it is assumed that Poisson's ratio is constant for all concrete types, and remains constant throughout the loading history, then the generic transverse stiffness of the cylinder is directly proportional to to the elastic modulus of the concrete (E_c), which, in turn, increases with increase in concrete strength, approximately in accordance with the following equation from CAN3 A23.3 M-84, clause 8.5.1:

$$E_c = 5000\sqrt{f'_c}, \qquad [6.8]$$

where f'_c is in MPa. Therefore, the generic transverse stiffness increases approximately in accordance with $\sqrt{f'_c}$.

The effectiveness factor (or degree of confinement) v is then a function of the interaction between the generic transverse stiffness of the concrete and the restraint offered by the beam at K, i.e.

$$v = f(\sqrt{f'_c}, G_K) \qquad [6.9]$$

The nature of the interaction is demonstrated in Fig. 6.4. For a given crack width w at load level σ_{1K}, (Fig. 6.4(a)), it can be seen that a higher degree of confinement is obtained in the case of the lower strength (and less stiff) concrete. The effectiveness factor v is therefore a decreasing function of $\sqrt{f'_c}$. Furthermore, for a given concrete strength and load level σ_{1K} (Fig. 6.4(b)), the degree of confinement increases as w decreases (i.e. as G_K increases). The effectiveness factor v is therefore an increasing function of G_K.

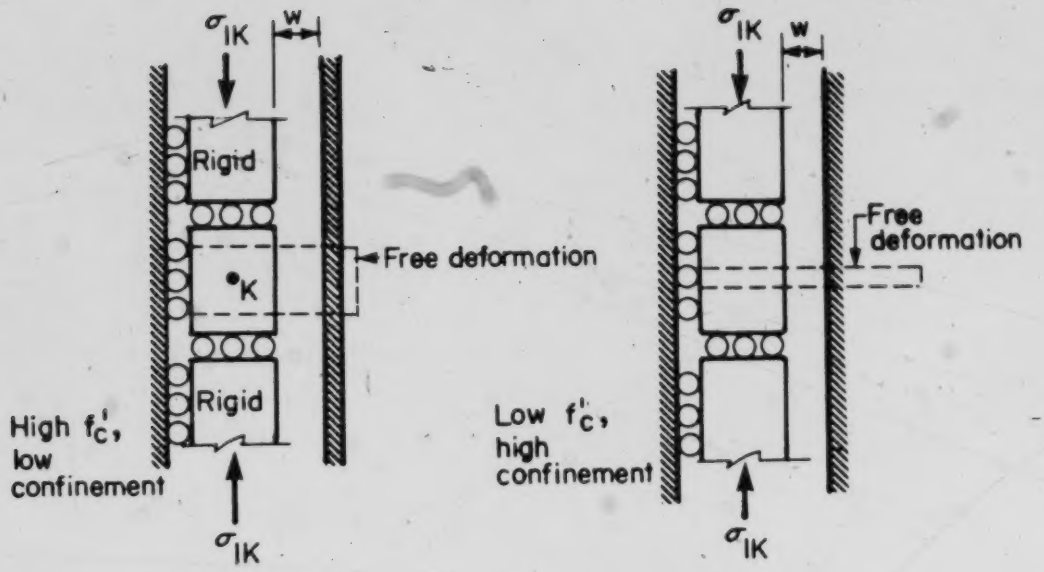

(a) Effect of f'_c (G_K constant)

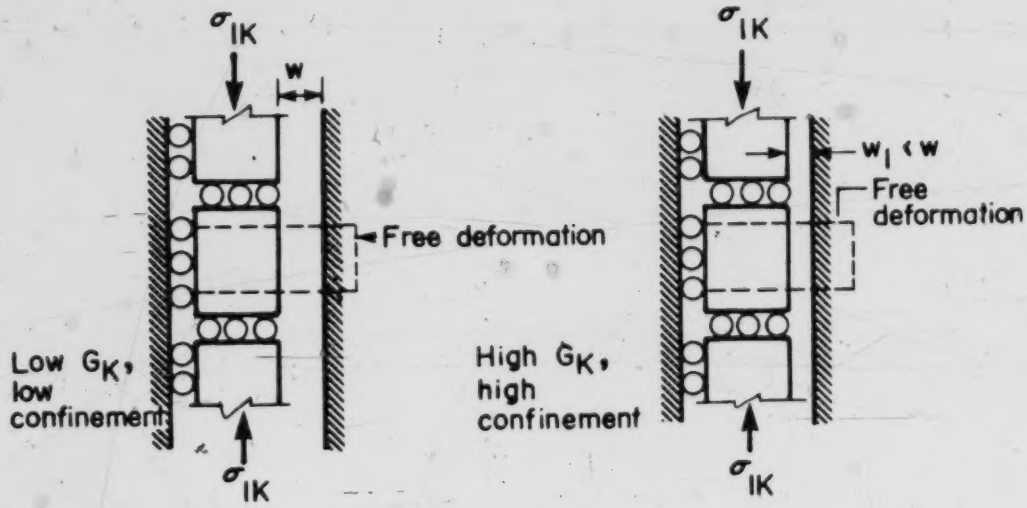

(b) Effect of G_K (f'_c constant)

Figure 6.4 Interaction between f'_c and G_K at K.

To estimate the mathematical form for equation [6.4], a regression analysis was performed on the test data using the statistical package Minitab (Ryan et al., 1985). The input values for the effectiveness factors measured in the tests (v_t) were calculated using

$$v_t = \frac{\sigma^*_{1K}}{f'_c} \qquad [6.10]$$

where f'_c is given in Chapter 3, and σ^*_{1K} is from Table 6.1. Since the confinement characteristic $G_K = \sigma_{1K}/w$ is independent of load level, it is convenient to calculate its value using the basic stress field. The concrete stress σ_{1K} is found using the techniques developed in Section 5.8. The crack width w at K can be calculated from [6.6] once the strain in the support plate ϵ_{sp} is known. This can most readily be calculated using

$$\epsilon_{sp} = \frac{T_{sp}}{E_{sp}t_{sp}} = \frac{u_c h_3}{E_{sp}t_{sp}} \qquad [6.11]$$

since $T_{sp} = u_c h_3$ (from [5.15]) and h_3 is also immediately available from the basic stress field. The calculations to generate the input data (v_t, $\sqrt{f'_c}$, G_K) for the regression analysis are given in Table 6.2.

The scatter plot for v_t against G_K is given in Figure 6.5 and suggests that the relationship between v_t and G_K is linear and increasing. The mathematical form of equation [6.9] is therefore postulated as

$$v = \frac{1}{\sqrt{f'_c}}\left[A + BG_K\right] = \frac{A}{\sqrt{f'_c}} + B\frac{G_K}{\sqrt{f'_c}}$$

where A and B are the constants to be determined from the

Table 6.2 Calculation of input data for regression analysis of υ.

	Calculation of υ_t			Calculation of G_K (from Basic Stress Field)							Regression Input		
Beam #	σ^*_{1K} (MPa)	f'_c (MPa)	$\upsilon_t = \frac{\sigma^*_{1K}}{f'_c}$	a (mm)	h_3 (mm)	E_{sp} (MPa)	t_{sp} (mm)	w (mm)	σ_{1K} (MPa)	$G_K = \frac{\sigma_{1K}}{w}$	υ_t	$\frac{1}{\sqrt{f'_c}}$	$\frac{G_K}{\sqrt{f'_c}}$
B4/1	59.64	62.9	0.948	415	44.6	218000	10.20	0.1720	35.78	208.0	0.948	0.1261	26.229
B4/2	65.76	62.4	1.054	415	44.6	202000	9.45	0.2000	35.78	178.9	1.054	0.1266	22.649
B4/3	60.36	61.3	0.985	415	44.6	202000	9.42	0.2010	35.78	178.0	0.985	0.1277	22.731
B4/4	65.94	63.3	1.042	415	44.6	218000	10.25	0.1710	35.78	209.2	1.042	0.1257	26.296
B6/1	65.12	54.5	1.194	663	44.7	211000	13.17	0.1505	32.97	219.0	1.194	0.1355	29.675
B6/5	69.93	60.2	1.161	663	44.7	211000	13.26	0.1494	32.97	220.7	1.161	0.1289	28.448
B6/6	53.58	39.5	1.357	663	44.7	211000	13.30	0.1490	32.97	221.3	1.357	0.1591	335.209
B6/7	70.79	61.3	1.155	750	46.0	211000	13.26	0.1560	43.10	276.3	1.155	0.1277	35.284
B5/1	72.55	44.6	1.627	534	47.8	211000	16.18	0.1267	35.60	281.0	1.610	0.1497	42.066
B5/2	72.98	46.3	1.576	534	47.8	211000	16.21	0.1265	35.60	281.4	1.560	0.1470	41.366
B5/3	45.85	48.7	0.941	544	47.8	219000	6.70	0.2957	35.60	120.4	0.932	0.1433	17.253
B5/4	45.39	50.8	0.894	544	47.8	219000	6.68	0.2968	35.60	119.9	0.884	0.1403	16.822
B5/5	44.60	51.7	0.863	544	47.8	219000	6.70	0.2957	35.60	120.4	0.853	0.1391	16.748

Notes

1. w is calculated from [6.6] & [6.11].
2. d = 250 mm, h_s = 50 mm, u_c = 50 MPa.
3. a, h_3 from Basic Stress Field.
4. f'_c, t_{sp} and E_{sp} from Chapter 3.
5. σ^*_{1K} from Table 6.1.

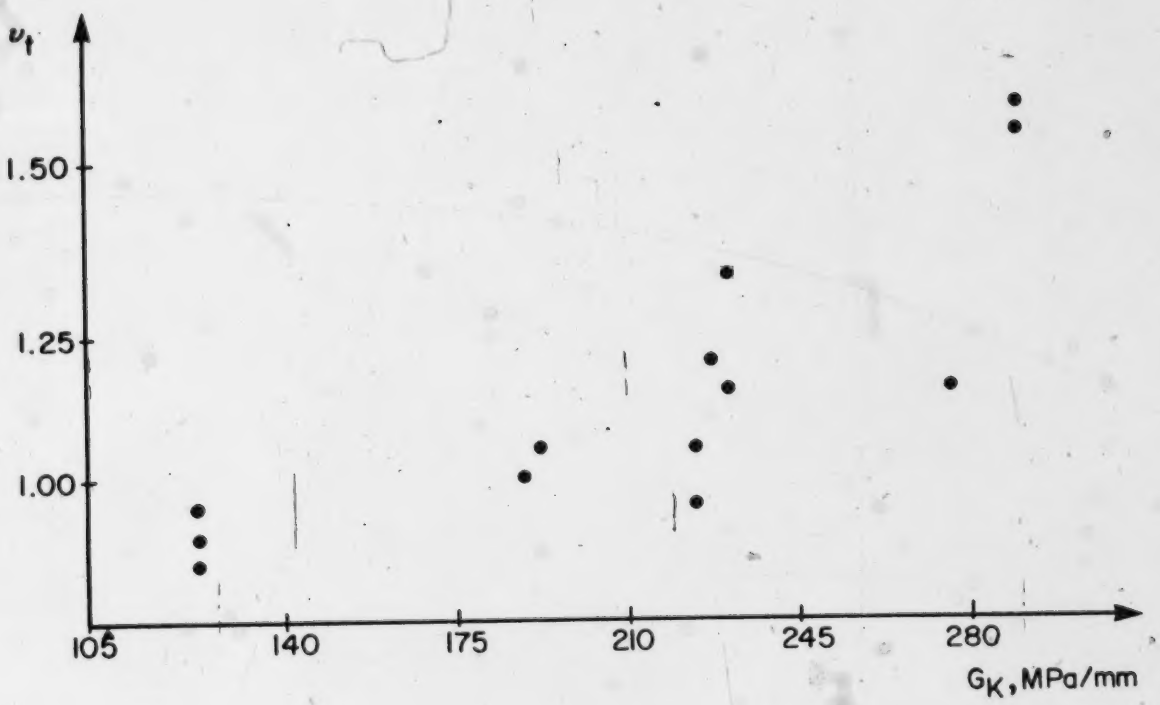

Figure 6.5 Scatter plot for the measured effectiveness factor υ_t against the confinement characteristic G_K.

linear regression analysis, using the data from Table 6.2. The results of the regression analysis are given in Appendix C, and are statistically satisfactory in all respects.

As a result of this regression analysis, the proposed expression for the effectiveness factor υ is

$$\upsilon = \frac{1}{\sqrt{f'_c}}\left[3.40 + 0.0243G_K\right] \qquad [6.12]$$

Equation [6.12] is plotted in Fig. 6.6(a), and the experimentally derived values υ_t are also shown on this figure. It is visually confirmed that the proposed expression [6.12] provides a good fit to the experimental data. Because of the linearity of the stress fields, the test-to-predicted ratios for the failure loads (p_t/p_p) can be expressed as

$$\frac{p_t}{p_p} = \frac{\upsilon_t}{\upsilon} \qquad [6.13]$$

and so the results of the regression analysis can be used directly to give test-to-predicted ratios. The results are shown in Fig. 6.6(b). The mean value is 0.998 and the standard deviation is 0.056.

Equation [6.12] was derived based on data with 40 MPa < f'_c < 65 MPa and 125 MPa/mm < G_K < 300 MPa/mm, and must be extrapolated with caution. However, an expression for the effectiveness factor υ developed by Exner (1979) is

$$\upsilon = \frac{3.2}{\sqrt{f'_c}}, \qquad [6.14]$$

and is almost identical to equation [6.12] when G_K is set equal to zero (i.e. when the contribution of the steel to providing confinement is small). This indicates that it may be possible to extrapolate [6.12] for values of G_K as low as

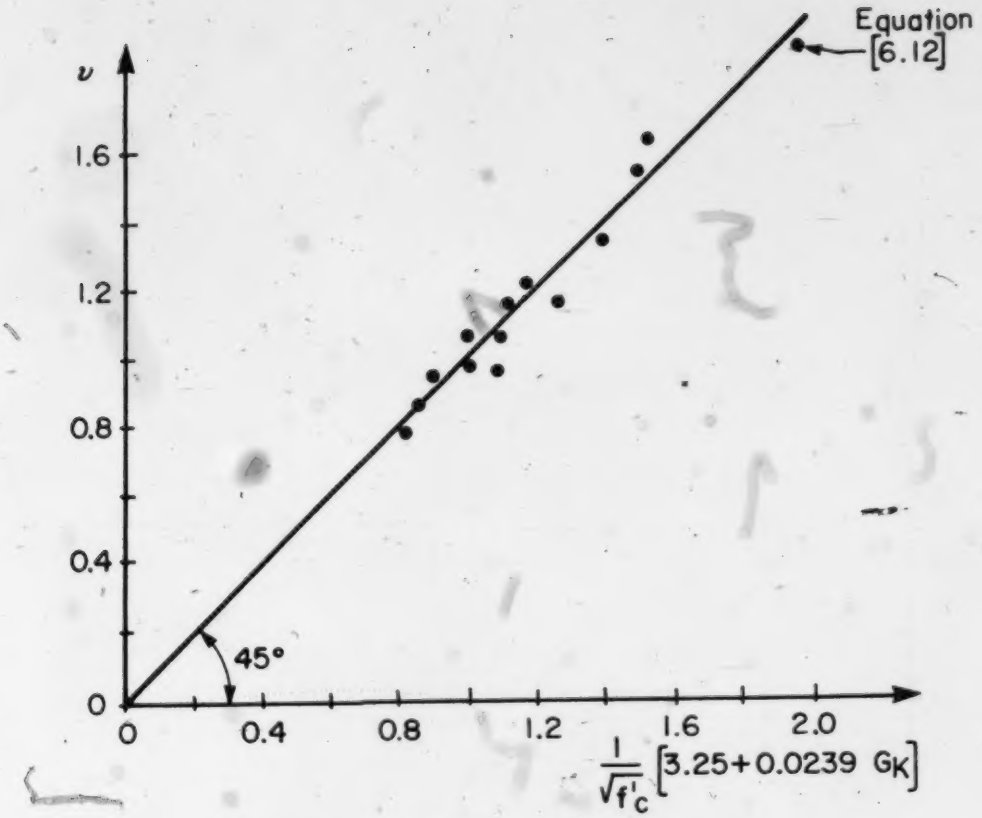

(a) Efficiency factors

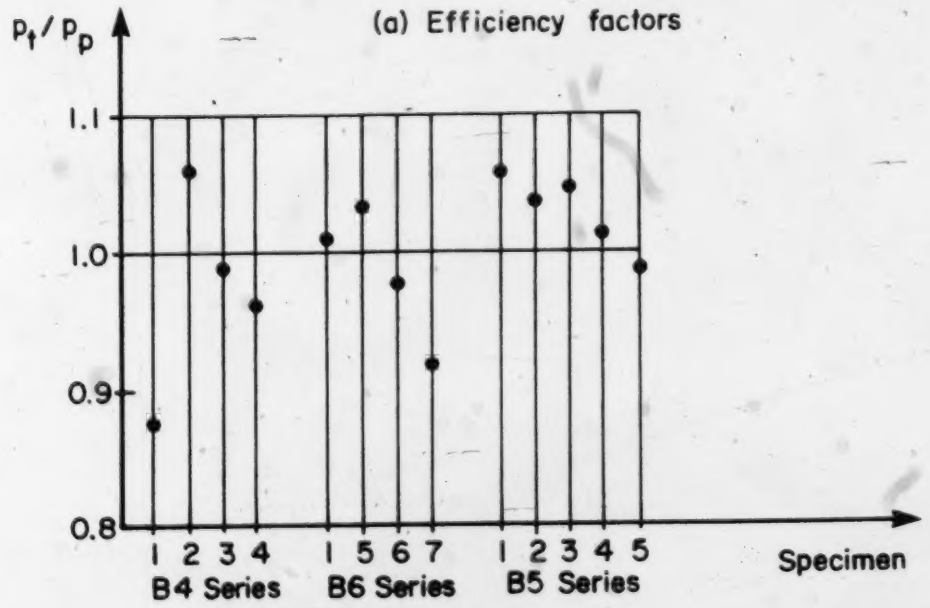

(b) Loads

Figure 6.6 Relationships between measured and predicted (a) effectiveness factors, and (b) loads, using equation [6.12].

zero, and for f'_c as low as 15 MPa. Fig 6.7 shows [6.12] plotted as υ vs. f'_c for different values of G_K. Extrapolated curves are shown as dotted curves in this figure, and Exner's equation ([6.14] is shown as the lower solid curve.

As a check on the extrapolation capabilities of [6.12], it is applied to specimen B6/2, which ultimately failed through concrete crushing even though the support plate had strain hardened at this stage (i.e. the assumption of elastic behaviour in the support plate is not satisfied). G_K is equal to 109.1 MPa/mm and f'_c is equal to 57.8 MPa for this specimen. The test-to-predicted failure load ratio is 1.09, which is surprisingly good considering the assumption made. It is therefore feasible that [6.12] may be applicable even when G_K is so low that the support plate is inelastic at failure. Since this tentative conclusion cannot be rationalised, additional experimental data are needed before it can be verified or refuted.

It can be seen from consideration of equations [6.6], [6.7] and [6.12] that the crack width w at K, and hence υ, are dependent on the dimension a, with υ decreasing as a increases. This suggests that a size effect might exist, i.e. for a given support plate strain ϵ_{sp} and concrete stress σ_{1K}, the effectiveness factor υ decreases with increase in beam size. Since data on tests for large scale composite tests are not available, equation [6.12] was used to predict the results of three single span, centrally loaded reinforced concrete deep beams which were tested by

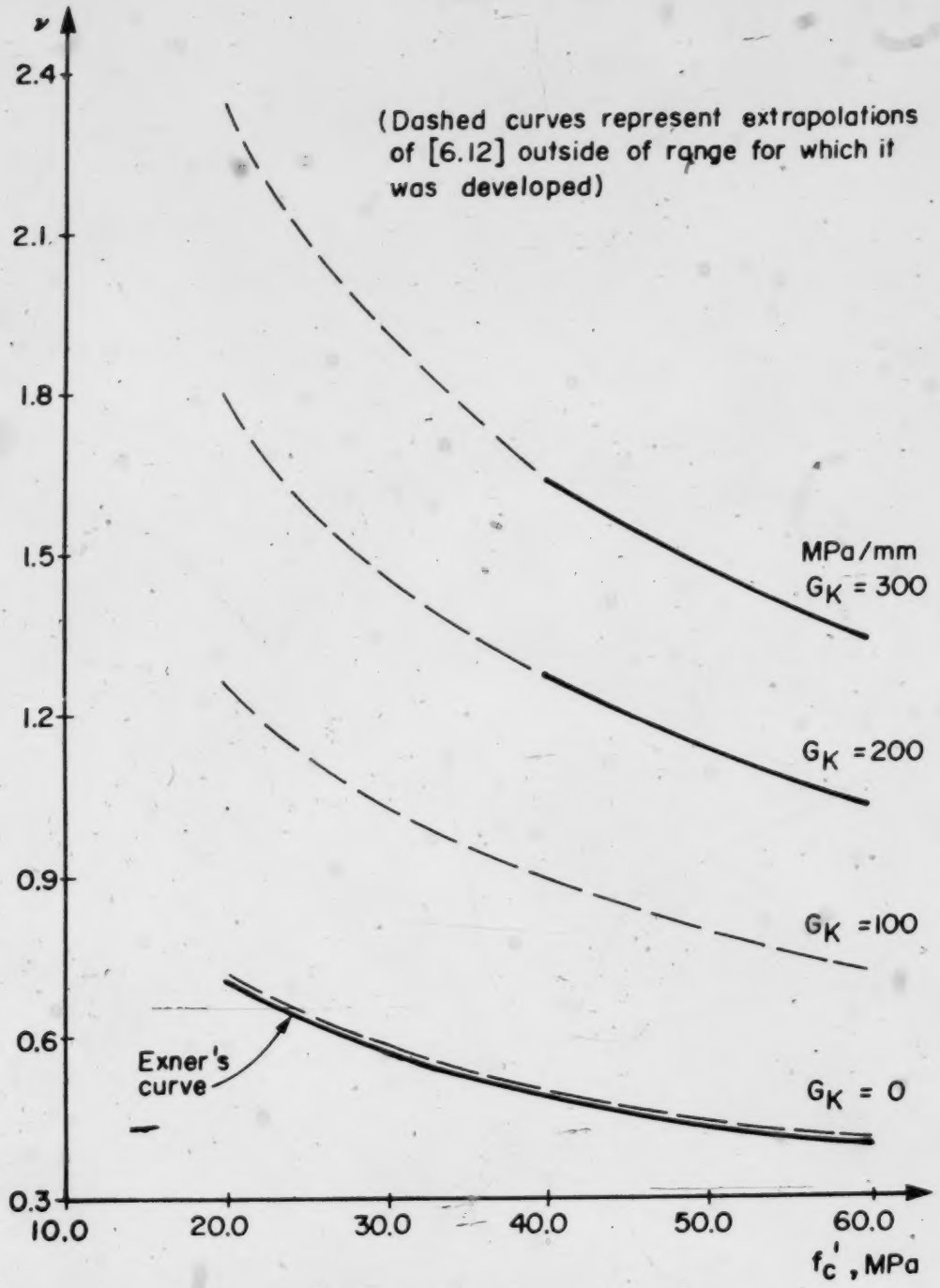

Figure 6.7 Relationship between ν and f'_c using equation [6.12].

Rogowsky and MacGregor (1983). Fig. 6.8 gives details of the beams, and shows the assumed failure location K. Basic stress fields were constructed using strut-and-tie models, as typically shown also in Fig. 6.8. Because of the large dimensions and small steel areas, the calculated values of G_K for the three beams B1/1.0, B1/1.5 and B1/2.0 were 24.0, 30.8 and 26.5 MPa/mm, respectively. These values are considerably lower than those for which equation [6.12] was developed. In addition, f'_c was equal to 26.1 MPa for beam B1/1.0, which is also outside of the development range of [6.12]. Nevertheless, the test-to-predicted failure load ratios for the three beams are 1.254, 0.800 and 0.867. These are considered to be reasonably good predictions, and indicate that the suggested size effect may actually exist.

In summary, equation [6.12] seems to give accurate predictions of failure loads over a wide range of values for f'_c and G_K, but more test data are neeeded to substantiate this conclusion. The estimate for the effectiveness factor υ is formally summarised as follows:

$$\upsilon = \frac{1}{\sqrt{f'_c}}\left[3.40 + 0.0243 G_K\right], \qquad [6.12]$$

where

f'_c = concrete cylinder strength (MPa)

$G_K = \frac{\sigma_{1K}}{w}$

= confinement characteristic (MPa/mm)

σ_{1K} = uniaxial stress (MPa) at location K determined from the basic stress field.

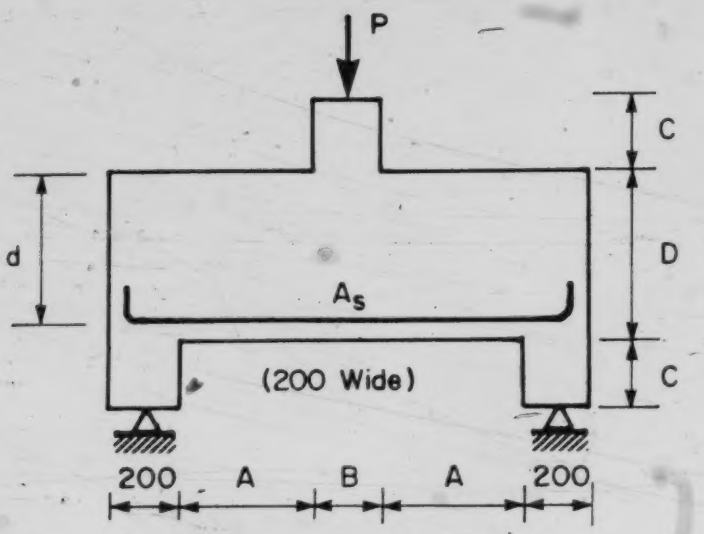

(Minimum stirrups ignored)

	Geometry (mm)					Materials				Load
Beam	A	B	C	D	d	A_s (mm^2)	F_y (MPa)	E_s (MPa)	f'_c (MPa)	P (kN)
B 1/1.0	750	300	450	1000	950	1800	380	200000	26.1	1204
B 1/1.5	750	300	300	600	535	1200	455	200000	42.4	606
B 1/2.0	800	200	300	500	455	800	455	200000	43.2	354

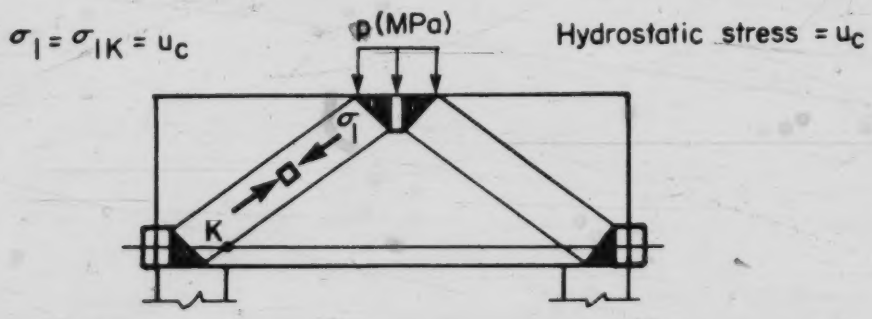

Typical basic stress field using strut-and-tie model

Figure 6.8 Details of beams B1/1.0, B1/1.5 and B1/2.0 as tested by Rogowsky (1983).

w= Crack width (mm) at K at load σ_{1K}

$$= \frac{T_{sp}a[1-(h_s/d)]}{E_{sp}t_{sp}\sqrt{1+(a/d)^2}}$$

T_{sp}= tension in unit width of support plate(N) at load σ_{1K}

= $h_3 u_c$ (from [5.15])

a= horizontal projection of critical crack length (mm)

h_s= height of stud(mm)

d= depth of concrete core (mm)

E_{sp}= elastic modulus of support plate (MPa)

t_{sp}= thickness of support plate (mm).

6.5 Summary of Analytical Procedure

In this procedure, the multiplier M which scaled the basic stress field to a stress field corresponding to the measured failure load p_t in [6.1] and [6.2] is redefined as the multiplier M which scales the basic stress field to the predicted stress field at failure, i.e.

$$M = \frac{p_p}{p}. \qquad [6.15]$$

The analytical procedure can then be summarised as follows.

1. Choose the section geometry, plate thicknesses and loading pattern.
2. Construct a basic stress field (say, using u_c=50 MPa) as detailed in Chapter 5, and find the corresponding applied load p. Calculate G_K, using σ_{1K} and h_3 which are

available from the basic stress field.

3. Calculate υ from equation [6.12].

4. Since $M\sigma_{1K} = \sigma^{*}_{1K} = f^{*}_{c} = \upsilon f'_{c}$, calculate M using

$$M = \frac{\upsilon f'_{c}}{\sigma_{1k}} \qquad [6.16]$$

5. Calculate the predicted failure load p_p (MPa) using [6.15] which is rearranged to give

$$p_p = Mp \qquad [6.17]$$

6. To ensure that [6.12] is valid, check that the support plate remains elastic at failure of the concrete, i.e.

$$Mu_c h_3 < t_{sp} F_{y,sp} \qquad [6.18]$$

6.6 Comparisons of observed failure loads with those predicted by other theories

6.6.1 CAN3 A23.3 - M84, General Method

The compression field approach allowed by CAN3 A23.3 - M84 "Design of Concrete Structures for Buildings", Clause 11.4.2.3., states that the diagonal crushing strength of concrete, $f_{2\ max}$, may be computed as

$$f_{2\ max} = \lambda \phi_c \frac{f'_c}{(0.8 + 170\epsilon_1)} \qquad [6.19]$$

where

λ = 1.0 for normal weight concrete

ϕ_c = performance factor for concrete = 0.6

f'_c = specified concrete strength (MPa)

ϵ_1 = principal tensile strain.

This equation is based on the experimental work of Vecchio and Collins (1982). It is rewritten here as

$$f_c^* = \upsilon_{vc} f_c$$

where

$$\upsilon_{vc} = \frac{1}{0.8 + 170\epsilon_2} \qquad [6.20]$$

= effectiveness factor according to Vecchio and Collins

and

ϵ_2 = principal tensile strain (positive) at failure.

Demec rosettes were located close to the failure location K in the B6 and B5 series (see Figs. 3.15 - 3.16), and so estimates of ϵ_2 at K at failure could be made. Even though two rosettes were available for each specimen, only one gave reliable results in each case. Unfortunately, no such rosettes were available for the B4 series (see Fig. 3.14).

Plots of principal tensile strain in the concrete near K vs. the applied load p (MPa) for the B6 and B5 series are given in Fig. 6.9. The principal strains were calculated using program DEMSTR (see Chapter 4). The dashed portions of these curves indicate extrapolations which were used to estimate ϵ_2 at the failure loads. The extrapolated values for ϵ_2 are used to calculate υ_{vc} from [6.20], and test-to-predicted ratios for the Vecchio/Collins theory are then calculated using a modified version of [6.13] i.e.

$$\frac{p_t}{p_p} = \frac{\upsilon_t}{\upsilon_{vc}}.$$

The results are shown in Fig. 6.10. They are good for the B6 series, but they are less satisfactory for the B5 series. This result is by no means a reflection of any innacuracy in

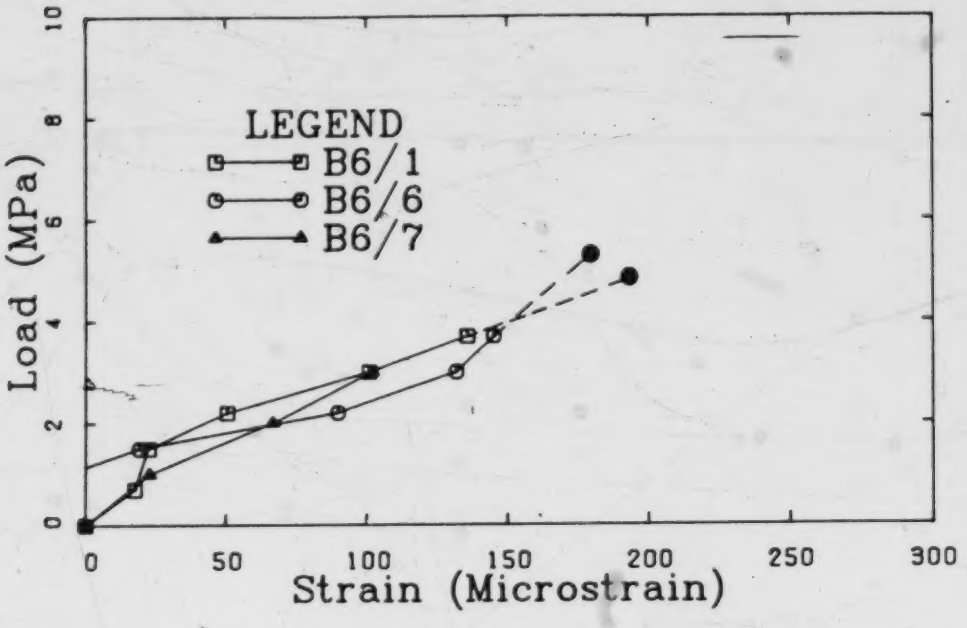

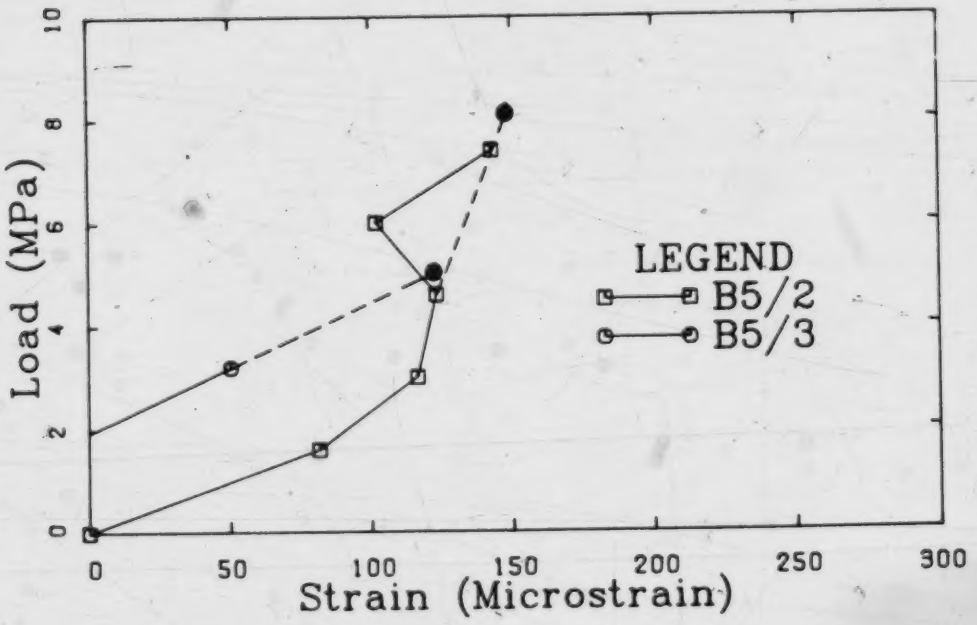

Figure 6.9 Measured principal strain in the concrete near K .vs. the applied load p (MPa) for the B6 and B5 series.

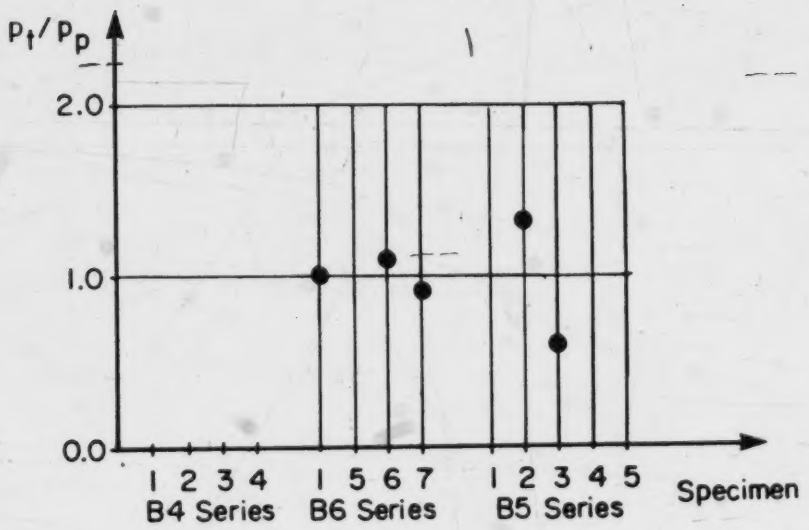

Figure 6.10 Test-to-predicted ratios for failure load using the CAN3 A23.3 M-84 General Method.

the Vecchio and Collins equation ([6.19]). Rather, it is a reflection in the method in which it is applied here. Equation [6.19] was derived from the results of tests performed on reinforced concrete panels subjected to homogeneous strain fields. Since strain gradients did not exist, arbitrarily large gauge lengths could be used to measure strain, and the effect of cracking across the gauge length was smeared. Indeed, in CAN3 A23.3 - M84, the use of [6.19] is allowed only for compression fields in which homogeneous strain conditions are assumed. However, large strain gradients exist across a 50.8 mm gauge length near location "K" (as indicated in Chapter 4), and it is unreasonable to smear cracks over such a short gauge length. Therefore, it is not proper to apply [6.20] in this case, and this fact is reflected in the results in Fig. 6.10.

The code discussion of the General Method also proposes a stress field and allowable concrete stresses for uniformly loaded reinforced concrete deep beams (Fig. 6.11). However, this method should not be applied to the analysis of the composite specimens reported here, since the reinforcement is external.

6.6.2 CAN3 A23.3 - M84 Simplified Method

According to the simplified method in the Canadian Code, the shear capacity of a rectangular member is given by

$$V_c = 0.2\phi_c\lambda\sqrt{f'_c}\,bd \qquad [6.21]$$

where

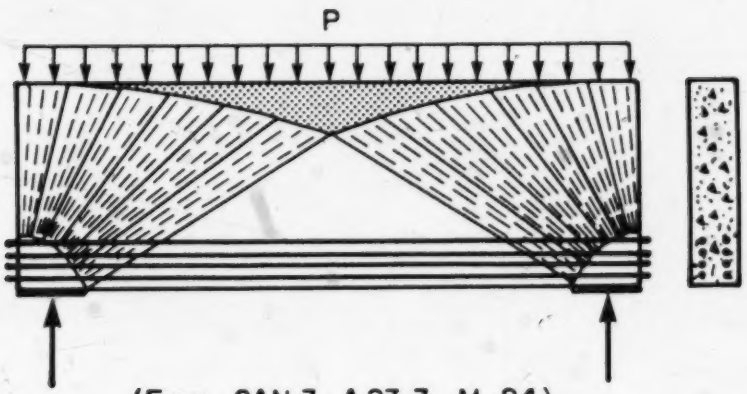

(From CAN 3-A 23.3 M-84)

Figure 6.11 Stress field for a uniformly loaded simply supported reinforced concrete deep beam according to the CAN3 A23.3 M-84 General Method.

ϕ_c= performance factor for concrete = 0.6

λ= 1.0 for normal weight concrete

f'_c= specified concrete strength (MPa)

b= width of section (mm)

d= effective depth of section (mm)

In this case, ϕ_c is set equal to unity, and "d" is taken as the depth of the concrete core. Then

$$V_c = 0.2\times1.0\times1.0\times\sqrt{f'_c}\times375.0\times250.0\times10^{-3}\ \text{kN}$$

$$= 18.75\sqrt{f'_c}\ \text{kN}.$$

The critical shear force V_t is taken as being equal to the maximum shear force at a distance "d" from the face of the support. This method, then, predicts failure on the short shear span in specimen B6/7. In the test, such a failure was not observed.

Using the above approach, the test-to-predicted ratios are

$$\frac{P_t}{P_p} = \frac{V_t}{V_c} \qquad [6.22]$$

and are shown in Fig. 6.12. It is obvious that the simplified method is grossly conservative in this case. Indeed, the Canadian Code recognises this fact in Clause 11.5 which states that the General Method should be used "for those parts of members in which

(a) the distance from the point of zero shear to the face of the support is less than 2d; or

(b) a load causing more than 50% of the shear at a support is located less than 2d from the support."

All of the specimens in this testing program are governed by

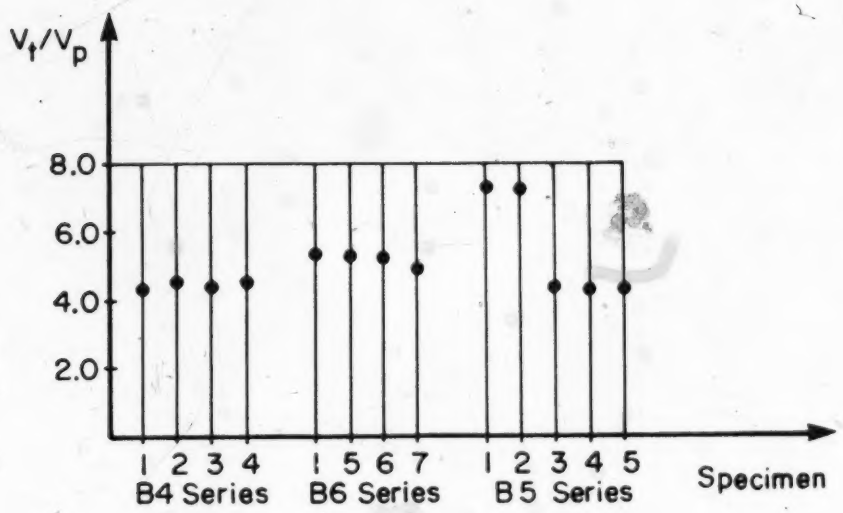

Figure 6.12 Test-to-predicted failure load ratios using the CAN3 A23.3 M-84 Simplified Method.

this requirement, and so the Simplified Method cannot be applied.

6.6.3 Niwa's Equation

An equation to predict the shear capacity of the concrete in deep reinforced concrete beams without transverse reinforcement has been proposed by Niwa (1984). The form of the equation was derived from finite element analysis, and the proportionality constant was found through calibration with published data and a subsequent series of tests. The equation is

$$V_c = \frac{K f_c'^{0.667} bd[1+3.33(r/d)](1+\sqrt{\rho})}{1+(a/d)^2} \qquad [6.23]$$

where

V_c= shear capacity of concrete (kN)

K= a constant, 2.4×10^{-4}

f_c'= specified concrete strength (MPa)

b= width of beam (mm)

d= effective depth (mm)

r= width of support(mm)

ρ= reinforcement ratio (%)

a= shear span (mm).

This equation was derived for beams subjected to symmetrically applied discrete point loads, in which case the shear span "a" is well defined. The shear span is not so readily defined for uniformly loaded beams. For the purpose of this comparison, however, the shear span is taken to be the horizontal projection "a" of the assumed critical crack,

as indicated in Fig 6.3. The applied shear, V_t, is defined as in Section 6.6.1., (i.e. at a distance "d" from the face of the support). For specimen B6/7, V_t was calculated for the long shear span, since failure occurred in this span. The reinforcement ratio ρ is defined as

$$\rho = \frac{100 t_{sp}}{d} \qquad [6.24]$$

where t_{sp} is the thickness of the support plate.

The results of the comparison are given in Fig. 6.13. It is seen that the results are good for the B6 and B5 series, but are very poor for the B4 series. The explanation lies in the definition for V_t. The choice of V_t at a distance "d" from the inside face of the support is quite arbitrary for deep sections. Indeed, for $l/d = 2.0$, $V_t = 0$ under this condition. The accuracy of the assumption improves as the member becomes shallower.

6.7 Comparison of Measured and Predicted Steel Strains

6.7.1 Loaded Plate

In section 5.6, it was shown that the shear stress, τ, at any point on the steel/concrete interface of the loaded surface is given by

$$\tau = p \mathrm{Tan}\theta \qquad [5.17]$$

where p is the applied normal load (MPa) and θ is defined in Fig. 5.13(a). It was also shown that it is reasonable to assume a linear variation in shear stress between locations at which the shear stress is known.

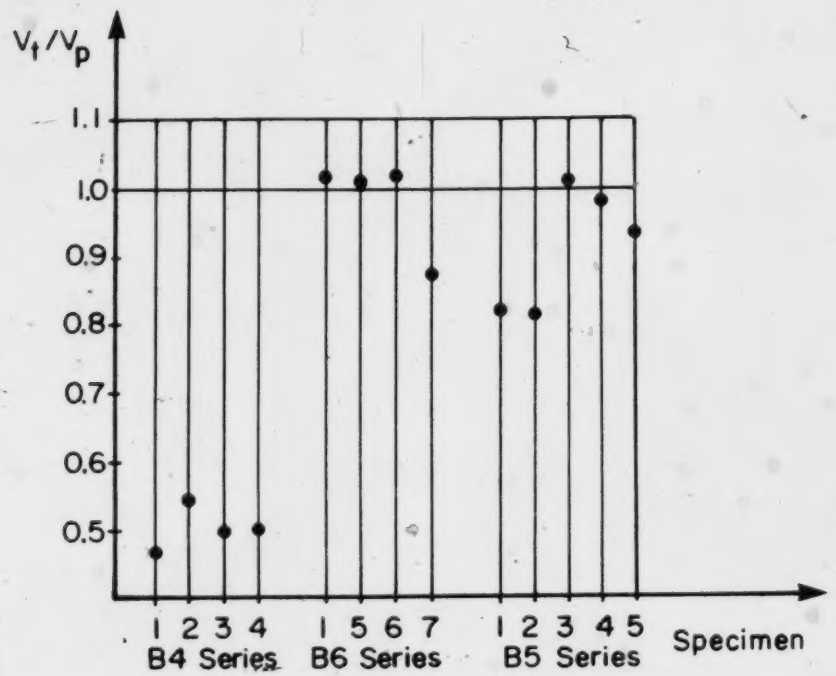

Figure 6.13 Test-to-predicted failure load ratios using Niwa's equation.

With reference to Fig. 5.13(a) and Fig. 5.6(b), the theoretical shear profile at the interface for a specimen with uniformly distributed loading is as shown in Fig. 6.14(a). The situation for a patch load is shown in Fig. 6.14(b). The sign convention assumes that positive shear causes clockwise rotation. These shear profiles are equilibrated by equal and opposite shear stresses on the steel plates, as also shown in Fig. 6.14. The steel strain in the loaded plate at any distance "x" from the cantilever tip is calculated using

$$\varepsilon_{1p}(x) = \frac{1}{E_{1p}t_{1p}} \int_0^x \tau(x)\, dx \qquad [6.25]$$

as indicated in Fig. 6.15. For a linear shear distribution, the integration can be conveniently performed numerically using the trapezoidal rule.

Fig 6.16 shows the predicted and measured strain distributions at failure in the loaded plates of specimens B4/1, B6/1 and B5/1. The measured strains were obtained from the gauges located at the mid-width of the plate. Increments of 100 mm were used for the numerical integration. With the exception of specimen B5/1, the predicted shapes of the strain distributions agree with those which were measured. The peaks in the strain distribution for B5/1 (indicated by "P" in Fig. 6.16) can be explained with reference to Fig. 6.17(a), which shows the locations of the gauges relative to the loading devices and the stud connectors. The gauges which correspond to the peaks in Fig. 6.16 are also indicated by "P" in this figure. The clamping action of the

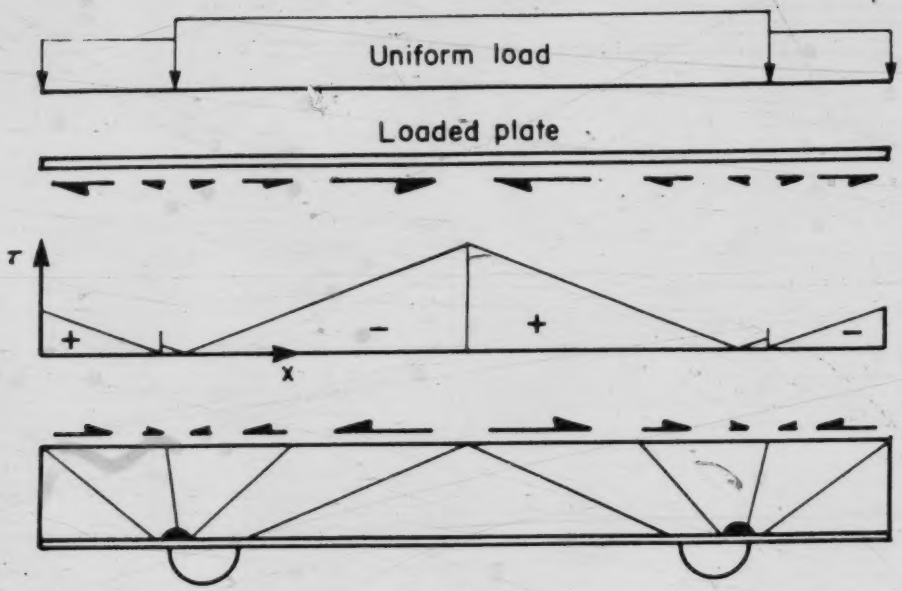

(a)

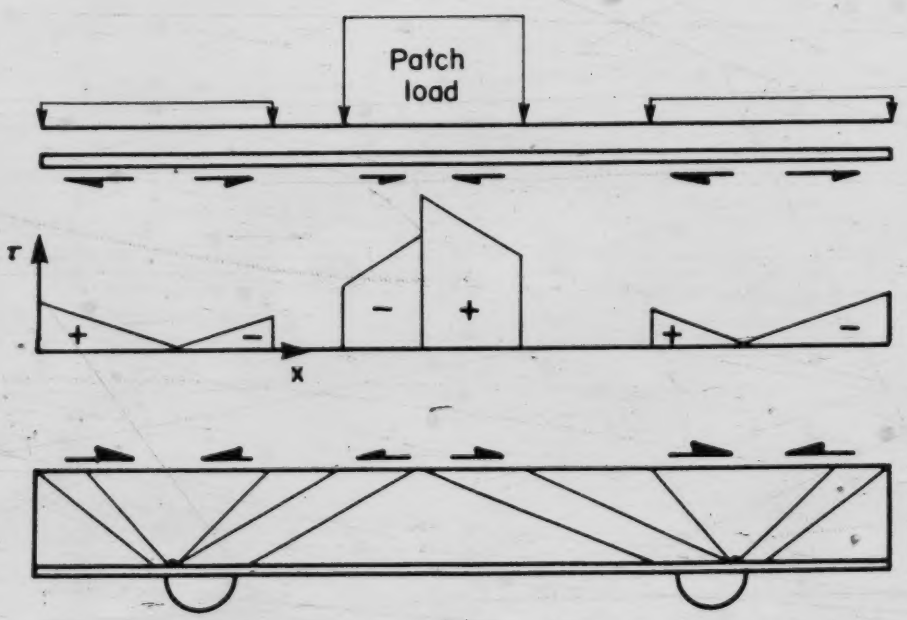

(b)

Figure 6.14 Theoretical shear stress distribution at the loaded plate/concrete core interface of a continuous composite beam.

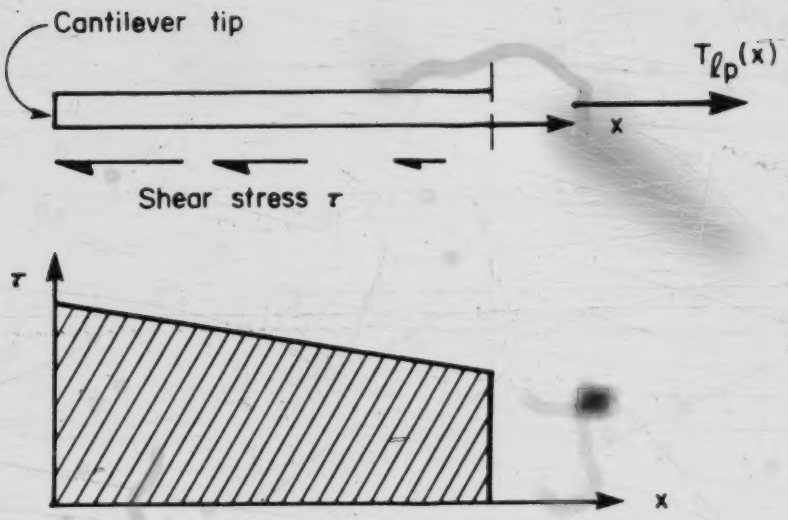

$T_{\ell p}(x)$ = Shaded area

$$\epsilon_{\ell p}(x) = \frac{T_{\ell p}}{E_{\ell p} t_{\ell p}}$$

Figure 6.15 Calculation of $\epsilon_{1p}(x)$.

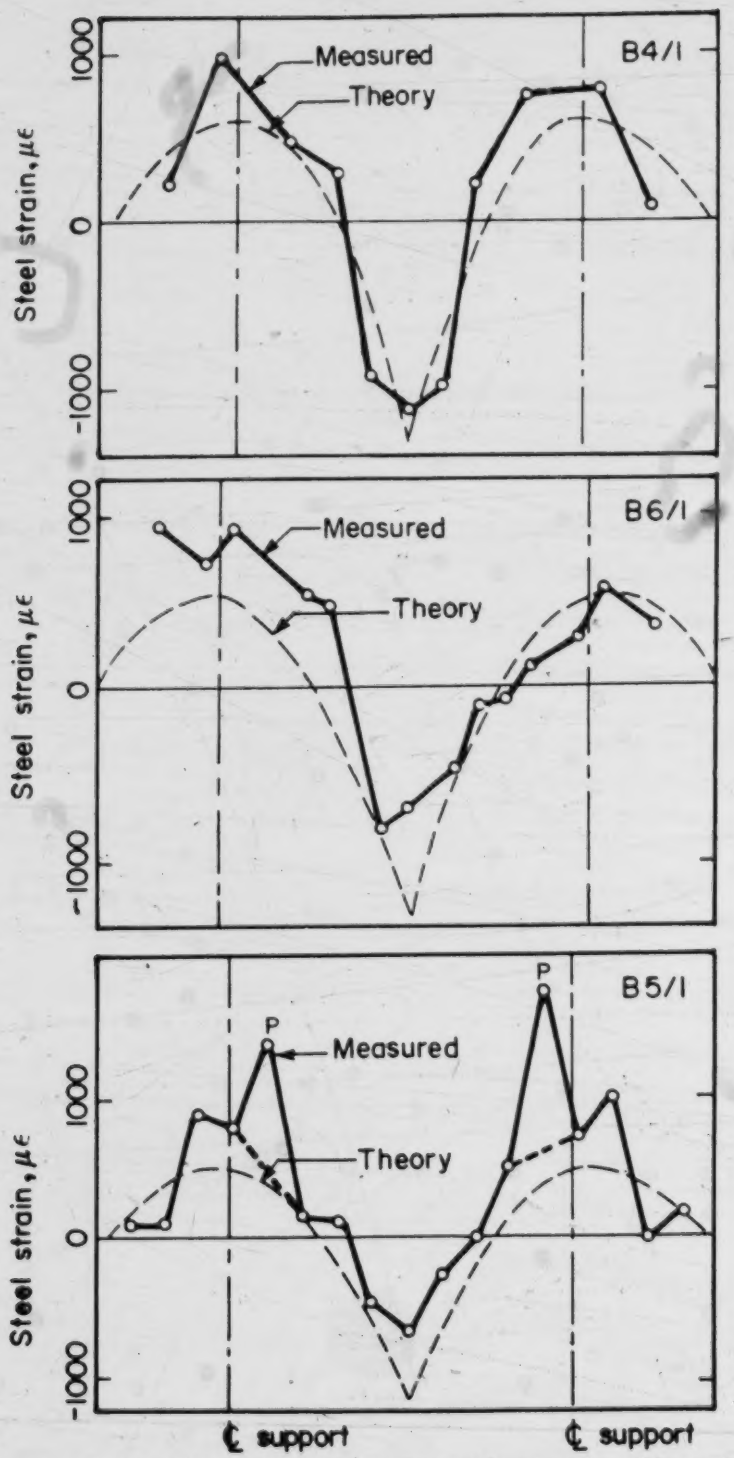

Figure 6.16 Predicted and measured strain distributions at failure in the loaded plates of the uniformly loaded specimens B4/1, B6/1 and B5/1.

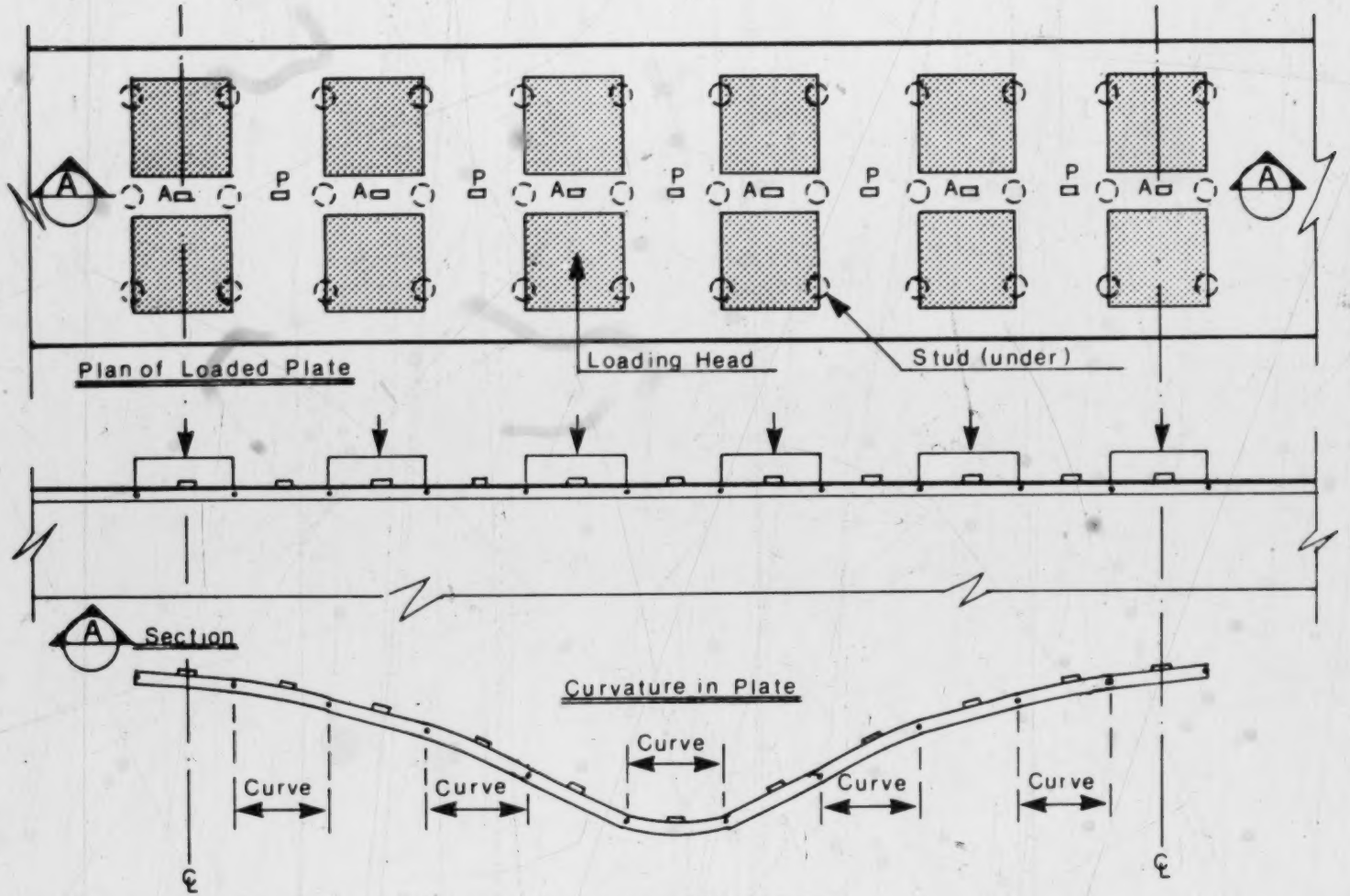

Figure 6.17 Explanation for the peak strains which were observed in the loaded plate of specimen B5/1.

loading devices inhibits curvature in the loaded plate at gauge locations "A", and the strains measured by these gauges are essentially free of bending effects. Curvature in the beam must then be concentrated in the vicinities of the gauges "P", and the strains measured from these gauges may include a curvature component (Fig. 6.17(b)). If the gauges "P" are ignored, then the shape indicated by the dotted line in Fig. 6.16 is also in agreement with that which is predicted.

Two significant differences between the predicted and measured strains can be observed from Fig. 6.16. Firstly, the measured tensile strains are higher than those which are predicted. The difference is mainly attributed to the fact that the average longitudinal strain across the width of the plate is approximately 0.9 times the strain measured at the midwidth of the plate, as shown in Section 4.6.3. Secondly, the predicted compressive strain at midspan is larger than that which is observed. The primary reason is that the concrete compressive zone at midspan is ignored in the analytical model, as explained in Section 5.4.4.

The measured and predicted strain distributions in the loaded plate of the patch loaded specimen (B6/7) are given in Fig. 6.18. It is seen that agreement is very poor over the "stress-free-zones", and a detailed investigation is warranted to explain the discrepancy. Fig. 6.19 shows the measured strain distributions in the loaded plate at load levels 3.0, 4.0, 4.5 and 5.0 MPa (i.e. at 0.55, 0.74, 0.83

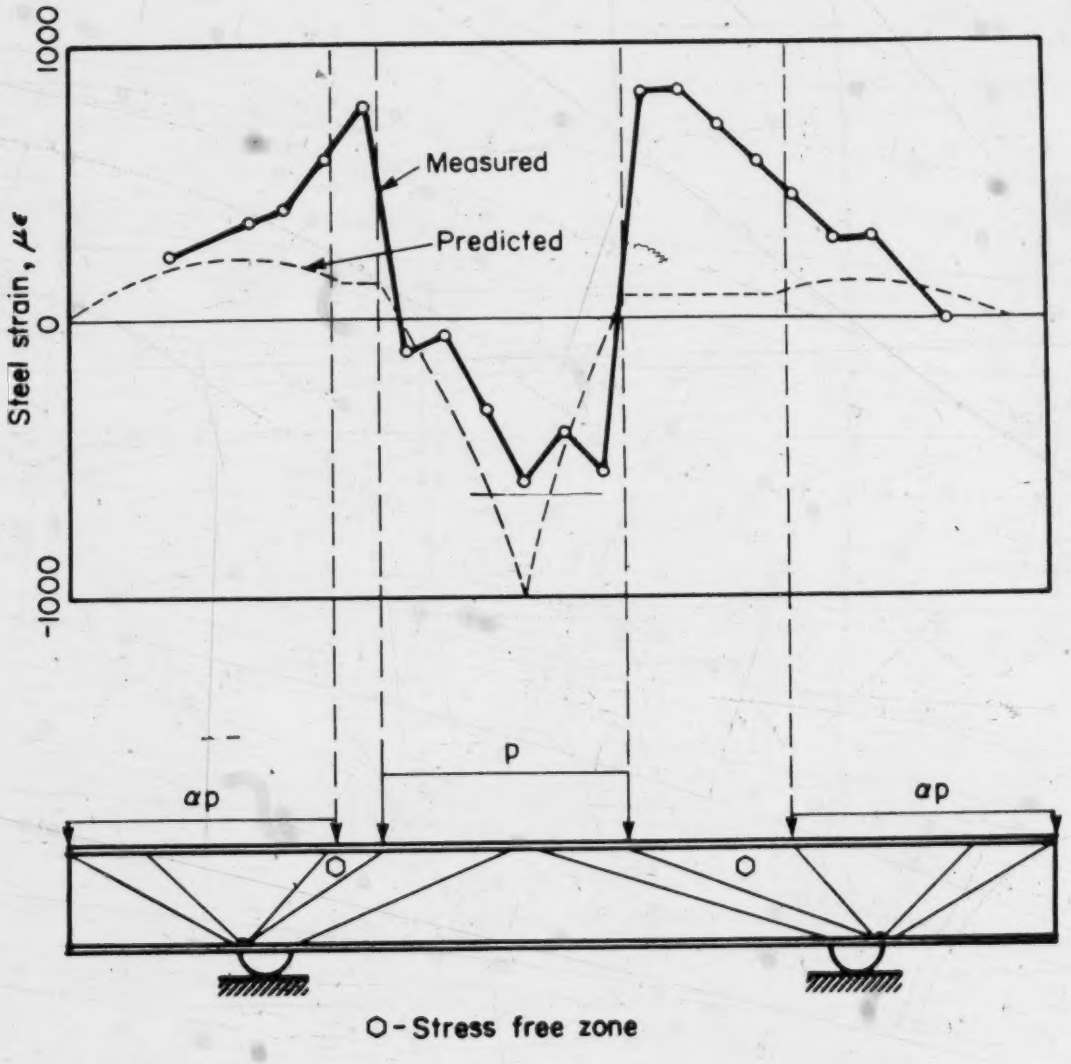

Figure 6.18 Predicted and measured strain distributions in the loaded plate of the patch-loaded specimen B6/7 at failure.

and 0.92 times the failure load, respectively). With reference to the strain distribution over the "stress-free-zone" on the right-hand side, it is seen that an abrupt change of shape occurred between load levels 4.5 MPa and 5.0 MPa. The change occurred almost immediately after the formation (at 4.4 MPa) of the cracks in the "stress-free-zone". (These cracks can be observed in Plate 4.8). An equivalent change of shape (albeit not as abrupt) can also be observed for the strain distribution over the "stress-free-zone" at the left-hand side. This change occurred between load levels 4.0 MPa and 4.5 MPa, and the test records indicate that cracks formed in this region at 3.8 MPa. The change of shape of the strain distribution may therefore be related to the formation of these cracks, as explained qualitatively for the right-hand side "stress-free-zone" hereunder and in Fig. 6.20.

In the analytical model, it is assumed that slip takes place between the steel plate and the concrete in the stress-free zone, since the steel plate is strained but the concrete is not (Fig 6.20(a)). This strain discontinuity is not possible because of the mechanical interaction at the interface and the limited plastic capabilities of concrete (i.e. the ductility requirement of the lower-bound theorem is not satisfied). Equal and opposite shear stresses may be required in this region to force compatibility at the interface. These are designated as compatibility shear stresses in Fig. 6.20(b), and would be responsible for

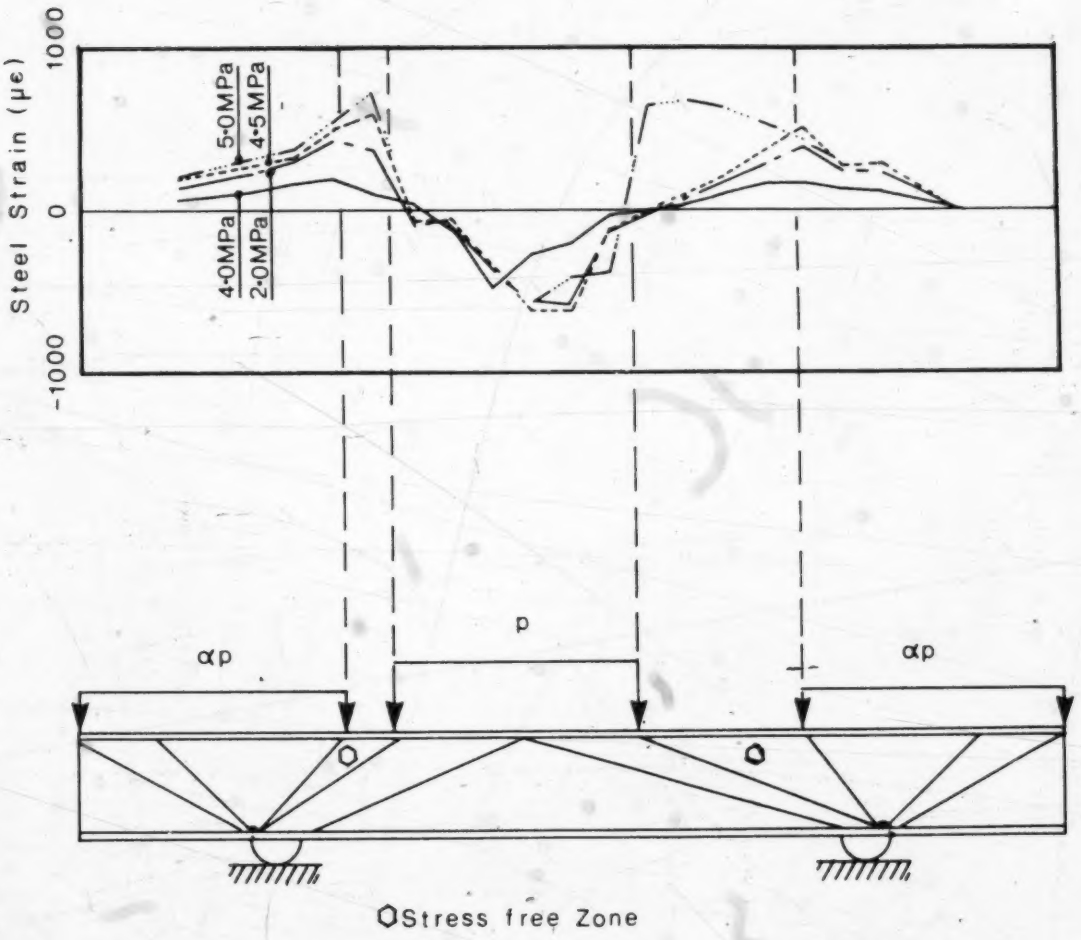

Figure 6.19 Measured strain distributions in the loaded plate of specimen B6/7 at various load levels.

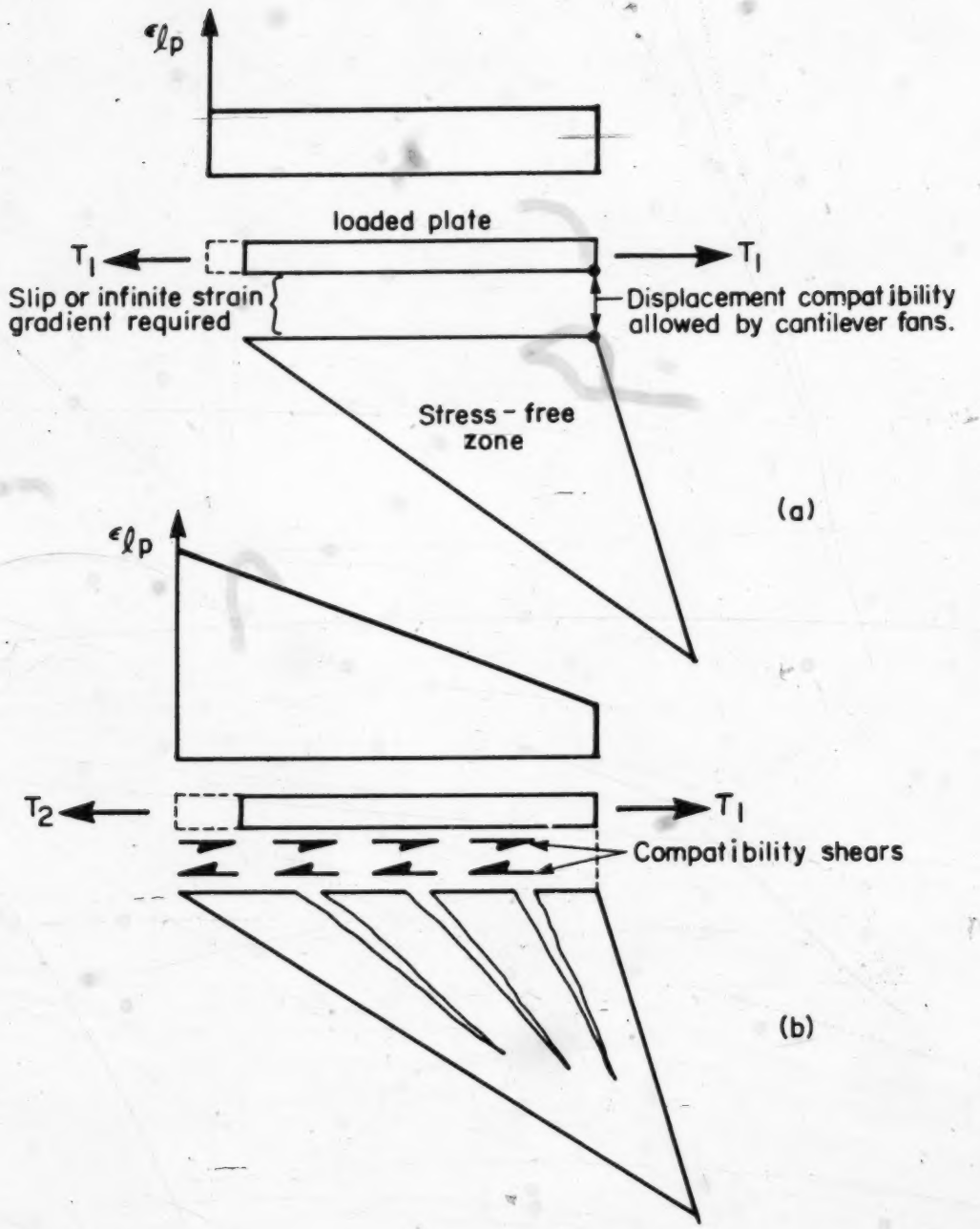

Figure 6.20 Compatibility shear stresses in specimen B6/7.

additional tensile strains in the plate.

It is clear that the analytical model for a patch-loaded specimen does not accurately describe the strain distribution in the loaded plate. Fortunately, it can still be used to predict the failure load for the specimen, since the concrete in the "tied-arch" which is used to transfer the patch load to the supports is essentially independent of the "stress-free-zones". Nevertheless, the poor (and unsafe) prediction of the strains in the loaded plate is cause for concern, and could be further investigated by future laboratory testing.

6.7.2 Support Plate

The measured and predicted strain distributions in the support plates of specimens B4/1, B6/1, B6/7 and B5/1 are given in Fig. 6.21. The solid squares in this figure represent average strains as indicated in Section 4.3.1. The predicted strains at failure were calculated using

$$\epsilon_{sp} = \frac{u_c^* h_3}{E_{sp} t_{sp}},$$

which is derived from Equation [5.15]. Tied-arch behaviour (i.e. constant strain) is confirmed in this figure, despite some differences between predicted and measured average strains.

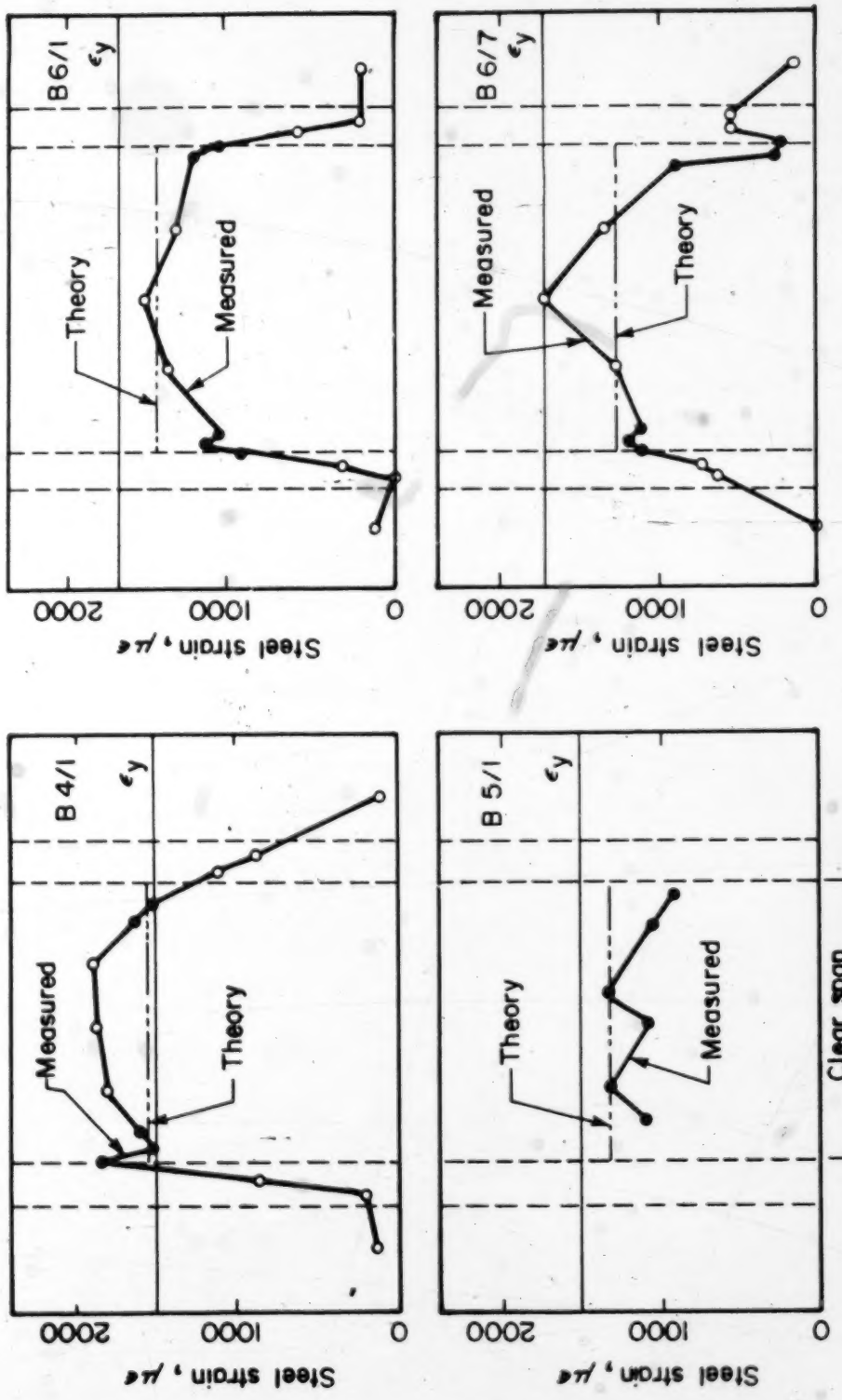

Figure 6.21 Predicted and measured strain distributions in the support plates of specimens B4/1, B6/1, B6/7 and B5/1.

7. CONCLUSIONS AND RECOMMENDATIONS

7.1 Introduction

In accordance with the philosophy of limit states design, several limit states can be identified for composite ice-resisting walls in Arctic offshore structures. The main serviceability limit states which have been identified are:

1. Degeneration of the concrete core by the effect of thermal gradients through the thickness of the wall (Clarke and Symmons, 1979).
2. Excessive vibration of the wall when it is subjected to periodic loads (Gerwick and Berner, 1987).
3. External deflection of the wall when it is subjected to frequently-encountered loads.
4. Corrosion and abrasion of the external steel skin.

Ultimate limit states are concerned with the behaviour of the wall when it has reached its maximum load-carrying capacity. Ultimate limit states which have been identified for composite ice-resisting walls include:

1. Loss of composite action between the steel plates and the concrete core.
2. Local buckling of the loaded plate between shear connectors (Matsuishi et al., 1977).
3. Fracture of the steel plate in tension (underreinforced failure).
4. Loss of load-carrying capacity of the concrete core (overreinforced failure).

Post-ultimate limit states can also be considered, since it has been shown in Figs. 4.1-4.5 and in Table 4.2 that even overreinforced walls may possess significant capacity for energy absorption after the concrete has failed. These limit states may be important under the action of an extreme ice event.

The work described herein has been primarily concerned with ultimate limit state No.4 above, i.e. examination of the ultimate behaviour of overreinforced composite ice-resisting walls. In particular, a method has been developed which predicts the strength of these walls.

7.2 Conclusions

7.2.1 General

1. Composite ice-resisting walls with span-to-depth ratios varying from 3 to 5 can withstand external pressures in the range of 1.0 MPa to 10.0 MPa.
2. Assuming there are adequate shear connectors, the capacity of an individual wall configuration is a function of the span-to-depth ratio, the concrete strength, the size and mechanical properties of the steel plates, and the loading.

7.2.2 Construction Details.

1. The type of shear connector used to provide composite action between the steel plates and the concrete core had no apparent effect on the failure load of the composite beams which were tested. Even though flexural cracks initiate earlier when plate connectors are used (as opposed to stud connectors), this is deemed to be of little practical consequence.
2. Stiffened plate bulkheads should be designed to take into account both the effect of the stiffener spacing on the concrete in the support area of the composite wall and the effect of the stiffener spacing on the strength and stability of the bulkhead itself. The effect of inappropriately-spaced stiffeners may be to initiate local degeneration of the concrete near the stiffeners at a load level which is significantly lower than the maximum load for the wall. Furthermore, this degeneration may ultimately lead to a reduction in the load-carrying capacity of the wall when it is subjected to cyclic loading.
3. The inclusion of diaphragm plates at the supports seems to have no apparent effect on the strength of the wall.
4. The addition of shear connectors on the support plate between the points where the wall is supported affects the crack pattern but does not have a significant effect on the strength of the wall.

5. The use of a higher strength concrete does not provide a proportionate increase in the load-carrying capacity of the wall. Rather, the tests indicated that the capacity increases only with $\sqrt{f'_c}$.
6. Data on the use of steel-fibre-reinforced concrete in composite ice-resisting walls are limited, but the preliminary results are encouraging. Of the five specimens which were designed to give a ductile failure (B6/2, B6/4, B5/3, B5/4, B5/5), the only specimen which did not ultimately fail by crushing of the concrete used steel-fibre-reinforced concrete. Furthermore, since ice-loading on offshore structures is essentially an energy-absorption phenemenon, the toughness characteristics of SFRC may be advantageous. The unit cost of SFRC is approximately twice that for a conventional plain concrete mix. However, this increase in cost may be small in comparison with the total cost of the structure.

7.2.3 Fan-type Stress Fields.

1. For the uniformly loaded composite specimens, fan-type stress fields give a simple and realistic assessment of the load paths in the concrete core. Accordingly, the associated predicted equilibrium states for both the loaded and support plates closely match those which were observed in the tests.

2. A fan-type stress field for a patch-loaded specimen does not realistically describe the load paths in the regions of the loaded plate over the "stress-free-zones", since this stress field demands the existence of strain discontinuities which the specimen cannot provide. Accordingly, the state of stress in the loaded plate is not accurately predicted. However, a fan-type stress field can nevertheless be used to predict the strength of the member, since the failure location is close to the support plate and within the "tied-arch" which is essentially independent of the "stress-free-zones".

7.2.4 Failure criterion.

1. A failure criterion for the concrete in composite specimens which accurately and rationally predicts the failure loads of the members has been developed. The criterion is similar in philosophy to the transverse strain criterion which is currently suggested in the General Method of CAN3 A23.3 M-84. However, the method uses an easily-determined confinement characteristic G_K in place of the transverse strain, which is difficult to determine, at the failure location.
2. The failure criterion was developed for specimens with concrete cylinder strengths in the range $40 \text{ MPa} < f'_c < 70 \text{ MPa}$ and for confinement characteristics in the range $125 \text{ MPa/mm} < G_K < 300 \text{ MPa/mm}$. However,

there is evidence to suggest that the failure criterion may also be applicable over larger ranges of both f'_c and G_K.

3. The failure criterion assumes that the concrete fails before the support plate yields. However, there is evidence to suggest that it may also be applicable for underreinforced specimens.

7.3 Recommendations.

7.3.1 An Appropriate Composite Ice-Resisting Wall Configuration.

The composite ice-resisting wall configuration which is recommended is shown in Fig. 7.1. Such a wall would be easy to construct, and has the following features:

1. The concrete core material is either plain concrete or steel-fibre-reinforced concrete.
2. Nelson stud shear connectors are attached to both the loaded and support plates, with a closer spacing in the support regions of the support plate.
3. The attachment of studs near the outer corners of the bulkheads is avoided in order that the heat affected zones due to the stud welding may be kept within the support widths.
4. Diaphragm plates are used at the support locations to space the two steel skins during fabrication and to tie them together during the pouring of the concrete core.

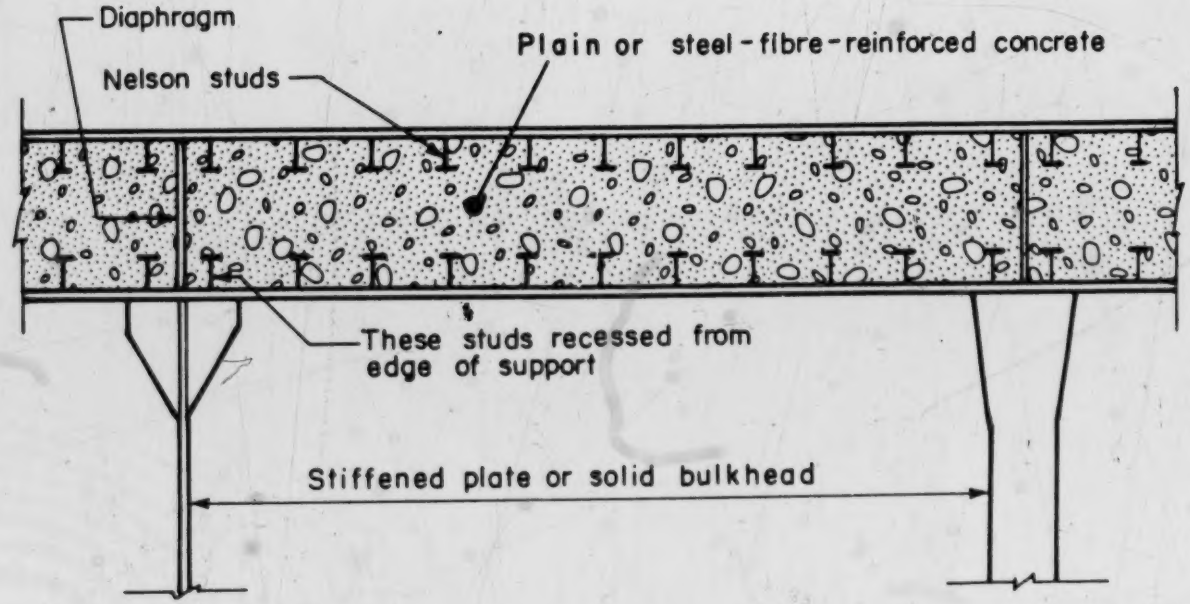

Figure 7.1 Recommended configuration for a composite ice-resisting wall.

5. Either solid or stiffened plates are used, but it is emphasized that the stiffener spacing must be designed to include their effect on the strength of the wall as well as on the strength and stability of the bulkheads.

7.3.2 Future Work.

1. The number of shear connectors on both the loaded and support plates was conservatively chosen to ensure that premature failure did not occur due to loss of composite action. A significant economic advantage could be realised if the number of studs could be reduced. This is particularly true for the support region, where a reduction of the congestion due to the large number of studs would be desirable.
2. The test series used similar plate thicknesses for both the loaded and support plates, and it was observed that the strains in the loaded plates were lower than those in the support plates. It may therefore be possible to reduce the thickness of the support plate without adversely affecting the strength of the member. However, such research should be tempered by the fact that the strain in the loaded plate may be unsafely predicted using fan-type stress fields for patch-loaded specimens.
3. The analytical model suggests that the failure load is sensitive to the support width. This could be confirmed by varying the support width in future tests.

4. Tests with varying stiffener spacing at the supports would yield valuable information.
5. The effect of patch-loading on the strains in the loaded plate needs to be further investigated by tests.
6. Steel-fibre-reinforced concrete is potentially attractive as an infill material, and could be further examined.
7. It has been assumed that diaphragm plates located at the supports would be adequate for resisting the hydrostatic pressure of the wet concrete during construction. The hydrostatic thrusts on the plates can be controlled by limiting the allowable height of the concrete lift, and it is anticipated that the skin plates would resist these thrusts by membrane rather than bending action. The permanent deformations and stresses in the steel skins due to the concrete pouring could be examined by further testing.

7.4 Closure.

Marti (1987) has written that;

> "At present, we must admit that we are unable to provide a comprehensive and accurate theory capable of predicting the response of reinforced concrete to general loading. We have to content ourselves with simplified approaches which provide at least answers to partial problems. This is not a serious drawback since we could never apply such a comprehensive theory in practice simply because we cannot accurately assess the initial conditions for any practical problem..... It is better to use several simple approaches which are capable of illuminating partial aspects of a problem rather than to apply one theory which pretends to cover all aspects".

In accordance with the lower bound theorem of plasticity, the use of fan-type stress fields in combination with the recognition of the strengths and deformation capabilities of the constituent materials will give a safe estimate to the load-carrying capacity of a composite ice-resisting wall. Perhaps more importantly, this approach also forces the designer to identify a realistic load path within the structure, and thereby to understand the structure, rather than to content himself with the (often blind) application of mathematical formulae or "canned" computer programs. Hardy Cross (1952) suggests that;

> "Students should be encouraged more to draw pictures of what they are thinking about. They should draw pictures of deformed structures, pictures of structural failure, pictures of stress distribution. To try to draw them raises, or should raise, hundreds of questions. If men can't draw them they don't know what they are talking about and the degree of detail shows the amount of familiarity with the subject..... To try to draw a picture will frequently answer or invalidate a question".

Practicing designers are continuing students, and it is the writer's opinion that the statement by Professor Cross

succinctly summarises the correct approach to be taken, not only in the design of composite ice-resisting walls, but in engineering design in general.

REFERENCES

ACI Committee 318, Building Code Requirements for Reinforced Concrete, (ACI 318 - 83), American Concrete Institute, Detriot, Michigan, 1983.

ACI Committee 544, State-of-the-Art Report on Fiber Reinforced Concrete, (ACI 544.1R - 82), American Concrete Institute, Detroit, Michigan, 1982.

ACI Committee 544, Measurement of Properties of Fiber Reinforced Concrete, (ACI 544.2R - 78), American Concrete Institute, Detroit, Michigan, 1978.

Akiyama, H., Koseki, K., Taira ,K., Sasaki, M., Strength of Steel/Concrete Composite Sandwich Members, Transactions of the Japan Concrete Institute, Vol. 8, 1986, pp. 337-344.

Allyn, N.F., Global and Local Ice Loads Including Dynamic Effects, Ice/Structure Interaction, PERD Task 6.2 Program Evaluation Workshops, Canada Oil and Gas Lands Administration, May - June, 1986, pp. I-1 - I-36.

ASTM (American Society for Testing and Materials), Standard Methods and Definitions for Mechanical Testing of Steel Products, ASTM A370-77, Philadelphia, Pennsylvania, 1977.

Bach, F., Nielsen, M.P., Braestrup, M.W., Shear Tests on Reinforced Concrete T-Beams. Series V, U, X, B, S, Copenhagen, Technical University of Denmark, Structural Research Laboratory Report No. R-120, 1980.

Bercha, F.G., Brown, T.G., Cheung, M.S., Local Pressure in Ice/Structure Interactions, Proceedings of the Conference Arctic '85, San Francisco, California, March, 1985, pp. 1243-1251.

Brandli, W., Durchstanzen von Flachdecken bei Rand- und Eckstutzen, Institut fur Baustatik und Konstruktion, ETH Zurich, Report No. 146, March, 1985.

Brattland, A., Kennedy, D.J.L., Shrinkage and Flexural Tests of Two Full-Scale Composite Trusses, Structural Engineering Report 143, University of Alberta, Edmonton, Alberta, 1986.

Bresson, J., Nouvelles Recherches et Application concernant l'Utilisation des Collages dans les Structures. Beton Plaque, Annales de l'Institut Technique du Batiment et

des Travaux Publics, No. 278, February, 1971.

CAN3 A23.2 - M77, Methods of Test for Concrete, National Standard of Canada, Canadian Standards Association, Rexdale, Ontario, 1977.

CAN3 A23.3 - M84, Design of Concrete Structures for Buildings, National Standard of Canada, Canadian Standards Association, Rexdale, Ontario, 1984.

CAN3 G40.21 - M81, Structural Quality Steels, National Standard of Canada, Canadian Standards Association, Rexdale, Ontario, 1981.

Chen, W.F., Plasticity in Reinforced Concrete, McGraw-Hill Book Company, New York, 1982.

Clarke, J.L., Symmons, R.M., Concrete in the Oceans, Effects of Temperature Gradients on Walls of Oil Storage Structures, Technical Report No. 3, CIRIA/UEG - Cement and Concrete Association - Department of Energy, Wexham Springs, England, 1979.

Croasdale, K.R., Sea Ice Mechanics; A General Overview, Marine Technology Society Journal, Vol. 18, No. 1, 1984, pp. 8-16.

Cross, Hardy, Engineers and Ivory Towers, McGraw-Hill Book Company, New York, 1952.

Exner, H., On the Effectiveness Factor in Plastic Analysis of Concrete, IABSE Colloquium, Plasticity in Reinforced Concrete, Final Report, Copenhagen, 1979, pp. 35-42.

Gerwick, B.C., Berner, D., Utilization of Composite Design in the Arctic and Sub-Arctic, Proceedings of POAC '87, Fairbanks, Alaska, August, 1987.

Goode, C.D., Fatheldin, Y.Y., Sandwich Cylinders (Steel-Concrete-Steel) Subjected to External Pressure, ACI Journal, Vol. 77, No. 3, March/April, 1980, pp. 109-115.

Halligan, D.W., Prestressed Concrete Nuclear Plant Containment Structures, PCI Journal, September/October, 1976, pp. 158-175.

Hattori, Y., Matsuishi, M., On the Ultimate Strength of Composite Steel-Concrete Structure, Proceedings of POAC '85, Narssarssuaq, Greenland, 1985, pp. 445-454.

Knowles, P.R., Composite Steel and Concrete Construction, Butterworth and Co. (Publishers) Ltd., London, 1973.

Kupfer, H., Hilsdorf, H.K., Rusch, H., Behavior of Concrete Under Biaxial Stresses, ACI Journal, Vol. 66, No. 8, 1969, pp. 656-666.

Lay, M.G., Structural Steel Fundamentals - An Engineering and Metallurgical Primer, Australian Road Research Board, Victoria, Australia, 1982.

Lerchenthal, C.H., Bonded Sheet Metal Reinforcement for Concrete Slabs, RILEM Bulletin, No. 34-37, 1967, pp. 263-269.

L'Hermite, R., Bresson, J., Beton Arme d'Armature Collees, RILEM Colloque International, Vol. 2, 1967.

Macdonald, M.D., The Flexural Behaviour of Concrete Beams with Bonded External Reinforcement, Transport and Road Research Laboratory, Supplementary Report 415, Crowthorne, England, 1978.

Macdonald, M.D., The Flexural Performance of 3.5m Concrete Beams with Various Bonded External Reinforcements, Transport and Road Research Laboratory, Supplementary Report 728, Crowthorne, England, 1982.

Marti, P., Zur Plastichen Berechnung von Stahlbeton, Dissertation No. 6602, ETH Zurich, 1980.

Marti, P., Basic Tools for Reinforced Concrete Beam Design, ACI Journal, January/February, 1985, pp. 46-56.

Marti, P., Application of Plastic Analysis to Shear Design of Reinforced Concrete Members, University of Toronto, February, 1987. (Unpublished).

Matsuishi, M., Nishimaki, K., Takeshita, H., Iwata, S., On the Strength of New Composite Steel-Concrete Material for Offshore Structure, Proceedings of OTC, Paper No. 2804, Houston, Texas, 1977, pp. 589-594.

Matsuishi, M., Nishimaki, K., Takeshita, H., Iwata, S., Suhara, T., On the Strength of Composite Steel-Concrete Structures of a Sandwich System (2nd Report) - Nonlinear Analysis Using the Finite Element Method -, Hitachi Zosen Technical Review, Vol. 39, No. 1, March, 1978.

Matsuishi, M., Nishimaki, K., Iwata, S., Suhara, T., On the Strength of Composite Steel-Concrete Structures of a Sandwich System (3rd Report) - Effect of Repeated Loadings -, Hitachi Zosen Technical Review, Vol 41, No. 1, March, 1980.

Mays, G.C., Smith, D.W., Slabs of the Future, Concrete, June, 1980, pp. 13-16.

Mindess S., Young, J.F., Concrete, Prentice-Hall, New Jersey, 1981.

Montague, P., Goode, C.D., El-din Shukry, M., Tests on Composite Cylinders under External Pressure at Manchester University 1976-1985, Simon Engineering Laboratories, University of Manchester, England, November, 1985.

Montague, P., Composite Vessels for Deepwater Operation; The Influence of Shell Length and Severe Damage, Proceedings of the Institution of Civil Engineers, Paper 8972, Vol 81, June, 1986, pp. 175-219.

Nelson, J.K., Beason, W.L., Pond, A.D., A Hybrid Structural Ice Defense Mechanism, Proceedings of the Conference Arctic '85, San Francisco, California, March, 1985, pp. 1166-1173.

Nielsen, M.P., Limit Analysis and Concrete Plasticity, Prentice-Hall, New Jersey, 1984.

Nishimaki, K., Matsuishi, M., Takeshita, H., Iwata, S., Suhara, T., On the Strength of Composite Steel-Concrete Structures of a Sandwich System (1st Report) - Experiment of Static Strength and Ultimate Strength Analysis -, Hitachi Zosen Technical Review, Vol 38, No. 3, September, 1977.

Niwa, J., Equation for Shear Strength of Reinforced Concrete Deep Beams Based on FEM Analysis, Concrete Library of JSCE, No. 4, December, 1984, pp. 283-295.

Nojiri, Y., Koseki, K., Structural Behaviour and Design Method of Steel/Concrete Composite Ice Walls for Arctisc Offshore Structures, Proceedings of OTC, Paper No. 5292, Houston, Texas, 1986.

Ong, K.C.G., Mays, G.C., Cusens, A.R., Flexural Tests on Steel-Concrete Open Sandwiches, Magazine of Concrete Research, Vol. 34, No. 20, September, 1982, pp. 130-138.

Orlov, P., Fundamentals of Machine Design, Vol. 1, Mir Publishers, Moscow, 1976.

Ozawa, K., Tanaka, Y., Ueda, T., Shear Resisting Mechanism of a Composite Member with Steel and Concrete, Transactions of the Japan Concrete Institute, Vol. 8., 1986, 1986, pp. 295-302.

Price, W.H., Factors Influencing Concrete Strength, ACI Journal, Vol. 47, No. 6, 1951, pp. 417-432.

Quazzaz, A.N., The Behaviour and Implosion of Plain Concrete

Cylindrical Shells When Subjected to External Pressure, Ph.D. Thesis, University of Manchester, England, 1984.

Rogowsky, D.M., MacGregor, J.G., Shear Strength of Deep Reinforced Concrete Continuous Beams, Structural Engineering Report No. 110, University of Alberta, Edmonton, Alberta, November, 1983.

Ryan, B.F., Joiner, B.L., Ryan, T.A., Minitab Handbook, Second Edition, Duxbury Press, Boston, 1985.

Schlaich, J., Schafer, K., Jennewein, M., Towards a Consistent Design of Reinforced and Prestressed Concrete, PCI Journal, May-June, 1987.

Shioya, T., Matsumoto, G., Okada, T., Ota, T., Development of Composite Members for Arctic Offshore Structures, VTT Symposium 71, POLARTECH '86, Technical Research Centre of Finland, 1986, pp. 660-677.

Solomon, S.K., Smith, D.W., Cusens, A.R., Flexural Tests on Steel-Concrete-Steel Sandwiches, Magazine of Concrete Research, Vol. 28-29, March, 1976, pp. 13-20.

Solomon, S.K., Gopalani, L.K., Flexural Tests on Concrete Beams Externally Reinforced by Steel Sheet, Indian Concrete Journal, September, 1979, pp. 249-253.

Sundararaj, P., DEMSTR - A Program for Converting Demec Readings to Strain Readings, University of Alberta, Edmonton, Alberta, 1986, (unpublished).

Taylor, R., Composite Reinforced Concrete, Concrete, Vol. 10, No. 8, August, 1976, pp.23-25.

Taylor, R., Mills, P.E., Rankin, R.I., Tests on Concrete Beams with Mixed Types of Reinforcement, Magazine of Concrete Research, Vol. 30, No. 103, June, 1978, pp. 73-88.

Thurlimann, B., Marti, P., Pralong, J., Ritz, P., Zimmerli, B., Anwendung der Plastizitatstheorie auf Stahlbeton, Institut fur Baustatik und Konstruktion, ETH Zurich, April, 1983.

Timoshenko, S.P., Goodier, J.N., Theory of Elasticity, McGraw-Hill Kogakusha Ltd., Tokyo, 1970.

Vecchio, F.J., Collins, M.P., Response of Reinforced Concrete to In-Plane Shear and Normal Stresses, Publication No. 82-03, Department of Civil Engineering, University of Toronto, March, 1982.

Watt, B.J., Ice Load Considerations for Concrete Structures,

Proceedings of the FIP/CPCI Symposia, Calgary, Canada, Vol. 2, August, 1984, pp.43-53.

Yee, A.A., Masuda, F.R., Kim, C.N., Doi, D.A., Daly, L.A., Concrete Module for the Global Marine Concrete Island Drilling System, Proceedings of the FIPPCI Symposia, Calgary, Canada, Vol. 2, August, 1984, pp. 23-30.

Zienkiewicz, O.C., The Finite Element Method, McGraw-Hill Book Company (UK) Limited, London, 1977.

APPENDIX A: CONCRETE TEST RESULTS.

The concrete cylinder strength (f'_c), the modulus of elasticity in compression (E_c), the splitting tensile strength (f_t) and the modulus of rupture (f_r) were recorded at intervals for each concrete mix used in the testing program. The values for the cylinder strength and the modulus of elasticity in compression were obtained from 300 mm × 150 mm diameter concrete cylinders, tested in accordance with CAN3 A23.2-9C. Splitting tensile strengths were obtained from split cylinder tests carried out in accordance with CAN3 A23.2-13C. Modulus of rupture was calculated from tests on 150 mm × 150 mm × 900 mm beams, tested under two-point loading in accordance with CAN3 A23.2-8C.

The concrete test results are presented in Tables A.1-A.7 and Figs. A.1-A.4. Table A.1 gives the age at which each composite specimen was tested, and correlates the composite specimens with the corresponding concrete mixes. Since the concrete cylinder strengths corresponding to the concrete in the composite test specimens at the age of testing are of particular interest for the development of the failure criterion in Chapter 6, these values have been extracted from Figs. A.1-A.3 for all composite specimens except B6/3, B6/4 and B6/6, and are presented in Table 3.1. The regression curves in Figs. A1-A3 were obtained from the data in Tables A2-A4 using the statistical package Minitab (Ryan et al., 1985). Since the numbers of cylinders

available for specimens B6/3, B6/4 and B6/6 were insufficient to allow meaningful regression analyses, the concrete cylinder strengths for these specimens were calculated using equation [3.1], where the values for t_1 were obtained from Table A.1, and the values for t_0 and corresponding values for f'_c were obtained from Tables A.5, A.6 and A.7 respectively.

Since the section on Toughness-Energy Absorption for steel-fibre-reinforced-concrete (SFRC) in ACI 544.2R-78 has been removed from the publication and is currently under revision, the load-midspan deflection curves for the SFRC modulus of rupture beams are reported in Fig. A.4 without any interpretation of the areas under the curves.

Table A.1 Mix designations and age at testing for each specimen.

Specimen #	Age at testing, t_1 (days)	Concrete Mix #
B4/1	79	H4
B4/2	73	H4
B4/3	62	H4
B4/4	84	H4
B4/5	31	H4
B6/1	24	H6
B6/2	42	H6
B6/3	35	H6/1.5
B6/4	49	H6/1.0
B6/5	63	H6
B6/6	31	L6
B6/7	77	H6
B5/1	13	H5
B5/2	16	H5
B5/3	21	H5
B5/4	27	H5
B5/5	30	H5

Table A.2 Concrete test results for Mix H4.

		Compression		Tension	
Cylinder (C) or Beam (B)	Age t (days)	f'_c (MPa)	E_c (MPa)	f_t (MPa)	f_r (MPa)
C	3	36.4	-	-	-
C	3	44.0	-	-	-
C	7	48.1	-	-	-
C	7	47.2	-	-	-
C	28	55.2	-	-	-
C	28	56.1	-	-	-
C	57	59.7	-	-	-
C	57	58.0	-	-	-
C	57	62.5	-	-	-
C	71	64.0	-	-	-
C	71	60.8	-	-	-
C	71	63.5	-	-	-
C	86	72.4	29 000	-	-
C	86	69.0	28 700	-	-
C	86	71.2	-	-	-
C	86	-	-	4.04	-
C	86	-	-	3.96	-
B	86	-	-	-	5.32
B	86	-	-	-	5.32

Table A.3 Concrete test results for Mix H6.

		Compression		Tension	
Cylinder (C) or Beam (B)	Age t (days)	f'_c (MPa)	E_c (MPa)	f_t (MPa)	f_r (MPa)
C	4	49.8	-	-	-
C	4	43.9	-	-	-
C	4	47.5	-	-	-
C	11	48.1	-	-	-
C	11	48.1	-	-	-
C	11	45.8	-	-	-
C	21	51.3	-	-	-
C	21	53.2	-	-	-
C	28	49.0	-	-	-
C	28	55.0	-	-	-
C	36	56.5	-	-	-
C	42	52.8	-	-	-
C	42	54.9	-	-	-
C	42	62.8	-	-	-
C	42	59.4	-	-	-
C	42	-	-	3.15	-
C	66	60.3	-	-	-
C	66	63.9	30 900	-	-
C	66	68.3	30 100	-	-
C	66	-	-	5.17	-
C	66	-	-	4.52	-
B	66	-	-	-	5.36
B	66	-	-	-	6.01

Table A.4 Concrete test results for Mix H5.

		Compression		Tension	
Cylinder (C) or Beam (B)	Age t (days)	f'_c (MPa)	E_c (MPa)	f_t (MPa)	f_r (MPa)
C	3	33.7	-	-	-
C	3	35.1	-	-	-
C	7	36.5	-	-	-
C	7	34.5	-	-	-
C	12	46.0	-	-	-
C	19	46.0	-	-	-
C	19	48.2	25 500	-	-
C	19	48.2	27 100	-	-
C	19	-	-	3.43	-
C	19	-	-	3.84	-
C	27	45.2	-	-	-
C	27	53.7	29 100	-	-
C	27	48.8	20 100	-	-
C	27	-	-	4.80	-
C	27	-	-	4.52	-
C	34	54.3	-	-	-
C	34	56.5	26 300	-	-
C	34	54.3	28 600	-	-
C	34	-	-	3.90	-
C	34	-	-	3.63	-
B	20	-	-	-	3.94
B	20	-	-	-	4.32
B	27	-	-	-	5.15
B	27	-	-	-	5.09
B	31	-	-	-	4.58
B	31	-	-	-	5.34

Table A.5 Concrete test results for Mix L6.

		Compression		Tension	
Cylinder (C) or Beam (B)	Age t (days)	f'_c (MPa)	E_c (MPa)	f_t (MPa)	f_r (MPa)
C	28	39.0	24 900	-	-
C	28	41.0	-	-	-
C	28	37.6	-	-	-
C	28	36.2	-	-	-
C	28	-	-	3.50	-
B	28	-	-	-	4.50

Table A.6 Concrete test results for Mix H6/1.5 (1.5% fibres/vol.).

		Compression		Tension	
Cylinder (C) or Beam (B)	Age t (days)	f'_c (MPa)	E_c (MPa)	f_t (MPa)	f_r (MPa)
C	36	53.9	-	-	-
C	39	61.7	29 900	-	-
C	39	-	-	5.34	-
B	39	-	-	-	6.46

Table A.7 Concrete test results for Mix H6/1.0 (1.0% fibres/vol.).

		Compression		Tension	
Cylinder (C) or Beam (B)	Age t (days)	f'_c (MPa)	E_c (MPa)	f_t (MPa)	f_r (MPa)
C	66	60.6	-	-	-
C	66	62.5	-	-	-
C	66	61.9	29 000	-	-
C	66	63.9	29 900	-	-
C	66	-	-	3.70	-
C	66	-	-	6.10	-
C	66	-	-	5.00	-
C	66	-	-	5.34	-
B	66	-	-	-	5.75
B	66	-	-	-	6.46

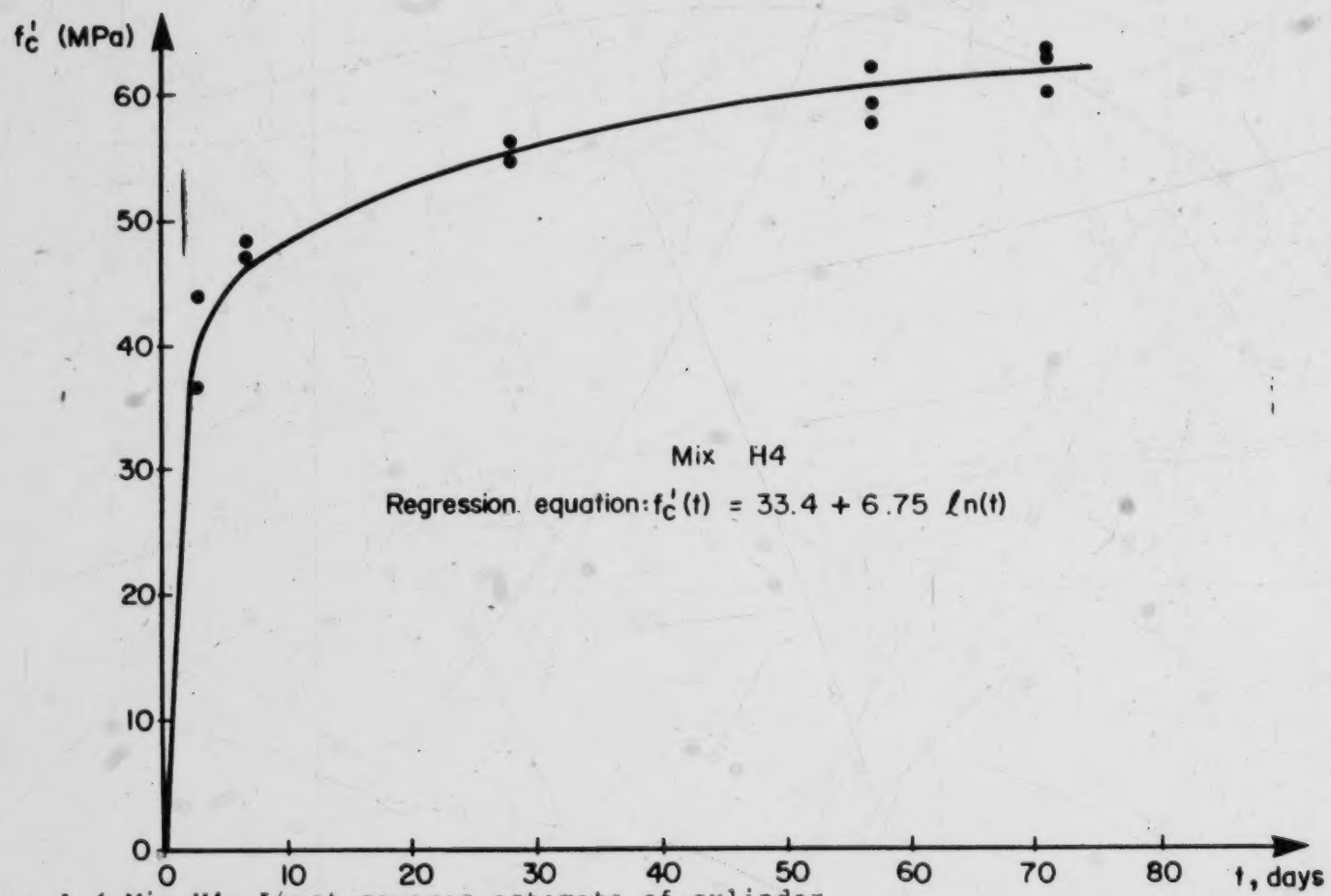

Figure A.1 Mix H4: Least squares estimate of cylinder strength/time curve.

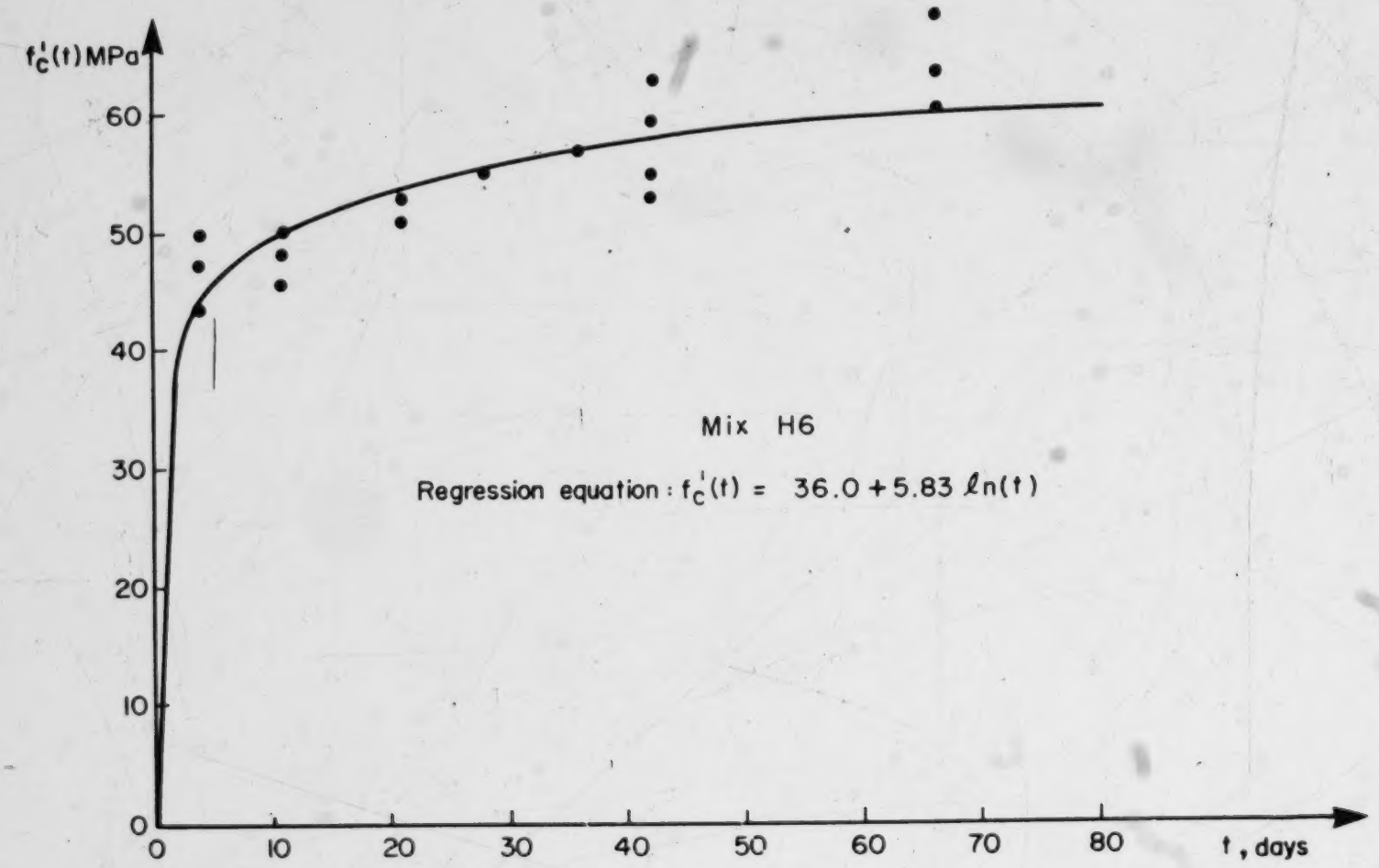

Figure A.2 Mix H6: Least squares estimate of cylinder strength/time curve.

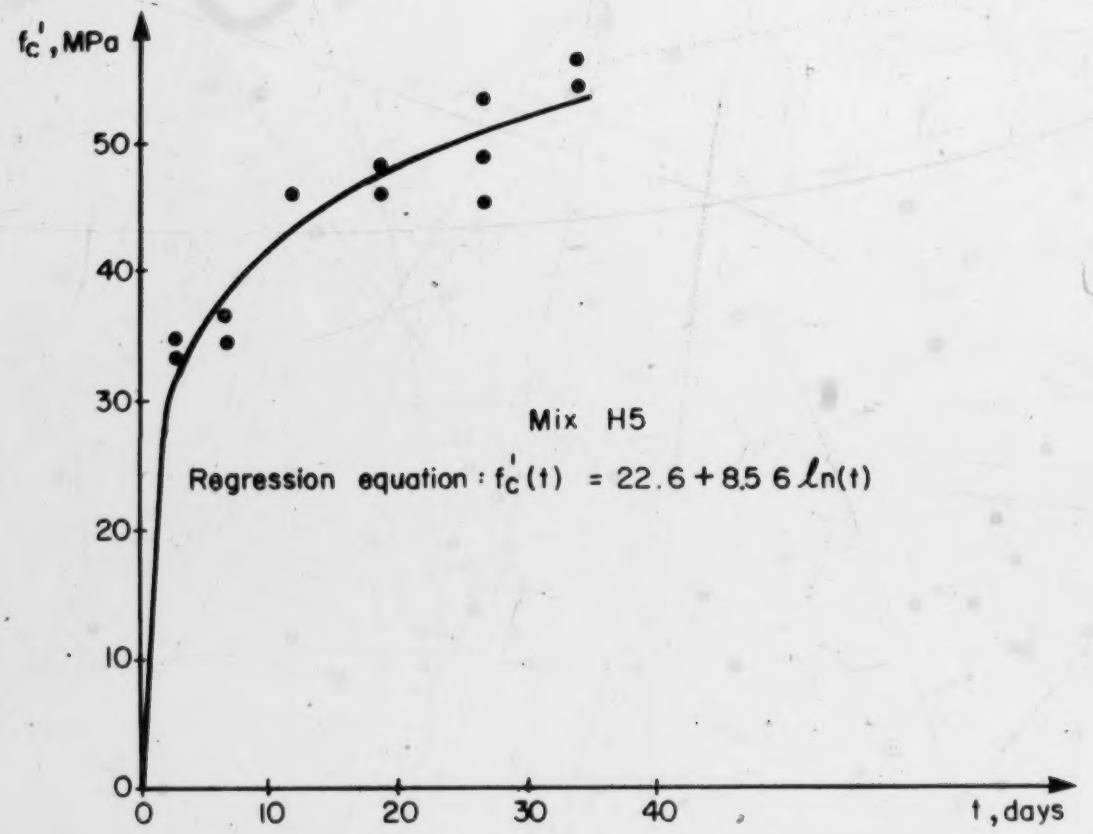

Figure A.3 Mix H5: Least squares estimate of cylinder strength/time curve.

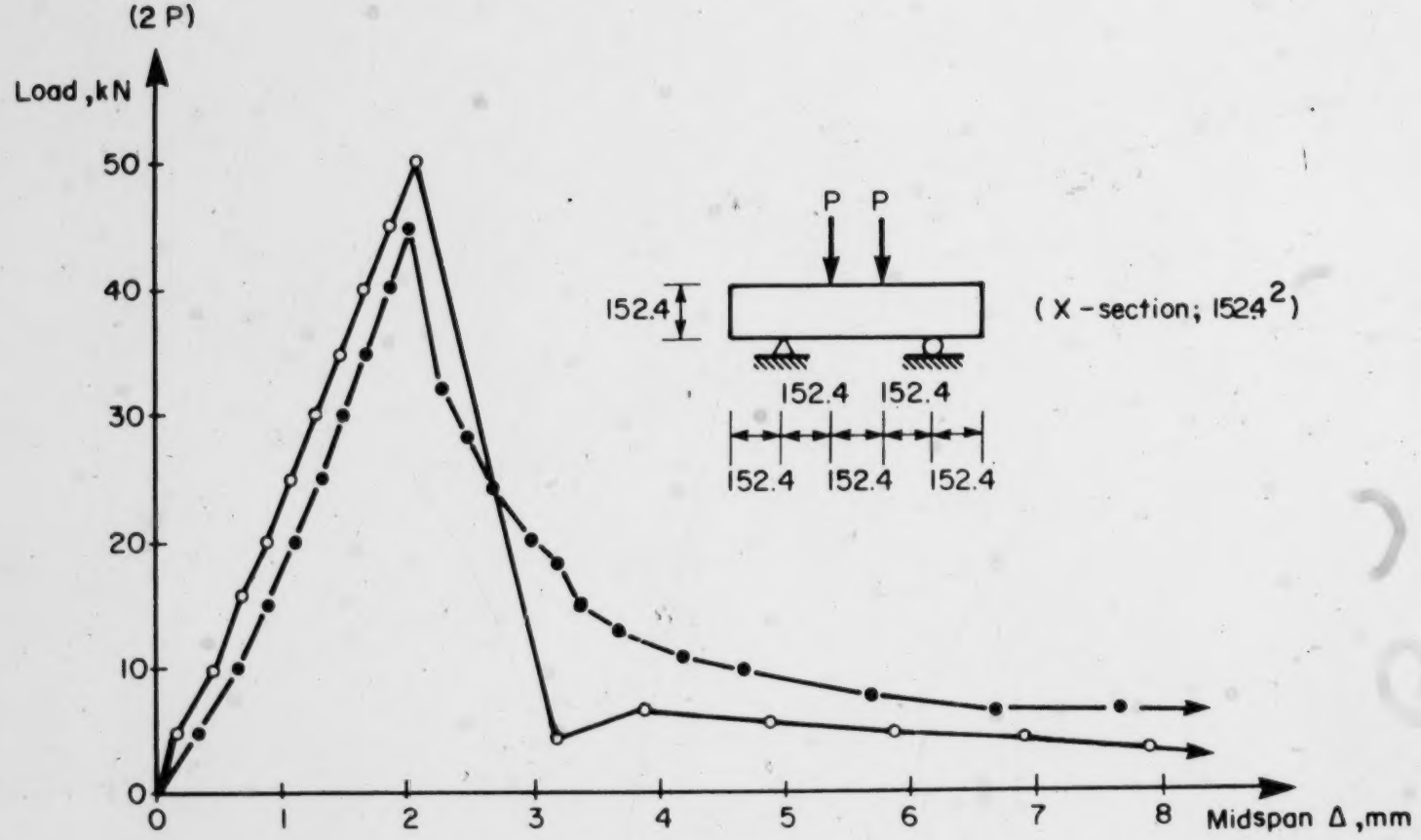

Figure A.4 Mix H6/1.0: Load/midspan deflection plots for modulus of rupture beams.

APPENDIX B: CALCULATIONS FOR THE BASIC STRESS FIELDS.

Since the basic stress fields for all three span-to-depth ratios have the same form for uniform loading, only the calculations for span-to-depth ratio = 5 are given in depth here, and they refer to Fig. B.1. The results of the corresponding calculations for span-to-depth ratios equal to 4 and 6 are shown in Figs. B.2-B.3. The calculations for the basic stress field for the patch loaded specimen B6/7 are also given, since the solution involves the use of additional techniques which were not used in the solution of the B5 series basic stress field. Since the hydrostatic stress u_c can be arbitrarily chosen, a value of 50 MPa is used. The notation is defined in the List of Symbols and is repeated throughout Chapter 5. Calculations are given only for the correct applied load p (MPa). If any other load had been used, equilibrium in Zone 3 would not have been satisfied, and another choice of p would have been necessary.

B.1 Uniform Loading: Basic Stress Field for l/d = 5.

The geometry for l/d = 5 is shown in Fig. B.1, where only half of the beam is shown because of symmetry. Assume that the applied load p = 4.0 MPa.

ZONE 1;

Load on cantilever = 0.769 × 4.1 = 3.153 MPa.

Σ (Forces in the vertical direction) = 0:

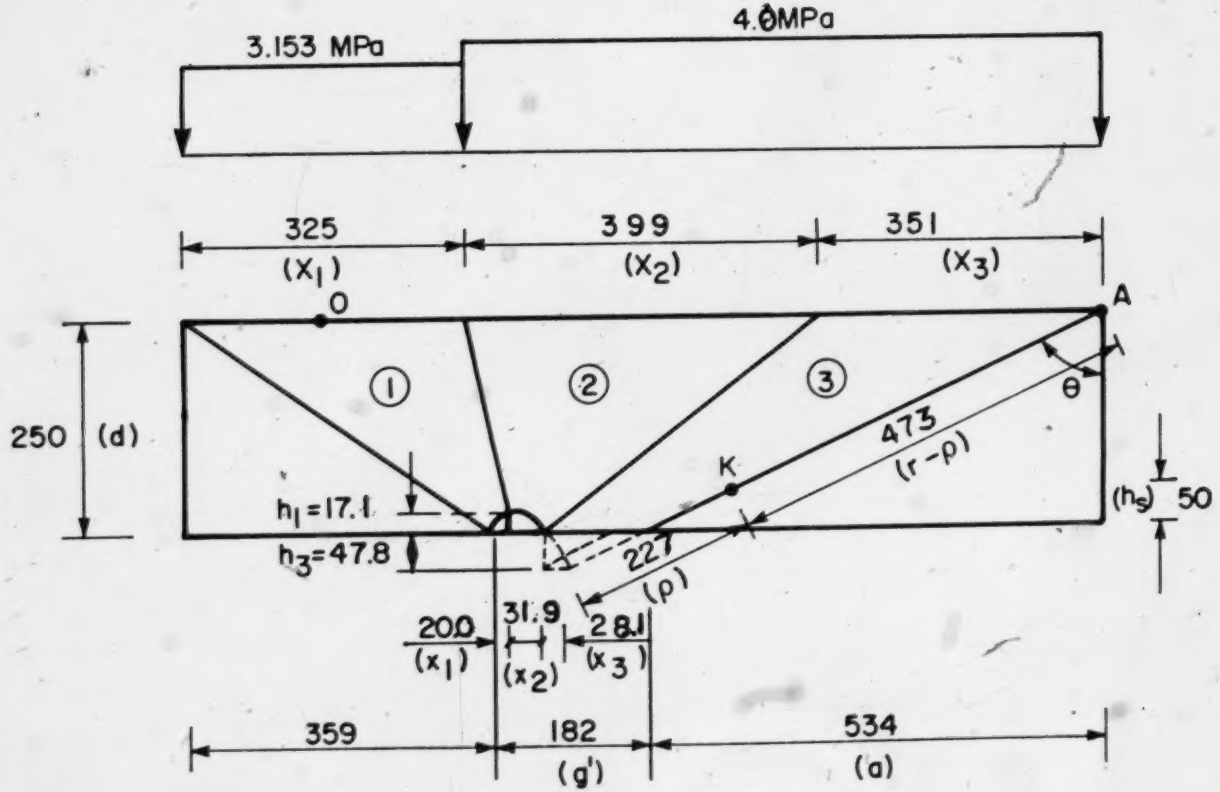

Figure B.1 Basic stress field for the B5 series with uniform loading.

$$x_1 = \frac{3.153 \times 325.0}{50}$$

$$= 20.0 \text{ mm.}$$

Σ (Moments about the point O) = 0:

$$50h_1(250 - \frac{h_1}{2}) = 50 \times 20.0 \times 208.$$

The solution to this quadratic equation gives h_1 = 17.1 mm.

$\therefore$ Zone 1 can be constructed.

ZONE 2;

THe non-dimensionalised height κ of vertical face of the node is

$$\kappa = \frac{h_1}{d} = \frac{17.1}{250} = 0.0684.$$

The slope s of the fan line which is common to both Zone 1 and Zone 2 is

$$s = \frac{359 + 20.0 - 325}{250 - 17.1} = 0.2319.$$

Calculate the non-dimensionalised horizontal distance ξ_1:

$$\xi_1 = \frac{s(1-\kappa)}{(u_c/p)-1} \qquad [5.7]$$

$$= \frac{0.2319(1-0.0684)}{(50/4.0)-1}$$

$$= 0.01879.$$

Calculate the maximum height ω_o of the hydrostatic node:

$$\omega_o = 1-(1-\kappa)\sqrt{1-\frac{s^2}{(u_c/p)-1}} \qquad [5.9]$$

$$= 1-(1-0.0694)\sqrt{1-\frac{0.2319^2}{(50/4.0)-1}}$$

$$= 0.07058.$$

Calculate the non-dimensionalised horizontal distance ξ_2:

$$\xi_2 = \sqrt{\frac{\omega_o(2-\omega_o)}{(u_c/p)-1}} \qquad [5.8]$$

$$= \sqrt{\frac{0.07058(2-0.07058)}{(50/4.0)-1}}$$

$$= 0.1088.$$

Knowing the non-dimensionalised quantities ξ_1 and ξ_2, the horizontal dimensions x_2 and X_2 can be calculated using:

$$x_2 = (\xi_1+\xi_2)d \qquad [5.10]$$

$$= (0.01879+0.1088) \times 250$$

$$= 31.9 \text{ mm},$$

$$X_2 = \left[\frac{u_c}{p}\right]x_2$$

$$= \frac{50 \times 31.9}{4.0}$$

$$= 399 \text{ mm},$$

and so Zone 2 can be constructed.

ZONE 3;

X_3 is known, since it is the amount of the top surface which has not been used up by Zones 1 and 2.

Σ (Forces in the vertical direction) = 0:

$$x_3 = \frac{p}{u_c}X_3 \qquad [5.12]$$

$$= \frac{4.0}{50} \times 351$$

$$= 28.08 \text{ mm}.$$

The height h_3 of the vertical face of the imaginary hydrostatic node can now be calculated by proportion using

$$h_3 = \frac{d}{a}\left[g'-(x_1+x_2+x_3)\right] \qquad [5.13]$$

$$= \frac{250}{534}\left[182-(20.0+31.9+28.08)\right]$$

$$= 47.8 \text{ mm}.$$

The overturning moment M_o is calculated using

$$M_o = pX_3\left[a+g'-x_1-x_2-\frac{x_3}{2}-\frac{X_3}{2}\right] \qquad [5.14(a)]$$

$$= 4.0 \times 351(534 + 182 - 20.0 - 31.9 -$$

$$14.04 - 175.5)$$

$$= 6.66 \times 10^5 \text{ Nmm},$$

and the restoring moment M_R is

$$M_R = u_c h_3 (d + \frac{h_3}{2}) \qquad [5.14(b)]$$

$$= 50 \times 47.8(250 + 23.9)$$

$$= 6.54 \times 10^5 \text{ Nmm.}$$

Since $M_o \cong M_R$, p =4.0 MPa is accepted as the correct value for the applied load. If M_o and M_R had not been close, then it would have been necessary to choose another value of p and repeat the procedure.

Since a statically admissible stress field has now been defined, the principal compressive stress σ_{1K} at K can be found using equations [5.1], [5.2] and [5.25] as follows. The angle Θ between the fan line through K and the vertical axis is

$$\Theta = \text{Tan}^{-1}\left[\frac{534}{250}\right]$$

$$= 64.913^\circ.$$

The principal compressive stress at A on the loaded surface is

$$\sigma_{1A} = \frac{2p}{1+\text{Cos}2\Theta} \qquad [5.25]$$

$$= \frac{2 \times 4.0}{1 - 0.6404}$$

$$= 22.25 \text{ MPa.}$$

The radius of curvature R corresponding to this fan line at the imaginary hydrostatic node is

$$R = \left[\frac{\sigma_{1A}}{u_c - \sigma_{1A}}\right] r, \qquad [5.2]$$

and r, the distance along the fan line between the imaginary hydrostatic node and A, is scaled from the drawing. Since r is scaled to be 700 mm, then

$$R=\left[\frac{22.25}{50 - 22.25}\right] \times 700$$

$$= 561 \text{ mm.}$$

The principal compressive stress at K, σ_{1K}, is then found using

$$\sigma_{1K}= \left[\frac{R}{R + \rho}\right]u_c \qquad [5.1]$$

The distance ρ along the fan line between the imaginary hydrostatic node and K is scaled as 227 mm.

$$\therefore \sigma_{1K}= \left[\frac{561}{561 + 227}\right] \times 50$$

$$= 35.60 \text{ MPa.}$$

For the purposes of the failure criterion in Chapter 6, the most important results from the above calculations are the stress σ_{1K}, and the height h_3 of the imaginary node in Zone 3, and are included in Tables 6.1 and 6.2. The values for the B4 series and the B6 series (shown in Figs B.2 and B.3) are also included in these tables.

B.2 Eccentric Patch Load: Basic Stress Field for Specimen B6/7.

The geometry and loading for specimen B6/7 are shown in Fig. B4. For u_c = 50 MPa, it is initially (and correctly) assumed that p = 3.3 MPa. The loads on the cantilevers are transferred to the support using a combination of Zones 1 and 3. The calculations are not shown here, since they are similar to those used for the B5 series basic stress field. The effect of the cantilever load is to use 20 mm of the support width at each support. The remaining 156 mm is therefore available for supporting the patch load.

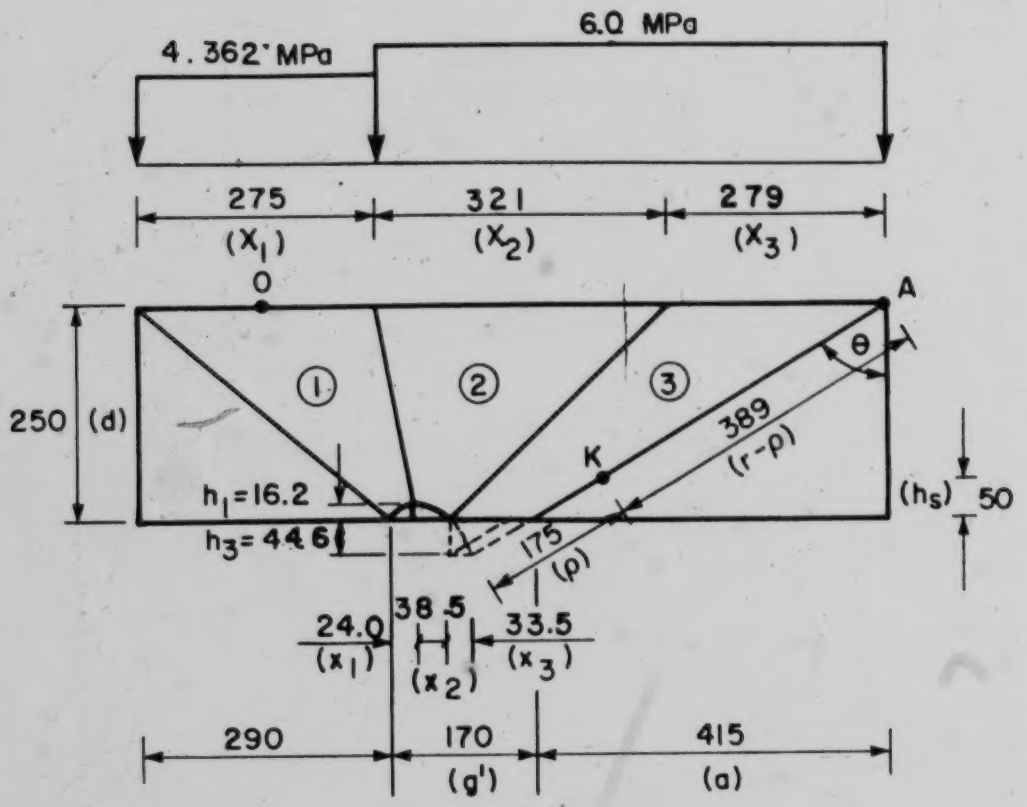

Figure B.2 Basic stress field for the B4 series with uniform loading.

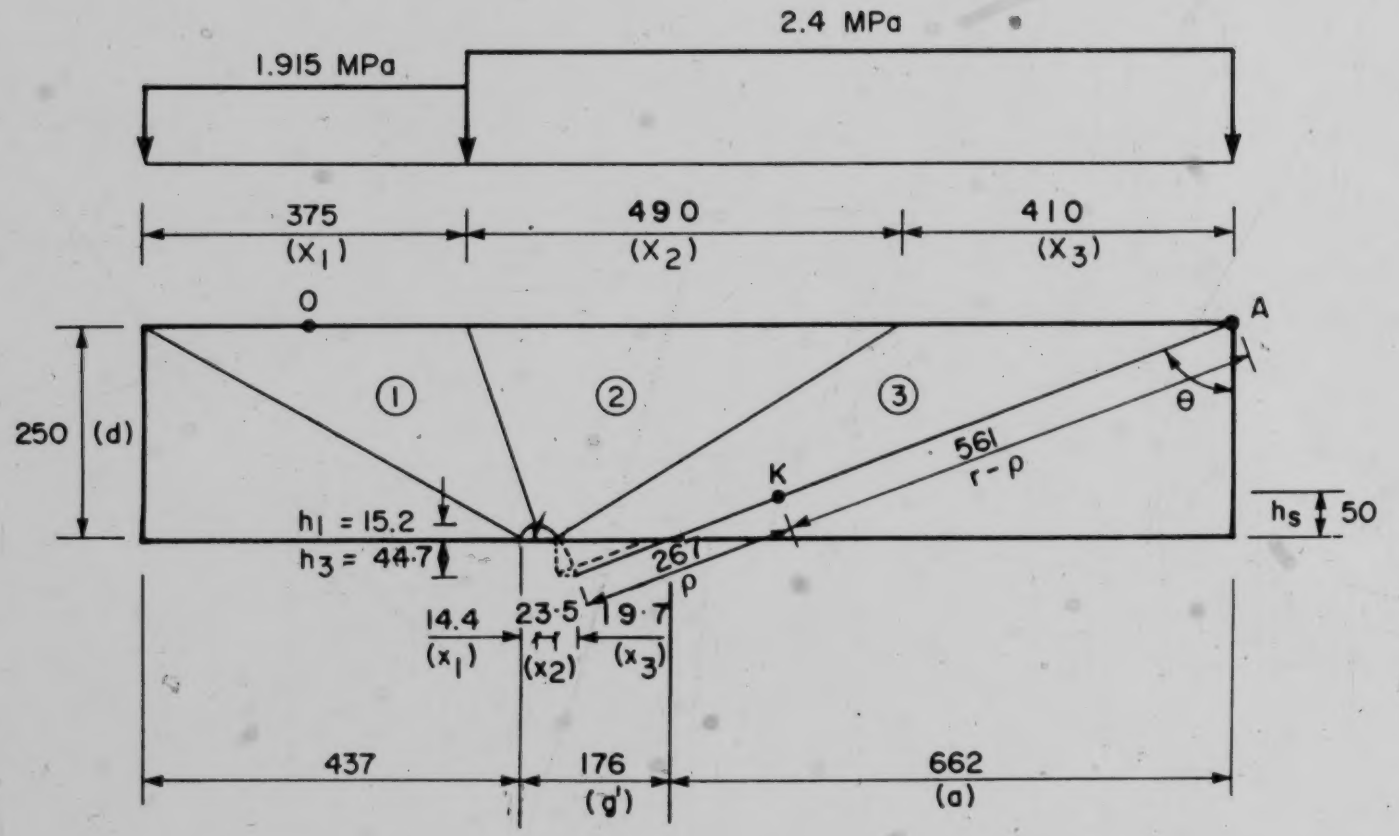

Figure B.3 Basic stress field for the B6 series with uniform loading.

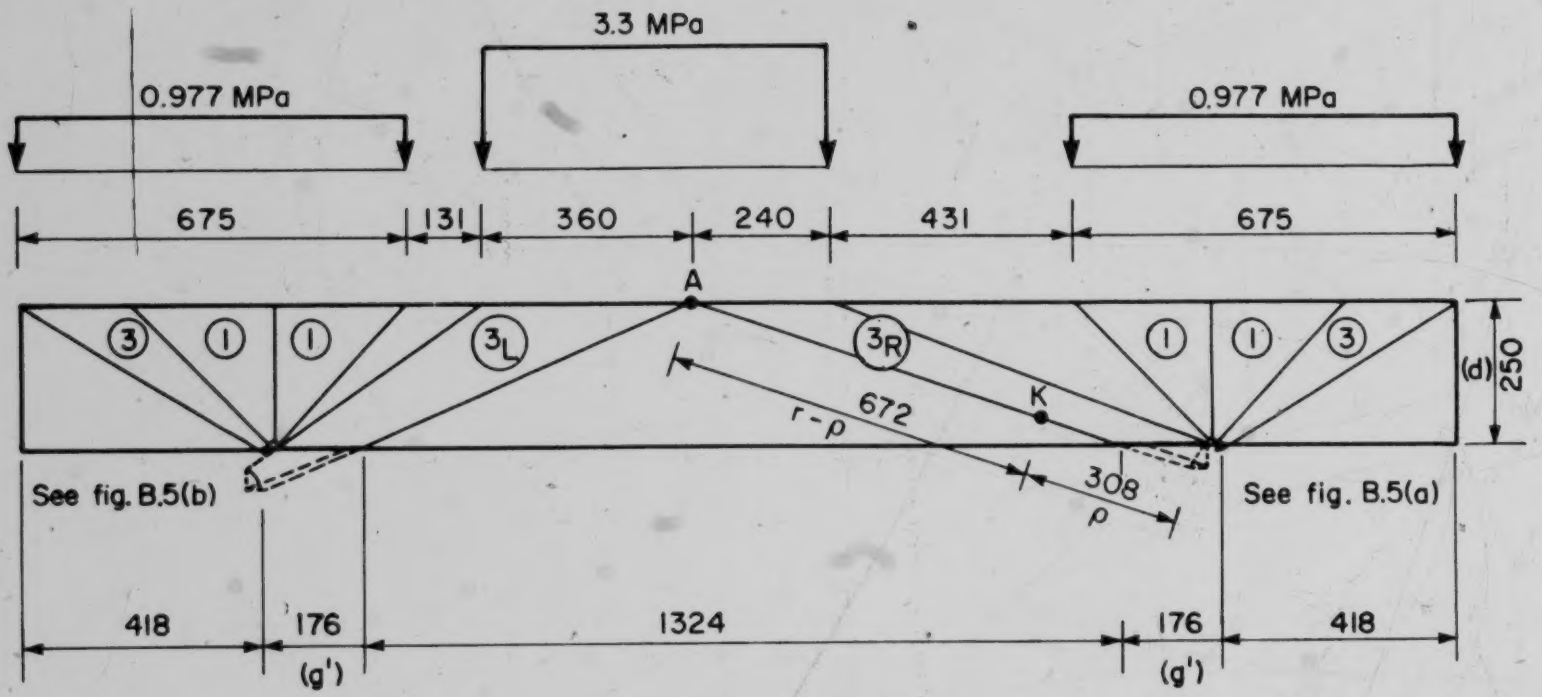

Figure B.4 Basic stress field for for specimen B6/7 with a patch load.

The patch load is transferred to the supports through two Zone 3 fans, designated as Zone 3_L and Zone 3_R. It is initially assumed that the imaginary hydrostatic node in Zone 3_R is in the optimum position (i.e. it is assumed that failure would occur in this span). The proportion of the patch load which is carried through Zone 3_R is obtained through trial -and-error by examining the equilibrium of Zone 3_R as follows:

1. Assume that the Zone 3_L:Zone 3_R split for the 600 mm patch load is 360 mm:240 mm.
2. Σ (Forces in the vertical direction) = 0:

$$x_{3R} = \frac{3.3 \times 240}{50}$$

$$= 16 \text{ mm.}$$

3. Then, h_{3R} is determined graphically to be 46 mm, as shown in Fig. B.5(a).
4. Calculate the overturning moment M_o

$$M_o = 3.3 \times 240 \times (675+431+120-20-8)$$

$$= 6.2 \times 10^5 \text{ Nmm}$$

and the restoring moment M_R

$$M_R = 50 \times 46 \times (250+23)$$

$$= 6.3 \times 10^5 \text{ Nmm.}$$

Since $M_o \cong M_R$, Zone 3_R is in equilibrium, and the assumed 360 mm:240 mm split is correct.

Zone 3_L is now checked for equilibrium under the applied load p = 3.3 MPa, as follows:

1. Σ (Forces in the vertical direction) = 0:

$$x_{3L} = \frac{3.3 \times 360}{50}$$

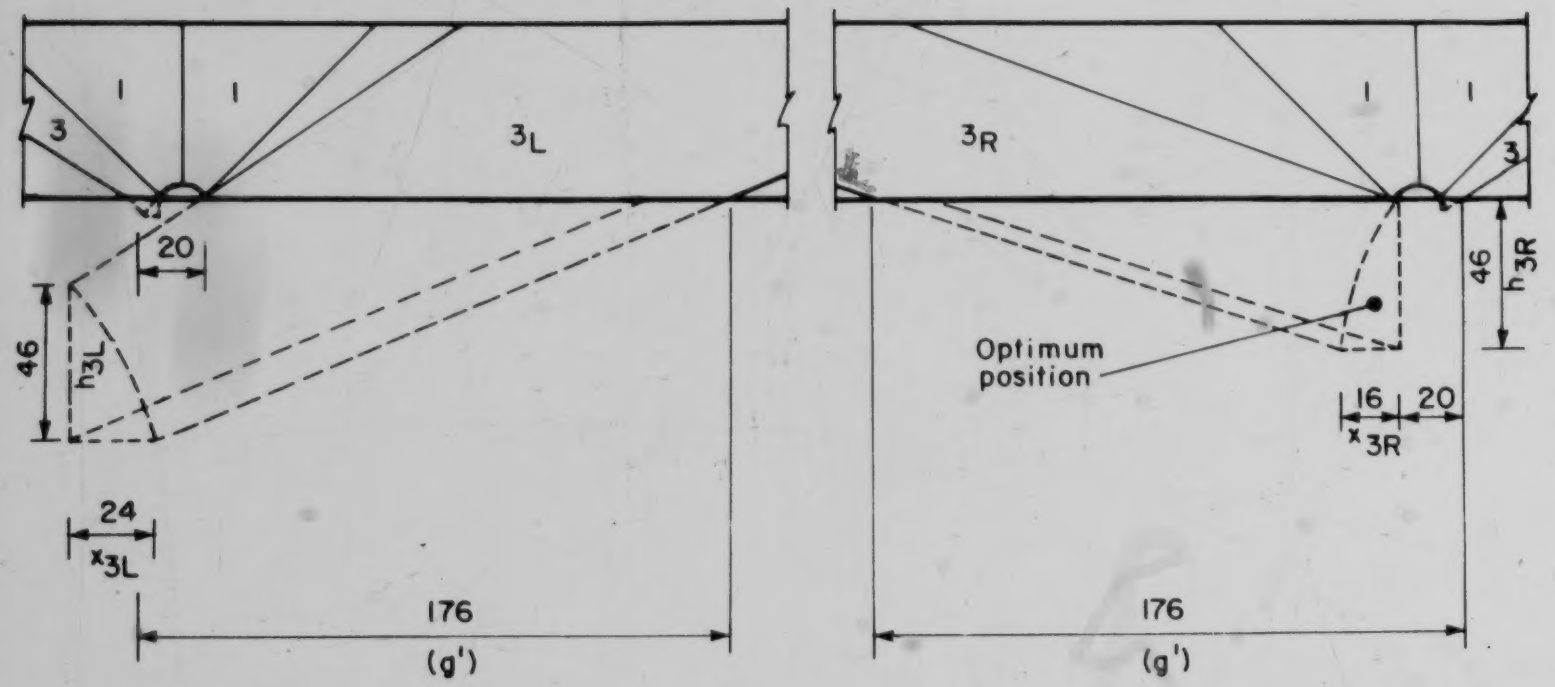

Figure B.5 Details of the construction of the imaginary hydrostatic nodes near the supports of specimen B6/7.

$= 23.7$ mm.

2. The requirement of constant tension in the support plate demands that

$$h_{3L} = h_{3R}$$
$$= 46 \text{ mm},$$

and the imaginary node may therefore be fitted graphically as shown in Fig B.5(b).

3. The overturning moment M_o is calculated as

$$M_o = 3.3 \times 360 \times 586$$
$$= 7.0 \times 10^5 \text{ Nmm},$$

since the horizontal lever arm is scaled as 586 mm. The restoring moment M_R is

$$M_R = 50 \times 46 \times 306$$
$$= 7.0 \times 10^5 \text{ Nmm},$$

since the vertical lever arm is scaled as 306 mm.

Since $M_o = M_R$, Zone 3_L is also in equilibrium, $p = 3.3$ MPa is the correct applied load.

If a different (incorrect) value for p had been initially chosen, the split of the patch load between Zones 3_L and 3_R would have been different, and rotational equilibrium would not have been satisfied in Zone 3_L. If the imaginary hydrostatic node had been located at the optimum location in Zone 3_L instead of in Zone Zone 3_R, then for equilibrium to be satisfied in both Zones 3_L and 3_R, the hydrostatic node on the right hand side would have been located within the concrete core. This situation is statically inadmissible ,since it would not be possible to

equilibrate the vertical face of the node.

APPENDIX C: REGRESSION ANALYSIS TO DETERMINE AN EXPRESSION FOR THE EFFECIVENESS FACTOR υ.

The regression analysis was performed using the statistical package Minitab (Ryan et al., 1985), and the output is given in the last two pages of this Appendix. The input data for the analysis have been calculated in Table 6.2. The following notation is used in the output:

υ V

$\frac{1}{\sqrt{f'_c}}$ 1/rfc

$\frac{G_K}{\sqrt{f'_c}}$ ..... GK/rfc

From the Minitab output, it is seen that the regression equation is

$$\upsilon = 3.25\left[\frac{1}{\sqrt{f'_c}}\right] + 0.0239\left[\frac{G_K}{\sqrt{f'_c}}\right].$$

From tables for the F-distribution, it can be seen that if the variables $1/\sqrt{f'_c}$ and $G_K/\sqrt{f'_c}$ were not affecting the response variable υ, there would be only a 1% probability of obtaining an F-ratio above 7.21. In fact, the Minitab output indicates that the F-ratio (= mean square for regression/mean square for error) is 8.7590/0.0052 = 1684, and the p-value (i.e. the probability of obtaining a sample

result at least as extreme as this) under the hypothesis that the variables $1/\sqrt{f'_c}$ and $G_K/\sqrt{f'_c}$ are not affecting the response μ is practically zero.

It is also noted that the t-ratios for the effects of the variables $1/\sqrt{f'_c}$ and $G_K/\sqrt{f'_c}$ individually are 6.33 and 9.58. These are highly significant. In fact, from tables of the t-distribution with 11 degrees of freedom, the probability of obtaining a value in excess of 3.106 is only 0.5%. Thus there is high statistical evidence that neither of the input variables $1/\sqrt{f'_c}$ and $G_K/\sqrt{f'_c}$ should be ignored.

MINITAB OUTPUT

The input data from Table 6.2 are echoed:

ROW	V	1/rfc	GK/rfc
1	0.948	0.1261	26.229
2	1.054	0.1266	22.649
3	0.985	0.1277	22.731
4	1.042	0.1257	26.296
5	1.194	0.1355	29.675
6	1.161	0.1289	28.448
7	1.357	0.1591	35.209
8	1.155	0.1277	35.284
9	1.627	0.1497	42.066
10	1.576	0.1470	41.366
11	0.941	0.1433	17.253
12	0.894	0.1403	16.822
13	0.863	0.1391	16.748

The regression equation is
V = 3.40 1/rfc + 0.0243 GK/rfc

Predictor	Coef	Stdev	t-ratio
Noconstant			
1/rfc	3.4018	0.5371	6.33
GK/rfc	0.024324	0.002540	9.58

s = 0.07199

Analysis of Variance

SOURCE	DF	SS	MS
Regression	2	17.5180	8.7590
Error	11	0.0570	0.0052
Total	13	17.5750	

SOURCE	DF	SEQ SS
1/rfc	1	17.0425
GK/rfc	1	0.4755

Obs.	1/rfc	V	Fit	Stdev.Fit	Residual
1	0.126	0.9480	1.0670	0.0184	-0.1190
2	0.127	1.0540	0.9816	0.0201	0.0724
3	0.128	0.9850	0.9873	0.0204	-0.0023
4	0.126	1.0420	1.0672	0.0184	-0.0252
5	0.135	1.1940	1.1827	0.0204	0.0113
6	0.129	1.1610	1.1305	0.0196	0.0305
7	0.159	1.3570	1.3976	0.0243	-0.0406
8	0.128	1.1550	1.2926	0.0300	-0.1376
9	0.150	1.6270	1.5324	0.0366	0.0946
10	0.147	1.5760	1.5062	0.0361	0.0698
11	0.143	0.9410	0.9071	0.0368	0.0339
12	0.140	0.8940	0.8864	0.0361	0.0076
13	0.139	0.8630	0.8806	0.0357	-0.0176